

MULTIMODAL SPECTROSCOPY AND IMAGING OF CHABAZITE ZEOLITE

Naomi Elyse Omori

Department of Chemistry

University College London

Thesis submitted for the degree of Doctor of Philosophy

2020

Declaration

I, Naomi Omori, confirm that the work presented in this thesis is my own except as specified in the text and acknowledgements.

.....

Abstract

Zeolites are a type of crystalline aluminosilicate material that when produced synthetically find use in a variety of contexts, many of which are directly beneficial to society at large. One such application, which is of interest not only from the perspective of commercial profitability but perhaps more pertinently in today's climate from an environmental point of view, is catalysis. Two important examples of commercialised catalytic reactions are selective catalytic reduction (SCR) and the methanol-to-olefins (MTO) reaction, which, respectively, involve the catalytic conversion of noxious NO_x gases to nitrogen & water, and waste methanol to higher value petrochemicals.

A central challenge in catalysis is the development of characterisation techniques capable of navigating the structurally and compositionally complex internal landscapes of zeolitic catalysts. While the bulk scale information gleaned through techniques like mass spectroscopy, XRD, and NMR provide an established benchmark against which zeolite behaviour is currently assessed, gaining spatially resolved insight into catalytic activity on a nanometric, single-catalyst length scale is highly desirable in current research efforts focused on optimising and improving existing catalytic systems.

Laser-based characterisation, being non-destructive and capable of molecular excitation, is identified here as a viable but underexplored option for studying zeolites in a catalytic chemistry context. Time-resolved photoluminescence spectroscopy (TRPS) and confocal-lifetime microscopy are applied to zeolite systems, providing fresh insight into aspects of the zeolite's synthesis process. TRPS is further combined with *in situ* setups to provide new information on zeolite behaviour during an active catalytic reaction as a function of time and temperature. Finally, combined IR spectroscopy and X-ray microscopy studies were conducted on Cu-containing forms of the high silica form (SSZ-13) of the zeolite chabazite (CHA).

Impact Statement

Zeolites are a group of materials that have a range of high-interest commercial applications, one of which is the multimillion-pound chemical catalysis industry. The work in this thesis has focused on applying advanced laser-based characterisation techniques such as time-resolved photoluminescence spectroscopy, confocal imaging, and Raman spectroscopy, which are not commonly utilised in the zeolite field, to provide new information on organic species adsorbed to zeolite frameworks. This is an important result because carbon-based molecules are notoriously difficult to visualise. Of particular relevance are the insights gleaned into calcination procedures in zeolites including the effect of temperature and the impact this may have on structural integrity. Additionally, the *in situ* experimentation tracking the methanol-to-olefins reaction demonstrates the scope for monitoring catalytic reactions in real time and generating meaningful data on chemical speciation.

The techniques used have been shown to be non-invasive, flexible, cost-effective, and capable of being coupled to *in situ* setups. Further to this, these techniques do not require samples to be modified. This is most successfully showcased in the label-free imaging studies of calcined zeolite samples. In a first for the field, the thesis presents a series of 3D images and fluorescence lifetime maps generated exclusively using the zeolite's autofluorescent signal, enabling conclusions of a chemical nature to be drawn.

Ultimately, the value of the project extends beyond the realm of catalytically active zeolites as the techniques may feasibly be applied to other inorganic functional materials including supported catalysts, gas storage materials, and other hybridised organic frameworks.

Acknowledgements

Sincere thanks first and foremost go to my primary supervisor Professor Andrew Beale for his undeterred open-mindedness that has always been in support of an exploratory and at times uncertain project. I credit my appreciation of the research process to his intelligent and pragmatic direction. I extend my gratitude to Johnson Matthey for sponsoring this project, and to my industrial supervisor Dr Paul Collier who consistently championed the project in an unfailingly optimistic manner. I also thank the staff of the Central Laser Facility who collectively devoted a significant amount of time and expertise to many of my experimental endeavours, including Professor Stan Botchway, Dr Igor Sazanovich, Dr Andy Ward, and Professor Pavel Matousek.

I take this opportunity to acknowledge the constellation of individuals I interacted with who each helped me in a different way at various points in my journey including Dr Ines Lezcano-Gonzalez, Emma Campbell, Peixi Cong, Dr Wilm Jones, Dr Yaroslav Odarchenko, Dr Kathryn Welsby, Dr Kay Sowoidnich, and Dr Abdullah Ahmed among many others. Special thanks go to Dr Leila Negahdar, Connor Barker, Dr Sara Mosca, and Dr Alex Greenaway.

Central to the success of many of the spectroscopic experiments was Dr Gianluca Valentini and his group at the Politecnico di Milano. I am extremely grateful for the collaborative opportunity he granted and the hospitality his group extended. Above all, I express my gratitude to Dr Alessia Candeo, without whom this collaboration would not have been possible. I count myself as highly fortunate for having crossed paths with her.

Finally, I thank my family including my parents, Dr Masaharu Omori and Elizabeth Omori, my brother Conan Omori, and my partner Dr Mantas Malys.

List of Acronyms

BAS	Brønsted acid sites
BET	Brunauer-Emmett-Teller
CCD	Charge-coupled device
DFT	Density Functional Theory
EPR	Electron paramagnetic resonance
ESR	Electron spin resonance
IR	Infrared
NIR	Near-infrared
NUV	Near-ultraviolet
OSDA	Organic structure directing agent
SEM	Scanning electron microscopy
TCSPC	Time correlated single photon counting
TGA	Thermogravimetric analysis
TMAda	Trimethyl-1-adamantamonium hydroxide
TRPS	Time resolved photoluminescence spectroscopy
UV-Vis	Ultraviolet-Visible
XANES	X-ray absorption near edge spectra
XRD	X-ray diffraction
XRF	X-ray fluorescence

Contents

Abstract	2
Impact Statement	3
Acknowledgements	4
List of Acronyms	5
The Scope of the Thesis	12
1 What is a Zeolite?	15
1.1 In Search of a Definition	15
1.2 Composition	17
1.3 Structure	18
1.4 Properties	22
2 Why are Zeolites Useful?	26
2.1 Zeolites in Industry	26
2.2 Zeolites in Research	30
3 How are Zeolites Made?	32
3.1 Hydrothermal Synthesis	32
3.2 Detemplation	33
3.3 Ion Exchange	34
4 How are Zeolites Characterised?	34
4.1 Standard Characterisation	35
4.2 Advanced Characterisation	35
1 Introduction to Photoluminescence	38
1.1 A Preamble	38
1.2 Photoluminescence in Molecules	38

1.3	Photoluminescence in Solids	44
1.4	Quantifying Photoluminescence	46
1.5	Measuring Photoluminescence	48
2	Photoluminescence in Zeolites.....	50
2.1	On Prior Art: The Aim of Previous Photoluminescence Studies	50
2.2	Studies of Introduced Photoluminescence	50
2.3	Studies of Intrinsic Photoluminescence	52
1	Introduction.....	55
2	Lasers	55
2.1	Principle of Operation.....	55
2.2	Construction.....	56
2.3	Modes of Operation	58
3	Laser-Based Characterisation Techniques	60
3.1	Time-resolved Photoluminescence Spectroscopy (TRPS).....	60
3.2	Confocal Laser Scanning Microscopy (CLSM).....	66
3.3	Fluorescence Lifetime Imaging (FLIM)	68
3.4	Raman Spectroscopy.....	70
4	Preliminary ‘Standard’ Zeolite Background Characterisation	72
4.1	Zeolite Background.....	72
4.2	X-Ray Diffraction (XRD)	72
4.3	SEM	74
4.4	TGA	75
4.5	UV-vis.....	77
5	Sample Preparation	78

1	Introduction	81
2	Experimental Section.....	82
2.1	Sample Preparation.....	82
2.2	Theoretical Calculations	83
2.3	Raman Spectroscopy	84
2.4	Time-Resolved Photoluminescence (PL) Spectroscopy and Data Analysis	84
3	Results & Discussion.....	86
3.1	Defining Organic Products Present During Detemplation	86
3.2	Effect of Confinement on Template Emission Inside Zeolite Pores	88
3.3	Proliferation of Carbonaceous Deposits in Part-Calcined Sample	93
3.4	Depletion of Template Signature from Uncalcined to Calcined Sample.....	97
3.5	Conclusion.....	100
1	Introduction	103
2	Experimental Section.....	105
2.1	Sample Preparation.....	105
2.2	Time-Resolved Photoluminescence (PL) Spectroscopy and Data Analysis	105
2.3	Pulsed Laser Characterisation	105
2.4	Data Collection Method.....	106
3	Results	107
3.1	Calcined Chabazite	107
3.2	Uncalcined Chabazite	109
3.3	Gated Spectra.....	110
3.4	Peak Intensity Analysis	111
4	Discussion.....	112

4.1	Effect of laser power on emission spectrum	112
4.2	Effect of temperature on emission spectrum.....	113
4.3	Conclusion	113
1	Introduction.....	116
2	Experimental Section	118
2.1	<i>In situ</i> Setup	118
2.2	Temperature Protocol.....	119
2.3	Si-only SSZ-13 Characterisation	121
3	Results.....	123
3.1	Uncalcined SSZ-13	123
3.2	Silicon-only SSZ-13.....	139
4	Discussion	143
4.1	Initial Observations	143
4.2	High Temperature Photoluminescence and Formation of Point Defects	144
4.3	Quenching Effects.....	155
5	Method	157
6	Results.....	157
6.1	Visual Changes	157
6.2	Continuous Wave Spectra.....	160
6.3	Mass Spectrometry.....	164
7	Discussion	164
7.1	Product Formation Leads to Quenching at High-Temperature	164
7.2	Evolution of Band Structure due to Product Formation.....	165
7.3	Active Reaction Sites	167

8	Conclusion.....	168
1	Introduction	171
2	From Spectroscopy to Imaging.....	174
2.1	Wavelength of Excitation	174
2.2	Signal-to-Noise.....	175
3	Method.....	176
3.1	Sample Preparation.....	176
3.2	Imaging.....	176
3.3	Raman Spectroscopy	177
4	Results	179
4.1	SEM Imaging.....	179
4.2	Confocal and Fluorescence Lifetime Imaging (FLIM)	182
4.3	Raman Spectroscopy & Mapping.....	202
5	Discussion.....	208
5.1	Ascribing Fluorescence to Chemical Speciation	208
5.2	Evidence of Different Emissive Species	215
5.3	Evidence of Morphological Features.....	219
5.4	Spatial Distributions of Emissive Sites Indicate Position of Brønsted Acid Sites	222
6	Conclusion.....	224
1	Introduction	229
2	Methods	232
2.1	Sample Preparation.....	232
2.2	Preliminary Zeolite Characterisation.....	232
2.3	Advanced Characterisation.....	233

3	Results & Discussion	234
3.1	Preliminary Zeolite Characterisation	234
3.2	Advanced Characterisation	238
3.3	Conclusion	243
1	Summary of Chapters	244
2	Considerations for the Presented Work	247
3	Future Work	248
	References	250

The Scope of the Thesis

Zeolites are known to exhibit complex photoluminescence behaviours that are not yet comprehensively understood. Photoluminescence is a form of light emission that can be measured and even mapped to create images. Traditionally in zeolite research, the laser-based techniques of spectroscopy and confocal imaging used to measure photoluminescence are not established as industry-standard characterisation methods. Similarly, for experienced spectroscopy and imaging practitioners, zeolites may represent a less frequently encountered subject of experimentation. And while certainly not the first to utilise such techniques for zeolite characterisation, the premise of this project represents a relatively untrodden bridge at the confluence of two traditionally disparate streams of research. The overarching research question for this project was to determine whether it is possible to utilise photoluminescent signal to gain new insight into the behaviour and catalytic potential of zeolites. Happily, we can conclude that the answer to this question is, yes.

The aim of the first two chapters of this thesis is to prime a reader with a broad yet functional context of the two major focus areas for this thesis: zeolites in Chapter One, and photoluminescence in Chapter Two. Subsequent chapters present novel pieces of research utilising time-resolved photoluminescence spectroscopy, *in situ* experimentation, and advanced multimodal imaging of zeolites.

Time-resolved photoluminescence spectroscopy has mainly been used in photonics applications of zeolites to understand how dyes are affected by confinement. This work builds on this catalogue of work but uses experimental conditions that are catalytically relevant with *in situ* configurations, higher temperatures, and industrially relevant zeolite frameworks. Rather than using zeolites to create materials with engineered emissive properties that are then optimally characterised using photoluminescence spectroscopy, this research starts with crystals that are broadly representative of those used in industry and attempts to use photoluminescence spectroscopy to gain additional information on the samples.

The work in this thesis is differentiated from existing work in the following ways:

- It probes photoluminescence from metal-free, dye-free zeolites
- It uses a high sensitivity setup designed for lowly emissive solid samples
- It monitors a wide time-gate extending into the microsecond regime owing to the use of a Q-switched laser
- It measures the effects on systems *in situ* under temperatures as high as 600 °C
- It does not use oversized zeolite crystals

Chapter I

An Introduction to Zeolites

1 What is a Zeolite?

1.1 In Search of a Definition

We start by introducing the material that forms the basis of all experimentation presented in this thesis: zeolites. The first documented studies of zeolites were conducted by mineralogist Axel Cronstedt in 1756. He coined the term by amalgamating the Greek terms ‘zeo’, meaning to boil, and ‘litho’, meaning stone, to describe a unique mineral materialⁱ originating from a volcanic deposit in Northern Sweden that would have seemed at first glance as unremarkable as any other rock had it not also appeared to intumesce and generate large amounts of steam upon heating. Upon further inspection, mineralogists realised that this was only one of a zeolite’s many fascinating properties, and much of the work conducted throughout the 1800s and into the early 20th century was focused on documenting the chemical behaviours of what they increasingly understood to be a class, rather than just a single type, of special materials. These properties included their reversible dehydration & ion exchange properties, adsorption behaviours as studied by Grandjean in 1909¹ with his work on chabazite adsorption of ammonia, hydrogen, and air, and molecular sieve properties as reported by Weigel and Steinhoff in 1925². Early historical definitions identified zeolites as aluminosilicates with open tetrahedral frameworks that allowed for reversible dehydration and ion exchange. While useful in differentiating zeolites from other types of aluminosilicate materials, the property-centric definition did not readily lend itself towards the classification of zeolites. Proposed classification systems that did exist remained convoluted such as Hey’s 1935³ proposal that attempted to classify zeolites based on dehydration characteristics, or acid species in the case of a system used by Dana in 1942⁴.

Although early attempts were made to conceptualise structure, such as Friedel’s work of 1896 that proposed zeolites possessed open spongy frameworks, it was not until 1930 that the first work on natrolite and feldspathoid structures using oscillation and Laue photographs was published by Linus Pauling^{5,6}. Structural characterisation represented an important shift in the way zeolites were viewed. Rather than being minerals exhibiting special properties, it became increasingly clear that zeolites also had complex, multi-layered structural hierarchies that presented new scope for definition and classification. Advances in characterisation techniques and synthesis methods meant that from the 1940s onwards, zeolite studies began to move out of the remit of mineralogists and into the hands of crystallographers and chemists. Pioneering work in the mid-century conducted by Robert Milton at Union Carbide saw his collaborators determining the structures of the newly synthesised zeolite A⁷, zeolite X, and faujasite frameworks using single crystal x-ray data around 1954, prompting a growing body of work within the zeolite community that has to

ⁱ This particular zeolite was more recently established as stilbite⁴²².

date identified 248⁸ unique zeolite frameworks. The deeper understanding of framework structure arising from sophisticated crystallography techniques facilitated more unambiguous structural means of classification, many of which were proposed through the 1960s by Breck⁹, Fischer & Meier¹⁰, and Smith¹¹. However, it also meant that something of a definition debate¹² began to arise in the 1980s, with some researchers advocating a more relaxed approach to the traditional properties-based definition of a zeolite, instead offering definitions that paid greater attention to the geometrical features of the frameworks redefining zeolites as materials “containing tunnels or larger polyhedral cavities interconnected by windows large enough to allow ready diffusion of the polyatomic guest species through the cavities”¹³. The discovery of a new aluminophosphate family of materials in 1982 that featured all the structural properties of zeolites in the absence of silica also served to challenge pre-existing notions of what constituted a zeolite.

The historical struggle to agree upon a definition of what a zeolite is parallels an important point regarding the nature of zeolite research as a whole. Complex and still not wholly understood, the study of zeolites is a deeply applied field of science that has since its inception been greatly interested with the practical applications of the fascinating chemical properties they display. Even today, the quest to understand the more fundamental intricacies of zeolites, such as structure, composition, or mechanisms of action, is an iterative narrative that continues to be developed in tandem with a topical body of research that pertains to well-established and extremely high value industrial applications. Where historically improvement in zeolite-based industrial process output was achieved through educated trial-and-error primarily guided by a researcher’s experience and intuition, significant advances in industrial optimisation in the 21st century have been borne of developments in characterisation technologies that allow researchers to obtain a deeper academic understanding of the materials in question and retrospectively make changes to existing operational parameters. Equally, the search for an appropriate definition of a zeolite is something that has developed, and likely will continue to develop, over time and may be slightly different depending on whether a more academic or industrially pragmatic approach is being adopted.

The International Zeolite Association (IZA) diplomatically considers structure, composition, and properties in their most up-to-date definition⁸ of a zeolite:

Classically, zeolites are defined as aluminosilicates with open 3-dimensional framework structures composed of corner-sharing TO₄ tetrahedra, where T is Al or Si. Cations that balance the charge of the anionic framework are loosely associated with the framework oxygens, and the remaining pore volume is filled with water molecules. The non-framework cations are generally exchangeable and the water molecules removable. This definition has since been expanded to include T-atoms other than Si and Al in the framework, and organic species (cationic or neutral) in the pores.

In defiance of brevity, it is a surprisingly open-ended definition, being required to capture three important definitional parameters. The following sections will elaborate upon these parameters, which are namely composition, structure, and chemical properties.

1.2 Composition

Zeolite composition can be broken down into three components. They are the framework, extraframework cations, and a sorbed phase.

The *framework* is the most structurally prominent component of the zeolite, and is made up of silicon, aluminium, and oxygen. Silicon is the principal element of the framework and co-ordinates tetrahedrally with oxygen, as shown in Figure 1. The silicon sites are also termed T sites, where T denotes the tetrahedra of the TO_4 configuration. In historical definitions of zeolites it is the T sites that previously only applied to silicon or aluminium, although in recent decades certain definitions, such as the IZA one presented previously, have been relaxed to include other atoms like phosphorous as present in silicoaluminophosphate molecular sieves (SAPOs)¹⁴.

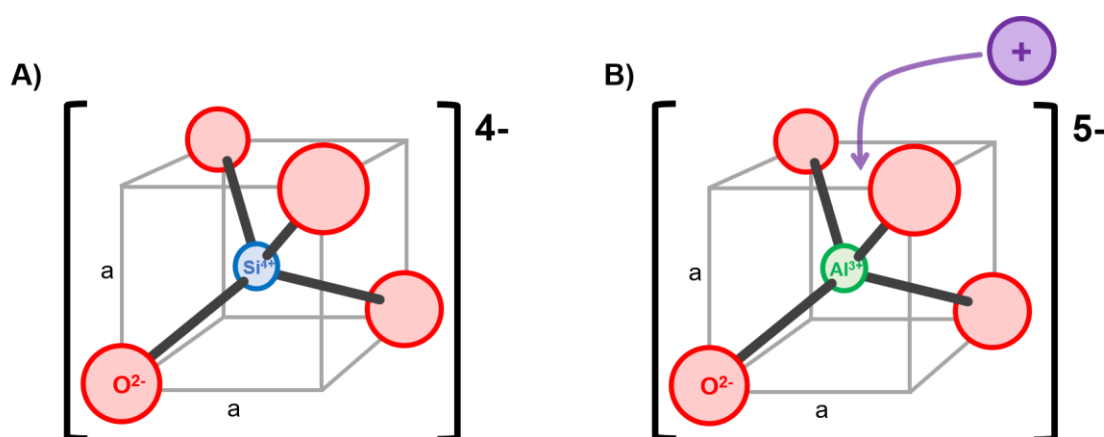


Figure 1 Understanding charge compensation in a dominantly silicon framework: A) Tetrahedral silicon configuration showing Si^{4+} (blue), occupying the T-site, co-ordinating to four O^{2-} (red) bridging atoms producing an overall neutral charge when co-ordinated to other Si-occupied T-sites, and B) Al^{3+} (green) substitution into the T-site generates an excess negative charge requiring charge compensation from a cation (purple). It is largely assumed that the position of the Al-occupied tetrahedra defines the location of the extraframework cationic species, as indicated here. This is relatively applicable for univalent cations (e.g. H^+ , Na^+ , NH_4^+) but is not necessarily applicable in cations with higher charge.

When trivalent aluminium (Al^{3+}) is isomorphically substituted into the dominantly silicon tetravalent (Si^{4+}) framework, an excess negative charge is generated. To achieve net lattice neutrality, a compensating positive cation is required to balance the charge. These may be from the alkali or alkaline earth groups, or with R_4N^+ (where $\text{R} = \text{H}$, aryl, alkyl) cations. These are *extraframework cations* and are associated with the framework by steric effects and electrostatic interactions. Extraframework cations have rich potential for changing the overall composition of the zeolite as they can be swapped with different types of ions. Following calcination, the final step of the synthesis process discussed in greater detail in Section 3, R_4N^+ transform into protons creating a strongly acidic catalyst due to the formation of Brønsted acid sites. Conversely, group IA & IIA compensated cations can be ion-exchanged for metals like copper or iron. Basic compositional variation through extraframework cations is of interest because it can drastically alter the chemical properties and performance of the zeolite.

A fundamental compositional consideration of the framework is the silicon-to-aluminium ratio (Si/Al, which describes the amount of aluminium present, and to an experienced zeolite scientist may give some indication about the properties and stability of the sample. A higher aluminium loading, for example, is associated with a higher degree of acidity. The limits of the SAR range from 1 to infinity, with a low SAR considered as under 5, a medium SAR as between 5 to 10, and a high SAR being over 10¹⁵. A related variant is the silica-to-alumina ratio, which reflects the ratio of feedstock materials used during the synthesis process.

Additionally, the pores of zeolites are often occupied with a *sorbed phase*. Being hygroscopic, this sorbed phase is commonly water, which often needs to be removed to vacate the microporous volume prior to using the zeolite in a chemical application. It is also possible to have an organic phase present in the cages, as is the case in as-made zeolites synthesised with an organic structure directing agent (OSDA), and similarly may require removal via thermal processes prior to zeolite usage.

All this compositional information may be generalised into the following empirical formula:

$$x_1 M_1^{n_1+}; x_2 M_2^{n_2+}; [(y_1 T_1; y_2 T_2 \dots) O_{2(y_1+y_2+\dots)}]^{x-} z_1 A_1; z_2 A_2 \dots$$

where M is the cation with charge n_1, n_2 that compensates the negative framework charge ($x_1 n_1 + x_2 n_2 + \dots = x$)

T are the tetrahedrally co-ordinating elements (i.e. Si, Al)

A is the water or ion pairs

1.3 Structure

In the diagram of tetrahedrally co-ordinated silicon in Figure 1, we start to get some indication about how structure begins to form. Unlike metals, zeolites, with their predominantly covalent bonding, do not form close-packed structures. Rather they are open structures with significant volumes of internal space. Like Lego pieces, if tetravalent units are the primary building blocks, it is possible to join these pieces into slightly larger units called secondary building units (or SBUs) as shown in Figure 2 where the corners of the polyhedra correlate with T atomsⁱⁱ. In a modular fashion, these SBUs may be pieced together in various ways to create unique zeolite frameworks.

ⁱⁱIn diagrammatic representations of zeolite frameworks, the most frequently encountered of which are of the ball-and-stick type as shown in Figure 2, the countercations and the oxygen atoms are not explicitly marked out and removed for clarity, with the balls marking out T sites, and bridging oxygens indirectly denoted by the sticks.

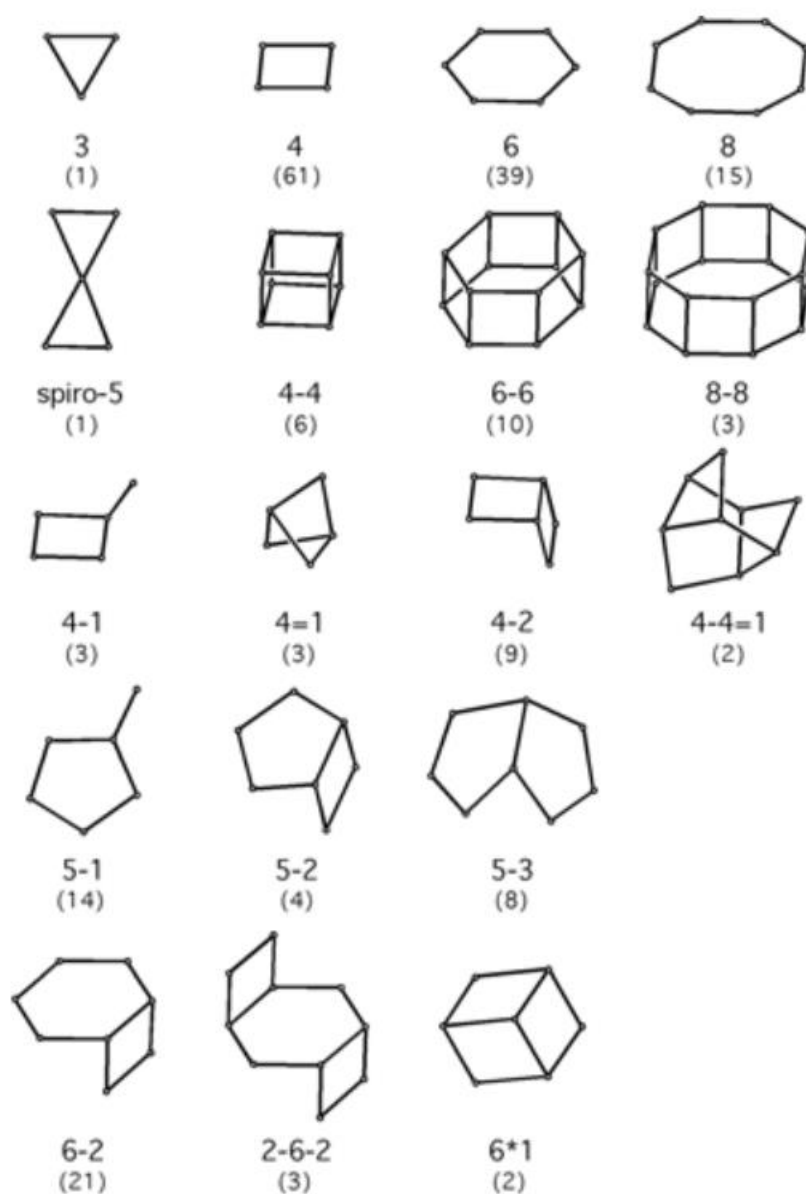


Figure 2 **Secondary building units and codes used to identify them.** Numbers in parentheses are the frequency with which the units feature in different frameworks. *Reproduced from the IZA Atlas of Framework Types*⁸.

Understanding zeolite structure by conceptually building them from the ground up out of finite units makes it easier to visualise the characteristic pore structures of zeolites, as they are most directly constructed out of these SBUs.

Alternatively, it is possible to take a top-down approach to structure by considering a zeolite as a crystal with long-range order and formalising the structure through constructs like crystal planes and larger, infinitely-repeating building blocks. More technically, this means defining structural parameters after performing geometrical refinement in the highest possible symmetry. This is a useful way to understand zeolite structure, not least because structural information from X-ray diffraction techniques pertains most directly to *hkl* planes in a crystal. More than this, combining

a ground-up with a top-down view of zeolite structure makes it possible to fathom zeolites as materials with rich, multi-layered structures that build and evolve over different length scales.

We so far understand that zeolites are solid, crystalline materials with open frameworks. Temporarily ignoring the implication of composition and chemical properties, let us consider the meaning of a structured solid. Crystalline materials are defined as having long-range order. The concept of ‘order’ is formalised through the lattice. The lattice is an abstract precursor to a zeolite’s actual structure and can be defined simply as a regular arrangement of points that propagate *ad infinitum* into space as shown Figure 3. The distance between each lattice point is further defined as a primitive vector. In two-dimensional space, the lattice will be defined in terms of two primitive vectors as demonstrated in Figure 3, where the vectors are labelled a and b . This is extended to three primitive vectors for crystals occupying three-dimensional space. The area bounded by the primitive vectors a and b is defined as the unit cell, shown by the shaded parallelogram in Figure 3, and represents the smallest repeating unit that the overall structure can be reduced down to. In principle, the environment of each lattice point should be equivalent to all other lattice points. In other words, if it were possible to sit on one of the lattice points and look at all the other lattice points around you in 360° , were you to move to another lattice point, the view of lattice points around you should appear identical to the view from your previous position. This concept of lattice point equivalence is how the term Bravais latticeⁱⁱⁱ is defined.

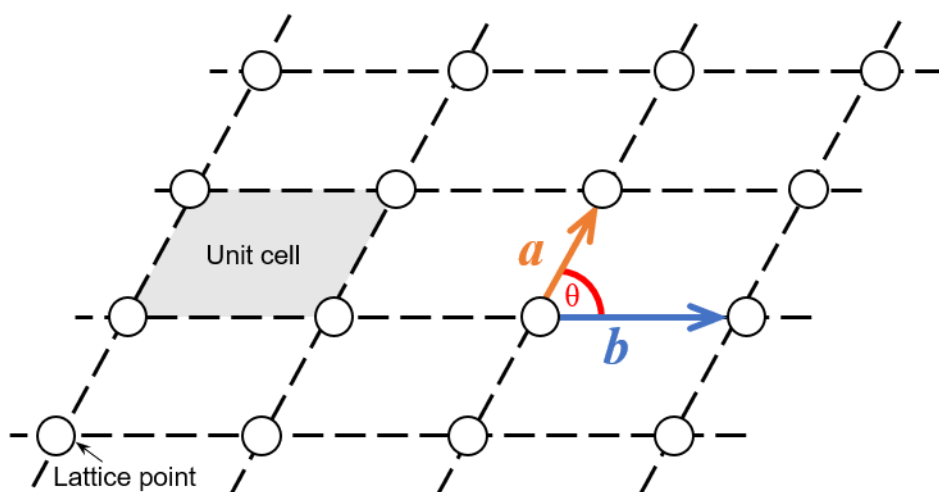


Figure 3 **Schematic diagram of a two-dimensional Bravais lattice** where lattice points are denoted by open circles, a and b are the primitive vectors, θ is the axial angle, and the shaded area represents a unit cell

In two-dimensional space there are four crystal families that may defined by the parameters in Table 1 and seven families in three-dimensional space. Note that the axial angle is defined as the angle formed between primitive vectors a and b . According to this table, we can tell that the lattice represented in Figure 3 is in fact a monoclinic crystal.

ⁱⁱⁱ The Bravais lattice can be described in more mathematical depth in terms of translation vectors, but this has been omitted for the sake of keeping this discussion focused on the meaning of structure in zeolites.

Table 1 Properties of crystal families in two and three dimensions including parameters for axial distances and axial angle and Bravais lattice families where *P* means primitive, *I* means volume centred, *C* means base centred and *F* means face centred. There are five 2D Bravais lattices and 14 3D Bravais lattices.

Crystal family	2D		3D		Bravais Lattice			
	Axial distances	Axial angle	Axial distances	Axial angle	<i>P</i>	<i>I</i>	<i>C</i>	<i>F</i>
Monoclinic	$a \neq b$	$\theta \neq 90^\circ$	$a \neq b \neq c$	$\alpha = \gamma = 90^\circ$ $\beta \neq 90^\circ$	<i>m</i> (2D) <i>mP</i> (3D)		<i>mS</i> (3D)	
Orthorhombic	$a \neq b$	$\theta = 90^\circ$	$a \neq b \neq c$	$\alpha = \beta = \gamma = 90^\circ$	<i>o</i> (2D) <i>oP</i> (3D)	<i>o</i> (2D) <i>ol</i> (3D)	<i>oS</i> (3D)	<i>oF</i> (3D)
Hexagonal	$a = b$	$\theta = 120^\circ$	$a = b \neq c$	$\alpha = \beta = 90^\circ$ $\gamma = 120^\circ$	<i>h</i> (2D) <i>hP</i> (3D)			
Tetragonal	$a = b$	$\theta = 90^\circ$	$a = b \neq c$	$\alpha = \beta = \gamma = 90^\circ$	<i>T</i> (2D) <i>tP</i> (3D)	<i>tl</i> (3D)		
Triclinic	-	-	$a \neq b \neq c$	$\alpha \neq \beta \neq \gamma$	<i>aP</i>			
Trigonal	-	-	$a = b = c$	$\alpha = \beta = \gamma \neq 90^\circ$	<i>hR</i>			
Cubic	-	-	$a = b = c$	$\alpha = \beta = \gamma = 90^\circ$	<i>cP</i>	<i>cl</i>		<i>cF</i>

It will suffice at this point to say that when the idea presented in Figure 3 is extended into three-dimensions, there are seven different crystal families and a total of 14 unique Bravais lattices when centring is taken into account, as shown in Table 1.

The explanation so far has not attempted to address any of the rules of symmetry that are so tantamount to crystallography. However, it is hoped that in considering free space and the seemingly infinite number of ways we may initially assume we can fill space with an ordered construct, a reader will appreciate how formalising the lattice as a set of vectors results, conveniently, in a relatively pared back list of options with which we can define a crystal.

As mentioned earlier, the lattice so far is an abstract point in space. Depending on the material, it is possible to have more than one atom repeated per lattice point, as shown in Figure 4. The unit that occupies a lattice point is termed a basis. The simplest basis exemplified in is a single atom, as would be found in a metallic crystal. It is also possible to have a basis with two atoms occupying a lattice point as exemplified with a real-life example of this being NaCl. Extending this idea, it is possible to imagine that as the basis becomes increasingly polyatomic as described in Figure 4, a more complex unit cell arrangement is produced, which is effectively the case in zeolites.

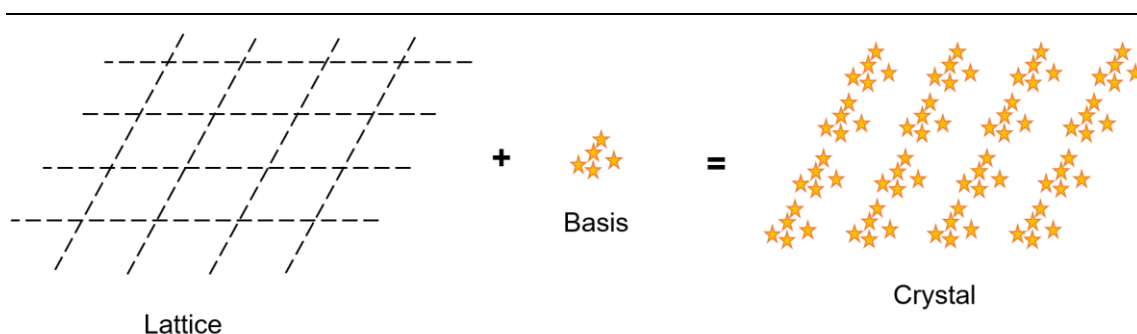


Figure 4 Schematic diagram in which the combination of the lattice with the basis describes the formation a crystal. An increasingly polyatomic basis yields a more complex crystal.

Where the lattice type and unit cell define the zeolite's crystallographic symmetry, the type of SBU and their configuration is what determines pore & channel diameter. In summary, zeolite structure is complex, and it is no coincidence that the increase in recognised framework types has been accompanied by significant advancements in X-ray diffraction characterisation capabilities.

1.4 Properties

Zeolites are frequently thought of in terms of their properties, the most important of which are their porosity, acidity, and their capacity for reversible dehydration. In discussing zeolite composition and structure, elements of these properties have already been indirectly explained.

1.4.1 Porosity

As discussed in Section 1.3, zeolites have complex, open frameworks. Owing to this high porosity, zeolites have large, highly accessible internal volumes. A typical void diameter may be between 0.2-0.8 nm, and a pore volume between 0.10 to 0.35 cm³/g. From a chemistry perspective these voids are considered to be quite large, and are capable of acting as 'molecular sieves', exercising size-selectivity to enforce a form of molecular traffic control over molecules moving in and out of the zeolites. Different frameworks feature different internal pore geometries, with some featuring a channel structure (e.g. MFI-type), and others featuring a pore-cage structure (e.g. CHA). These are harnessed in size-selective catalytic reactions, some of which are highlighted in Figure 5, where the nature of the pore structure dictates which reactants or products are permitted to diffuse through the framework¹⁶. In the case of reactant selectivity, reactants are required to be small enough to fit through the pores. Product selectivity is applicable to hydrocarbon pool mechanisms where bulkier molecules may be generated within the larger cages but fail to diffuse through the smaller channel openings. For restricted transition state selectivity as depicted in Figure 5C some reactions are limited because the transition state occupies more space than what is available inside the pores.

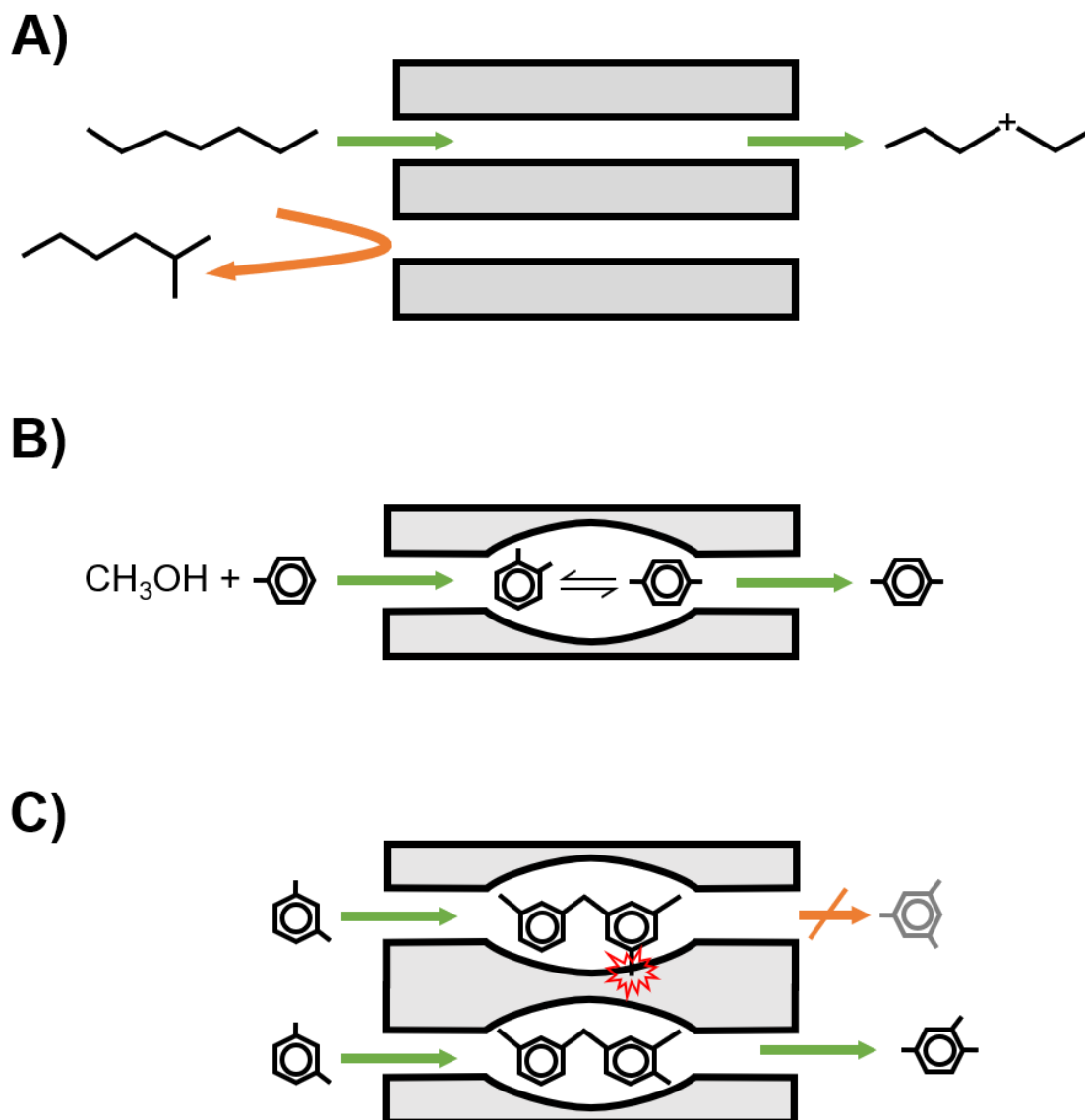


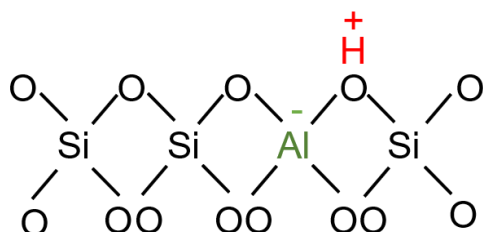
Figure 5 **Schematic diagram showing three types of shape selective catalytic processes** including A) reactant selectivity exemplified here with the cleavage of linear hydrocarbons, B) product selectivity exemplified here by the methylation of toluene, and C) transition state selectivity exemplified here by the disproportionation of *m*-xylene.

1.4.2 Acidity

An important feature of aluminium substitution is the generation of a negative charge, which requires charge compensation by a cation (as discussed in Section 1.2). When the framework charge is balanced by protons, a strong Brønsted acid site (BAS) is formed across the bridging Si-(OH)-Al site, as shown in Figure 6A. Generally, BASs give rise to the overall acidity of the zeolite, which in turn make them highly applicable in industrial catalytic reactions. They may be characterised in the IR spectrum as a band between 3650 and 3500 cm^{-1} ¹⁷ or in ^1H MAS NMR as a peak between 3.6-8 ppm¹⁸. Given they are closely linked to the presence of Al, changes in the silicon:aluminium ratio affect both the concentration and strength of the overall zeolite acidity.

Another form of acid site present in a zeolite are Lewis acid sites (LAS), shown in Figure 6, which arise on tricoordinate silicon or aluminium sites, here considered a small structure defect that acts as an electron-acceptor. LAS structures are varied and may be generated following heating as well as from extraframework alumina species, three-fold-coordinated alumina, and even silanol nests^{19,20}.

A) Brønsted acidity



B) Lewis acidity

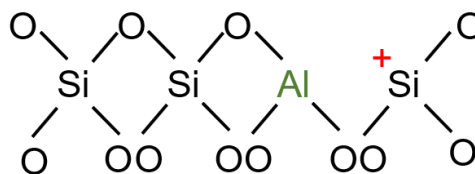


Figure 6 **Schematic diagram of aluminium substitution generating acidity within in a framework** showing A) Brønsted acid sites or B) Lewis acid sites

1.4.3 Reversible Dehydration

Reversible dehydration can be explained in terms of both their structure and bonding. High internal surface area, which may be as great as 300-700 m²/g, enables zeolites to accommodate large volumes of water^{21,22}. In thermal dehydration experiments that monitor water loss with temperature, it has been observed that volume changes occur across a range of temperatures. This can be explained by water being held across a range of semi-discrete energies dictated by different types of interactions with extraframework cation sites and framework atoms. Externally adsorbed water is thought to be bound more loosely than water contained within framework cavities. Within the internal pore structure, water is bound to extraframework cation sites with the degree of hydration inside the structure being heavily dependent on the hydration energy of the cations present. For example, cations with a higher hydration energy such as Ca²⁺ are able to retain more water to a higher temperature within the framework than cations with a lower hydration energy such as K⁺²³. Further to this, it is important to note that there is a spectrum across which the term ‘reversible’ holds true. While the term implies frameworks are unvarying in the face of thermal treatment, structural stability is often dependent on the type of framework and their charge, with some zeolites experiencing semi-permanent volumetric changes due to bond damage. Alberti and Vezzalini²⁴ proposed three categories of reversibility based on the structural effects observed before and after water loss: 1) reversible dehydration with no modification to the framework; 2) reversible dehydration with significant distortion of the framework and cell volume loss; and 3) partially reversible dehydration with breaking of T-O-T framework bonds.

Considering dehydration properties is relevant for two reasons. Firstly, it highlights how intrinsic the sorbed phase, as first mentioned in Section 1.2, is to the zeolite. Although sometimes desirable

to isolate the framework from a sorbed phase, even when handled carefully, thermal treatment is not always able to remove all water from the zeolite in an experimental setting. In some of the results presented in this thesis, it is necessary to consider the sorbed phase as an integral part of the zeolite system as a whole, rather than results that aim to solely probe the framework. Secondly, accounts of varied dehydration pathways²⁵ illustrate the internal zeolite environment as being dynamic landscapes. Rather than seeing frameworks as rigid, static scaffolds around which molecules adsorb and react, dehydration induces a state of flux within the framework where cation sites, unit cell parameters, and covalent bonds are liable to shift, change, and remodel themselves^{26,27}. This is an idea that shapes the interpretation of some of the results presented in this thesis.

2 Why are Zeolites Useful?

Over the years, the unique properties of zeolites discussed in Section 1 have been successfully translated into a number of exceedingly practical applications in industries ranging from automotive emissions control to agriculture. As such, zeolites command an exceedingly high combined market value and a large cost-saving potential, making them interesting research subjects for both industrial scientists and academics alike. Section 2.1 describes some commercially established industry applications zeolites are currently used in. Section 2.2 outlines novel applications of zeolites currently being investigated in an academic context. The research presented in this thesis has primarily focused on zeolites within a catalytic context, however, future areas of growth in the zeolite industry have been highlighted to suggest where the characterisation techniques studied in this project may also be applied.

2.1 Zeolites in Industry

Zeolites are used in three main industrial applications: catalysis, adsorption, and ion exchange.

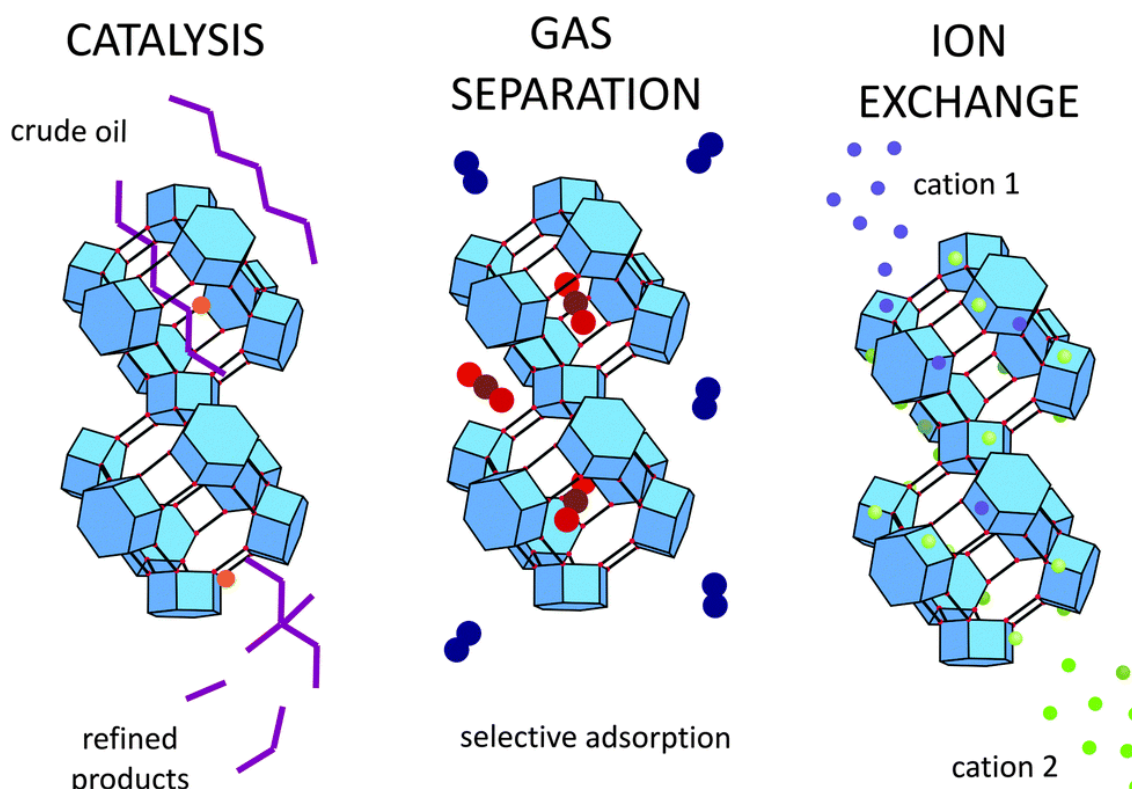


Figure 7 **Three main applications of zeolites in industry:** catalysis, gas separation, and ion exchange²⁸. Reproduced from Ref. 28 with permission from The Royal Society of Chemistry

2.1.1 Catalysis

Catalysis is the process of accelerating a chemical reaction using a rate-altering material that is not itself consumed in the reaction²⁹. Early on in a discussion of catalysis, reactions are usually

categorised as being either homogenous or heterogeneous. This is because the benefits and challenges of each type are distinct. A homogeneous catalyst will be in the same phase as the reactant molecules (e.g. molecular catalyst in solution dispersed in a liquid reactant), making for catalysts that are highly selective, active, and easy to characterise but potentially difficult to operate at high temperatures. A heterogeneous catalyst will not be in the same phase as the reactant (e.g. solid catalyst with reactant gases adsorbed on the surface), resulting in catalysts that are generally more stable under extreme conditions. Ultimately, the difficulty in separating a homogeneous catalyst from its reaction products is a costly deterrent that limits their use in scaled up industrial processes. It is estimated that almost 90% of chemical processes use heterogeneous catalysis at some point in the production chain, with industries as wide-ranging as pharmaceuticals, automobiles, and clean energy all making use of different types of catalysts³⁰.

Zeolites are one of the commonest types^{iv} of heterogeneous catalysts used in industrial chemical reactions. Catalytic applications exclusively utilise synthetic zeolites rather than natural zeolites, because of their more flawless microstructure, phase purity, and controllable composition, factors which all contribute to a crystal that is exponentially more tolerant of cyclical thermal gas treatments. Illustrating the scope of the synthetic zeolite market alone, it is estimated that around 2 million metric tons are consumed globally each year. During the period 2018 – 2025, the market for synthetic zeolites is expected reach a market value of over USD\$8 billion³¹, an almost 4-fold increase on estimations of market size a decade earlier³², fuelled by a continued demand for refining applications. When considering the multi-billion-dollar value of the products output from zeolite catalysed reactions, the industrial interest in fundamental zeolite research is appreciable.

By far the most common current catalytic application of zeolites is fluid catalytic cracking (FCC). FCC is used in petroleum refineries to separate high-molecular weight crude oils into higher value gasoline and olefinic gases. It is estimated that FCC accounts for almost 95%³³ of all synthetic zeolite consumption worldwide.

Two other catalytic reactions with growing future interest are selective catalytic reduction (SCR) and the methanol-to-olefins (MTO) reaction. SCR is a reduction reaction that converts toxic nitrogen oxides (or NO_x) into nitrogen gas and water using a reducing agent like ammonia and zeolites as the catalyst³⁴. First patented in the late 1950s by the Engelhard Corporation and first commercially applied in thermal power plants in Japan two decades later, SCR technology was developed for installation in gas turbines, coal-fired power plants, and boilers throughout the 1990s. In the last decade, SCR has been adapted as an emissions control measure in the automotive industry. Increasingly stringent environmental regulations for mobile engines in the US, Japan, and Europe have led to a surge in research surrounding emissions control. At present, SCR is the technology of choice for current manufacturers needing to meeting regulations like

^{iv} Examples of other types of catalysts include precious metals and metal oxides.

the US EPA NO_x SIP Call (2003) or the latest European standard Euro 6c (2017). The most popular commercial SCR catalysts are extruded TiO₂ anatase monoliths³⁵ embedded with active base metal components like V₂O₅³⁵ and WO₃. However, an increasing amount of work is being conducted on copper and iron ion-exchanged zeolite systems, which present themselves as viable alternative catalytic materials due to their higher temperature operating window that makes them well-suited to use inside diesel engines³⁶. A study of copper catalysts used in the SCR process is presented in Chapter 8.

The MTO reaction is a process that involves converting methanol into higher value olefin-based petrochemicals. The value of MTO lies in its two-fold potential of firstly consuming waste methanol, which is a common unwanted by-product of many chemical reactions, and secondly reducing the pressure on non-renewable sources of petrochemicals. Although initially proposed by Mobil in the 1970s, subsequent research unveiled the complexity of the reaction and highlighted the need for a number of technical challenges to be overcome before a commercially applicable technology would become viable. The fruit of a thirty-year-old research and development effort prompted by an oil crisis in the late 1970s³⁷, China's Dalian Institute of Chemical Physics has been successful in the last ten years in commercially scaling up the MTO process. After four years of operation, China's Wison Clean Energy Co. plant in Nanjing claimed to have produced more than 110 million kilograms of light olefins³⁸, illustrating both a hefty local appetite and the size of a potential international market for scaled up MTO products. An *in situ* study of the MTO process is presented in Chapter 6.

A summary of some of the established and emerging catalytic applications of zeolites are included below in Table 2.

Table 2 Summary of zeolites employed in established and emerging industrial catalytic applications

Process	Zeolite
Fluid catalytic cracking (FCC) ^{39,40}	<ul style="list-style-type: none"> • Zeolite Y • ZSM-5
Selective catalytic reduction (SCR)	<ul style="list-style-type: none"> • Copper zeolites (e.g. Cu-ZSM-5, Cu-SSZ-13, Cu-IM5, Cu-SAPO-34⁴¹) • Iron zeolites (e.g. Fe-ZSM-5) • Other metal-exchanged zeolites (e.g. Co-ZSM-5, Ga-ZSM-5, Ce-ZSM-5, Mn-ZSM-5, In-ZSM-5)
Methanol-to-olefin (MTO)	<ul style="list-style-type: none"> • SAPO-34 • DDR⁴² • SSZ-13 • ZSM-5
Methanol-to-gasoline (MTG) ^{43,44}	<ul style="list-style-type: none"> • ZSM-5 • UZM-12
Catalytic partial oxidation (CPOX) ^{45,46}	<ul style="list-style-type: none"> • Fe- and Cu-ZSM-5 • Cu-SSZ-13

2.1.2 Adsorption

Owing to their high porosity and hygroscopicity, zeolites have found use in situations where it is desirable to adsorb certain materials. In these instances, the zeolites are not integrated into a reaction step like they are in catalytic processes. Rather, they simply utilise their property of being able to trap particular molecules in their shape-selective sieve-like frameworks. The permutations of what substance needing to be removed from what bulk material is vast, and this section mentions industries where zeolites have found greatest use. This is also the application for which natural zeolites are used most often. Annual consumption for natural zeolites worldwide is approximated to be 2.5 million metric tonnes. In contrast to the high specifications demanded by catalytic processes, adsorption may still be achieved with less structurally exacting and more cost-effective zeolite specimens originating from natural deposits. Major commercial distributors of zeolites from natural deposits are found in Arizona, Northern Italy, and Saudi Arabia⁴⁷.

An early application of natural zeolites was in agriculture. Pioneered heavily by Japanese researchers from the 1960s onwards, the adsorptive properties of zeolites have been utilised in crop improvement and incorporation into animal feed⁴⁸. When mixed into arable soil, zeolites can act as fertilisers carrying trapped nutrient elements for sustained release into their surroundings. Conversely, they can also be used as substrates to deliver pesticides. They are also useful for trapping trace heavy metal in soil and preventing their later uptake into the food chain. In livestock, zeolites are FDA approved for usage as an anti-caking agent and feed additive (21 CFR 582-2727). An amusing but nonetheless practical consequence of feeding livestock zeolites such as chabazite is the improvement in excrement odour due to the ammonium trapping abilities of the ingested frameworks⁴⁹.

In aquaculture, natural chabazite and clinoptilolite are used to remove ammonia and toxic heavy metals from water, improving the quality of the environment in which fish are kept. Similar to agriculture, zeolites are also incorporated into fish food regimens. As an example, clinoptilolite has been used as a feed additive to improve growth performance^{50,51} and to improve the quality of fish meat farmed^{52,53}.

2.1.3 Ion Exchange

In aqueous media, cations in the framework can be made to exchange with other cations. One useful application of this is in water softeners, where sodium cations in the framework can be exchanged to remove unwanted calcium or magnesium in water. This is often achieved with zeolite A⁵⁴, which is the most commonly used replacement for phosphate builders in detergents, but is also possible with natural clinoptilolite⁵⁵.

Nuclear is also an industry that has high requirements for dealing with waste. Two examples of commercialised processes in the nuclear industry for dealing with waste gases include the removal of iodine from light-water reactors over Ag-mordenite zeolites⁵⁶ and NO_x & ozone removal from accelerators using silicalite⁵⁷. They are also used with unplanned nuclear waste to adsorb radioactive products and were used in the aftermath of the Fukushima Daiichi nuclear disaster to adsorb caesium from seawater surrounding the power plant³¹.

2.2 Zeolites in Research

Within the research community, zeolites are often assessed for their viability in other niche applications. Two areas where academics have turned their attention are pharmaceuticals and photonics applications.

In pharmaceuticals, porous zeolite frameworks have been identified as potential candidates for sustained-release drug delivery systems. Sustained-release (SR) drug formulations are an important area of research for pharmaceutical companies as reformulation of an existing drug represents a less costly investment when compared to the cost of bringing a new drug to market.

Additionally, drugs such as analgesics and medications for chronic disease that can be taken once and released over the course of a day can have improved prospects for quality of life, reduce the risk of overdose, and improve patient compliance. Researchers have been able to load drugs like ketoprofen⁵⁸ and piroxicam⁵⁹ into matrices and assess for encapsulation.

Zeolites have also been researched in a photonics context and considered as replacement for some semiconductor-based devices. A comprehensive review of some of these photophysics applications has been compiled by Alarcos et al.⁶⁰ Some practical examples include using lanthanide doped zeolites which emit luminescent random patterns to create 'keys' for use in anti-counterfeiting applications⁶¹, or loading zeolites with dyes to create light-harvesting antenna systems⁶².

3 How are Zeolites Made?

Zeolites may occur naturally or synthetically. Of the 248 framework structures recognised by the International Zeolite Association (IZA)⁸, the vast majority can only be created synthetically. This is especially true for more complex frameworks such as those with odd-ring numbers or extra-large pores of 16 rings or more, which require synthetic intervention to stabilise. Natural zeolites tend to be occluded with a wide range of contaminant metal ions and be mixed with more than one type of naturally occurring framework structure. Synthesising a zeolite allows for a greater amount of control over variables such as composition, crystal size distribution, crystallinity, and phase purity.

3.1 Hydrothermal Synthesis

Generally speaking, zeolites are produced under hydrothermal conditions, a process that mimics their formation in nature and involves crystallising zeolite out of high temperature, high vapour pressure aqueous media. When composition and structure become more complex, it is also possible to synthesise zeolites via heteroatom substitutions and topotactic transformation⁶³. However, the most common synthesis process for conventional, commercially relevant zeolites (e.g. CHA, MFI, FAU), and the process used to synthesise the zeolites studied in this thesis, is a hydrothermal synthesis in the presence of an organic structure directing agent (OSDA).

Organic SDAs, also known as templating agents, are purpose-built molecules that effectively act as shape templates for the framework's pore and channel morphologies around which the aluminosilicate materials assemble. By engineering the size, shape, and polarity of the organic SDA molecule, it is possible to create a templating agent for a different type of framework. Some common examples of SDAs include quaternary and diquaternary ammonium cations and phosphorous containing SDAs, and less common examples might include metal complexes, imidazolium derivatives, and proton sponges. Organic SDAs are one of the most expensive ingredients in the synthesis process, and template-free or self-assembling synthesis processes are topics of interest within the zeolite research community.

A number of authoritative reviews of zeolite synthesis providing comprehensive overviews of the history and mechanism of zeolite growth already exist, so the following explanation acts only as a brief summary^{63–65}. Zeolite genesis typically begins in a concentrated reaction gel medium that includes an aluminium and silicon feedstock (e.g. Al_2O_3 and SiO_2), organic SDA, solvents, and a mineraliser. When first combined, the mixture is a non-equilibrium *primary amorphous phase* of components. Upon heating, a series of equilibrium reactions begin, redistributing components between the liquid and solid phases. Aided structurally by the organic SDA, silicate equilibrium reactions begin generating solid material that feature early indications of chemical composition and local order of the final zeolite. Still lacking in long-range order, the reaction gel at this point

in the synthesis is called the *secondary amorphous phase*. Heterogenous nucleation sites arise out of this semi-ordered phase, from which the final long-range ordered structures slowly self-propagate. The resultant product, sometimes termed the as-synthesised zeolite, is a zeolite framework with organic SDA occluded within its pore structure.

3.2 Detemplation

OSDA is not integral to the zeolite's functionality and needs to be removed prior to its use in catalytic applications or otherwise to vacate the framework's internal volume. The removal process is called *detemplation*. During synthesis, the aluminosilicate will often order itself tightly around the organic SDA molecules leaving them sterically confined deep within the pore structures. Detemplation, therefore, necessitates the breakdown of SDA molecules into fragments small enough to extricate themselves from the framework.

The conventional method of achieving this is via a thermal calcination process, which involves slowly heating the as-synthesised zeolite to temperatures as high as 550 °C under an abundant supply of oxygen and decomposing the organic SDA over the course of 12 hours. The success of a thermal detemplation is typically assessed using X-ray diffraction to ensure crystallinity has been maintained, and UV-vis to ensure organic SDA has been removed. Thermal detemplation is favoured because of its simplicity; the heating protocol can largely be automated, it doesn't require gases with complex safety protocol, and the ovens used are readily available, reliable pieces of equipment.

However, detemplation is often acknowledged to be imperfect, posing challenges in the reproducibility domain especially where the sample might have been heated too fast, too much, or too little⁶⁶. The process has been known to precipitate problems in the framework such as dealumination^{67–70}, framework damage (e.g. loss of crystallinity, formation of defect structures)^{71,72}, coke-like residues⁷³, and thermal stress cracking^{74,75,76}, which can be attributed to its exothermic nature, as well as the formation of steam and CO₂ and the volume expansion of the solid framework due to gaseous phase OSDA within the micropores. Total removal of coke-like residues can be challenging, as although one-step dry-air calcination can be effective for maintaining crystallinity and avoiding dealumination⁷⁷, a substantial amount of carbonaceous material (up to 20 % by some accounts) can remain on the zeolite surface at temperatures as high as 430 °C as a result of aromatic catalytic conversion happening alongside the template degradation process^{70,78,79,80}. This has led to the propensity for using a two-step calcination process involving calcining first in an inert gas and then in air in a bid to circumvent some of the problems listed above⁷². It is posited that in single-step high-temperature detemplation of high-silica frameworks, the abrupt decomposition of OSDA molecules across a large temperature differential leads to an uncontrolled increase in the internal pressure of the lattice, resulting in framework damage. A two-step method may mitigate these effects by introducing temperature and

compositional changes into the lattice gradually. While a modest body of research exists to support this claim⁸¹, literature supporting the one-step method also exists⁷⁷ with minimal research addressing factors such as air flow. This highlights, to some extent, how preferences for thermal detemplation are derived from a received wisdom rather than being entirely evidence based. Alternative methods of detemplation researched in the last decade include H₂O₂ mediated oxidation⁶⁹ and ozonation, a technique tested in DDR⁸² and MFI^{83,84} topologies that involves heating the as-synthesised zeolite in an ozone environment at approximately half the temperature required for a traditional thermal detemplation.

A mechanistic understanding of the breakdown of template molecules is not fully understood and is likely to be dependent on the chemical nature of the OSDA used. Pr₄N⁺ (Pr = *n*-propyl) templates in MFI-type zeolites^{70,85} and tetraethylammonium (TEA) in zeolite β ⁸⁶ have been studied previously leaving broad scope for further dedicated research in different topologies.

3.3 Ion Exchange

Ion exchange may be performed either during or after the hydrothermal synthesis. This depends in part on the nature of ions being exchanged in and out of the framework. Chapter 8 focuses on the study of copper zeolites, so zeolite preparation based on the inclusion of copper will be discussed here as an exemplar.

If synthesising directly, a copper complex may be incorporated into the primary amorphous phase as a mineraliser⁸⁷ or as a template⁸⁸. Incorporation into a parent material may be achieved in either liquid, solid, or gas phase. Wet ion exchange is a common way of achieving this and usually involves mixing the parent zeolite in a solution of copper, such as CuSO₄ in water, and creating a slurry that is then mixed for some hours, filtered, dried and calcined. The process of immersing the zeolite in copper solution may be repeated to control the amount of copper exchanged into the framework. Copper might also be introduced by a vapour deposition process, which involves heating a copper source (e.g. Cu-nitrate in a stoichiometric excess) and the vapour floated over a bed of the parent zeolite in a reactor. This preparation method has the disadvantage of exhibiting a copper gradient across the bed from the surface to the underlying bulk, meaning copper zeolite might require separation from a more under-exchanged sample. Solid state exchange is yet another alternative preparation that involves manually combining a copper source with the parent zeolite via mechanical grinding for a period of time, followed by washing, filtering, drying, and calcining the resultant zeolite again.

4 How are Zeolites Characterised?

Zeolite characterisation might be split into two categories: standard, and advanced.

4.1 Standard Characterisation

Standard characterisation refers to a well-established battery of tests that benchmark the important fundamental parameters of the zeolite in question. The instrumentation required to perform these tests is typically commercialised and readily available in any chemistry lab. These include:

- X-ray diffraction (XRD) for structural information
- Brunauer-Emmett-Teller (BET) isotherms to estimate the surface area
- Thermogravimetric analysis (TGA) or differential scanning calorimetry (DSC)⁸⁹ for information on adsorbed phases
- Scanning electron microscopy (SEM) for visual confirmation of structure
- UV-vis for information on absorption properties

4.2 Advanced Characterisation

Advanced characterisation refers to techniques that are more specialised and provide unique insight into the zeolites themselves and their catalytic behaviour. These techniques often require more specialised instrumentation or greater skill to operate than standard characterisation techniques. As a result, these techniques are not necessarily applied to zeolite samples across the board, with some particular groups and institutions specialising in specific advanced characterisation techniques. In the case of beamlines, these setups may only be found at national facilities. Some examples include:

- Solid-state nuclear magnetic resonance (NMR) spectroscopy to provide quantitative information on the local coordination state in a solid
- X-ray techniques, especially beamline options, such as X-ray fluorescence (XRF), X-ray absorption near edges spectroscopy (XANES), or X-ray tomography to provide compositional information
- Electron imaging methods like transmission electron microscopy (TEM) and scanning transmission electron microscopy (STEM) to provide high resolution images of the structure of the sample
- Vibrational spectroscopies such as infrared, Raman, and fluorescence spectroscopy to provide information on inter-atomic potentials that relate to structural and dynamic properties of materials and adsorbates

A class of techniques used quite extensively in zeolite catalysis studies are *in situ* and operando experiments. *Operando* refers to an experimental method where a spectroscopic measurement is performed simultaneously with measurement of catalytic activity, usually via a mass spectrometer. This means a catalytic reaction is performed in real-time under controlled temperature and environmental settings, usually a special type of reaction cell⁹⁰. *In situ* refers to a similar type of experiment that simulates real-life catalytic conditions but is not collecting information on

catalytic activity (i.e. no mass spectrometer connected to the setup). It is possible to couple operando setups into almost any spectroscopic modality from NMR⁹¹ to infrared⁹² to X-ray absorption⁹³ and beyond. As such, while not necessarily standard practice, the use of operando techniques to assess the catalytic activity of a whole reaction is becoming increasingly common.

In situ and operando experiments are usually saddled with a host of logistical challenges, the most common of which often relates to determining how the bulky reaction cells can be accommodated within the geometry of a pre-existing spectroscopic setup. However, the pay-off can be significant as the technique provides invaluable information that is directly applicable to real-world scenarios, showcasing how zeolite systems evolve with time under a given set of conditions.

Chapter II

An Introduction to Photoluminescence

1 Introduction to Photoluminescence

1.1 A Preamble

Speaking in the broadest of terms, photoluminescence is a consequence of a light-matter interaction occurring when photons are absorbed, and light is re-emitted. Defined with greater specificity, it is a spontaneous emission process occurring when excited orbital electrons return to a lower energy state via the emission of photons. Any form of matter may potentially exhibit photoluminescent properties. In the case of zeolites, a researcher would be primarily concerned with solid-state photoluminescence. We have established in the previous chapter two compositionally distinct phases of interest that co-exist to form a zeolite, which may be excited to luminesce: firstly, the sorbed phase, which is typically molecular in nature; and secondly, the zeolite framework^v itself, which has previously been illustrated to be a complex aluminosilicate crystal.

Although it is known that zeolites may luminesce (see Section 2), it is very difficult to pinpoint precisely where the luminescence is originating from. This difficulty arises most likely from the fact that these two phases have different photoluminescence mechanisms, which upon excitation may be occurring simultaneously and perhaps even interacting with each other. The photoluminescence observed is therefore likely to be an amalgamation of emission from various complex origins that, due to their non-singular source, are difficult to quantitatively analyse. What will ensue from this point forward is a discussion of the basic theoretical principles of photoluminescence. A standard molecular model using a Jablonski diagram is used to predicate how emission is likely to arise from the sorbed phase is first presented. Thereafter, a discussion of photoluminescence in solids is also presented to demonstrate how the emission mechanism is different in infinitely ordered structures.

1.2 Photoluminescence in Molecules

1.2.1 Addressing the Jablonski Diagram

Jablonski diagrams are schematic representations of molecular energy levels. First proposed in 1933 by the Polish molecular photophysics pioneer Aleksander Jabłoński, this diagrammatic representation of energy states is intended to simplify the visualisation of different molecular absorption and emission processes. Figure 8 shows one such example with energy oriented along the vertical axis. Horizontal lines represent eigenstates. The bold horizontal lines represent electronic energy states and the thinner lines clustered around each bold electronic energy state are the vibrational energy states. For clarity, the rotational energy states associated with each

^v Framework here would also refer to extraframework cation species, which in the previous chapter differentiated as a different component to the aluminosilicate framework.

vibrational energy state are omitted from this diagram. The diagram is further subdivided into two columns. Each column represents a different spin multiplicity, with the column on the left denoting singlet states, and the column on the right denoting triplet states. Actual absorption and relaxation processes are illustrated by vertical lines, with straight ones representing radiative processes and wiggly ones representing non-radiative processes.

It is worth recognising that as molecules become increasingly polyatomic the number of vibrational modes increase in a way the diagram does not reflect, at a rate of approximately three times per additional atom⁹⁴. The manifold of modes is therefore immense and impossible to accurately picture in this style of visual representation. This means that Jablonski diagrams are at best adumbrative representations. Indeed, considering the complexity of zeolite systems, being overly-dogmatic in the simplification of process mechanisms can pose a barrier to interpretation. Rather, it is necessary to adopt a more flexible approach to the abstraction of how these principles apply to zeolites, being open-minded to the possibility of non-standard observations.

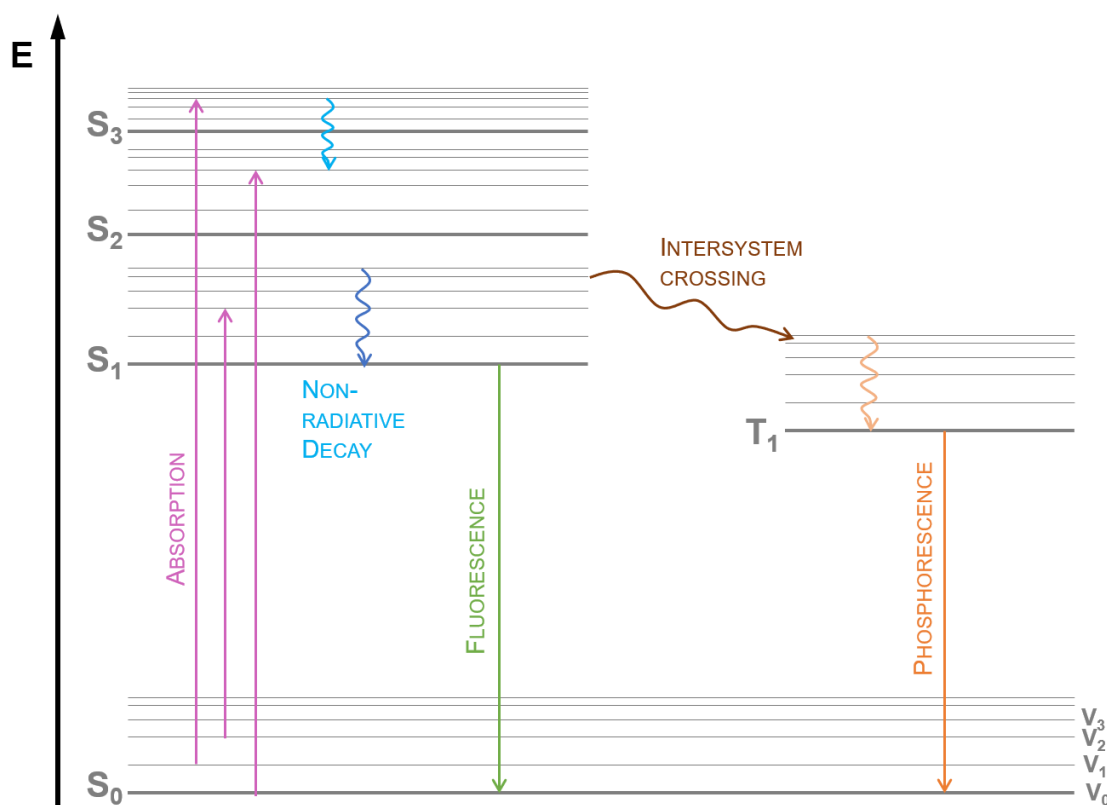


Figure 8 **A Jablonski diagram** with energy on the vertical axis. Thick lines represent electronic states and thinner lines represent vibrational energy states. Vertical lines linking higher and lower energy levels depict different processes involved in the phenomenon of photoluminescence including absorption, non-radiative decay, fluorescence, intersystem crossing, and phosphorescence⁹⁴.

Another point of simplification in this diagram that will be pointed out is the linear presentation of the five main events of photoluminescence, namely: absorption, non-radiative decay processes, fluorescence, intersystem crossing, and phosphorescence. While these five processes are usually explained in a linear cause-and-effect manner, it is better to see photoluminescence as being

random with these different processes occurring simultaneously in competition with each other and having a probability of occurrence attached to them. The likelihood of an event begins to determine which processes will dominate at different stages of the molecule's energy transitions.

1.2.2 Absorption

Upon exposure to an excitation source, energy from an incident photon is transferred to an orbital electron. Photon energy, as indicated by the Planck-Einstein relation, is determined by its frequency:

$$E = h\nu = h \frac{c}{\lambda}$$

where E = photon energy

h = Planck's constant

ν = frequency

c = speed of light

λ = wavelength

The inverse relationship with wavelength implies that light residing closer to the ultraviolet end of the electromagnetic spectrum will have higher energy. Depending on the energy gap between eigenstates, certain wavelengths of excitation light may or may not be able to promote an electronic transition. Assuming an excitation source with a sufficient amount of energy, this process of absorption is the first transition documented in a Jablonski diagram. Absorption is depicted by an arrow spanning the distance between the ground state and a higher energy state. It is possible to appreciate here that depending on the amount of energy introduced into the system, the exact excited eigenstate may be different. It is also statistically most likely that with the majority of electrons residing in a Boltzmann distribution across the vibrational levels of the ground state, the vast majority of absorption events occur typically between the ground state and higher states (i.e. S_0 to S_n) rather than between excited states (e.g. S_2 to S_4).

1.2.3 Relaxation

Following energy absorption, a molecule begins a multistep process of energy dissipation. The relaxation processes described here all occur in competition with each other with varying degrees of probability. Initially in this discussion, it is assumed that these processes are occurring within the singlet manifold.

1.2.3.1 Vibrational Relaxation & Internal Conversion

The next set of oscillating lines depicted in Figure 8 represent non-radiative decay processes; that is energy dissipation processes not involving the emission of light. The dark blue curved line between vibrational levels of the same electronic level in Figure 8 describes vibrational relaxation, which occurs when excess energy is dissipated kinetically across other vibrational modes. Where

40

vibrational energy levels and electronic energy levels overlap significantly, it is also possible for excited electrons to transition to a lower state in a transition called internal conversion, as demonstrated by the light blue curved line in Figure 8. Mechanistically it is the same process as vibrational relaxation and happens on the same time scale, but distinction is made due to the transition between different energy levels. At higher energies, the distribution of vibrational and electronic eigenstates becomes closer making the probability of an internal conversion event more likely.

A large energy difference typically exists between the first excited state and the ground state. Surmounting this energy gap by kinetic energy dissipation is less likely to occur, and subsequently internal conversion is rarely the mechanism by which the system makes its final ground state transition. Instead, radiative means of energy dissipation are more likely to take place.

1.2.3.2 Fluorescence

Relaxation from an excited singlet state to a lower electronic state (typically the ground state) when accompanied with the emission of electromagnetic radiation is termed fluorescence. In most cases this the most probable means by which a system will broach the S_1 to S_0 transition. The excited molecule will exist in this first excited state for a duration of time often spanning some nanoseconds before the final relaxation step occurs.

1.2.3.3 Intersystem Crossing

It is possible for transitions to occur between electronic states with different spin multiplicity. This is a non-radiative process termed intersystem crossing. According to the Pauli exclusion principle, electrons in the ground state will have paired opposite spins as shown in Figure 9. Singlet states, which have been the focus of the discussions so far, feature excited electrons with spin that remains paired with the ground state electrons. In triplet states, excited electrons do not have paired spin and are instead parallel, or with the same spin state. Although crossing between different spin multiplicities is technically forbidden, certain situations can facilitate the process such as molecules with a large spin-orbit coupling or situations where the $S_0 \rightarrow S_1$ is $n \rightarrow \pi^*$ type.

Within the triplet manifold, it is then also possible for vibrational relaxation and internal conversion to occur. Through these mechanisms, the molecule relaxes down to the first triplet state⁹⁵.



Figure 9 **Schematic diagram of spin pairing in singlet and triplet energy states.** Arrows correspond to spin.

1.2.3.4 Phosphorescence

Phosphorescence is, consequently, the final radiative relaxation step between the first triplet state and the ground state. In returning to the ground state, phosphorescence also represents another intersystem crossing event as the system returns to a paired ground state spin configuration.

While phosphorescence is not as common in solution-based photoluminescence studies due to the higher number of quenching processes available to compete, in solid systems like zeolites, we may expect to see phosphorescence. Some well-known examples of minerals exhibiting phosphorescence include calcite⁹⁶, celestite⁹⁷, and fluorite⁹⁸.

1.2.4 Process Timescales

Each of the processes described occur on different timescales. A summary of the approximate timescales of all of these processes are included below in Table 3. These timescales can be used to relatively reliably estimate what is happening in a system. For example, fluorescence and phosphorescence is experimentally identified by whether the emission appears to have a nanosecond or millisecond lifetime.

Absorption is the fastest process, theoretically occurring instantaneously (i.e. femtoseconds) before any molecular movement can take place. In contrast, relaxation processes are some orders of magnitude slower. This is because many of these relaxation pathways occur via kinetic processes. The timescale on which non-radiative decay processes occur is in the vicinity of 10^{-14} to 10^{-11} s and is dictated by the time required for collision-like interactions to take place. As it is fast, it is likely to occur shortly after absorption has taken place and will almost always happen before fluorescence occurs (which happens on a nanosecond timescale) meaning that radiative emission usually arises out of a thermally equilibrated S_1 state. Phosphorescence has the longest time scales due to the statistical unlikelihood for intersystem crossing to happen.

Table 3 *Approximate timescales for absorption and emission processes*⁹⁴

Process	Timescale (s)
Absorption	10^{-15}
Internal Conversion	10^{-14} to 10^{-11}
Vibrational Relaxation	10^{-14} to 10^{-11}
Fluorescence	10^{-9} to 10^{-7}
Intersystem Crossing	10^{-8} to 10^{-3}
Phosphorescence	10^{-4} to 10^{-1}

1.2.5 Quenching

Quenching is a term describing processes, of which there are many, that decrease the fluorescence signal emitted. It typically involves an alternative relaxation pathway to the ground state that sees energy being dissipated by means other than photon emission during the $S_1 \rightarrow S_0$ transition. A likely example is collisional quenching, which is a dynamic quenching method involving the fluorophore either dissipating energy via an increased rate of kinetic interactions in a situation such as heating, or by encountering particular molecules that are known quenchers via particular interactions they tend to have⁹⁴. Examples of quenchers include oxygen, halogens, and amines, all of which induce quenching by different mechanisms (e.g. electron transfer, spin-orbit coupling)^{99–102}. Exciplex formation can induce quenching when quenchers form complexes with the fluorophores in the excited state. It is also possible for static quenching to occur when quenchers form non-fluorescent complexes with the fluorophore in the ground state, which actually means that upon contact with the quencher fluorescence does not happen at all. Non-molecular quenching pathways can also exist, such as the reabsorption of emitted light by either the fluorophore itself or the medium around it¹⁰³.

1.3 Photoluminescence in Solids

So far in molecular fluorescence, the critical energy transition associated with photoemission is $S_1 \rightarrow S_0$, which can also be called the *optical gap*; that is to say the energy of the lowest excited state that can be reached through the absorption of one photon^{vi}. When molecules are extended to form structures with long-range order (i.e. interatomic distance between atoms in a given area is decreased and a periodic bonding structure is established), electron probability distributions overlap to form what is effectively a continuous band of energy levels. The lower band is usually referred to as the valence band and the upper band is termed the conduction band. The width and spacing of these bands depend on the nature of the bonding in the crystal (as shown in Figure 10A), and the gap between these two is called the *band gap*. Materials where the band gap is large are considered insulators, while materials with overlapping bands are conductors. Semiconductors then represent materials with a moderate spacing between the bands.

In the case of semiconductors, there exist two types of band gaps: a direct gap and an indirect gap, also shown in Figure 10B. In direct band gap semiconductors, the maximum value of the valence band and minimum value of the conduction band feature the same momentum or k-value. In an indirect band gap semiconductor, the maximum and minimum values of the valence and conduction bands respectively do not have the same momentum value. In practical terms, this means that direct band gap semiconductors can form electron-hole pairs more readily, whereas an indirect band gap requires a photon of energy E_{gap} to change momentum through interaction with a phonon to form an electron-hole pair. Indirect gap processes, therefore, happen at a slower rate as they require an intermediate phonon-mediated step to occur. Direct band gap semiconductors like gallium arsenide may, therefore, be used to create optical devices like light emitting diodes (LEDs), where indirect band gap semiconductors may not.

^{vi} Remember that in general discussions of fluorescence, we are contemplating the effects of the redistribution of electrons throughout a system where electrons and holes are still electrostatically bound and not excited to the extent they are ionised. The optical gap can be easily confused with other ‘gaps’ including the fundamental gap or the HOMO-LUMO gap.

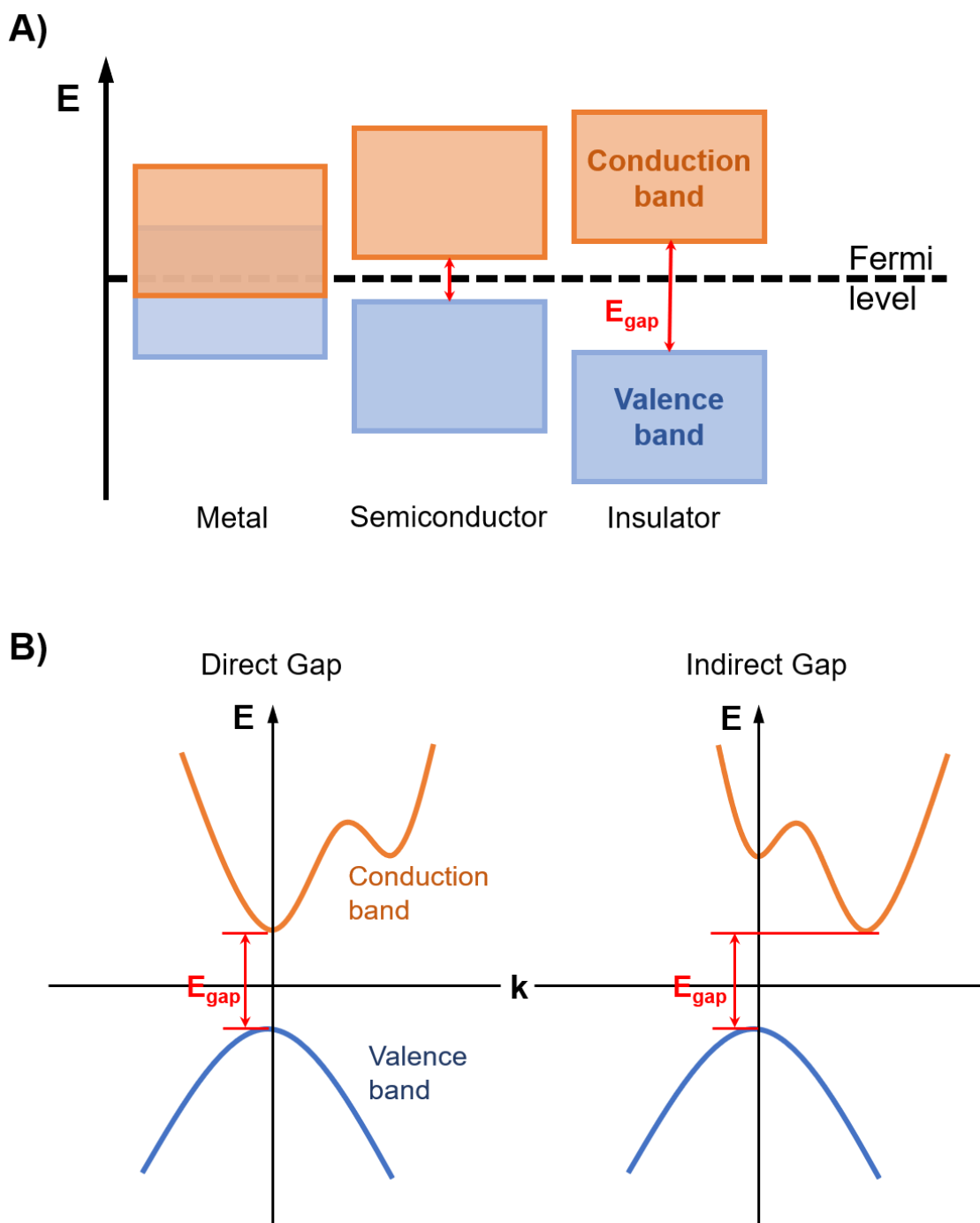


Figure 10 **Schematic diagram of band structure in solid materials with energy (E) oriented along the vertical axis:** A) The two bands closest to the Fermi band are the valence and conduction band. In metals the bands overlap whereas in semiconductors and insulators they are separated by a band gap that becomes larger as the material becomes more insulating. B) Semiconducting materials may have a direct or indirect bandgap, which is dependent on the alignment of the crystal momentum (or k -vector) of the conduction and valence bands. Indirect gaps require photons to pass through an intermediate state, transferring momentum to the crystal lattice.

How then might we expect to see photoluminescence in a solid? It follows that in terms of photoluminescence mechanisms, the band gap in a solid is somewhat analogous to the optical gap in a molecule. Insulators like LiF ($E_g=13.7$ eV, ≈ 90 nm) have incredibly large bandgaps that would not be responsive to even deep-UV irradiation, making them both transparent in the visible and ideal for optical applications like UV-transparent windows in laser setups¹⁰³. Conversely,

conductors like metals do not exhibit an optical response upon irradiation due to their metallic bonding, which creates an overlap of the conduction and valence band and hence no optical gap over which to excite or emit.

However, semiconductor materials exhibit band gaps surmountable by visible excitation (~ 1 eV). Although electrons may be promoted to the conduction band via the absorption of a photon, emission processes in semiconductors may vary depending on whether the band gap is direct or indirect. Simple recombination of conduction band electrons with their corresponding valence band holes may produce photoluminescence in some materials or be too fast to create radiative emission in others¹⁰⁴. Alternative slower decay pathways may be created by the introduction of defect sites. Additionally, photoluminescence may be induced in a solid material via the introduction of an isolated luminescent centre¹⁰⁵. This involves introducing a dopant ion, typically a metal, with an excited energy level lower than that of the host crystal, which may luminesce upon excitation.

Modelling the electronic structure of zeolites is computationally demanding because of their structural complexity, exceedingly large unit cell size, and abundance of structurally ‘soft’ bridging oxygen units¹⁰⁶. Consequently, the optical properties of zeolites are still not completely understood on a theoretical level. Studies suggest their band gaps sit between that of an insulator and a semiconductor, with SiO₂ chabazite calculated to have an indirect band gap of 5.5 eV¹⁰⁷.

In the interest of concision, the generic discussion on photoluminescence in solids is not extended further, and an additional discussion pertaining directly to zeolites continues in Section 2.3. The point of this brief comparison of photoluminescence in solids is to highlight that although the basic principles of spontaneous emission are analogous for both molecules and crystals in that they are concerned with changes in the energy of a system, they differ in what constitutes the energy level. I hope to have implied in Section 1.2 that the energy levels of the molecule are largely predetermined by its composition and structure; a molecule is either a fluorophore at a particular wavelength of excitation or it is not. Being small, it is not possible to make large changes to the molecule to create a photoluminescent effect without fundamentally changing the molecule to something completely different^{vii}. In comparison, there is a greater possibility to induce or augment the optical properties of a solid through chemical interventions like doping or defect-creation, although this is highly dependent on the sample.

1.4 Quantifying Photoluminescence

Any photoluminescence observed may be described using four key concepts. On a simple observational level, it can be described in terms of the (1) *wavelength emission*, λ , and the (2)

^{vii} This is to note that this discussion speaks incredibly broadly about photoluminescence and is set up to be read in the context of inorganic zeolites. For example, it does not consider the effect of solvent interactions as much as biology-based fluorescence spectroscopy resources would.

intensity, or how brightly the sample is emitting. Plotting these two parameters against each other allows for the construction of a photoluminescence spectrum.

The most important parameters are the (3) *fluorescence lifetime* and the (4) *quantum yield*. Fluorescence lifetime, τ , is the time it takes for a molecule to relax from an excited state to the ground state and is defined by the total time taken for a combination of radiative and non-radiative processes to occur. τ may be denoted in numerical terms as roughly:

$$\tau = \frac{1}{\Gamma + k}$$

where Γ = radiative decay rates

k = non-radiative decay rates

Where decay processes are purely radiative, the intrinsic or natural lifetime of the fluorophore, τ_0 can be defined as:

$$\tau_0 = \frac{1}{\Gamma}$$

A challenge of fluorescence, especially when it comes to quantifying information, is that not all components of the fluorescence descriptors above are intrinsic. Non-radiative decay processes are often dictated by local micro-environmental factors. For example, particular molecules such as oxygen are efficient at non-radiative quenching of fluorescence through external conversion. Similarly, changes in temperature and viscosity can impact on the amount of external conversion in a system. As such, when k must be described in terms of separate components;

$$k = k_{ic} + k_{ec} + k_{is}$$

where k_{ic} = rate of internal conversion

k_{ec} = rate of external conversion

k_{is} = rate of intersystem crossing

and an expression for k_{ec} may become further complicated simply by taking into account quenching alone;

$$k_{ec} = k_0[Q]$$

where $[Q]$ is the concentration of the quencher, and k_0 is related to the diffusivity and hydrodynamics of reactants. This example serves to demonstrate how considering one component of non-radiative decay alone begins to complicate a descriptor such as fluorescence lifetime into a multifactorial entity beyond the realm of numerical predictability:

$$\tau = \frac{1}{\Gamma + k_{ic} + k_{is} + k_0[Q]}$$

Quantum yield is a dimensionless ratio of the number of photons emitted per excitation photon absorbed:

$$Q = \frac{\text{number of photons emitted}}{\text{number of photons absorbed}} = \frac{\Gamma}{\Gamma + k} = \frac{\tau}{\tau_0}$$

It can also be expressed as a ratio of rate constants where $\Gamma + k$ describes the rate at which the excited state is depopulated, or alternatively by substitution as a ratio of fluorescence lifetimes. It can be thought of as a descriptor of photon conversion efficiency and will be a number ranging from zero to one, where unity represents, in practical terms, a very bright fluorophore. Perceived intensity of the fluorophore is therefore directly linked to quantum yield.

Both the lifetime and quantum yield are effectively non-intrinsic properties, as they are susceptible to external influences that may change the rate constants. In this respect, the photoluminescence signal cannot be readily analysed in an absolute sense; quantitative analysis must be conducted with great consideration, and results should always be analysed with due respect to the context. Drawing conclusions from photoluminescence data requires more of a ‘big picture’ approach than other methods, which may be considered either a pro or a con depending on what the application is.

1.5 Measuring Photoluminescence

Photoluminescence can be used to characterise samples in two principle ways, which are namely spectroscopy and imaging. Each of these methods can also be measured in two modes: steady-state or time-resolved.

1.5.1 Type of Measurement

1.5.1.1 Spectroscopy

Spectroscopy involves directing emitted photoluminescence onto a Charge-Coupled Device (CCD) detector and recording intensity as a function of wavelength, to obtain a spectrum that reflects the emission properties of a sample. It is possible to measure both the absorption and the emission spectra of a sample, sometimes with variable wavelength excitation. Emission spectroscopy is an important method of characterising photoluminescence.

1.5.1.2 Optical Imaging

In optical imaging, emitted signal is directed onto an imaging CCD, and an image is generated as a function of intensity. Imaging provides spatially resolved information on where and how brightly fluorophores emit across a sample. Using photon-counting add-ons it is possible to gain pixel-by-pixel information on the lifetime of emitted light in a mapping technique called fluorescence lifetime imaging microscopy (FLIM)¹⁰⁸. Optimising the configuration with the use of a pinhole to create a confocal imaging setup can serve to improve the resolution of the setup,

although optical microscopy is an intrinsically diffraction-limited technique. Achieving sub-200 nm images is, nevertheless, possible through technological achievements in a field called ‘super-resolution microscopy’^{109–112}.

1.5.2 Measurement Mode

1.5.2.1 Steady-State

Steady-state is the simplest type of measurement. It involves irradiating the sample with a constant source of light and measuring the photoluminescent intensity as a function of wavelength. The measurement obtained in this mode captures all transitions across the entire temporal range as the sample is being illuminated constantly. In this respect, the spectrum will show almost an average of all the radiative transitions, with the emission band often being quite broad.

1.5.2.2 Time-Resolved

Time-resolved measurements use a pulsed light source. Compared to steady-state, time-resolved measurements are decidedly complex but offer a wealth of information inaccessible with only a continuous irradiation source. It is only possible to obtain very detailed time-resolved information if the excitation pulse width and the detector temporal resolution used are less than the decay time of the fluorophore. Achieving this necessitates the use of laser and detection instrumentation, which can quickly escalate in price the more exacting the specifications of the laser and detection system become.

2 Photoluminescence in Zeolites

2.1 On Prior Art: The Aim of Previous Photoluminescence Studies

Prior art on the subject of zeolite photoluminescence can be split into two categories: (i) studies that probe and analyse this autofluorescence, and (ii) studies that artificially introduce fluorescence signal into the framework through tagging. These two types of studies tend to exhibit distinctly different experimental aims.

In the case of introduced fluorescence, or what is also termed ‘tagged studies’, the researcher is able to select a fluorophore that emits at a convenient wavelength, often with a quantum yield high enough to generate a clear, bright signal uncompromised by noise and background signals. With intelligent fluorophore selection, it is possible to some extent to engineer the wavelength the sample emits at. This enables experimental design to become more complex, especially if samples can be tagged with multiple dyes, each emitting at different wavelengths. Multi-channel imaging, Förster resonant energy transfer (FRET) experiments, and super-resolution imaging experiments are all made possible with selective tagging. Dyes are, therefore, used as a stepping-stone to gain either deeper structural information, information on spatial distribution of active sites, or monitor secondary effects in the tag that happen as a result of a two-step chemical process in the zeolite.

Conversely, studies that monitor autofluorescence are generally focused on assigning the origin of the signal. Given that autofluorescent signal is often uncontrollable, broad, low, and at times difficult to assign, sophisticated imaging techniques are challenging to apply. However, the absence of any fluorescent labelling means that any signal recorded originates from a source that provides ‘real’, primary information on factors such as chemical speciation, defect sites within a framework, or even dopant composition. The absence of tags also mitigates the risk of altering underlying chemical and physical processes, meaning that any data generated is more greatly representative of the chemistry occurring across the sample.

The following section briefly reviews the literature in both these areas.

2.2 Studies of Introduced Photoluminescence

‘Introduced photoluminescence’ here refers to emissive molecular dyes that are incorporated into the zeolite frameworks in a guest-host manner. Although there is arguably some degree of overlap between the concept of ‘introduced’ and the ‘intrinsic’ photoluminescence discussed in Section 2.3, introduced photoluminescence is defined to be occurring in zeolites that have been expressly treated or synthesised with a non-structurally, non-catalytically functional component that purely exists within the zeolite to luminesce with desirable properties. A number of authoritative reviews and book chapters on tagged zeolite research already exist^{113,114–116,60,117,118}.

Early work focused on methods of floating dyes into the pore structures ensuring an even distribution throughout the framework to avoid problems causing augmentation to the emission such as surface aggregation, crystallisation, and excimer formation. In the simplest cases, zeolites could simply be stained with dye uptake occurring via physisorption. Where incorporation was achieved in this way or by ion-exchange, geometrically compatible linear dye molecules and parallel, one-dimensional framework types (e.g. LTL, AFI) were favoured^{119,120,121}. The development of self-assembling and ship-in-a-bottle synthesis methods facilitated the incorporation of dyes too bulky to enter pores such as fluorescein^{viii} in zeolite Y¹²² among others¹²³.

Once samples are loaded with dye, it is possible to start looking for areas of photoluminescence. Distribution of dyes is demonstrated most compellingly through confocal imaging, which provides visual confirmation of emissive locations. Where linear channel zeolites are used, emissive sites can clearly be seen along the crystal axis or, depending on the dye, plugged at either end of the crystal as demonstrated by Calzaferri⁶² and Hashimoto¹²⁴. Calzaferri also demonstrated the presence of Förster resonance energy transfer (FRET) between dye molecules encapsulated in adjacent channels, establishing important ground work for the effects of 1D confinement on guest molecules¹²⁵. In studies where zeolites are simply stained with dye confocal imaging has been used to visualise dye uptake as determined by diffusion, pore size and accessibility, and structural hierarchy. Examples include oxazine 1¹²⁶ and 4-(4-diethylaminostyryl)-1-methylpyridinium iodide (DAMPI)¹²⁷ staining of ZSM-5 to show mesoporous defects in large crystals. Furfuryl alcohol condensation, which becomes emissive upon oligomerising on active catalytic (acid) sites, has also been identified by Roeffaers *et al.* as a fluorescent marker useful for seeing hierarchical pore structures in zeolites¹²⁸ and metal-organic frameworks¹²⁹. They have successfully used this marker in their high-resolution single molecule mapping method termed Nanometre Accuracy by Stochastic Catalytic reActions (NASCA) microscopy¹³⁰, a technique which shares similar principles to single molecule super-resolution microscopy techniques like stochastic optical reconstruction microscopy (STORM)¹³¹. This technique has been utilised to great visual effect in catalytically relevant zeolite systems such as ZSM-5 containing fluid catalytic cracking (FCC) particles to study reactivity¹³².

It is also possible to monitor photoluminescence through spectroscopic methods. Spectroscopy tends to be the favoured method of analysis when studying dye-encapsulation in zeolites for photonics applications. This is because phenomena like engineered quenching, blinking, or energy transfer become more relevant when research is being conducted to use zeolites as antennae, sensors, or waveguides. Recent advances in ultrafast laser systems have allowed for a greater understanding of molecular dynamics of confined dyes. Time-resolved spectroscopy has been used even before the advent of ultrafast laser setups to probe some of these dynamics. An extensive review by Alarcos *et al.*⁶⁰ focusing on fast-occurring photodynamics identified inter-

^{viii} An extremely common tag for basic confocal microscope experiments.

and intra-molecular proton and electron transfer reactions as well as energy-transfer as potential confinement induced events that may impact on the emission behaviour of dyes. Prior to this, Hashimoto's¹¹⁷ review of primarily aromatic fluorescent guest molecule studies summarised a similar set of effects including inter-cage confinement, cationic and framework interaction, and intra-cage charge and electron transfer that could all be responsible for changes in the emission spectra. Spectroscopic studies show that it is indeed expected for emissive dyes to experience significant spectral changes upon introduction to a zeolite framework, although specific justification as to what causes these changes is difficult to generalise, being heavily dependent on the size of both the dye molecule and the framework, and the structure, composition, and stability of the dye.

2.3 Studies of Intrinsic Photoluminescence

'Intrinsic photoluminescence' here refers to luminescence that arises as a result of the zeolite material itself. In line with the definition provided in Section 2.2, zeolites that exhibit intrinsic photoluminescence have not been expressly treated to be luminescent. Admittedly, the inclusion of luminescent centres from framework-associated metal ions treads the bridge between these two definitions, as some researchers use metals rather than dyes as the emissive tag. However, given that the research in this thesis is borne out of an applied catalytic zeolite context where metals are introduced into a framework to impart some kind of catalytic benefit such as improving conversion efficiency, metallic luminescent centres are discussed here as a form of intrinsic photoluminescence.

Section 1.3 focused on the origin of photoluminescence in solids where the premise of the band gap was discussed. Zeolites have large band gaps generally insurmountable by the energy of visible light making them optically transparent. This is not to say that guest electronic states may not be introduced into the band gap¹³³, similar to what is achieved with the rare-earth-doping of the insulating material garnet, variants of which are used as solid gain media in certain lasers. These additional states may be created by the inclusion of defects or optically active luminescent centres such as transition metal ions, rare-earth ions, or other miscellaneous luminescent ions like bismuth. Some well-studied examples include silver and iron inclusions^{134–136}. The mechanism behind defect states is not as well studied as that of metal inclusion, which has been extensively modelled¹³⁷ and tested for a range of different frameworks and metal ions¹³⁸.

Natural zeolites from well-known deposits throughout the world are often assessed with steady-state spectroscopy and basic time-resolved apparatus. It was originally thought that natural zeolites do not exhibit luminescence under any form of visible or UV light until noted by Claffy in 1951 that base-exchanging copper and silver, under particular hydration conditions, could induce a reversible luminescence¹³⁹. It has since been demonstrated that natural zeolites do exhibit photoluminescence (some examples of which include natrolite and heulandite¹⁴⁰, clinoptilolite¹⁴¹,

and chabazite-Ca¹⁴²), and this early oversight was likely related to the lower sensitivity of detection equipment being used at the time. Recent studies of natural zeolites assign a large portion of luminescent behaviour to the presence of trace metals (e.g. Eu³⁺ and Ce³⁺ in the chabazite-Ca study, Fe³⁺ in the natrolite and heulandite study). However, there is often a broad, featureless aspect to these spectra that may not be satisfactorily assigned to particular electronic transitions of trace metal speciation. This component of the spectrum in natural zeolites is usually speculatively assigned as arising due to either adventitious organic species or structural defects associated with the presence of trace metal, but without complex systematic experimentation it is difficult to know what the unequivocal answer to this question is. This background is recognised relatively ubiquitously in synthetic zeolites as well but is rarely studied. Indeed, it is specifically cited as the reason why high quantum yield fluorophores need to be investigated to enable imaging¹¹⁶ as dye candidates are required to overcome the background signal. For synthetic zeolites there is also a small body of research by Karwacki *et al.* and others studying the combustion and coking products formed during the detemplation process. Detemplation, as explained in Chapter 1 Section 3.2, sees the breakdown of typically quaternary ammonium OSDA molecules into coke that darkens the zeolite. Karwacki *et al.* used confocal microscopy to show that in CrAPO-5¹⁴³ (AFI), SAPO-34¹⁴⁴ (CHA), and ZSM-5¹⁴⁵ (MFI) zeolites the proliferation of coke products gave rise to a strong light emission that persisted even at high temperatures.

A considerable amount of proof-of-concept work has been demonstrated in the literature to date concerning studies of intrinsic zeolite photoluminescence. However, a primary challenge is the difficulty in extracting specific information regarding chemical speciation using basic confocal techniques. This is because although photoluminescence setups can be incredibly sensitive, they are not necessarily lauded for their specificity. Additionally, catalytic systems pose a highly complex backdrop of evolving chemistry that can be difficult to control. As such these previous studies have not been able to conclusively comment on the specific nature of chemical species observed. Utilising more advanced and multimodal characterisation techniques is one avenue via which this body of work on intrinsic photoluminescence could be extended.

Chapter III

Characterisation Techniques

1 Introduction

This chapter discusses the main characterisation techniques used in this thesis. The primary techniques used are time-resolved photoluminescence spectroscopy, confocal microscopy, fluorescence lifetime microscopy, and Raman spectroscopy/microscopy, all of which utilise lasers as the main excitation source. Lasers are differentiated from other sources of light such as lamps or light emitting diodes (LED) in three principal ways. Firstly, they can be spatially coherent, which means they are capable of being tightly focused down to spot sizes of only a few hundreds of nanometres – a spatial scale of the emitted light. Secondly, they can be temporally coherent, which means they can output clean, single wavelength, practically monochromatic light. Finally, although not exclusively, they can have controllable power output, which is one of the key factors that determine different modes of operation.

A section on standard characterisation techniques is also included here. These include X-ray diffraction, scanning electron microscopy, thermogravimetric analysis, and Brunauer-Emmett-Teller gas analysis. These characterisation techniques are used to establish a baseline understanding of the structure and composition of the samples. As the same SSZ-13 zeolite samples are experimented upon throughout the thesis, a single set of results applicable to all the chapters is presented here.

2 Lasers

2.1 Principle of Operation

A laser is a source of coherent, monochromatic light generated through stimulated emission of electromagnetic radiation. The term ‘laser’ is itself originally an acronym that stands for ‘Light Amplification by Stimulated Emission of Radiation’. Laser light is generated consequent to the competitive co-existence of three types of atomic transitions depicted in Figure 11: absorption, spontaneous emission, and stimulated emission.

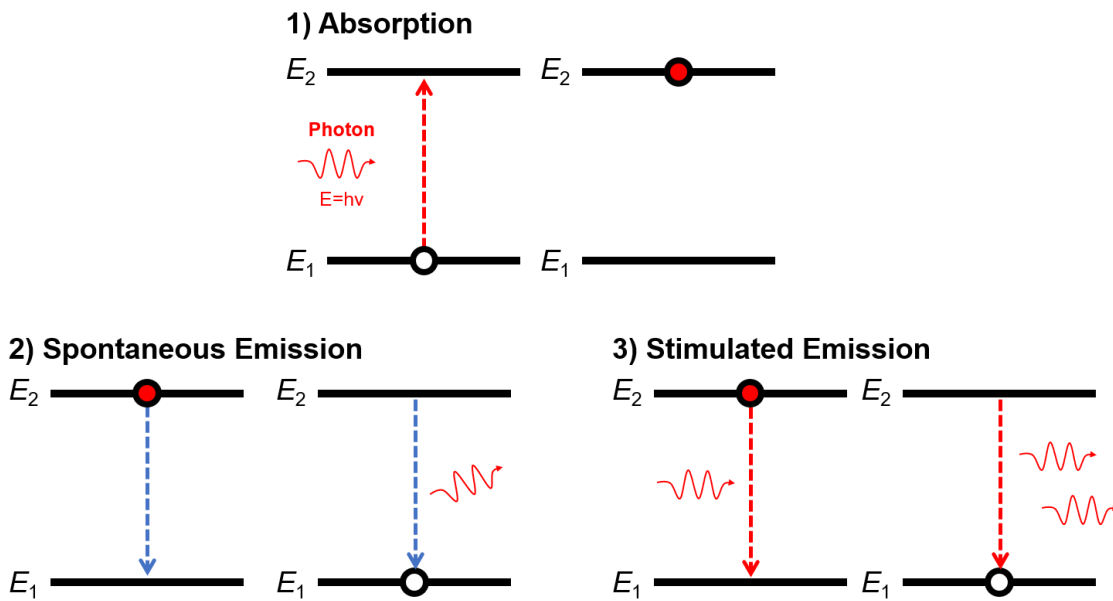


Figure 11 **Three types of atomic transitions involving electromagnetic radiation:** 1) Absorption, 2) Spontaneous Emission, 3) Stimulated Emission

Absorption is the process whereby an atom reaches a metastable excited state upon interacting with a photon. From the excited state, the atom may radiatively return to the ground state in two different ways. It may occur in its own time through *spontaneous emission*, which results in the release of a photon with random phase and direction. It may also be forced back to the ground state through an interaction with a photon of a specific frequency in a process called *stimulated emission*, which results in the emission of a photon with electromagnetic properties (e.g. frequency, phase, polarization, direction of travel) identical to that of the incident photon, producing an optical amplification effect. It is light produced by stimulated emission that ultimately constitutes the coherent output of a laser.

If we consider that the three processes of absorption, spontaneous emission, and stimulated emission occur simultaneously in competition with each other, a laser may in principle be considered a set of conditions that cause stimulated emission to be favoured over spontaneous emission and absorption. Firstly, to favour stimulated emission over absorption, it is necessary to have more excited-state atoms than ground-state atoms. Placing a system in a state where more atoms are in the excited-state rather than the ground-state is called *population inversion* and is a critical step in the construction of a laser. Secondly, to favour stimulated emission over spontaneous emission, it is necessary to ensure atoms in the excited-state are being depopulated via stimulated emission faster than spontaneous emission, which may be facilitated by increasing the concentration of photons.

2.2 Construction

To create the conditions described above, three components are utilised, as demonstrated in Figure 12. They are:

1. The optical resonator
2. The pump source
3. The gain medium

The optical resonator is the means by which light is concentrated, which in turn induces the system to favour stimulated rather than spontaneous emission. A construct called an optical cavity or Fabry-Pérot cavity is often employed. In its simplest iteration, this may be constituted by two curved mirrors arranged opposite each other with an inter-mirror distance that allows for the formation of a standing wave. More complex resonators may have arrangements of more than two mirrors to create a longer optical path length, but the principle of operation remains the same. To enable laser light to exit the cavity, one mirror is often partially reflective. This mirror is also termed the output coupler and enables light to exit the cavity at a rate dependent on the reflectivity, and transmissivity of the mirror material.

The gain medium, also known as the laser medium, is the material whose atoms will be excited to a metastable state to induce stimulated emission. This medium has the biggest influence on the output properties of the laser, such as wavelength. Depending on the application, one of four types of gain media may be used, which include: liquids, gases, solids, or semiconductors. Liquids are typically dyes dissolved in organic chemical solvents and are used in dye lasers. Common examples of gas lasers include argon, krypton, and helium-neon lasers. The most typical types of solid gain media used are crystals with a doped impurity, by far the most common of which are yttrium aluminium garnet (YAG) crystals and titanium doped sapphire crystals. Semiconductors are solid crystals that can be pumped with a simple electric current making them ideal for compact laser applications.

Finally, the pump source is the energy input source for the system that excites atoms in the gain medium. Examples include lamps, electrical discharges, or even laser light from another laser. The pump source, gain medium, and optical resonator are all co-dependent on each other, and the exact type or material used for one will depend on the material used in another.

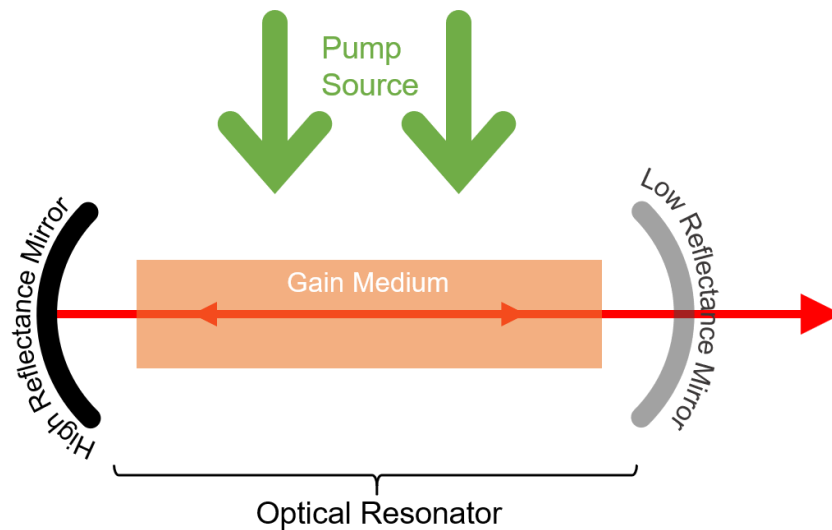


Figure 12 **Components of a laser** including the optical resonator, gain medium, and pump source

With this arrangement of components, laser light is generated thusly:

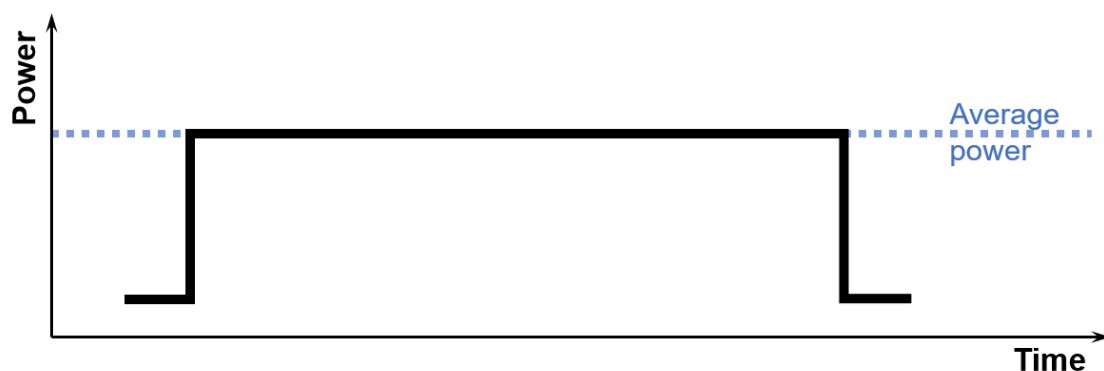
1. The gain medium is pumped with an external energy source to encourage spontaneous emission. Due to careful materials selection, the gain medium is able to reach a state of population inversion.
2. Over a period of time, spontaneously generated photons travel back and forth between the mirrors, amplifying and proportionally increasing the amount of stimulated emission events. Electromagnetic radiation travelling collinearly with the axis of the cavity will be promoted, while non-aligned light is lost. The light may be reflected between the mirrors many hundreds of times during the amplification process before it exits the cavity.
3. After reaching a lasing threshold, the light output from the laser can become coherent and monochromatic.

2.3 Modes of Operation

Lasers can output power in two different ways, as shown in Figure 13. In the first mode of operation, continuous wave (CW) output, power is continuously output at a stable rate. In high power lasers, the power and even wavelength may be tuneable, whereas in low power lasers the power level is usually fixed by design. In the second mode of operation, the laser power is pulsed intermittently.

As shown in Figure 13B, pulsed lasers are defined by a number of parameters including the duration of the pulse (i.e. the pulse width), how frequently the pulses are output (i.e. the repetition rate), and the peak power of each pulse.

A) Continuous Wave Output



B) Pulsed Output

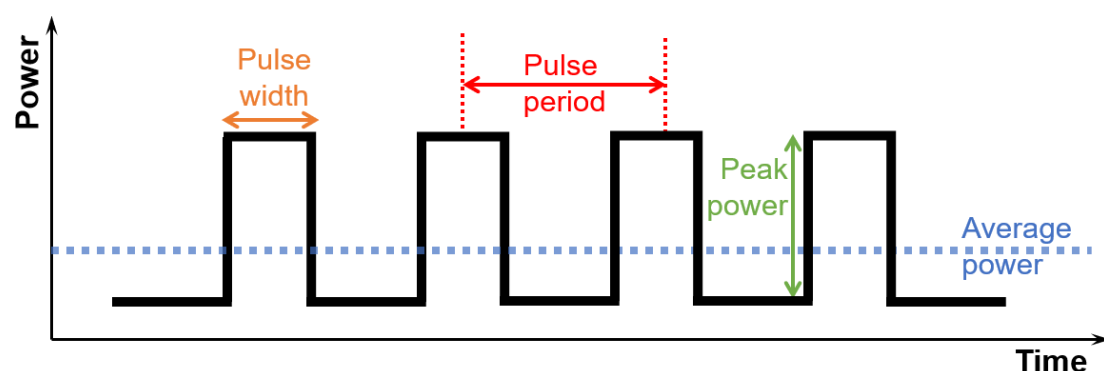


Figure 13 **Two modes of laser operation** including A) Continuous Wave (CW) and B) pulsed output

Depending on the timescale of each of the parameters listed above, the characteristics and application of the pulsed laser will be different. For example, a laser with a millisecond pulse width and low repetition rate in the Hz region would be considered a ‘long-pulse’ laser with lower peak power than an ‘ultrafast’ laser, which may have a pulse width of only femtoseconds and a repetition rate, often, in the order of kHz - MHz. A reliably timed pulse train is what allows for time-resolved studies. In the case of single-excitation source setups, it is the downtime between each laser pulse that is used as a window of opportunity to observe how emission dynamics change (see Section 3.1.3 for further details). Alternatively, in multi-laser setups, a pulsed laser can be used as a timing device to trigger gates (e.g. Kerr-gate Raman¹⁴⁶) or as a pump in pump-probe spectroscopic setups. The wealth of information generated in time-resolved studies is coupled with an increasing complexity and requirement for precision within experimental setups, which is discussed in the following section.

3 Laser-Based Characterisation Techniques

3.1 Time-resolved Photoluminescence Spectroscopy (TRPS)

The time-resolved photoluminescence spectroscopy apparatus generates time-resolved photoluminescence emission spectra. The experimental setup can be divided into two components: the optical path, which is governed by the principles of classical optics; and the electronic setup, which is concerned with synchronising the timing and triggering of signals, data collection, and driving apparatus. Both components of the setup contribute to the quality of the final dataset generated. Finessing elements of the optical setup results in maximal spectral resolution and high signal-to-noise in detected spectra, whereas temporal resolution is primarily dictated by the quality of the electronic timing setup.

3.1.1 Optical Path

The optical pathway is defined as a trained route of light that starts at the excitation source and ends at the detector. The optical pathway can be split into two primary sections: the excitation pathway, and the detection pathway (i.e. before and after the sample). The excitation pathway describes all optical components between the laser and the sample, the said of which serve to attenuate and deliver the laser onto the sample in an appropriate manner. The detection pathway describes all the optical components between the sample and the detector, which conversely serve to capture and deliver any light emitted from the sample following exposure to the excitation source onto the detector. Each section of the optical pathway has different requirements for optimisation.

Optics in the excitation pathway handle higher energy, coherent laser light. Optimised components in this region will therefore be resistant to the effects of beam damage and transmit a clean, undistorted and non-attenuated beam. For lenses handling visible, or near-visible, light this generally means fused silica or quartz with an antireflective coating. A close-up of the excitation pathway is shown in Figure 14.

For the specific setup used in this research, before delivering laser light onto a sample, the excitation source needs to be:

- a) Refined to output of 355 nm only;
- b) Attenuated to a lower power; and,
- c) Focused onto the sample

The 355 nm excitation source is generated by frequency tripling a 1064 nm Nd:YAG laser (CryLas FTSS 355-50, Crylas GmbH, Berlin, Germany). Frequency tripling is a non-linear optical conversion process usually realised in a cascaded process with lithium triborate crystals¹⁴⁷. Even after frequency tripling through the use of a dedicated unit, it is still possible to see faint residual from the harmonic orders of 1064 nm, so these additional wavelengths are removed with a high

quality 355 nm laser line bandpass filter (not shown in Figure 14) placed at the output of the laser unit. Harmonic separators with refractory coatings may also be used.

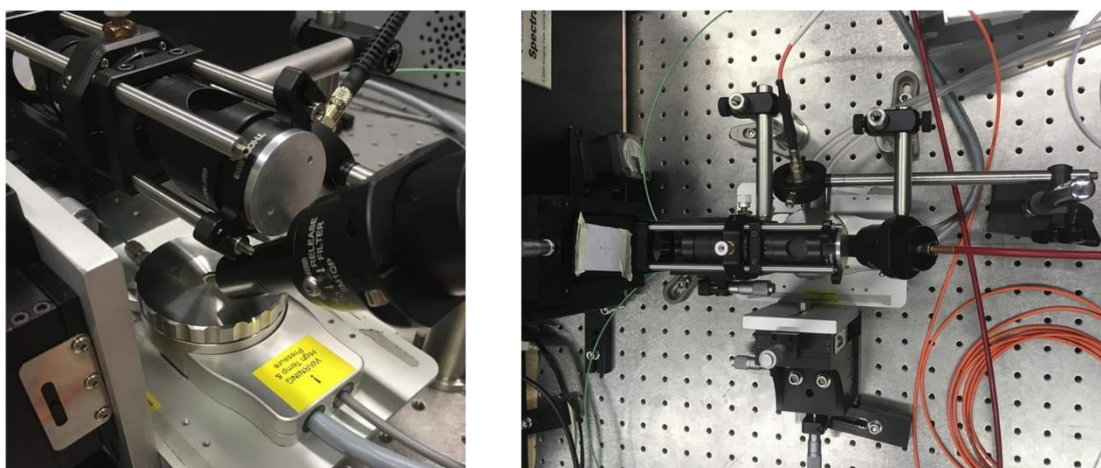
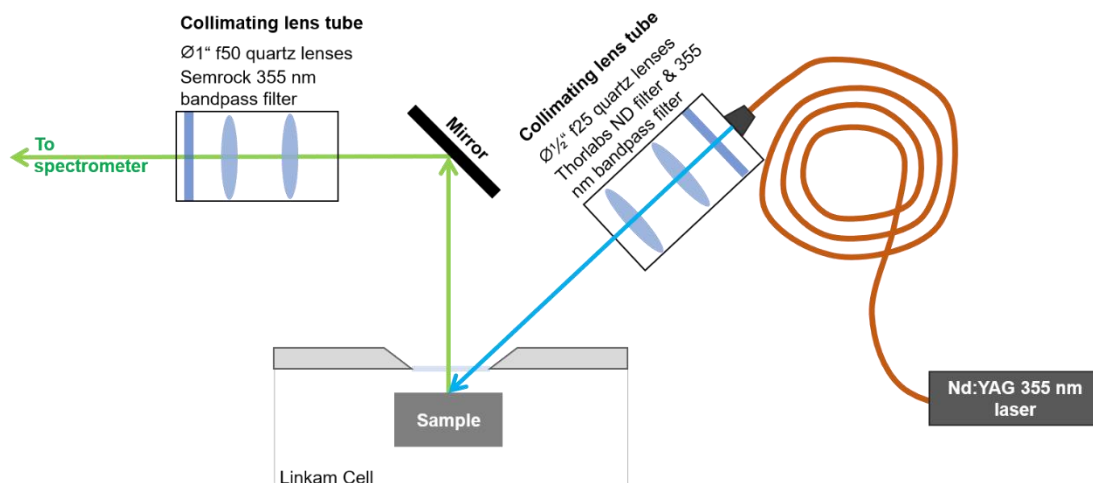


Figure 14 **Optical path of time-resolved photoluminescence spectroscopy setup** from the *ARTIS lab* in the *Department of Experimental Physics at the Politecnico di Milano* with schematic diagram (top) and photographs (bottom)

Following the first clean-up filter, the laser light is directed into a subminiature assembly (SMA) fibre-optic coupling. The 600 μm core fibre-optic is cut to a specific length to delay the optical pulse by about 50 ns. This is the time required for the electrical circuit, which in itself requires time to operate, to initiate gating. The overall effect of this delay is to synchronise the optical pulse train with the electronic drivers. The fibre-optic has the additional benefit of channelling laser light safely up to the optical bench, which is typically positioned some distance away from the enclosed laser source for safety reasons.

Figure 14 displays laser light being delivered onto the sample at an angle from the fibre-optic coupling via a lens tube stacked with a neutral density filter and a pair of UV-coated fused silica collimating optics ($\varnothing\frac{1}{2}$ ", $f = 25$). An additional bandpass filter (FL355-10, Thorlabs) is included to ensure clean 355 nm illuminates the sample. Although it is theoretically possible to include ND

filters at any point, attenuating the laser power as early as possible in a free-coupled optical path is desirable, primarily from a safety perspective as it limits the amount of power being transmitted through exposed regions of the setup.

The primary goal of the detection side is to maximise the amount of light reaching the spectrometer (Acton SP-2300i, Princeton Instruments, USA). A bare-minimum approach to optical components is taken, with a mirror used to step the emitted light up to the plane of the detector, and a set of achromatic collimating lenses ($\varnothing 1"$, $f = 100$) matched to the aperture of the spectrometer ($f/4$). Following the pair of collimating lenses, a final lens is included to focus the beam onto the slit. The setup, being optimised for lowly emitting solid samples, includes an intensifier (C9545-03, Hamamatsu Photonics, Japan) coupled to the CCD (Retiga R6, Q-imaging, Canada), necessitating the use of yet another 355 nm bandpass filter to ensure any scattered laser light capable of saturating the sensitive camera is removed. A 150 line/mm grating with blaze at 300 was used.

3.1.2 *Electronic Setup*

A small mirror on the side of the laser unit directs some of the scattered laser light into a photodiode. The photodiode converts the optical pulse into an electronic pulse or signal, which is in turn sent into a delay generator. The delay generator (DG535, Stanford Research Systems, Sunnyvale CA, USA) is coupled to a homemade circuit based on a fast photodiode coupled to a constant fraction discriminator, which were used to synchronise the laser pulses with the gated intensifier. Delays were controlled by the generator itself, while the gated camera and acquisition software is controlled via a computer. The overall jitter of the detection system was below 250 ps.

3.1.3 *Modes of Data Collection*

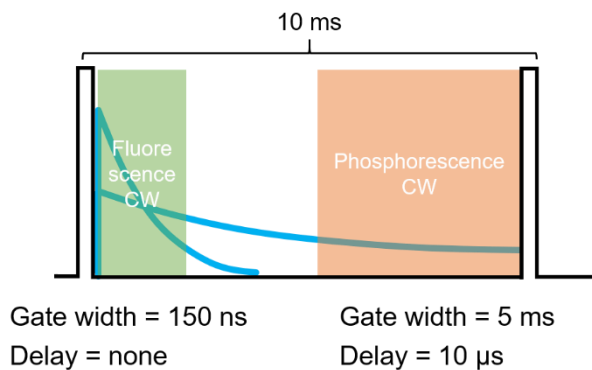
Figure 15 shows the three types of datasets collected. The laser used has a low repetition rate of 100 Hz, which means pulses occur every 10 ms. The pulse width is 1 ns, which makes for an extremely low duty cycle of 0.00001%. The long period of the laser and the proportionally large amount of time the laser spends without actual irradiation means there is flexibility with how data is acquired between pulses. By changing the gate width and delay time in a gated camera it is possible to create three types of measurements: quasi-CW spectra, gated spectra, and lifetime measurements.

By utilising a very wide gate it is possible to generate a spectrum that mimics a CW spectrum as it acquires information across a wide, indiscriminate time interval. The sample is not continuously irradiated, however, resulting in the term ‘quasi-CW’ spectra. The gate width should be large considering the type of information required. In the case of fluorescence, a faster emission process, a gate width of 150 ns acquired with no delay with respect to time zero (i.e. the laser pulse) is deemed sufficient to temporally capture the entire fluorescence process. Phosphorescence, which

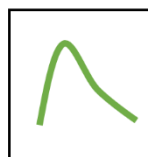
is a significantly longer micro-millisecond regime, forbidden triplet transition, requires a larger gate width. Here 5 ms was selected, as well as a delay of 10 μ s selected to ensure signal gathered is not convoluted with the fluorescence signal.

Gated spectra are acquired by setting the gate width to 10 ns and a series of delays established every 10 ns without temporal overlap, starting from a 0 ns delay with respect to the laser pulse. This results in a series of spectra that slice different temporal regions of fluorescence decay and show how the emission dynamics change with time. Depending on the origin of fluorescence, different samples will exhibit different degrees of spectral evolution with time. Single fluorophore systems, for example, will likely exhibit less variability with time making this dataset less interesting. In the case of the zeolite samples, emission behaviours are not well understood so the gated spectra dataset provides striking insight into what components the broadband illumination is made up of.

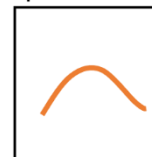
A) CW Measurements



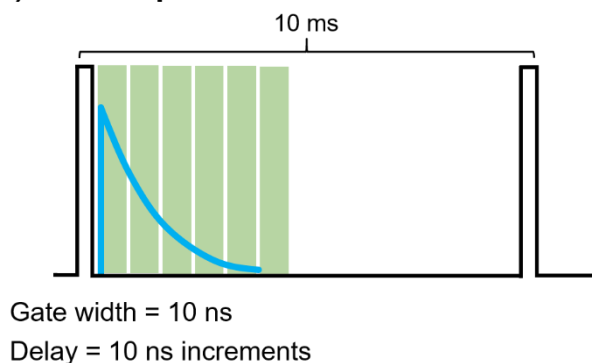
Fluorescence spectrum



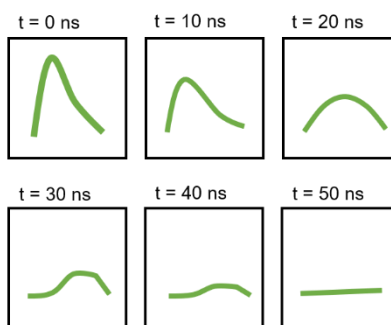
Phosphorescence spectrum



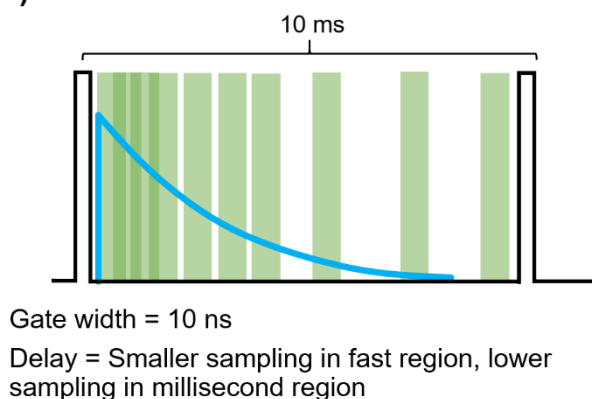
B) Gated Spectra Measurements



Time-resolved fluorescence spectrum



C) Lifetime Measurements



Lifetime fit

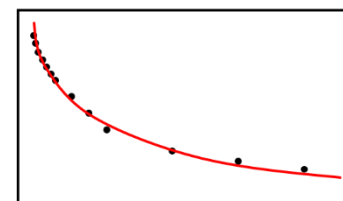


Figure 15 Typical modes of data collection using time-resolved photoluminescence setup. Diagrams are not to scale. A) CW measurements are obtained by taking proportionally wide sampling gates in the fluorescence (i.e. ns) region and phosphorescence (i.e. ms) region. B) Gated spectra are obtained by sampling in a 10 ns gate that is delayed with 10 ns increments to obtain a time resolved series of spectra. C) Lifetime measurements are obtained by sampling a 10 ns window more frequently in the 'fast' fluorescence window (i.e. overlapping in the first 5 ns) and sampling less in the millisecond region to create a series to fit for the lifetime.

The final type of measurement acquired were lifetime measurements. Unlike previous measurements where the gate width and delay are set to visually optimise the spectrum output, lifetime measurements, which also acquire a series of spectra, are optimised with the view to perform a mathematical fit on the data generated. A series of delayed spectra with 10 ns gate width were acquired at varying non-linear delays d . To optimise the fit, spectra were sampled

more heavily in the early portion of the decay curve immediately following excitation. Uneven temporal sampling was adopted to account for the different decay times of the emission components. Each lifetime dataset was analysed across smaller spectral regions, as defined in the results section. The spectral elements of each interval were summed to give three decay curves, which were fitted independently to a multiexponential model function to recover the amplitude and lifetime of two or three emission components.

The model function is:

$$F(d) = \sum_{i=1}^N A_i \tau_i (1 - e^{-W/\tau_i}) + W \cdot Offset,$$

where F = the total fluence (i.e. the integral of the emission intensity within the gate window)

d = the acquisition delay for each time point of the sequence

A_i and τ_i ($i = 1, 2, 3$) = the amplitude and lifetime of the emission components

The term $[1 - \exp(-W/\tau_i)]$ is required to correct for the finite width (W) of the sampling window (10 ns). The fitting method was based on a standard least mean square algorithm derived from the math library provided by the Numerical Algorithms Group¹⁴⁸.

3.2 Confocal Laser Scanning Microscopy (CLSM)

A confocal microscope uses the principles of fluorescence to detect light emitted from a sample. A basic microscope configuration is depicted in Figure 16. A focused laser acts as the excitation source. It is directed onto the sample with a reflective dichroic mirror. The laser spot is rastered across the sample, such that an image is built up point-by-point.

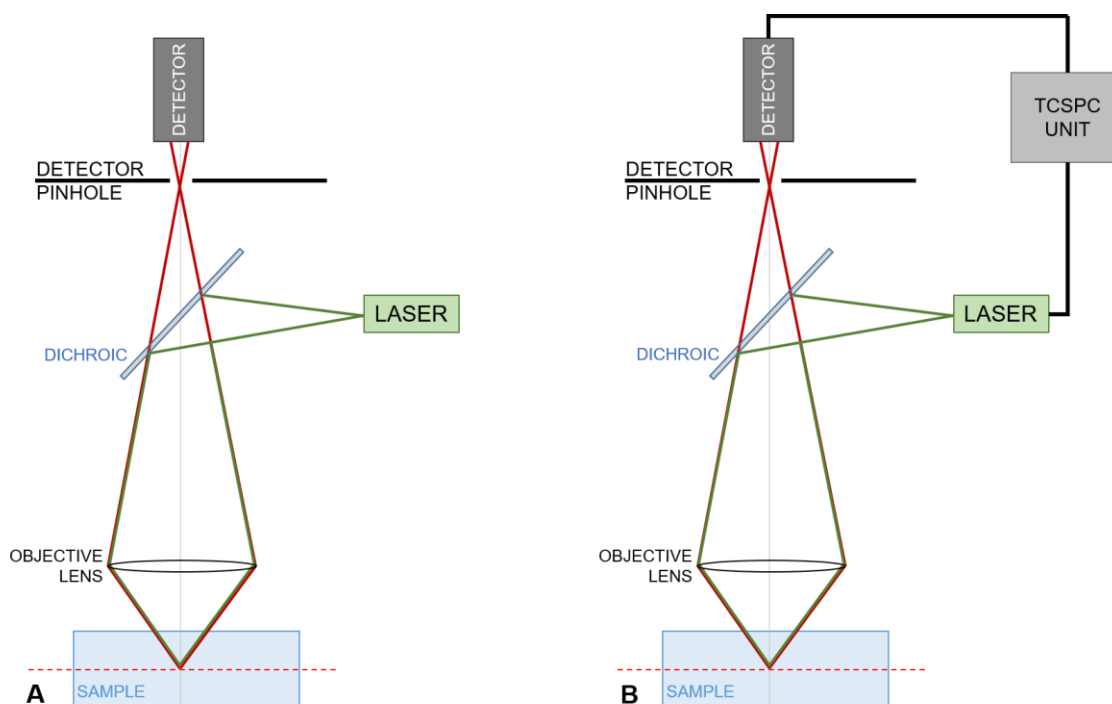


Figure 16 **Diagram showing the setup for a** A) Confocal laser scanning microscope (CLSM), and B) Fluorescence lifetime imaging microscope (FLIM)

A confocal microscope is differentiated from a basic epifluorescence microscope through the use of a pinhole in front of the detector. The addition of a pinhole prevents out of plane light from convoluting the signal from the focal plane, as shown in Figure 17. Rejecting out of plane light means that the thickness of the focal plane becomes thinner than the volume of the sample. By stepping through the z-axis of the sample, it is possible to generate a series of images, or a ‘z-stack’ that provide representative images of the internal volume of the sample.

Confocal experiments were carried out on a Leica TCS SP8 microscope equipped with a 405 nm UV laser and a tuneable super-continuum white light laser.

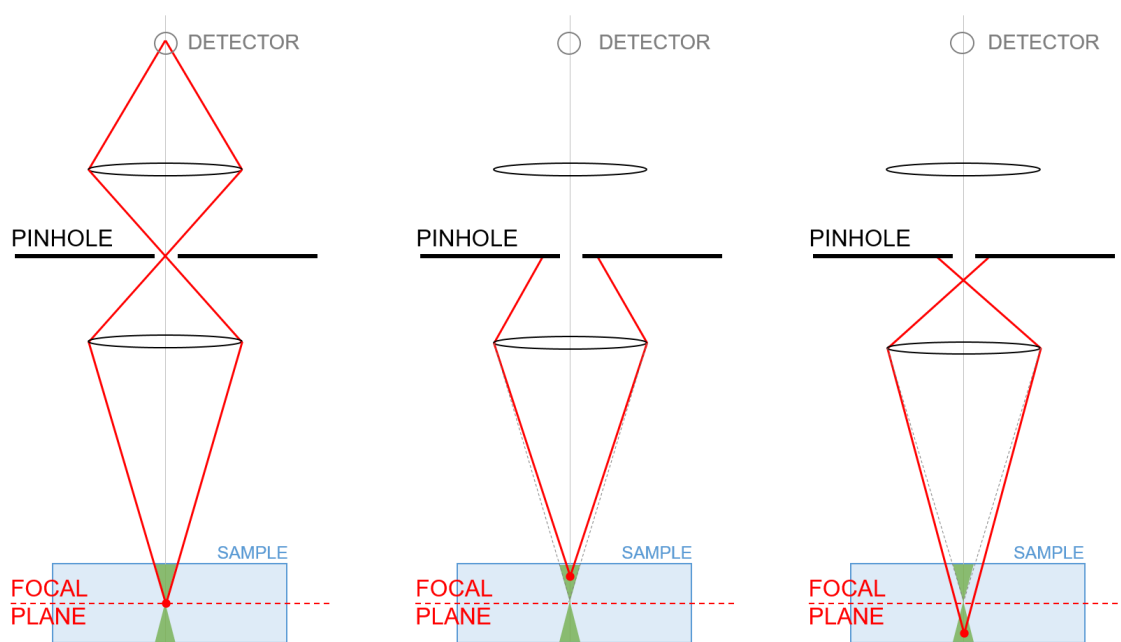


Figure 17 **Schematic diagram of focal planes and the relationship with the pinhole.** Light emitting from above or below the focal plane is geometrically rejected by the pinhole.

3.3 Fluorescence Lifetime Imaging (FLIM)

FLIM is an imaging technique that maps fluorescence lifetimes pixel by pixel. As mentioned earlier in Chapter 2, the fluorescence lifetime is an important quantitative descriptor of the fluorescence emitted and can be described as the amount of time the fluorophore spends in the excited state before returning to the ground state. It can be seen from Figure 5, the optical setup used is exactly the same as a confocal microscope, with the addition of a Time Correlated Single Photon Counting (TCSPC) card. Although confocal imaging can be performed with a CW laser, TCSPC requires a pulsed laser.

TCSPC is a statistical technique that revolves around individually detecting a high volume of single photons, measuring their arrival times with respect to a reference signal (locked to the excitation laser pulse) and then reconstructing a histogram of photons detected with time, as shown in Figure 18. This is a different means of reconstructing fluorescence decay curves compared to the method used in the TRPS setup. TCSPC counts individual photons, which therefore requires a statistically significant volume of photons to be collected for this technique to work. In a simpler analogy, TCSPC could be likened to a stopwatch, where a starting pulse signals the beginning of the measurement, after which point the detection system starts recording the arrival of photons, and a stop pulse signals the end of the measurement.

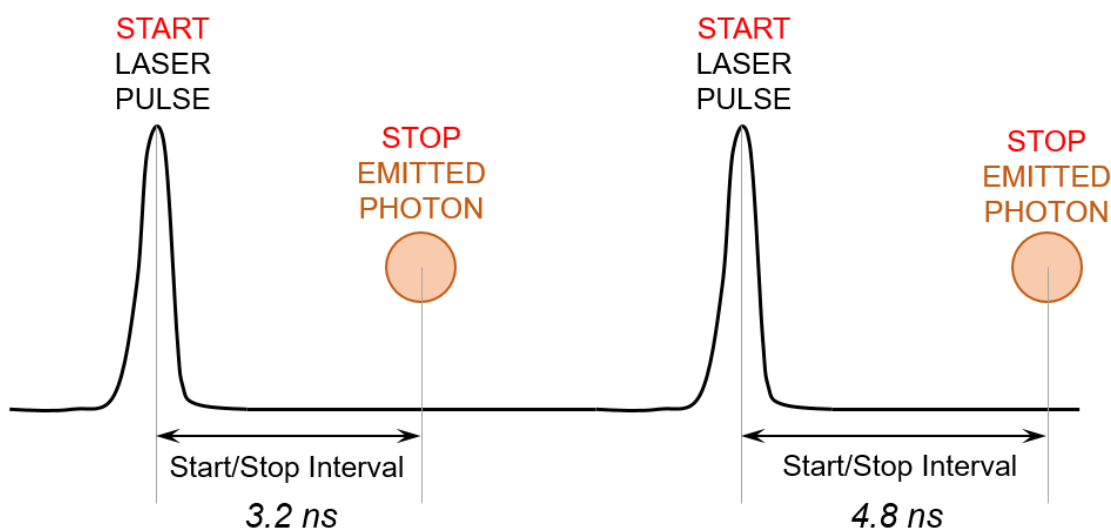


Figure 18 Schematic diagram of start/stop triggering in TCSPC. The laser pulse acts as the start trigger and the detection of an emitted photon acts as the stop pulse. The time duration between the start and stop pulse is digitally recorded and binned in a computer software. The total ensemble of counted photons are then gathered together to form a decay curve, which is then numerically fitted to yield lifetime values.

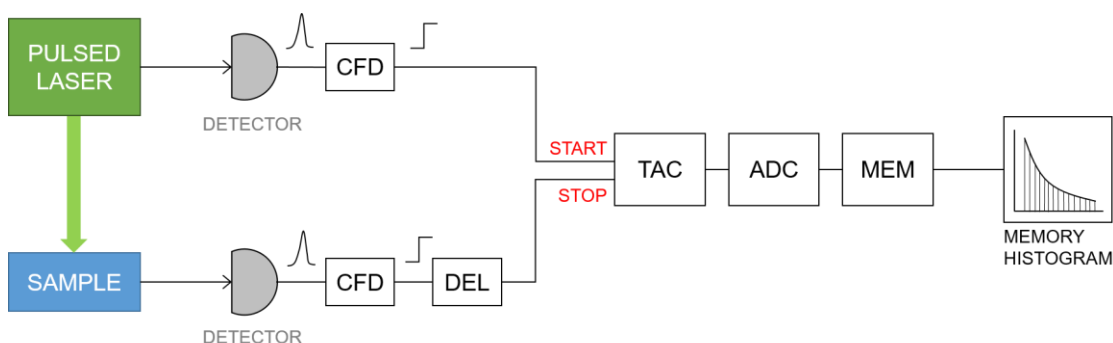


Figure 19 **Primary electronic components in TCSPC signal processing** including a Constant Fraction Discriminator (CFD), electrical delays (DEL), Time-to-Amplitude Converter (TAC), Analogue to Digital Converter (ADC), and digital memory (MEM).

Figure 19 shows the main electrical components on a TCSPC card for signal processing. The system receives two inputs; the start-signal direct from the laser and the input signal emitted from the sample. At first, the electronics evaluate pulse height and discard pulses below a given threshold to eliminate small amplitude noise. The CFD then analyses and normalises the pulse shape of individual pulses, to extract timing information from pulses of variable amplitude. This information allows the system Instrument Response Function (IRF) to be more finely tuned. The CFD analysis is especially important when the detector is a photomultiplier tube (PMT), as the pulse amplitudes can vary significantly.

Normalised pulses from the CFD are then fed through to the TAC, which is a linear ramp generator initiated and halted by the start and stop signals respectively. The resulting output is voltage proportional to the time difference between the two signals. Voltage from the TAC is fed to the ADC, which assigns digital timing values to allow the reconstruction of the histogram. All measured TAC pulse amplitudes are sorted into different time bins. The ADC resolution will determine how many discrete time values are allowed, although higher resolution generally means that processing power must be exceedingly fast to prevent lag in the system.

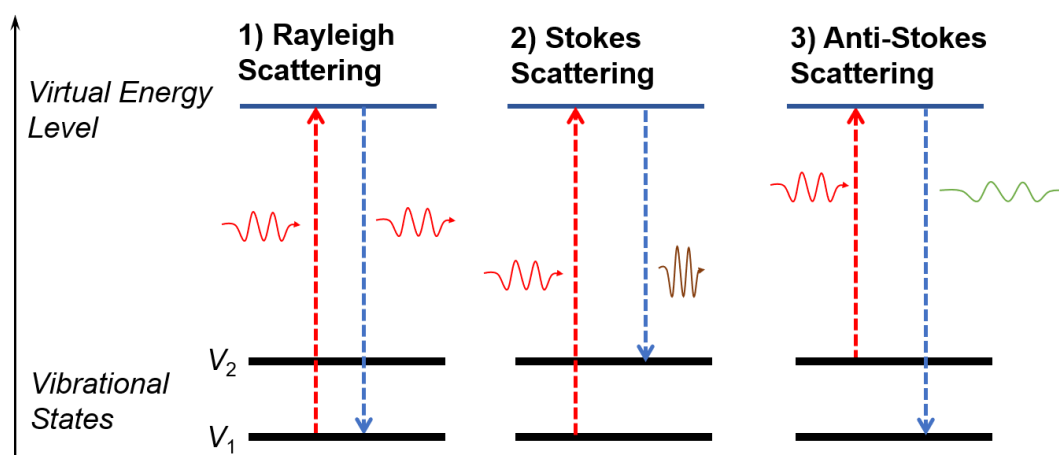
Lifetime values are obtained by fitting the reconstructed TCSPC data with a multiexponential function. In this respect, it is worth noting that the lifetime values are virtually all numerical, and changes to the fitting method or algorithm can yield different lifetimes. Fitting may be performed using different methods including a tailfit or an exponential reconvolution^{149–151} and is typically evaluated using a χ^2 metric.

3.4 Raman Spectroscopy

Another type of light-matter interaction that can be measured is inelastic scattering, also known as Raman scattering. Raman scattering is one of four main types of scattered radiation that may arise during a light-matter interaction, the others being Mie and Rayleigh, which are elastic methods meaning the energy of the incident photon is conserved, and Brillouin, which is another form of inelastic scattering meaning the energy of the resultant radiation differs to that of the incident.

Raman scattering is theoretically conceptualised in a quantum manner in polarisable molecules as a change in vibrational state via promotion to an intermediate virtual excited state (see Figure 20A). A virtual state differs from an actual energy state in that it is not an eigenfunction of a real state and is effectively unobservable. Incident light is absorbed exciting the molecule to the virtual state and re-emits upon return to the ground state, which is the same energy level but with a different vibrational energy; higher in the case of Stokes Raman scattering and lower in the case of anti-Stokes Raman scattering.

A) Quantum Model



B) Classical Model

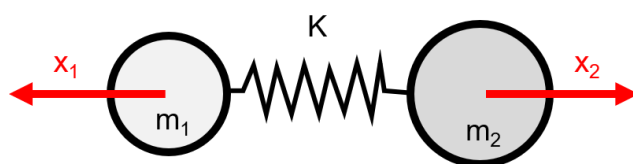


Figure 20 **Two models to explain Raman scattering.** A) Quantum model for Raman scattering showing energy changes between different vibrational states via promotion to a virtual state and B) Classical model for Raman scattering using a diatomic molecule in a mass on a spring model where m_n is the mass, x_n is the force displacement, and K is bond strength.

A classical model may also be offered (see Figure 20B) if light is considered in its particle form as a photon that is incident on a molecule. Using a diatomic molecule as a model for a mass on a spring, where m is atomic mass, x is displacement, and K is bond strength, it is possible to apply Hooke's law, which would state that the displacement of the two masses oscillate as a cosine function dictated by the bond strength and atomic mass, meaning that particular bonds have a unique oscillatory function. If an electromagnetic wave vector (i.e. incident light source) were to interact with a polarisable molecule, classical theory would state that an electric dipole moment would be induced, deforming the molecule and causing a characteristic scattered light vibration.

Raman scattering may be measured spectroscopically using the same principle components used in a photoluminescence spectroscopy setup (i.e. a laser excitation source, a diffraction grating, a CCD detector). Unlike photoluminescence, however, Raman scattering does not involve excitation to a higher eigenstate and instead occurs practically instantaneously. This negates the need for any time-resolved dimension to the experimental setup. The focus of a Raman spectroscopy setup is rather to improve sensitivity, as Raman scattering is known to be very weak, and spectral resolution, as Raman scattering produces spectra with discrete, spectrally narrow bands associated, typically, with molecular vibrations. The technique can be also combined with microscopy to facilitate spatial resolution, a technique termed Raman microscopy.

4 Preliminary ‘Standard’ Zeolite Background

Characterisation

4.1 Zeolite Background

Chabazite (CHA) is a triclinic crystal, noted for its unique network of cages connected by narrower channels (see Figure 21Error! Reference source not found.A). Structure-wise, it is a well-known member of the ABC 6-family of zeolites, comprised of a stacked sequence of 6-rings arranged to form double 6-rings at the apices of its rhombic unit cell. The eight ringed cages have an aperture of roughly $3.8 \times 3.8 \text{ \AA}$ ¹⁵². The largest internal cage diameter is 8 \AA , and the pore limiting diameter is 4.2 \AA .

Trimethyladamantammonium hydroxide (TMAda) is a quaternary ammonium hydroxide (see Figure 21Error! Reference source not found.B) that is used as the OSDA for synthetic high-silica form of chabazite called SSZ-13. While TMAda reliably produces a high quality SSZ-13 product, it is generally the most expensive component of the synthesis process and some studies have focused on finding alternative cheaper templating agents¹⁵³ or even template-free methods^{154,155} for synthesis. It is generally thought that OSDAs direct zeolite crystallisation through charge compensating interactions between the OSDA and the framework, with the shape, size, charge, hydrophobicity, and flexibility of the template all influencing how effectively the structure is directed¹⁵⁶. Rather than requiring one OSDA molecule per cage, the templating effect of a few cages then enables longer range crystallisation. OSDAs have also been shown to be closely associated with the location of aluminium T-sites¹⁵⁷, meaning that the amount and distribution of OSDA will be associated with the Si/Al and the distribution of Al.

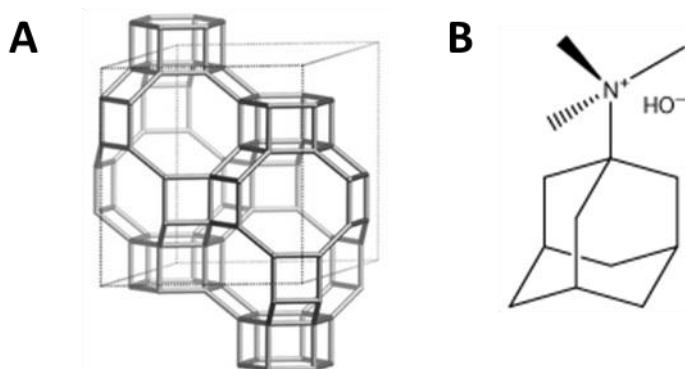


Figure 21 **Structural diagrams of zeolite and organic structure directing agent.** (A) Chabazite-type zeolite structure⁸ and (B) trimethyladamantylammonium hydroxide (TMAda) structure

4.2 X-Ray Diffraction (XRD)

4.2.1 Technique Background

X-ray diffraction (XRD) employs an x-ray source to generate bulk average information on the crystallinity of a sample. It works on the principle of diffraction and results in a spectrum of peaks

correlating with constructive interference arising from Bragg's law. It determines, in the first instance, whether a sample is amorphous or crystalline as only regularly arranged materials with long-range crystal planes will act as a diffraction grating. An amorphous material will not generate a diffraction pattern. Where materials are crystalline, XRD provides information on lattice spacing and plane alignment.

XRD works by illuminating a monochromatic X-ray source at a sample at an angle, with diffracted rays being detected. The sample is scanned through a range of diffraction angles to capture all lattice plane orientations generating a spectrum of X-ray counts vs. 2θ °. As crystalline materials typically have characteristic d-spacings based on bonding and composition, XRD can be used to fingerprint materials.

4.2.2 Method

Powder X-ray diffraction was measured using a Rigaku Miniflex X-ray instrument with a Cu tube source of 600 mW and 1D D/teX detector and divergent slits. Diffraction patterns were collected between 5-50 2θ ° with an increment of 0.017° (2θ) and an acquisition time of 1 sec/step.

4.2.3 Results & Discussion

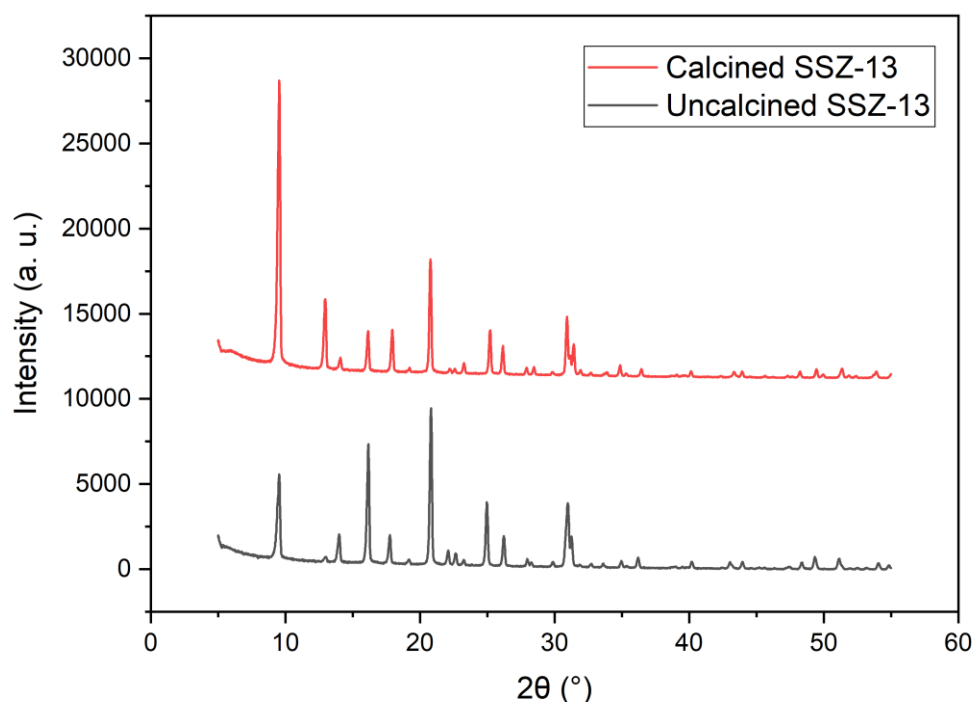


Figure 22 XRD patterns for calcined (red) and uncalcined (black) SSZ-13 material

Figure 22 shows XRD patterns for the uncalcined and calcined SSZ-13 material. The clear ensemble of peaks in both samples indicates the satisfactory crystallinity of both samples, further implying that the framework has not been adversely affected by the thermal calcination process. The position of reflections are consistent with IZA data⁸.

4.3 SEM

4.3.1 *Technique Background*

Scanning electron microscopy (SEM) involves irradiating a sample with a focused electron beam in a vacuum chamber. The use of a highly focused electron beam creates a significant depth of field in images. Many different types of detectors can be incorporated into an SEM, but images are usually generated by detecting secondary electrons (i.e. electrons emitted from the sample following excitation with the incident electron beam) with an Everhart-Thornley detector. It is also possible to detect reflected or back-scattered electrons, X-rays, and cathodoluminescence. Secondary electrons are emitted from the sample surface resulting resolution as low as 1 nm. When coupled with the large depth of field, SEM's high-resolution renders images with a distinctive 3-dimensional quality and a realistic, photographic feel. This makes the technique particularly well suited to visualising morphology and surface texture in a sample.

4.3.2 *Method*

Zeolite powder was sprinkled sparingly onto a carbon tab and then coated with gold for 35 seconds. Actual layer thickness is unknown. SEM images were obtained on a JEOL JSM-6701F Field Emission Scanning Electron Microscope. 10 keV voltage, 8.7 working distance, and 250x magnification were used to acquire both images.

4.3.3 *Results & Discussion*

Widefield SEM images of uncalcined and calcined SSZ-13 are shown in Figure 23. Some slight charging is visible. Both samples show a relatively uniform size distribution (around 30 μm) of crystals with good cubic regularity. Heat treatment does not appear to have affected the external crystallinity of the samples. Some evidence of crystal intergrowth appears in both samples, arising as a result of the synthesis process.

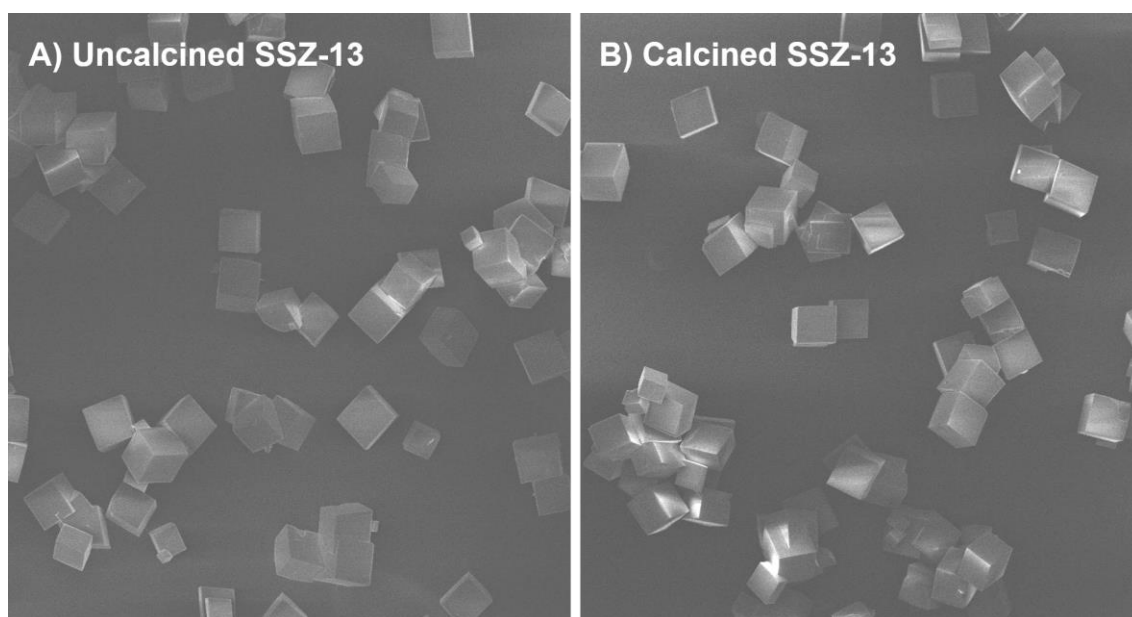


Figure 23 **SEM images** of A) uncalcined and B) calcined SSZ-13 zeolite (10 keV, WD 8.7, 250x)

4.4 TGA

4.4.1 Technique Background

Thermogravimetric analysis (TGA) involves heating a sample continuously up to a set temperature and monitoring changes in mass. The results of TGA can provide information on phase transitions, desorption, decomposition, or chemical reactions. In zeolites, TGA is most commonly applied to determine what percentage of its mass is from adsorbed species such as water, which would be seen as a mass loss around 100 °C, or organic material.

4.4.2 Method

8 mg of calcined sample and 39 mg of uncalcined sample were loaded separately into a Q50 TGA Instrument (TA Instruments, Denver, USA). N₂ flowed at 40 mL/min was used as a balance gas and 60 mL/min of 21% O₂ in He was used during the actual measurement. The samples were heated in air at 1 °C/minute up to 150 °C and held for 2.5 hours. They were then heated to 350 °C at 2.2 °C/minute and held for 3 hours, and then heated at 0.8 °C/min to 580 °C and held for 3 hours.

4.4.3 Results & Discussion

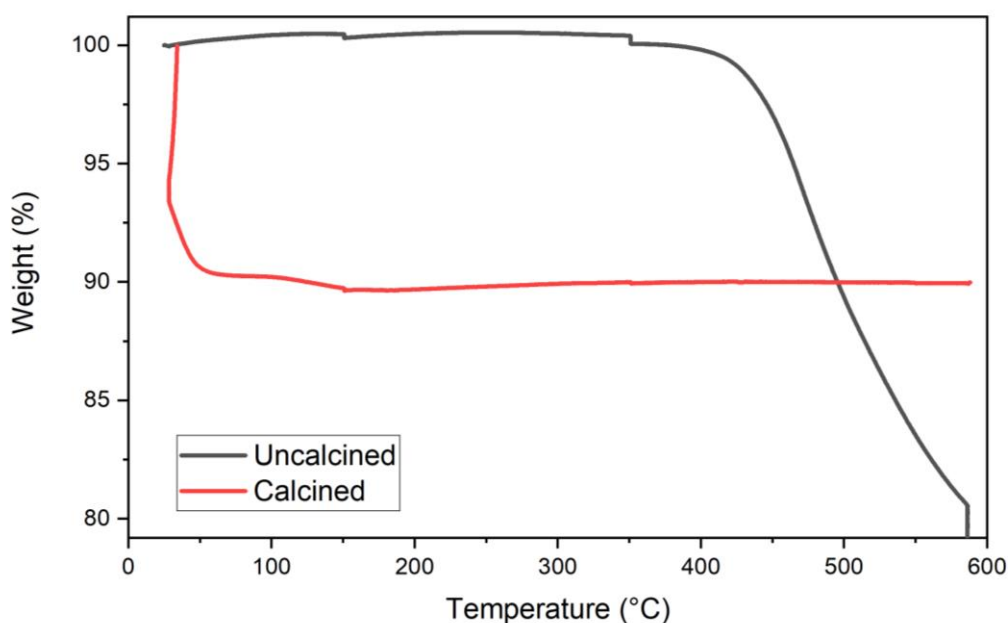


Figure 24 **TGA curves of uncalcined (black) and calcined SSZ-13 (red)** showing the percentage of the original sample weight as a function of the temperature at the sample

Table 4 **Mass loss of uncalcined and calcined SSZ-13 based on TGA data**

Sample	Mass loss (wt %) $T < 250\text{ }^{\circ}\text{C}$	Mass loss (wt %) $250\text{ }^{\circ}\text{C} < T < 500\text{ }^{\circ}\text{C}$	Mass loss (wt %) $500\text{ }^{\circ}\text{C} < T$	Total mass loss (wt %)
Uncalcined SSZ-13	-0.5	11.5	10.2	21.2
Calcined SSZ-13	10	0	0	10

Figure 24 shows TGA data for uncalcined and calcined SSZ-13 samples. Overall, the uncalcined sample loses 21% of its total mass and the calcined sample loses 10%. The uncalcined sample is known to contain organic templating agent so the higher overall mass loss is attributed to this. Below 250 °C uncalcined sample does not experience significant mass loss (see Table 4), indicating that the template is either broadly stable or yet to decompose sufficiently to evacuate the pores up to this temperature. A modest mass loss is visible at 150 °C during the isothermal portion of the temperature programme. The relative stability of the trace until 300 °C could also be due to hydrocarbon pool chemistry in an oxidising environment, which causes the formation of bulkier molecules that continue to be retained in the framework¹⁵⁸. Between 250 and 500 °C the largest proportion of the total mass loss is seen, and this is attributed to the removal of organics. At temperatures exceeding 500 °C and during the isothermal hold for 3 hours at 580 °C, additional mass loss is seen, implying that in template material is progressively depleted at these higher

temperatures. A true detemplation would see the as-synthesised material being held for at least 550 °C for 10-12 hours, ensuring as much organic material is removed as practically possible.

Unlike the uncalcined SSZ-13, the calcined sample experiences the majority of its mass loss below 250 °C. The rapid mass loss below 200 °C is attributed to water loss. Beyond this temperature, the sample mass is exceedingly stable. Additionally, at 580 °C there is not any significant change in the trace. This indicates that the sample was appropriately calcined as there is no major indication of organic-related mass loss, and it indicates that the framework is thermally stable up to at least 580 °C.

4.5 UV-vis

4.5.1 *Technique Background*

Ultraviolet-visible spectroscopy (UV-vis) is a type of absorption spectroscopy that irradiates sample using light in the ultraviolet and visible regions. It operates on the principle that molecular species can absorb photon energy to excite electrons to higher orbitals. The wavelength of the light absorbed corresponds to different type of energy transitions with more readily excited electrons absorbing longer wavelengths. As an analytical technique for zeolites it is frequently used to determine the presence of different molecular species and transition metal ions.

4.5.2 *Method*

UV-vis spectra were acquired under ambient conditions with a Shimadzu 2700 UV-vis spectrophotometer fitted with an optical integrating sphere for solid powdered samples. Zeolites were pressed into a sample holder and mounted vertically in the integrating sphere. A standard barium sulfate (BaSO₄, Sigma-Aldrich, 99%) sample was used for baseline scans. Spectra were collected from 200-1400 nm at a scan speed of 150 nm/min, and a resolution of 0.5 nm.

4.5.3 *Results & Discussion*

UV-vis data for calcined and uncalcined SSZ-13 are included in Figure 25. The uncalcined material features a broad absorption band at 700 nm, which is attributed to the occluded OSDA. In contrast, the calcined material shows a flat spectrum indicating overall a minimal amount of absorption due to the OSDA being largely evacuated from the framework. Absorption at around 250 nm is associated with the framework and has been similarly reported by Wardani et al¹⁵⁸.

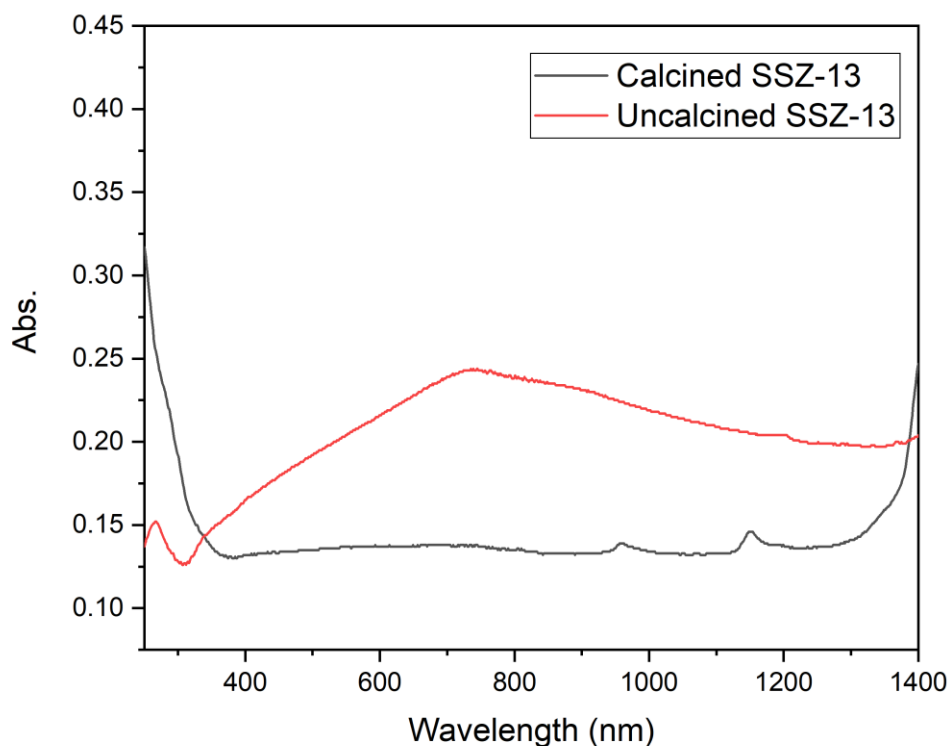


Figure 25 UV-vis spectra of uncalcined (black) and calcined SSZ-13 (red)

5 Sample Preparation

Sample was synthesised by Ines-Lezcano Gonzalez of the Beale group.

Template stabilised SSZ-13 zeolite (Si/Al = 15) was synthesised under hydrothermal conditions with TMA (Sachem) as the organic structure directing agent as previously described^{159,160}. 20.83 g of tetraethyl orthosilicate (TEOS) and 1.36 g of aluminium isopropoxide were hydrolysed in 79.82 g of 13.2 wt% n,n,n-trimethyl-1-adamantylammonium hydroxide (TMAda) to form the synthesis gel. After stirring the mixture at room temperature 2.08 g of 48 wt% HF was added as a mineraliser. The mixture was then mechanically stirred for 8 hours to homogenise. The molar ratio was:

$\text{SiO}_2:0.033 \text{ Al}_2\text{O}_3:0.5 \text{ TMAda}:0.5 \text{ HF}: 3 \text{ H}_2\text{O}$

The gel was then autoclaved at 150 °C and the solid zeolite recovered with filtration. As-made zeolite was then dried overnight in air at 80 °C to form a white powder that was stored in glass vials under atmospheric conditions. This dried sample is termed the ‘uncalcined sample’. A portion of the as-made zeolite was subjected to a standard calcination procedure to obtain the proton form. This involved placing the sample in a ceramic dish in a static oven and heating in

air to 120 °C at 1°C/min and holding it at this temperature for 2.5 hours, then heating it further, to 550 °C at 4 °C/min and holding at this temperature for 10 hours to create the white calcined sample.

Chapter IV.

Understanding the Dynamics of Fluorescence Emission During Zeolite Detemplation using Time Resolved Photoluminescence Spectroscopy

In collaboration with the Valentini group in the Experimental Physics Department at the Politecnico di Milano

Published in Journal of Physical Chemistry C as Omori N, Greenaway A, Sarwar M, Collier P, Valentini G, Beale A, Candeo A. (2020) Understanding the Dynamics of Fluorescence Emission During Zeolite Detemplation Using Time Resolved Photoluminescence Spectroscopy. J. Phys. Chem. C. 124(1), 531-543

doi:[10.1021/acs.jpcc.9b09050](https://doi.org/10.1021/acs.jpcc.9b09050)

1 Introduction

Photoluminescence in zeolites has been previously reported, most frequently in the context of a background signal that convolutes the bands seen in vibrational spectroscopy methods such as Raman and IR spectroscopy, particularly in *in situ* studies with increasing temperature¹⁶¹. This is often the case when organic products begin to form in catalytic reactions or when coking starts to occur¹⁶². In such studies the presence of photoluminescence mars the ability to collect meaningful spectra and gating systems may be employed to remove the background, although these have limited effectiveness and are often complex and costly¹⁴⁶. Instead of considering this fluorescence emission as an unwanted signal to be subtracted out as a background, it is possible to analyse light emission from fluorophores that proliferates naturally throughout the course of a catalytic reaction as a signal in its own right. The origin of this optical activity has been attributed to various sources. Some studies such as those by Liu et al. who recorded the emission from SDA in zeolite structure ITQ-26¹⁶³ and a prolific body of work by Hashimoto et al.¹¹⁷ focus the interpretation of emission spectra on the presence of adsorbed organic species. The effect of metal loading on PL spectra has also been previously acknowledged in studies on copper species^{164,165,166}, silver clusters¹³⁶, lanthanoid complexes¹⁶⁷, manganese doping¹⁶⁸, and europium exchanged frameworks¹⁶⁹, as well as non-metallic sulphide clusters¹⁷⁰. Studies also exist that focus on PL emission of the framework itself such as Planells et al. and their work on PL in crystallised silicalite-1 films¹⁷¹ and Wang et al. in their work on zeolite derived glasses, which attribute PL to an ordered-disordered transition¹⁷²⁻¹⁷³. Theoretically, studying photoluminescence (PL) is an excellent way to gain further insight into the adsorbed organics residing within the complex internal landscape of zeolite microstructures because it directly pertains to molecular-level processes of energy absorption and emission. Subsequently, changes in emission lifetime and spectral peak positions can be linked to guest molecule behaviour and numerous non-intrinsic material properties such as different non-radiative decay pathways, energy transfer, and intersystem crossing, all of which may be influenced by environmental factors.

In this chapter, time-resolved photoluminescence spectroscopy (TRPS) has been identified as an alternative complementary means of analysing carbonaceous species in catalysis. TRPS is an established non-destructive spectroscopy technique that uses laser excitation to induce characteristic photoemission from a sample¹⁷⁴. Using an intensified camera and a pared back optical geometry, fluorescence and phosphorescence information can be detected with a high degree of sensitivity. Although traditional steady-state fluorescence measurements often yield broad, relatively featureless spectral profiles with limited chemical specificity, TRPS features the addition of a time gate to the detection system, which imparts datasets with an enhanced capability to differentiate emissive components within the sample. Analysis can, therefore, be conducted in two directions, namely temporal or spectral, with the possibility to visualise data by either time-

gated spectra, decay profiles in specific spectral regions, or simultaneously in both. The use of a UV-laser makes the system well-placed to specifically probe volatile organic species.

The purpose of this chapter is to demonstrate the capabilities of TRPS when analysing adsorbed organics in zeolites, and to demonstrate how this technique could be applied to more complex systems in the future. For this reason, a controlled detemplation of an industrially relevant chabazite (CHA) topology zeolite was selected. To ensure stable crystallisation during the synthesis process, commercial zeolites are commonly manufactured with organic structure directing agents (OSDA), the commonest of which are typically amine or alkyl cations. The OSDA, which is not integral to the zeolite's catalytic functionality, is decomposed and removed from the framework via a thermal calcination process called detemplation. Characterisation of the carbogenic species formed during detemplation have previously been attempted using UV-vis & fluorescence microspectroscopy¹⁴⁵ and positron annihilation lifetime spectroscopy¹⁷⁵, with both studies focusing on MFI-type zeolites. In this paper, a comparative study between three zeolite samples quenched at different stages of the calcination procedure (i.e. an uncalcined, a partially calcined, and a fully calcined chabazite zeolite) was conducted.

In the first section, the PL spectrum of the OSDA N,N,N-trimethyl-1-adamantylammonium hydroxide (TMA) was established, and subsequently probed in the uncalcined sample. A focus was placed on the confinement effects guest molecules experience when trapped inside chabazite's characteristic cage-channel structure. In the second section, gated spectra are used to highlight the similarities and differences between PL spectra of an uncalcined and a partially calcined zeolite. In the third section, a comparison between an uncalcined and a calcined zeolite show that gated spectra and lifetime analysis can track the depletion of TMA molecules. By studying lifetime components discernible in different spectral regions, it was possible to attribute certain spectral variations to the steric effects of occlusion, and other variations to the formation of new combustion species that disappear following a full calcination. In studying the long-lived microsecond range, phosphorescent signatures attributed to the presence of occluded template were recorded.

2 Experimental Section

2.1 Sample Preparation

Four samples were analysed in this study: template material, uncalcined chabazite, calcined chabazite, and a chabazite sample quenched halfway in temperature through the calcination process. Template material was measured in solution form and comprised 25 % TMAda and 75 % water (Sachem).

Template stabilised SSZ-13 zeolite (Si/Al = 15) was synthesised as described previously in Chapter 3 Section 5 under hydrothermal conditions¹⁷⁶ with TMAda (Sachem) as the organic structure directing agent. As-made zeolite was dried overnight in air at 80 °C to form a white powder that was stored in glass vials under atmospheric conditions. This dried sample is termed the ‘uncalcined sample’. A portion of the as-made zeolite was subjected to a standard calcination procedure. This involved placing the sample in a ceramic dish in a static oven and heating in air to 120 °C at 1 °C/min and holding it at this temperature for 2.5 h, then heating it further, to 550 °C at 4 °C/min and holding at this temperature for 10 h to create the calcined sample.¹⁷⁷ The intermediate sample was synthesised by observing the same calcination conditions but quenching the sample after completion of the temperature ramp to 550 °C.

2.2 Theoretical Calculations

Theoretical calculations were performed by Dr. Misbah Sarwar from Johnson Matthey.

A combined Monte Carlo-Simulated Annealing procedure is used to determine low energy sites for the TMAda template molecule in the CHA framework. The calculations were run using the Sorption and Forcite modules within Materials Studio 2017¹⁷⁸. The COMPASS forcefield¹⁷⁹ was used to describe all zeolite-template interactions. The Monte Carlo part of the calculations was used to locate possible sites for the sorbate molecule within the zeolite structure. The CHA framework was optimised prior to the Monte Carlo simulation. During the Monte Carlo simulation both the zeolite framework and the template molecule are assumed rigid, which results in a strained system. To find the global minimum a simulated annealing procedure was used on the lowest energy configurations obtained from the Monte Carlo simulations where the framework, template, along with the cell parameters were optimised. The zeolite framework was assumed to be siliceous and the balancing charge accounted for by scaling the charges on the framework atoms¹⁸⁰. The charges used in the simulation are given in Table 1.

*Table 5 **Charges for simulation** where q is charge measured in electrostatic units of charge (esu). Calculated by Dr. Misbah Sarwar.*

Atom	q (esu)
Si	+0.862
O	-0.445
C attached to N and methyl group	0.248
C attached to N and C	0.407
sp3 C	-0.106
C with 3 C neighbours	-0.053

H	0.053
N	-0.628

2.3 Raman Spectroscopy

Raman spectra were obtained from an InVia confocal Raman microscope equipped with a 50x objective lens (Nikon, L Plan Apo, 50x/0.45, WD17) and Peltier cooled CCD. Sample was irradiated with either an 830 nm diode laser with 500 mW maximum power output, or a 514 nm argon laser (Stellar PRO, Modu-laser) with 50 mW maximum power output. A grating with 1200 lines/mm was used. Attenuated power at the sample is achieved using neutral density filters.

2.4 Time-Resolved Photoluminescence (PL) Spectroscopy and Data Analysis

The time-resolved fluorescence spectroscopy setup used is a variation of the Q-switched laser & gated camera setup previously described by Dozzi et al.¹⁸¹. Powdered samples were flattened on an aluminium plate and liquid samples were measured in a quartz cuvette. The sample surface was irradiated at a 45° angle with the 355 nm third harmonic of a pulsed Nd:YAG (CryLas FTSS 355-50, Crylas GmbH, Berlin, Germany). The system works at low rep rate of 100 Hz with a laser pulse width of 1 ns, allowing us to measure the lifetime of both permitted singlet transitions in the nanosecond regime and dipole forbidden triplet transitions in the microsecond or millisecond regime. A low power density of 0.9 $\mu\text{W}/\text{cm}^2$ was used. A mirror was placed above the sample at 45° to step the emitted signal (375 – 750 nm) onto a simple optical system comprised of two lenses (\varnothing 1 inch, $f = 100$ mm) that focused the light onto the slit of an Acton SP-2300i spectrometer (focal length = 300 mm, $f/4$ aperture) matching its aperture. Signal was detected with a high-speed image intensifier (C9545-03, Hamamatsu Photonics, Japan) and CCD camera (Retiga R6, Q-imaging, Canada). The image intensifier provides a minimum gate time of 3 ns and a variable amplification factor. The CCD camera is coupled to the image intensifier by a lens system. The detector was fully characterized in terms of spectral sensitivity, photometric gain and temporal response before the experiment. A delay generator (DG535, Stanford Research Systems, Sunnyvale CA, USA) and homemade circuit based on a fast photodiode coupled to a constant fraction discriminator were used to synchronise the laser pulses and gated intensifier. The overall RMS jitter of the detection system was below 500 ps, which sets the accuracy of lifetime measurements below 1 ns.

Data were collected in three modes. The first mode was ‘quasi-CW spectra’, where the gate width on the intensifier was set to 150 ns synchronous with the laser pulses for fluorescence regime CW, and to 5 ms with a 10 μs delay capturing the CW spectrum of any longer-lived

phosphorescent components. For fluorescence, a gate much longer than its average decay time was used to capture almost all the signal, while removing the ambient light and reducing the electronic noise; for phosphorescence, the gate was required to remove the short living emission. The second mode was ‘gated spectra’, where the gate width was set to 10 ns and a series of delayed spectra were acquired every 10 ns, starting from a 0 ns delay with respect to the laser pulses. This was to ensure no temporal overlap between the spectra measured. Finally, ‘lifetime measurements’ were acquired by setting a gate width of 10 ns and acquiring a series of delayed spectra at varying delays d . To optimise the fit, spectra were sampled more heavily in the early portion of the decay curve immediately following excitation. Uneven temporal sampling was adopted to account for the different decay times of the emission components. Each lifetime dataset was analysed across specific spectral regions, as defined in the results section. The spectral elements of each interval were summed to give spectrally resolved decay curves, which were fitted independently to a multiexponential model function to recover the amplitude and lifetime of two or three emission components.

The model function is:

$$F(d) = \sum_{i=1}^N A_i \tau_i (1 - e^{-W/\tau_i}) + W \cdot Offset,$$

where F is the total fluence, i.e., the integral of the emission intensity within the gate window, d is the acquisition delay for each time point of the sequence, while A_i and τ_i ($i = 1, 2, 3$) are the amplitude and lifetime of the emission components. The term $[1 - \exp(-W/\tau_i)]$ is required to correct for the finite width (W) of the sampling window (10 ns). The fitting method was based on a standard least mean square algorithm derived from the math library provided by the Numerical Algorithms Group (NAG).

3 Results & Discussion

3.1 Defining Organic Products Present During Detemplation

To highlight the capability of TRPS, detemplation of chabazite was selected due to the relative predictability of the organic products present within the zeolite framework at different stages in the detemplation process. Following synthesis, uncalcined chabazite appears white to the naked eye (see Supplementary 1A). Prior to the calcination procedure, TMAda molecules are contained within the cages of the framework. Template molecules for chabazite framework are large relative to the cage size. Energy minimised modelling (see Figure 26) reveals that a maximum of one template molecule may occupy a single cage. Shown to be highly spatially restricted and only able to sit in one alignment within the cage volume, there is no scope for multiple TMAda molecules to occupy a single cage. This means that in this uncalcined zeolite system, we do not expect to see significant TMAda molecule-molecule interactions such as excimer formation, which has been postulated in zeolite studies of adsorbed organics to augment PL lifetime dynamics^{182,183,184}.

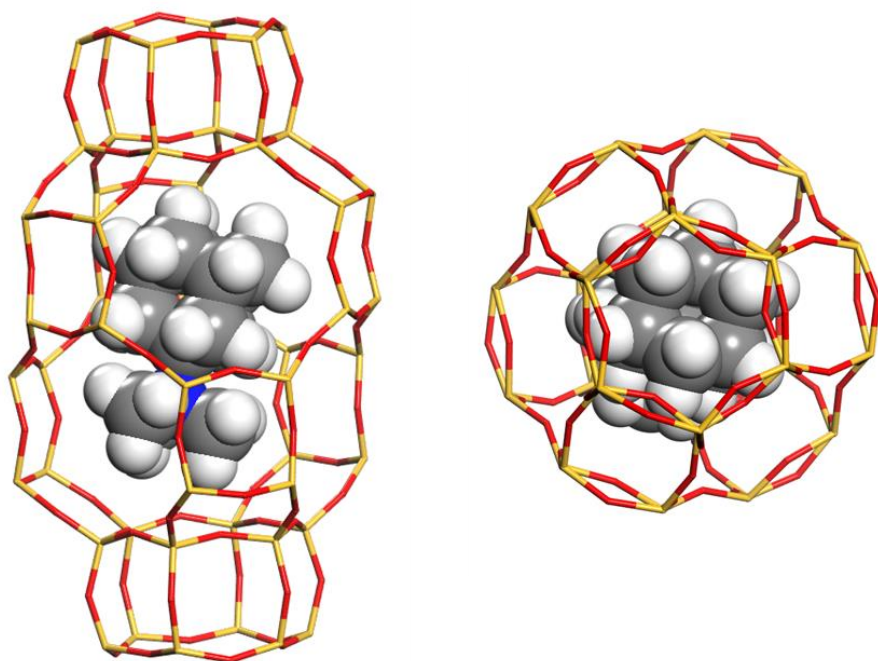


Figure 26 Energy minimized optimized structure of TMAda inside a chabazite cage. Calculations performed by Dr. Misbah Sarwar from Johnson Matthey

During the calcination process, the zeolite sample begins to discolour and darken (see Supplementary 1B). This is as a result of the proliferation of bulky template combustion derivatives and coke⁸⁵. At this stage it is expected that a mixture of template molecules and calcination products will be present in the zeolite. Following the calcination process, the sample

returns to being white (see Supplementary 1C). It is expected that whole template molecules will no longer remain following an extended thermal treatment process and given the colour change of the sample it is unlikely that significant amounts of coke remain however it is possible that trace amounts of smaller template combustion derivatives may be present.

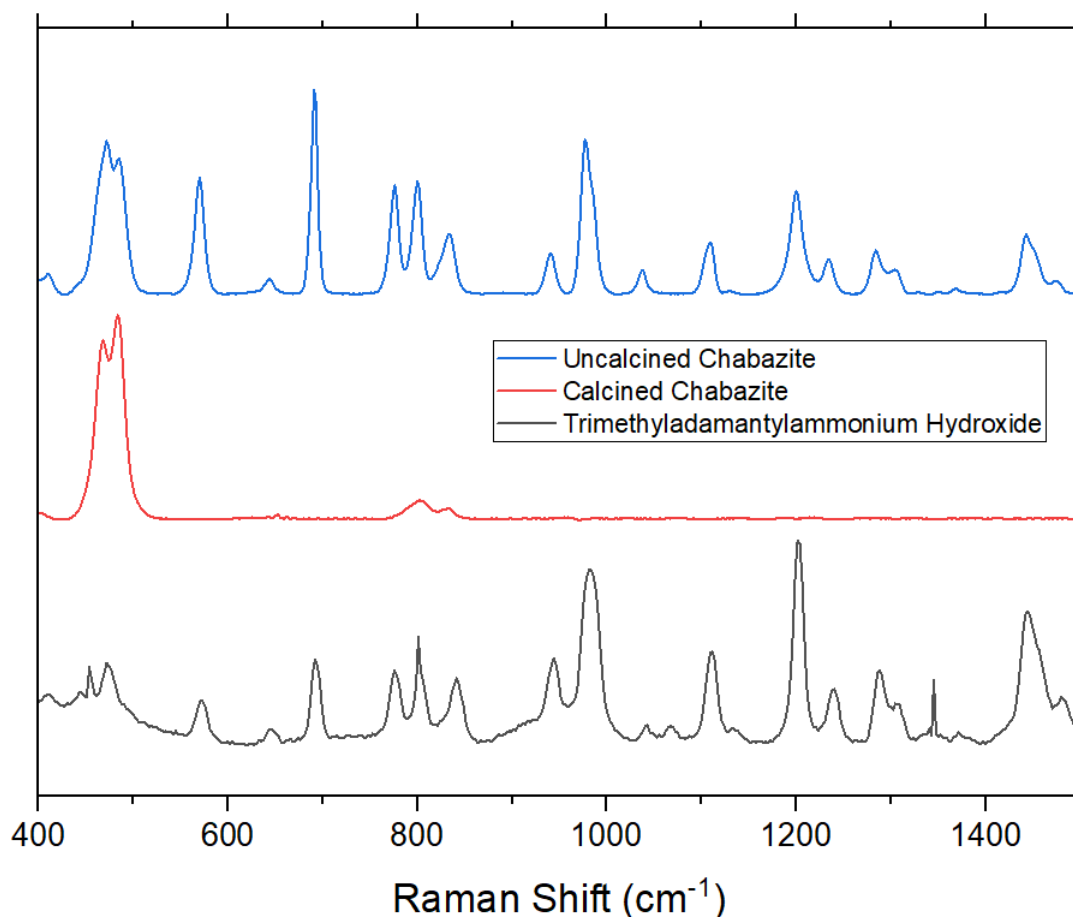


Figure 27 **Raman spectra at 830 nm 250 mW excitation** of synthetic uncalcined chabazite (blue), calcined chabazite (red), and 514 nm 25 mW excitation of OSDA (black) acquired with 1200 l/mm

The presence of TMAda in uncalcined chabazite was confirmed using Raman spectroscopy (see Figure 27). Specifically, the bands in uncalcined chabazite at 777, 800, 941, 977, 985, 1103, 1200, 1283, 1305, 1368, 1444, and 1452 cm^{-1} display agreement with the template spectrum and can be attributed to C-C stretching and H-C-C bending of the adamantane structural base unit¹⁸⁵. Following calcination, these bands are no longer visible, implying that whole TMAda molecules are no longer present following the thermal treatment. Residual in the calcined chabazite are a double peak at 466 & 484 cm^{-1} and at 803 and 831 cm^{-1} . The band at 466 cm^{-1} is dominant in the calcined chabazite sample and is well established as the class A vibration of the SiO_2 unit cell^{186,187} and the 484 cm^{-1} is characteristic to the chabazite framework. The bands at 803 and 831 cm^{-1} are assigned to weaker symmetric $\nu_s(\text{T-O-T})$ stretches^{188,189} of the framework. There are no obvious D or G bands associated with graphitic carbon structures, so it is likely that the hydrocarbon speciation present is predominantly molecular. Characteristic Raman spectra showing template

fingerprint or molecular combustion derivative peaks could not be obtained from the partially calcined chabazite using conventional 514 nm or 830 nm Raman spectroscopy due to the high fluorescence background. However, an alternative method of Kerr-gated Raman (see Figure 28) shows a D and G band confirming the presence of amorphous and graphitic carbon structures as part of the coke build-up.

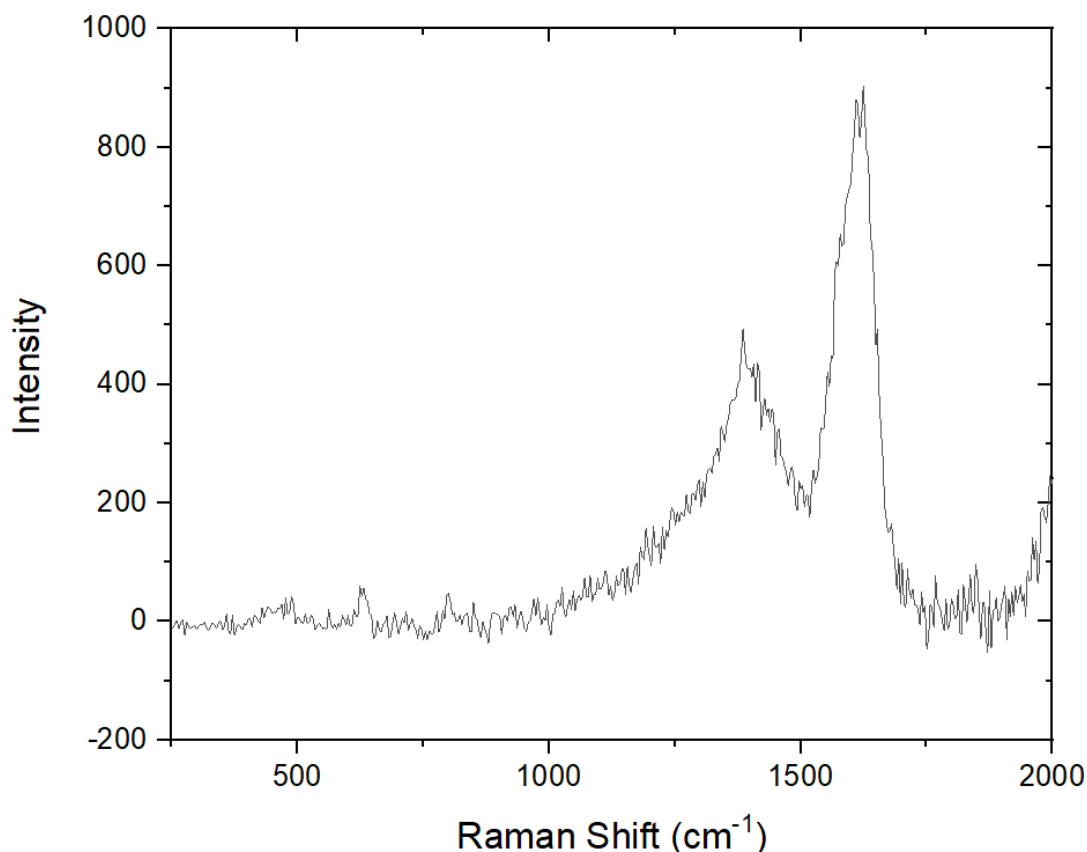


Figure 28 Kerr-gated Raman spectroscopy of partially calcined sample acquired at 400 nm

3.2 Effect of Confinement on Template Emission Inside Zeolite

Pores

In the following section, the emission behaviour of TMAda is established and then compared with the emission behaviour of an uncalcined, template-laden chabazite sample. The discussion surrounding this comparison is focused on how the emission behaviour of TMAda changes when it is confined within the pores of a zeolite.

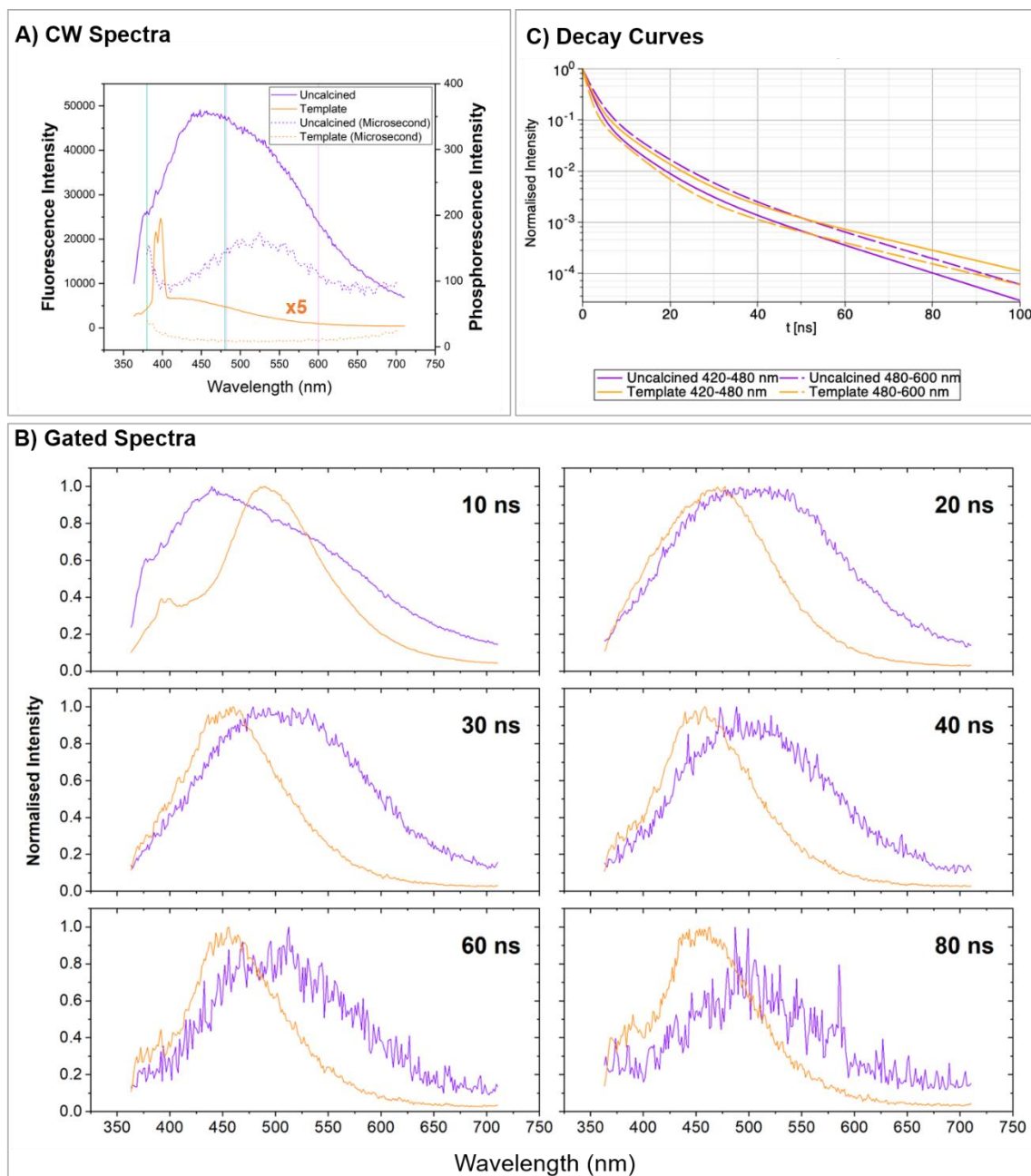


Figure 29 **Comparison of TRPS ensemble data for uncalcined zeolite and template.** A) Continuous wave spectra of uncalcined zeolite (purple) and template (orange) fluorescence emission in solid line and phosphorescence emission in dotted line, B) Gated spectra of uncalcined zeolite (purple) and template (orange) at 10 ns gate intervals C) Lifetime analysis in two spectral regions (417-480 and 480-600 nm) with decay curves.

Table 6 **Table of lifetimes and amplitudes in two spectral regions (417-480 nm and 480-600 nm)**

Sample	Wavelength Range (nm)	A ₁ %	A ₂ %	A ₃ %	T ₁	T ₂	T ₃	A ₁ T ₁ %	A ₂ T ₂ %	A ₃ T ₃ %	T _{Av}
Template	417-480	0.79	0.20	0.01	1.6	6.5	21.8	46.1	45.3	8.6	5.6
	480-600	0.83	0.16	0.01	1.1	5.6	21.2	47.4	45.3	7.3	4.6
Uncalcined	417-480	0.84	0.14	0.01	1.6	5.9	16.2	55.1	35.2	9.7	4.5

The CW fluorescence and phosphorescence emission spectra of TMAda and uncalcined chabazite are presented in Figure 29A. TMAda has a significantly lower emission intensity than uncalcined chabazite. This can be explained by the fact that uncalcined chabazite is a highly scattering powder, whereas TMAda is measured as a liquid being in solution with water. High levels of scattering in the powder produce a large increase in the laser intensity in the superficial layer of the sample as the photons repeatedly bounce back and forth before being either absorbed or reflected. Similarly, the solution form of TMAda is likely to experience quenching as the fluorescence intensity and lifetime are influenced by the solvent polarity and viscosity, and by the concentration.

The CW spectrum of TMAda features a broad emission curve peaking at 420 nm, with a sharp double peak at 388 nm and 396 nm. The double peak is ascribable to a Raman signature. The 396 nm peak is equivalent to the Raman band of O-H for water at 3400 cm^{-1} , which is further confirmed by a variable excitation wavelength study where the peak position shifts accordingly with respect to the excitation wavelength¹⁹⁰, and the 388 nm band (equivalent to a 2395 cm^{-1} Raman shift) is likely a C-H stretch Raman peak associated with the template material. The instantaneous nature of these bands, which appear at a time on par with the response function of the TRPS system, is evident in the gated spectra (see Figure 29B) where the bands are no longer visible from the second time gate onwards and are consistent with their Raman origin. The CW spectra of uncalcined zeolite is a broad fluorescence emission profile with a peak at 450 nm and a broad shoulder appearing from 540 nm onwards. When a millisecond gate was applied, phosphorescence signal from the template was no longer observable. However, uncalcined chabazite exhibits a phosphorescence signal with a peak at 525 nm. A more extensive analysis of the phosphorescence is included further on in Figure 31.

Time gating makes it possible to decouple the Raman contribution from true photoluminescence signal in the template material. In gated spectra measurements (see Figure 29B), it is possible to see that TMAda has two different spectral profiles. In the first window, the fluorescence profile has a peak at 490 nm, whereas from 30 ns onwards the peak is at 450 nm. At 20 ns the peak appears to be at an intermediate position at 470 nm. Rather than a peak shift, this suggests that TMAda has two primary emissive components with different lifetimes that combine to form different profiles at different time gates. The first gate, therefore, shows a fast-living component that appears to have predominantly disappeared after 30 ns, as the emission spectrum from this time-gate onwards is centred around 450 nm.

Similarly, the uncalcined chabazite's broad fluorescence emission curve also changes across different time windows. The dynamic appears more complex than the TMAda alone, and there are at least two discernible components. The first component can be seen clearly in first time gate

where the profile looks similar to the CW spectrum but with the peak at 440 nm appearing more pronounced. This means the CW spectrum is being dominated by fast-living species that decay within the first 10 ns. The second component is visible from the second time gate onwards where the spectrum is centred around 500 nm. There are also visible differences in the full width half maxima (FWHM) of the spectrum at 20-30 ns compared to 50 ns onwards, implying there is likely contribution from a complex of other fluorescence components. The use of time-resolved spectra enables the identification of TMAda's two primary components and demonstrates that the second component instead appears to red-shift from 450 nm to 500 nm upon confinement.

Based on the emission dynamic visible for both samples in the gated spectra, two spectral regions were selected for lifetime analysis. 417-480 nm was selected to capture both the longer-living component in the TMAda and the fast component in the uncalcined material, and 480-600 nm was selected to separate out the uncalcined material's longer-living component. Both samples were fit to a triexponential function. As indicated from the gated spectra, the fluorescence amplitude of τ_1 is the greatest for both samples in both spectral regions. In the spectral region 417-480 nm, the lifetimes are all shorter in the uncalcined sample with a τ_{av} of 4.5 ns versus 5.6 ns in the template. However, a lengthening of τ_1 & τ_2 is seen in the spectral region 480-600 nm, where $\tau_1 = 1.1$ ns & $\tau_2 = 5.6$ ns for the template and $\tau_1 = 2.0$ ns & $\tau_2 = 6.7$ ns for the uncalcined chabazite. Although in this temporal domain τ_3 is shorter in this region for the uncalcined chabazite, this sample also exhibits a microsecond length phosphorescent component not present in the template material.

Overall, in this spectral region there is a significant increase in emission lifetimes. This is coupled with an increase in fractional amplitude values for τ_2 & τ_3 in this region ($A_2\%$, $A_3\%$ = 0.20, 0.02 for uncalcined chabazite; and 0.16, 0.01 for template), highlighting an interesting change in emission dynamics when TMAda is confined within the framework structure. It is postulated that confinement reduces permutations for steric conformation and by extension self-quenching of the TMAda leading to an extended triplet state lifetime and greater intersystem crossing efficiency. Room temperature phosphorescence (RTP) of TMAda has been previously reported by Ramamurthy et al.^{191,192} who suggest that cationic sites in zeolites may induce singlet-triplet spin conversion in molecules. Casal et al.¹⁹³ also observed an increase in the lifetime of β -phenyl-propiophenone at room temperature in silicalite, attributing an increased stability of the triplet state to steric confinement within the channels.

It is known that zeolite samples have complex photoluminescence mechanisms that have variably been attributed to composition¹⁴², metal loading¹⁶⁵ or metals stabilised inside a matrix¹³⁴, and product formation¹⁴⁵ in previous studies. It has been assumed here that in the case of uncalcined chabazite, a significant proportion of the emission is arising as a result of the photoemissive excitation of TMAda. The assumption does not discount contribution from other emission

pathways. Indeed, uncalcined zeolite systems offer an interesting model for studying the confinement effects of a crystalline lattice on photoexcitable molecules. Although photoluminescence studies on confinement effects exist where highly emissive molecules are floated into zeolite pores¹⁸⁴ and monitored for changes in spectral profiles, a host of problems often arise during the sample preparation process that critically hamper deeper interpretation of results, including surface aggregate formation and crystallisation¹¹⁷. These are problematic in that they no longer represent a measurement from a sample with evenly distributed, geometrically confined fluorophores. Further to this, the size discrepancy between the host cages and adsorbent molecules poses as a double-edged sword; zeolite channels need to be large enough (or adsorbent molecules small enough) to achieve confinement of introduced molecules in the first place, but the sites of entrapment may not be restrictive enough to induce effects of electronic orbital deformation on the molecules. The OSDA is an ideal candidate for observing changes in emission properties due to confinement effects as they are distributed more evenly throughout the sample and represent the upper size limitation for molecules that can be accommodated within a zeolite cage, and by extension experience a significant degree of steric and electronic confinement. In the case of chabazite, the TMAda acts to template the cage portion of chabazite's cage-channel structure and would be impossible to retrospectively introduce a molecule of this size into the pores due to the size selectivity of the channel diameters.

3.3 Proliferation of Carbonaceous Deposits in Part-Calcined

Sample

Size selectivity of chabazite channels necessitates the decomposition of bulky TMAda molecules into smaller before pores can be successfully evacuated. When colour changes become discernible to the naked eye, it is a reasonable indication that coke has begun to build up on the zeolite sample.

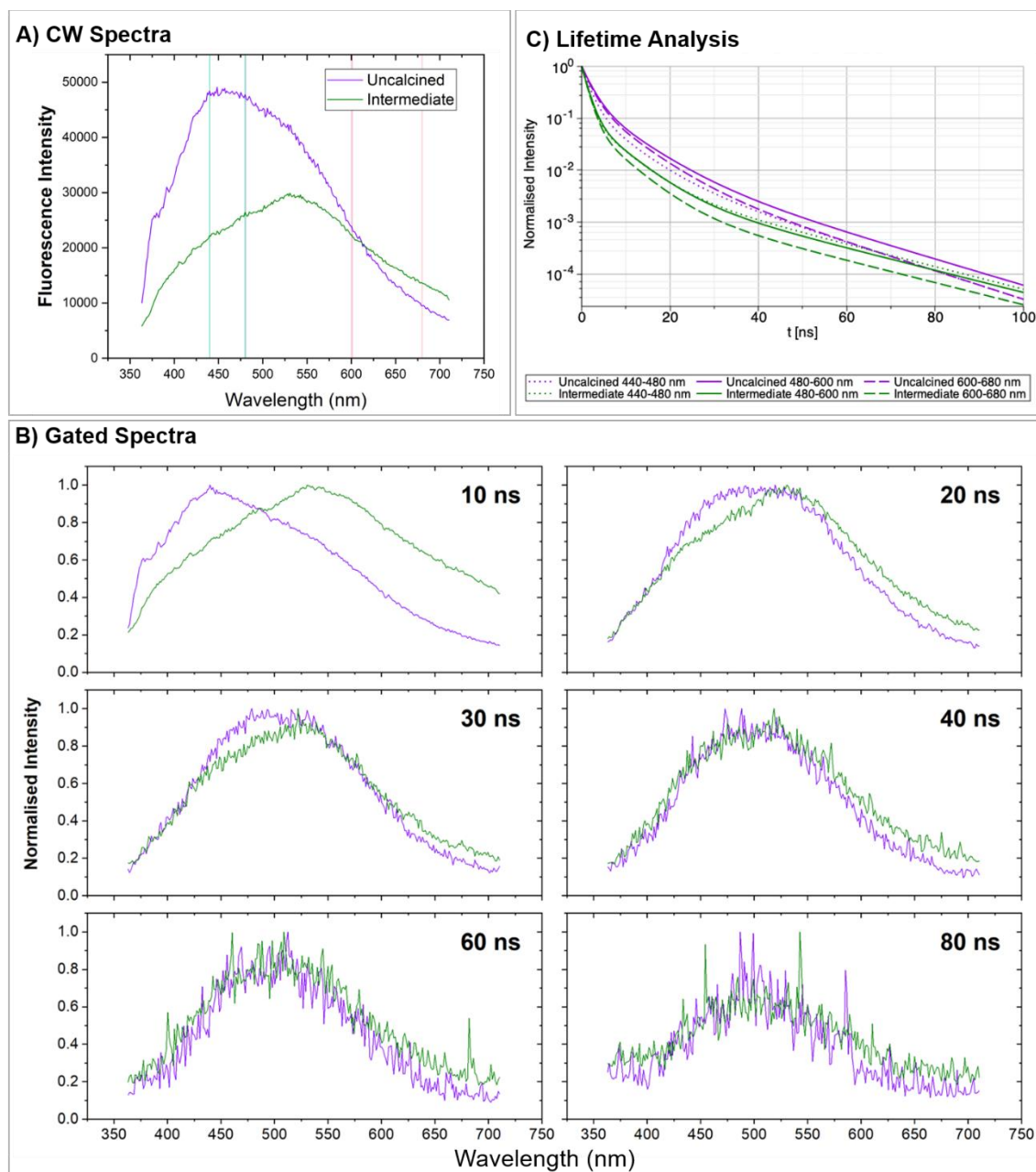


Figure 30 Comparison of TRPS fluorescence ensemble data for uncalcined zeolite and intermediate zeolite. A) Continuous wave spectra of uncalcined zeolite (purple) and intermediate zeolite (green) fluorescence emission in solid line and phosphorescence emission in dotted line, B) Gated spectra of uncalcined zeolite (purple) and intermediate zeolite (green) at 10 ns gate intervals C) Lifetime analysis in three spectral regions (440-480, 480-600 and 600-680 nm) with decay curves

Table 7 Table of lifetimes and amplitudes in three spectral regions (440-480, 480-600 and 600-680 nm)

Sample	Wavelength Range (nm)	A ₁ %	A ₂ %	A ₃ %	T ₁	T ₂	T ₃	A ₁ T ₁ %	A ₂ T ₂ %	A ₃ T ₃ %	T _{Av}
Uncalcined	440-480	0.82	0.16	0.02	1.6	5.8	15.9	0.52	0.37	0.11	4.8
	480-600	0.77	0.21	0.02	2.0	6.7	17.3	0.47	0.42	0.11	5.6
	600-680	0.77	0.21	0.02	1.9	6.3	15.9	0.48	0.43	0.09	5.0
Intermediate	440-480	0.88	0.11	0.01	1.2	5.6	20.1	0.58	0.34	0.08	4.2
	480-600	0.89	0.11	0.01	1.3	5.9	20.4	0.61	0.33	0.06	4.0
	600-680	0.91	0.08	0.00	1.3	5.6	20.4	0.68	0.27	0.04	3.3

CW spectra in Figure 30A show that the intermediate zeolite has a peak at 540 nm, and an emission intensity lower than the uncalcined sample. The CW emission intensity of this sample is neither directly comparable with the uncalcined sample nor representative of the concentration of fluorophore molecules present as it is significantly darker and likely to be reabsorbing some of the emission.

Gated spectra in Figure 30B show that the intermediate sample has a fast component present with a peak at 540 nm in the first 10 ns window that heavily influences the profile of the CW spectrum. This faster component, which so far appears characteristic to the intermediate sample is attributed to the proliferation of new hydrocarbon products. The difference in peak position between the uncalcined material at 440 nm and the intermediate sample at 540 nm implies there has been a dramatic change in the speciation of fast emitting components following a thermal treatment.

From 40 ns onwards, the gated spectra show that the intermediate and uncalcined samples exhibit a significant degree of similarity. The component visible in the uncalcined sample from 40 ns onwards was assigned to the presence of the occluded template molecules. Detection of this signal in the intermediate sample suggests that whole TMAda molecules are still present after 6 hours of ramping the sample up to 550 °C under air flow. Comparisons between the uncalcined and the intermediate sample serve as worthwhile examples of how pulling apart the temporal aspect of an emission spectrum can be very useful in systems with complex origins of emission. In both samples, it is evident that fast components, which can vary hugely in concentration and composition across a sample, may cloud the interpretation of CW spectrum. Probing different time windows makes it possible to discern how template molecules and combustion by-products co-exist alongside each other, each with different local microenvironmental influences.

Lifetime analysis was conducted in three spectral regions: 440-480 nm, which captured the fast component of the uncalcined sample; 480-600 nm, which was selected as the probe region for occluded TMAda as per the previous section; and 600-680 nm, which covers the tail of both curves. A triexponential fit was used.

Although a strong visual correlation between the uncalcined and intermediate samples in the gates from 40 ns onwards exists, the lifetime analysis in the template probe region of 480-600 nm shows differences in τ values. In the intermediate samples τ_1 and τ_2 become shorter, with the fractional amplitude of the faster component τ_1 increasing with respect to τ_2 (i.e. $A_1\% = 0.89$, $A_2\% = 0.11$ in intermediate zeolite; $A_1\% = 0.77$, $A_2\% = 0.21$ in uncalcined zeolite), relating to the overall decrease in whole TMAda molecules in the intermediate sample and the proliferation of new hydrocarbon species. Although having a lower percentage amplitude than the uncalcined sample, the τ_3 of the long-living components in the intermediate samples are markedly longer (20 ns vs. 15 ns) across all spectral regions. In the long wavelength region (480-600 nm) we observe a significant reduction in the average lifetime of the intermediate ($\tau_{Av} = 3.3$ ns) sample with respect to the uncalcined sample ($\tau_{Av} = 5.0$ ns). This confirms that the emission in this band is dominated by reaction products that, being likely small organic molecules, exhibit fast relaxation dynamics. This is well represented in Figure 30C, where the fastest fluorescence decay is that of the intermediate sample in the third band. It is expected that the template derivatives present in the intermediate sample, being smaller and capable of travelling along size-selective diffusion pathways, will have a greater freedom of distribution across the crystals, with some remaining in the centre following quenching and others residing towards the surface⁸⁰. By extension, not all combustion products will necessarily experience the degree of steric confinement imposed upon the TMAda molecules, opening up a wider range of possibilities of lifetime states one might expect to see.

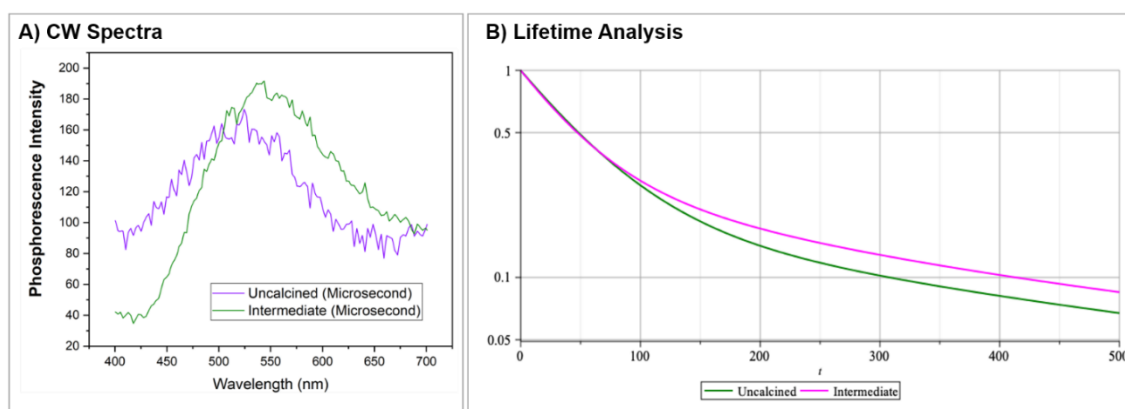


Figure 31 **Comparison of TRPS phosphorescence ensemble data for uncalcined zeolite and intermediate zeolite.** A) Continuous wave spectra of uncalcined zeolite (purple) and intermediate zeolite (green) fluorescence emission in solid line and phosphorescence emission in dotted line, B) Lifetime analysis in one spectral region (480-600 nm) with decay curves and table of lifetimes and amplitudes.

Table 8 **Fractional amplitude and lifetime values for phosphorescence measurements in uncalcined and intermediate samples**

Sample	$A_1\%$	$A_2\%$	$A_3\%$	τ_1	τ_2	τ_3	$A_1\tau_1\%$	$A_2\tau_2\%$	$A_3\tau_3\%$	τ_{Av}
Uncalcined Phosphorescence	0.80	0.10	0.10	53.1	239.5	811.3	0.28	0.17	0.55	368.0
Intermediate	0.69	0.18	0.13	44.3	185.4	840.7	0.18	0.19	0.64	356.8

Phosphorescence										
------------------------	--	--	--	--	--	--	--	--	--	--

Both the uncalcined and intermediate zeolites exhibit measurable phosphorescence behaviour. The CW spectra in Figure 31A show that the intermediate sample peaks at 545 nm and the uncalcined sample peaks at 520 nm. Lifetime analysis was conducted across the entire spectral region, and triexponential fits were used. Even if data are rather noisy due to the scarcity of photons in the long tail of the emission, a tentative lifetime fit could be done also for the phosphorescence dataset (Figure 6B). It may be noted that in the leading edge of the fitted curves uncalcined and intermediate behave in a similar way, with the intermediate displaying a slightly slower damping before reaching the same slope (i.e. lifetime) of the uncalcined in the long term. Notwithstanding some caution in drawing conclusions from a non-completely reliable dataset, it could be speculated that the same triplet states of TMAda, which might be the origin of the phosphorescence in the uncalcined sample, are also present in the intermediate sample with the possible existence of additional long emitting compounds.

3.4 Depletion of Template Signature from Uncalcined to Calcined

Sample

In the final section of this discussion, the depletion of template material is monitored in a comparison of uncalcined and calcined chabazite. Immediately discernible differences are visible in the CW spectra (see Figure 32A), where the calcined sample, when compared to the uncalcined sample, appears to have a generally simpler, Gaussianesque spectral profile centred around 410 nm. The peak intensity is also over two times lower than the uncalcined sample. Gated spectra in Figure 32B highlight the simpler emission dynamic of the calcined material, with minimal changes occurring between the 10 ns and 20 ns windows when compared to the uncalcined material. Compared to the uncalcined material, all gated spectra of the calcined material show a marked decrease in luminescence activity in the red region (i.e. from 480 nm onwards). Although the normalisation in Figure 32B effectively shows the contrast in peak positions, the CW spectra comparison in Figure 32A more accurately highlights the large discrepancy in emission in this region. This is directly attributable to the depletion of whole TMAda molecules and the majority of coke products, which appear broadly to have been removed as demonstrated by previous Raman measurements (see Figure 27) and the white sample colour. The loss of phosphorescent signal in the calcined sample is compatible with the depletion of TMAda and further supports the notion that the phosphorescence exhibited in the uncalcined and intermediate samples in synthetic zeolites pertains to occluded hydrocarbon material rather than arising from the framework itself. Phosphorescent lifetimes can be easier to fit than multiexponential fluorescence lifetimes that require more refined sampling around time zero. This enhanced component separation makes phosphorescent signatures ideal for flagging the presence of templating material. In future work, this approach may be utilised in *in situ* detemplation monitoring.

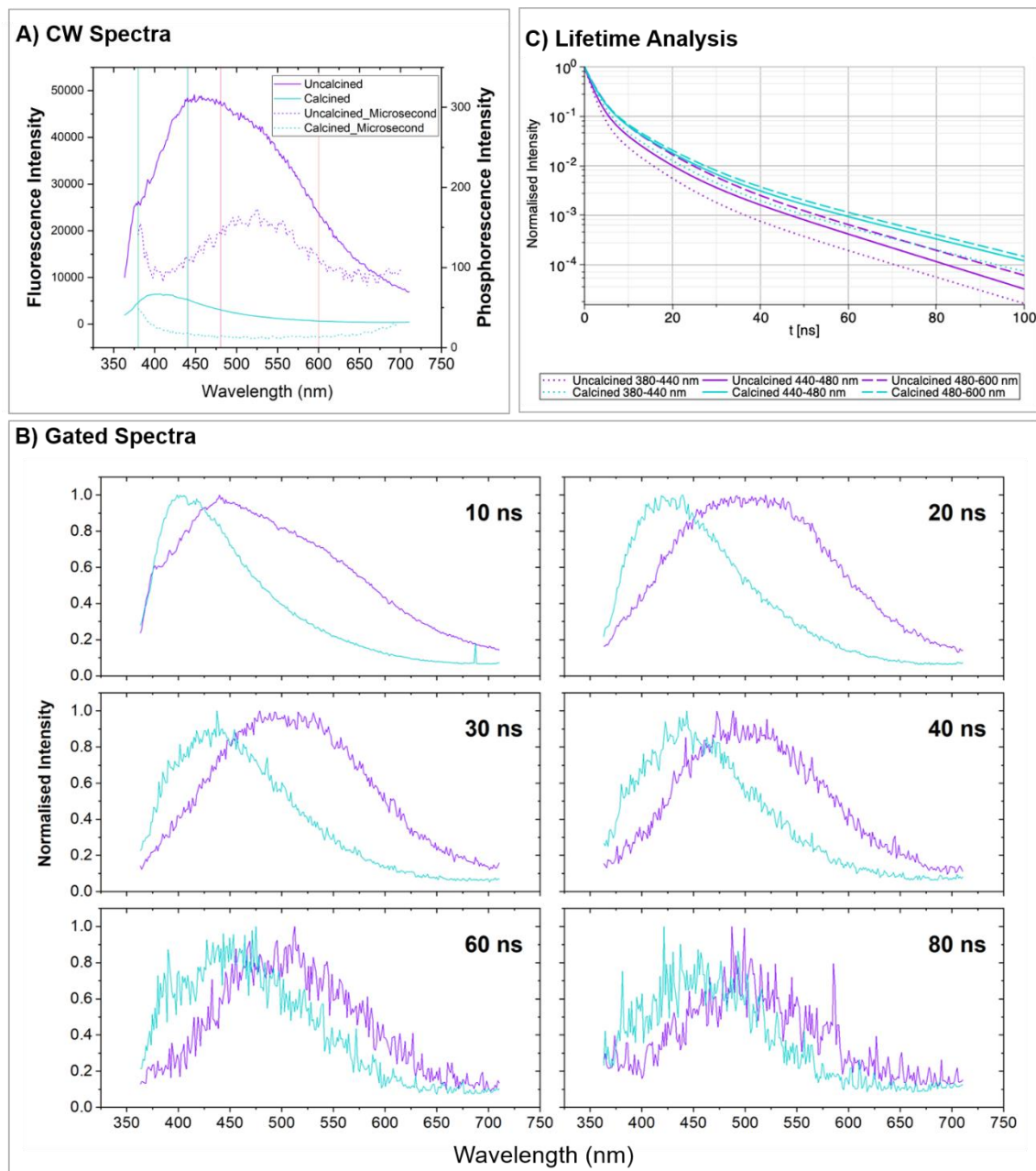


Figure 32 **Comparison of TRPS ensemble data for uncalcined zeolite and calcined zeolite.** A) Continuous wave spectra of uncalcined zeolite (purple) and calcined zeolite (aqua) fluorescence emission in solid line and phosphorescence emission in dotted line, B) Gated spectra of uncalcined zeolite (purple) and calcined zeolite (aqua) at 10 ns gate intervals C) Lifetime analysis in three spectral regions (380-440 , 440-480 and 480-600 nm) with decay curves

Table 9 **Table of lifetimes and amplitudes in three spectral regions (380-440, 440-480 and 480-600 nm)**

Sample	Wavelength Range (nm)	A ₁ %	A ₂ %	A ₃ %	T ₁	T ₂	T ₃	A ₁ T ₁ %	A ₂ T ₂ %	A ₃ T ₃ %	T _{Av}
Uncalcined	380-440	0.89	0.10	0.01	1.5	5.9	16.4	0.65	0.29	0.06	3.7
	440-480	0.82	0.16	0.02	1.6	5.7	15.7	0.51	0.37	0.12	4.8
	480-600	0.77	0.21	0.02	2.0	6.7	17.3	0.47	0.42	0.11	5.6
Calcined	380-440	0.83	0.15	0.01	1.9	6.9	19.8	0.55	0.37	0.08	5.2

440-480	0.78	0.21	0.02	1.9	6.9	19.8	0.45	0.43	0.11	6.1
480-600	0.77	0.21	0.02	1.9	7.1	19.8	0.43	0.43	0.13	6.5

Lifetime analysis was conducted in three spectral regions: 380-440 nm, which again captured the fast component of the calcined sample; 440-480 nm; and 480-600 nm, which is the probe region for the template. A triexponential fit was used. Compared to the uncalcined sample, the τ values in the calcined sample are virtually identical across all spectral ranges, giving an average of $\tau_1 = 1.9$ ns, $\tau_2 = 7.0$ ns, $\tau_3 = 19.8$ ns. A notable difference in the calcined sample is the fractional amplitude values in the spectral region 380-440 nm, which has a greater contribution from $A_1\%$ and less from $A_2\%$ when compared to the two other spectral regions. This means that the region 380-440 nm is generally faster than the regions 440-480 and 480-600 nm, where longer-lived components have a slightly greater bearing in the overall composition of lifetimes. In comparing the uncalcined sample with the calcined sample, the lifetimes in the calcined sample are longer for all three components across all three spectral regions with the exception of τ_1 in region 480-600 nm of the calcined sample, which is 0.1 ns shorter than the uncalcined sample. It should be noted that the significantly decreased signal in this region for the calcined sample makes meaningful lifetime fitting more challenging. The global increase of lifetimes here would be consistent with the depletion of contribution from occluded hydrocarbons, which are shown to have a faster lifetime. Coupled with the depletion of phosphorescence, which was previously flagged as an alternative way of tracking the presence of occluded template, this lengthening of lifetimes can be used to show that TRPS is capable of detecting the presence of OSDA but even further decouple the original OSDA emission from an additional PL signal.

Based on this, it is possible to speculate the emission source in the calcined zeolite originates primarily from a single type of fluorophore that experiences different quenching effects, with the multiexponential fit correlating to different relaxation pathways. In this case, variations visible in the decay curves as presented in Figure 32C can be justified assuming the fluorophore experiences a varied response to quenching; more specifically that molecules with a higher Stokes shift will experience fewer quenching effects.

While the implication is that whole molecules of TMAda are no longer extant in the sample, this does not necessarily mean hydrocarbons are completely eradicated from the sample as it is possible that other molecules may have different emission signatures to TMAda. At this point, the following question offers itself for debate: is the emission measured from a calcined zeolite borne of trace carbon surviving the calcination, or is it an intrinsic photoluminescent signature of the framework? The presence of two residual Raman bands in Figure 27 at around 800 cm^{-1} could be interpreted as alluding the presence of a small amount of hydrocarbon material left in the sample but they have also been assigned to framework stretches, and the fluorescence spectra in Figure 32, if assigned to trace carbonaceous species, would appear to reflect a simpler molecular hydrocarbon configuration leftover in the zeolite cages. The lack of phosphorescence additionally

implies that any hydrocarbon remaining is likely to be small relative to the size of the cages and perhaps even mobile within the pore structures, experiencing less confinement and subsequently not exhibiting any phosphorescence.

It is also possible that the PL emission originates from the framework itself, as supported by a series of studies conducted on other silica-based mesoporous structures. Glinka et al.¹⁹⁴ recorded a series of PL emission spectra from MCM-41 mesoporous sieves and noted the similarity in PL emission from silica nanoparticles, attributing the emission to non-bridging oxygen hole centres. The molecular sieves in this study do, however, utilise an OSDA in the synthesis process, so it is not entirely possible to exclude the contribution of emission from an organic molecule. Equally, there are other studies postulating that UV excitation can induce PL from defect sites in a one-photon process in non-templated silica based materials like silica particles¹⁹⁵, silicon quantum dots embedded in an array¹⁹⁶, bulk amorphous SiO₂^{197,198,199,200}, and fused silica²⁰¹.

Ultimately, it is the time-resolved aspect of this study that bolsters the conclusion that the emission arising in the calcined sample is likely to be coming from the framework. Previous comparisons with organic-heavy samples (i.e. uncalcined and intermediate samples) show that organic-based emission in zeolites is most characteristically defined by a fast-lived component that is no longer extant beyond the 10 ns window, a complex ensemble of emission profiles relating to the range of different species and decay pathways, and a phosphorescent component arising as a result of steric confinement. In contrast, the calcined sample appears to display a comparatively simple, single-source emission dynamic that experiences less change in the gated spectra, minimal difference in lifetime analysis across different spectral regions, and exhibits no phosphorescence. It is possible then that the PL signal in calcined CHA is arising due to defect sites in the aluminosilicate framework, representing an intrinsic zeolite emission. The overall intensity of the calcined sample is also significantly lower than the uncalcined material, implying that this intrinsic framework signal is being drowned by the more intense organic-based emission arising in the uncalcined material.

3.5 Conclusion

Detemplation of chabazite has been successfully studied using a sensitive TRPS method. Three signatures were established for the different samples:

- 1) A characteristic emission spectrum for the OSDA was established with a red-shift occurring upon confinement.
- 2) Phosphorescence signal can be used to signature the presence of occluded organic material.
- 3) An intrinsic zeolite emission related to framework defects is recorded in the calcined sample.

In future studies, it is envisioned that this technique will be able to inform researchers on other topical questions regarding adsorbed organics, a common example of which is the formation of carbonaceous deposits in catalytic reactions, which affect the conversion efficiency of acidic zeolites.²⁰² Proliferation of coke deposits are problematic as they have been correlated with progressive deactivation of the catalyst^{203,204}. The flexibility of the setups mean it is also possible to accommodate *in situ* operando studies of zeolite systems, which could form the basis of future experimentation.

Chapter V

Power Dependency Study

In collaboration with the Valentini group in the Experimental Physics Department at the Politecnico di Milano

1 Introduction

In the previous chapter, emission spectra for calcined and uncalcined chabazite were obtained with 355 nm irradiation at room temperature and analysed. Emission signature arising from the occluded OSDA was established, as was a characteristic emission postulated to be arising from the framework itself in the case of the calcined material. In this chapter, a study on the effect of laser power as a function of zeolite composition, temperature, and laser positioning is presented. This study is conducted as a precursor to *in situ* experimentation, which is presented in Chapter 6.

Beyond the experiments presented here, laser-based analytical techniques are already gaining traction within the community as increasingly popular options for characterising zeolite materials. Vibrational spectroscopy techniques such as Raman and IR spectroscopy¹⁶¹, photoluminescence spectroscopy¹⁴², and optical imaging techniques^{132,205,206}, which all employ a laser excitation source, have been used to great effect in the last decade to reveal new insights on zeolite structure and chemical behaviour. Particularly in the field of catalysis, lasers, with their relatively compact, benchtop-friendly size and operation, have shown themselves to be excellent candidates for the primary excitation source in *operando* spectroscopy setups and are frequently used to study product formation in catalytic reactions in real time.

It is known that zeolites can be susceptible to laser damage. Irradiation damage can be either seen on the sample itself, where the surface may appear to become discoloured or burned after a period of laser exposure¹¹⁷, or in the recorded spectra or image, where signal may appear to bleach or rise dramatically, peaks to broaden, or background noise to overwhelm meaningful signal.

In experiments performed under ambient conditions without particular time constraints on the measurement (e.g. the experiment in Chapter 4), laser damage is avoided simply by reducing the amount of power at the sample while maintaining a reasonable signal-to-noise ratio, and by reducing the total exposure by switching the laser off between experiments. However, avoiding laser damage becomes increasingly difficult in situations where samples are subjected to repeated irradiation over an extended period of time like in *operando* experiments, which can see data being collected hundreds of times over the course of five hours or more. In these cases, dedicated equipment is often incorporated into the setups to either raster the sample under a fixed laser²⁰⁷, raster the laser over a fixed sample²⁰⁸, or to fluidise the sample bed^{209,210}, all with the view to reduce the contact time between the sample and the laser beam. In experiments where temperature is a consideration, a UV excitation source can be used instead of an infrared source to avoid the background effects associated with black-body radiation^{211,212,213}, although it is known that UV irradiation can induce its own set of photophysical effects in the zeolite framework¹⁷¹.

Assessing the degree to which a measured spectrum is being influenced by laser irradiation is, therefore, an important challenge. Preventing damage to the sample is desirable on a practical level to increase the longevity of the sample in extended experimentation. But more importantly, the primary goal of understanding power regimes within which zeolite samples may be influenced by the laser light is for a researcher to decouple the effects of ‘real’ photonic absorptive and emissive processes from laser-induced artefacts in a spectrum such as peak broadening or artificial peak shifting.

In this chapter, time-resolved photoluminescence spectroscopy was used to record photoluminescence spectra at different laser powers to determine the influence of laser power on peak intensity and spectral profile. As a precursor to *in situ* catalytic studies also carried out during this project, the power study was conducted with respect to: i) high and low temperature regimes to assess the environmental effects of *in situ* experimentation; ii) calcined and uncalcined zeolites to assess the effects of organic adsorbents that vary widely in concentration and composition throughout the course of a catalytic reaction; and iii) static and moving laser arrangements to mimic the effect of rastering. For each experiment, the aim was to comparatively determine whether the laser influences the spectra acquired, with the view to decouple laser effects from ‘pristine’ sources of emission and interpret spectra more meaningfully.

2 Experimental Section

2.1 Sample Preparation

In this chapter an uncalcined and a calcined chabazite sample were studied. The preparation is the same as described in Chapter 4. Preliminary UV-vis and Raman characterisation are also supplied in Chapter 4.

2.2 Time-Resolved Photoluminescence (PL) Spectroscopy and Data Analysis

The time-resolved fluorescence spectroscopy setup used is as described in Chapter 3. Sample was loaded into a temperature-controlled FTIR600 Linkam cell sealed with quartz windows and aligned in the beam path. Inert He gas was flowed through the cell during measurements.

2.3 Pulsed Laser Characterisation

To characterise the Q-switched laser, the average power, repetition rate, and pulse duration were measured. From these parameters, the energy per pulse and peak power were calculated as follows:

$$E_{pulse} = \frac{P_{average}}{R_{rate}}$$

Where E_{pulse} = Energy per pulse in joules
 $P_{average}$ = Average power in watts
 R_{rate} = Repetition rate in pulses per second

$$P_{peak} = \frac{E_{pulse}}{D_{pulse}}$$

Where P_{peak} = Peak power in watts
 D_{pulse} = Pulse duration at FWHM in seconds

A repetition of 100 Hz was used with a pulse duration of 1 ns (1×10^{-9} s). A power meter (Gigahertz-Optik, P9710 Optometer) was used to measure the average power. A range of operating powers were achieved using neutral density filters (Thorlabs) with optical densities ranging from 0.1 to 3, attenuating the power at the sample. It is worth noting that the theoretical value of the optical density of the filters only holds for visible light. Table 10 presents theoretical and actual power values.

Table 10 *Power values for neutral density filters used to attenuate power at sample*

Optical Density	Theoretical Attenuation	Theoretical Average Laser Power (μ W)	Measured Average Laser Power (μ W)	Energy per pulse (μ J/pulse)	Peak Power (W)
0.1	1.26	900	900	9	9000
0.5	3.16	358.86	415	4.15	4150
1	10	113.4	90	0.9	900
2	100	11.34	22	0.22	220
3	1000	1.13	0.9	0.09	90

2.4 Data Collection Method

A total of eight power series were collected as a function of three different parameters: temperature, calcination state, and laser spot handling. Comparisons were made between room temperature (25 °C) and high temperature (350 °C+), calcined⁹ and uncalcined zeolite, and a stationary laser spot and a laser spot moved between each measurement. Table 11 outlines the eight experiments conducted.

Table 11 *Outline of eight power study experiments conducted*

	Uncalcined	Calcined
Room Temperature	Stationary Laser	Stationary Laser
	Moving Laser	Moving Laser
High Temperature	Stationary Laser	Stationary Laser
	Moving Laser	Moving Laser

⁹ Calcined material was subjected to a complete *ex situ* calcination in an oven prior to experimentation. It was then dehydrated *in situ* at 150 °C prior to acquiring measurements at 25 °C.

3 Results

3.1 Calcined Chabazite

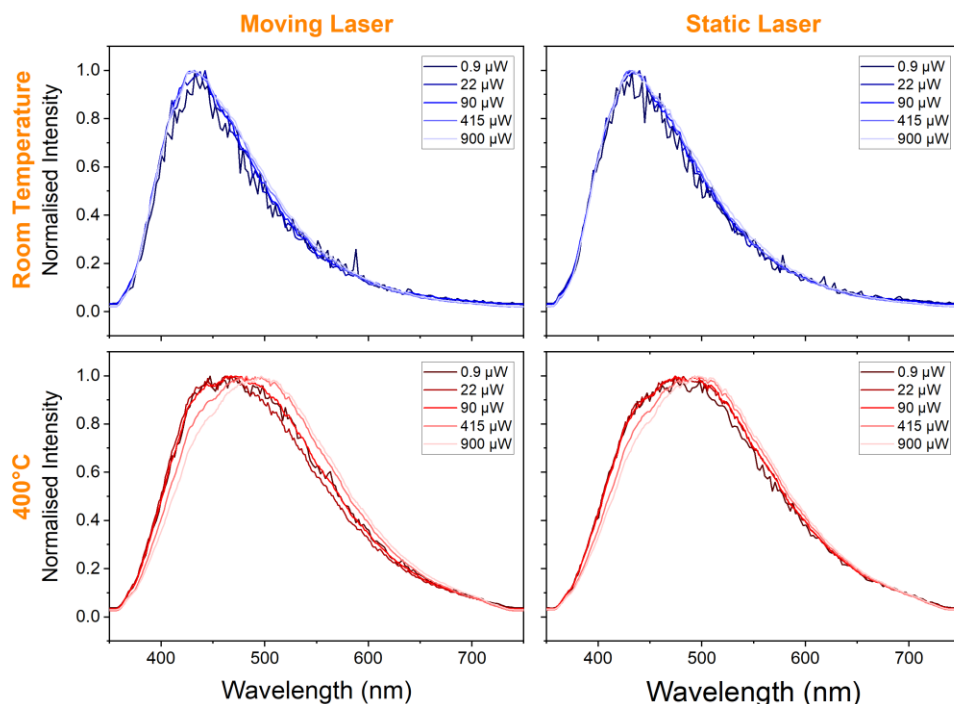


Figure 33 **Photoluminescence (PL) measurements of calcined chabazite**. A) Normalised PL power series spectra of sample at (top left) room temperature with moving laser position, (top right) room temperature with fixed laser position, (bottom left) 400 °C with moving laser position.

Figure 33 shows the normalised spectra of calcined chabazite grouped with respect to temperature and laser position. At room temperature for both the moving and static laser experiments the peak for all spectra is at 430 nm. The spectral profile does not appear significantly different for varying laser powers for either the moving or static laser experiments.

At 400 °C, the intensity is over 5 times greater than the room temperature measurements (see Figure 34) and the spectral profile is generally broader with the peak appearing to red-shift from 440 nm at room temperature to 480 nm at elevated temperature. In both the moving and static laser experiments, there appears to be a peak shift between 90 and 415 μW from 470 nm to 500 nm, although the shift is more pronounced in the moving laser experiment.

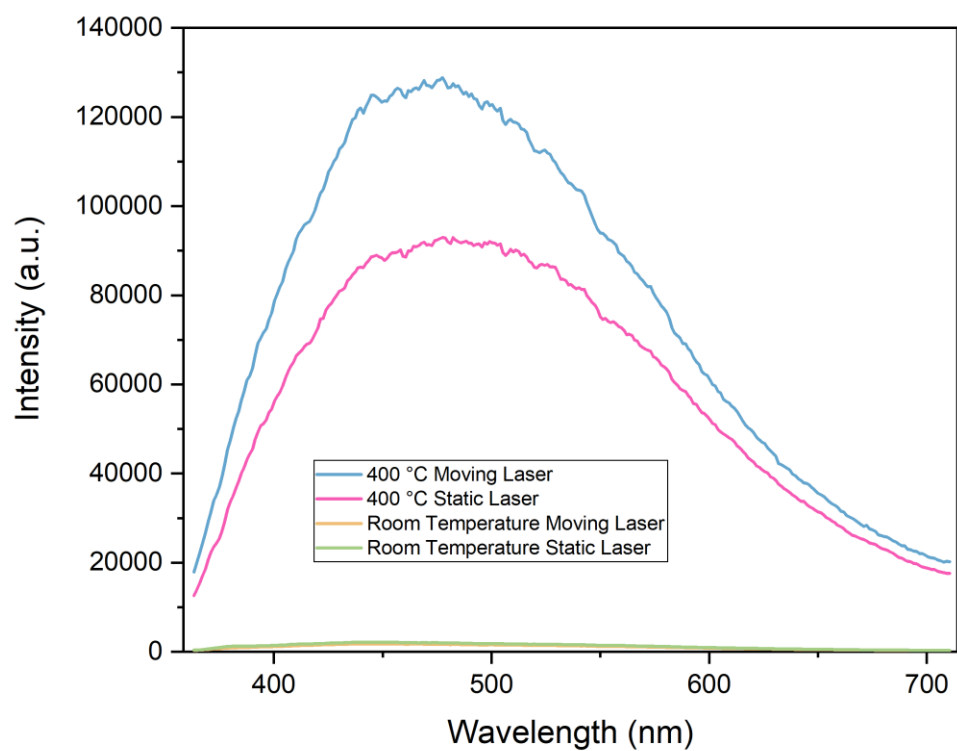


Figure 34 **Comparison between non-normalised room temperature and high temperature spectra** for calcined zeolite at 90 μ W demonstrating differences in peak height

3.2 Uncalcined Chabazite

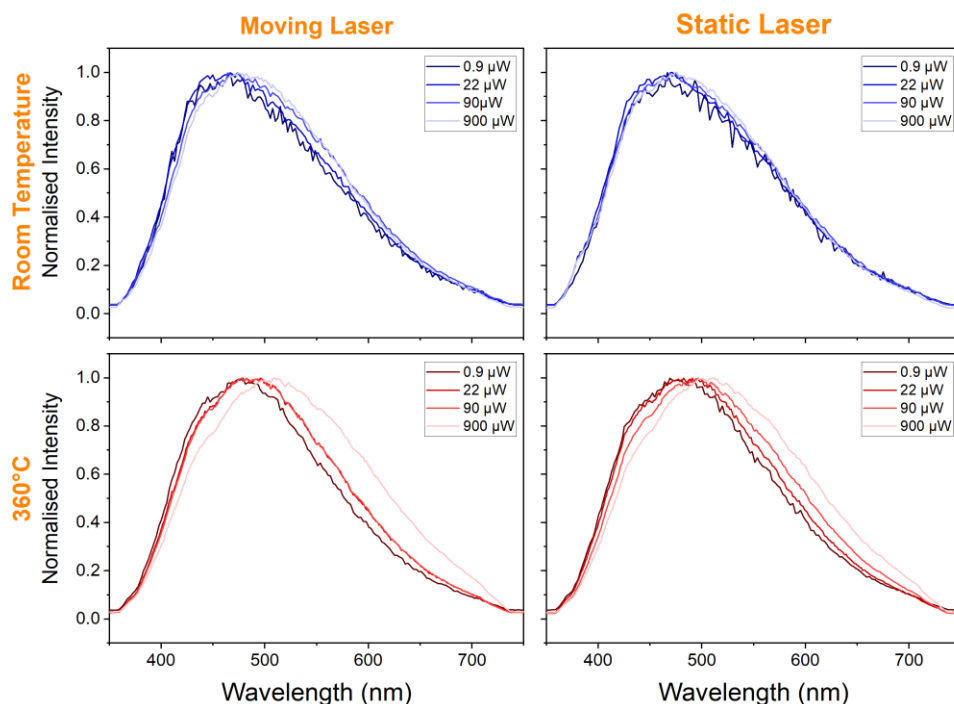


Figure 35 **Photoluminescence (PL) measurements of uncalcined chabazite.** A) Normalised PL power series spectra of sample at (top left) room temperature with moving laser position, (top right) room temperature with fixed laser position, (bottom left) 360 °C with moving laser position, and (bottom right) 360 °C with fixed laser position.

Figure 35 shows the normalised spectra of uncalcined chabazite grouped with respect to temperature and laser position. Across all temperatures and laser positions, the recorded spectra appear to slightly red-shift above 22 μW . At room temperature with 0.9 μW irradiation the peak is centred at 460 nm, and with 900 μW irradiation the peak is centred at 475 nm. At 360 °C with 0.9 μW irradiation the peak is centred at 475 nm, and with 900 μW irradiation the peak is centred at 505 nm representing a total peak position change of 30 nm.

3.3 Gated Spectra

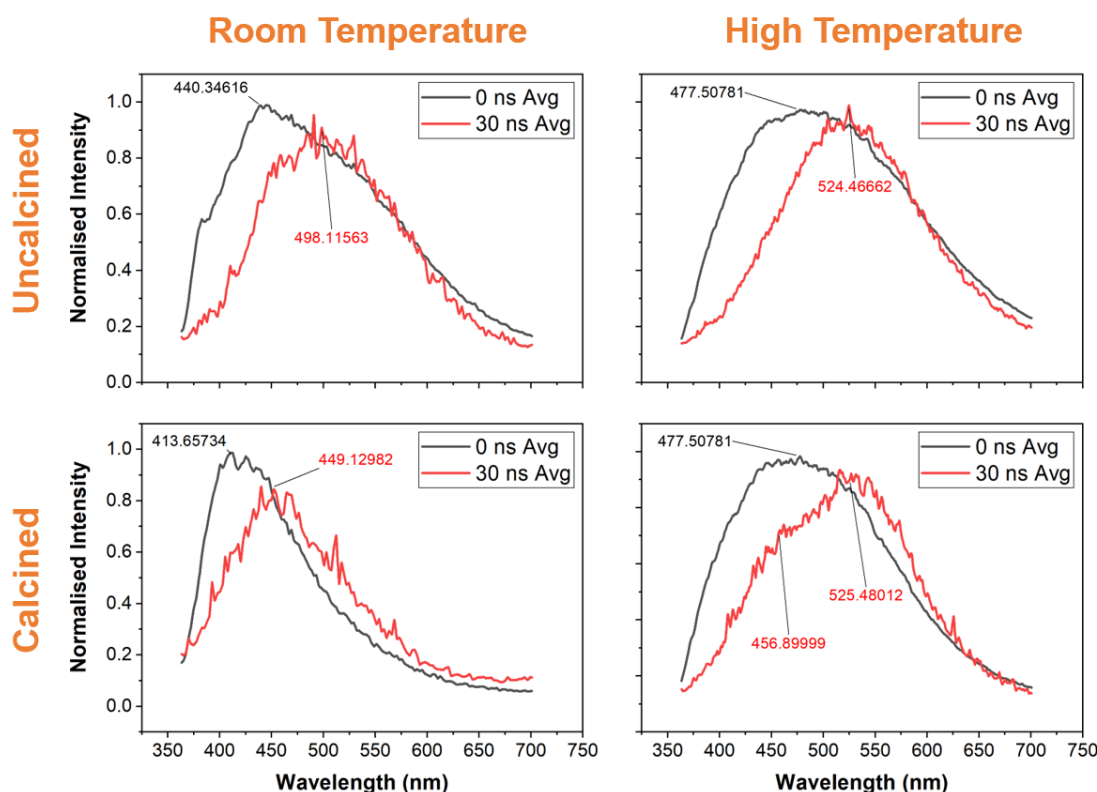


Figure 36 **Averaged gated spectra of calcined and uncalcined chabazite at room and high temperature.** Spectra were close enough at each different power that for each time gate (i.e. 0 ns, 30 ns) the spectra for each power (e.g. 0.9-900 μ W) were averaged. Spectra were obtained with a 10 ns gate width moved with a 30 ns delay interval. From 60 ns onwards the signal was not high enough.

Gated spectra are presented in Figure 36. At room temperature, the spectra for both the calcined and the uncalcined material appear are in agreement with the previous gated spectra analysis presented in Chapter 4. As previously, the uncalcined features a sharper peak at 440 nm in the 0 ns window and a broader peak at 500 ns in the 30 ns window. This was previously attributed to the confinement effects of template material. The calcined material also shows a peak in the 0 ns window at around 410 nm, as previously shown, and exhibits a less shifted peak in the 30 ns window at around 450 nm. This narrower peak profile was attributed to framework luminescence in Chapter 4.

The high temperature gated spectra of the uncalcined material show that although the CW measurements at room temperature and high temperature appear to have the same peak position, the time-resolved the emission components exhibit a slight difference. The fast luminescence in the 0 ns region features a broad emission peak at 477 nm in both cases. In the 30 ns window, the uncalcined material features an emission spectrum with a single peak at 525 nm. The calcined material also appears to have a peak at 525 nm, but it also additionally has a shoulder feature at 456 nm. This implies that in the calcined material, there is may be an additional emissive process occurring or that the sample may have somehow been changed by the calcination process resulting

in an additional longer lived peak. It is interesting to note again that for both samples at high temperature the peak profile and positions are different to that at room temperature, implying that a different emissive process is taking place at low and high temperatures.

3.4 Peak Intensity Analysis

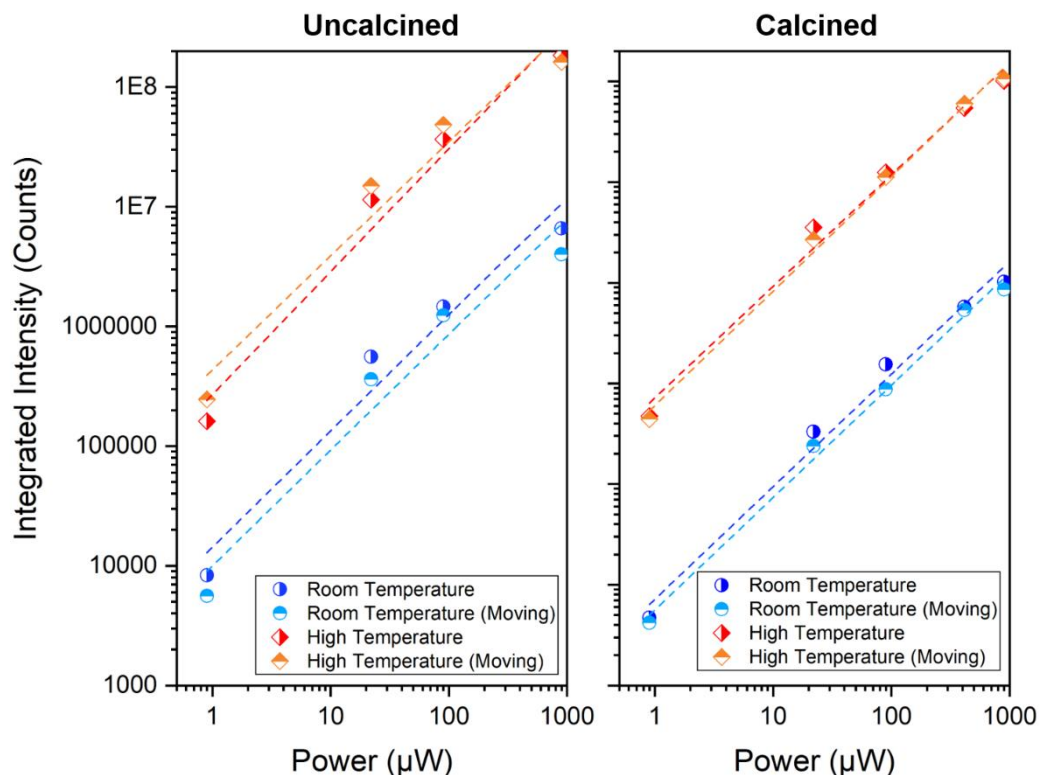


Figure 37 **Integrated intensity plotted as a function of power** at A) Room temperature at 430 nm for calcined chabazite and 465 and 510 nm for uncalcined chabazite, and B) high temperature at 430, 470, and 500 nm for calcined chabazite and 480 and 500 nm for uncalcined chabazite.

Table 12 **Fit data for peak intensity data plotted as a function of power**

	RT (Uncalc/Calc)	RT Moving (Uncalc/Calc)	HT (Uncalc/Calc)	HT Moving (Uncalc/Calc)
Intercept	4.2±0.14/	4.0±0.29/	5.4±0.24/	5.6±0.28/
	2.86±0.15	2.75±0.10	4.86±0.14	4.7±0.10
Slope	0.97±0.14/	0.97±0.15/	1.0±0.13/	0.95±0.15/
	1.12±0.07	1.12±0.05	1.11±0.07	1.14±0.05
Residual sum of squares	0.17/	0.22/	0.15/	0.2/
	0.09	0.04	0.08	0.04
R-square	0.96/	0.95/	0.97/	0.96/
	0.99	0.99	0.99	0.99

Figure 37 shows the integrated intensity plotted on a log scale as a function of power. As expected, the intensity increases with power. The residual sum of square (RSS) values are worse for the uncalcined material than the calcined material. Between 22 -900 μW a more linear fit can be made and within which region it doesn't appear that there is a significantly disproportionate response with increasing laser power as a result of factors like laser damage or non-linear optical effects. At extremely low power (i.e. 0.9 μW) in the uncalcined material this response does not appear to be completely proportionate, resulting in poorer RSS values. This is likely related to the organic material present in the sample, which may bleach more readily at higher laser powers. In this case it is suggested that effects of photobleaching on organic material are considered as systematic issues.

4 Discussion

4.1 Effect of laser power on emission spectrum

The power study appears to show two primary results. The first is that at room temperature and high temperature, both samples do not appear to be adversely affected by an increase in laser power in a significant way.

As expected from the previous chapter, there are some visible differences in the spectral shape. The broader emission of the uncalcined sample in Figure 35 when compared to the calcined sample in Figure 33 is attributed to the presence of OSDA, which remains within the cages of the zeolite structure following synthesis and prior to calcination. In contrast, the spectra of the calcined material, being devoid of significant concentrations of organic material, is narrower and lower in intensity.

In both cases, neither the peak position or spectral shape in Figure 33 and Figure 35 appear to be significantly affected when the power is increased. This appears to be the case in both the moving laser and static laser experiments. This implies that within the power range studied here, the photoluminescence of the zeolite framework itself is relatively impervious to the influence of laser. This is further supported by the plot of power against peak intensity, which shows a linear agreement between 22 – 900 μW .

The uncalcined chabazite demonstrates slightly more spectral variation at room temperature with changing power. Although the peak position is unchanged at different powers for both the static and moving laser experiments, the width of the falling edge of the spectrum does show a slight increase as laser power increases. This effect is more pronounced in the moving laser experiment, which could be attributed to either a slight photobleaching effect occurring by overexposing the sample in the static experiment, or to inhomogeneity in the zeolite that becomes evident as the laser is moved to different areas of the sample. This effect may feasibly be attributed to both as the red region of the uncalcined PL spectrum is due to occluded organic material, which is both

volatile under the influence of a laser and likely to vary in concentration across the sample. In complex emission systems at room temperature, it is perhaps the case that increasing laser power preferentially pumps different fluorophores to produce spectra with slightly different peak centres. Overall, the variation is attributed to the organic material, which is generally more susceptible to photobleaching

4.2 Effect of temperature on emission spectrum

In both samples there is a significant increase in emission intensity when the temperature is increased. This phenomenon has been reported previously in zeolites and is acknowledged as a particular challenge as a background that needs to be overcome in *operando* Raman studies¹⁶¹. Such a dramatic increase in emission intensity is remarkable as it is typically expected that photoluminescence signal would quench with increasing temperature⁹⁴. Temperatures exceeding 360 °C would certainly be considered an extreme environment for a molecular fluorophore to be emitting so effectively.

Interestingly, although the calcined and uncalcined samples possess distinct spectral features at room temperature spectra, at high temperature the difference between the samples is no longer clearly evident. Rather, at high temperature the spectral series for each sample begin to look the same. At irradiation up to 90 μ W, samples exhibit broadened spectra with a peak centred at around 460 nm. From 415 μ W and above, the spectra are instead centred at around 500 nm.

Further to this, the high temperature gated spectra show similarity between both samples. At 0 ns the fast signal was centred at 477 nm, and at 30 ns the peak is centred at 525 nm. This indicates a common emission mechanism is responsible for PL at high temperature. Additionally, the marked differences between the room temperature and high temperature spectra in each sample, as well as the similarity between the high temperature datasets for the calcined and uncalcined sample, imply that the emission mechanism at high temperature differs from the emission mechanism at low temperature. At elevated temperature, the emission might be attributed to an alternative, non-molecular radiative pathway in the chabazite framework itself, which is the common denominator between the two samples. In the high temperature calcined sample, there is an additional feature in the 30 ns gated spectra at 456 nm. This phenomenon is explored in greater depth in an *in situ* study in Chapter VI.

4.3 Conclusion

In this study, a comparative analysis was conducted between a series of power studies acquired as a function of temperature, laser position, and sample composition. In the region of 0.9-900 μ W, the calcined and uncalcined sample were both found to be relatively stable. In the region between 22-900 μ W the power relationship appeared linear. This means that operating laser

characterisation at powers below 900 μW are unlikely to damage the sample too significantly. Higher than this, it is likely that the effects of photobleaching will become more pronounced.

At high temperature, an unexpected increase in emission intensity occurred. The sample did not, however, behave unexpectedly with increasing power at high temperature maintaining a proportional increase in signal intensity with power. This unexpected result will be explored further in the following chapter with an *in situ* experiment.

Chapter VI

***In situ* Time-Resolved Photoluminescence Spectroscopy Studies of Detemplation and MTO**

In collaboration with the Valentini group in the Experimental Physics Department at the
Politecnico di Milano

To be submitted to in Journal of Physical Chemistry C

1 Introduction

In Chapter IV, a room temperature emission signature was measured for a zeolite undergoing detemplation. It was established that this signal was arising from a molecular origin of either occluded template material or template derivatives forming during the detemplation process. A non-molecular emission component was also speculated to be visible in the calcined sample. At this stage, it was proposed that the signal may be somehow intrinsic to the aluminosilicate framework. Chapter V constituted a power study, performed to determine whether the emission signal exhibited any power dependency under different temperature and sample conditions, and to determine whether experiments were being conducted in a ‘safe’ power region that wasn’t causing excessive non-linear damage to the sample. In this chapter, yet another characteristic emission signal was observed when the sample was elevated to a high temperature. Across two compositionally differing samples, a calcined and an uncalcined sample, the imposition of temperature resulted in an emission spectrum that appeared almost identical irrespective of the presence of an adsorbed molecular phase. This prompted speculation that zeolites may exhibit interesting behaviours at high temperatures (i.e. >300 °C).

In this chapter, the same time-resolved photoluminescence spectroscopy is extended to include an *in situ* setup with the aim of discovering how the photoluminescence effects recorded in previous chapters evolve and change with time. The results are split into two sections: Part A, and Part B. Part A builds directly on the work in Chapter IV focusing on *in situ* detemplation experiments, performed in real time in a reaction cell. To the best of this author’s knowledge the only other similar *in situ* study¹⁰ noted was a combined UV-vis/fluorescence spectroscopy study by Karwacki et al¹⁴⁵ of detemplation in an MFI crystal, which is discussed further in Section 4.1.1. The experiments presented in this chapter would therefore appear to be unique and without direct literature precedent. As a complement to the detemplation experiments, two additional *in situ* experiments were also conducted. The first is a heating study of calcined SSZ-13, conducted to discern the effects of temperature on a zeolite framework in the absence of significant concentrations of adsorbed organic species. The second is a heating study of calcined silicon-only SSZ-13 in air, conducted to discern the effects of temperature on a framework in the absence of aluminium and significant volumes of adsorbed molecular species.

Part B showcases how the technique may be extended to study actual catalytic reactions by successfully recording spectral differences during the methanol-to-olefins (MTO) reaction. The MTO reaction has been introduced in Chapter I and involves the conversion of methanol into

¹⁰ This is not to say that other studies on related topics do not exist. A selection of those that do explore the effects of heating on a zeolite are discussed in Section 4, but these are not performed under *in situ* conditions combined with a TRPS setup.

higher value hydrocarbons over a zeolite catalyst. In this thesis, the same SSZ-13 sample is used to catalyse this reaction¹¹.

A major conclusion drawn from the results of the experiments in this chapter is that there is a high-temperature emission mechanism differing from the room temperature signal acquired in Chapter IV attributed to a molecular origin. The origin of this high-temperature emission mechanism is assigned in the discussion to the proliferation of oxygen point defects. Oxygen point defects have been relatively extensively theorised in modelling of silica materials. However, providing experimental evidence is very challenging because doing so requires, in effect, atomic level resolution of bonding differences in an element that is vastly abundant in the sample. Point defects are not necessarily accompanied by significant changes in composition or sample structure, but it is expected that local electronic properties in the material would be different where defects are arising, which is something photoluminescence spectroscopy would be capable of detecting if the defects create new energy states that can act as emission pathways.

In this chapter, this postulate is supported by:

- Previous modelling studies in silica and zeolite materials that predict the formation of oxygen point defects
- Temperature behaviours in the detemplation and silicon-only chabazite fulfilling some of the theoretical expectations of point defects
- Changes in spectral intensity and shape during the MTO reaction correlating with oxygen point defects acting as potential active sites in the catalyst

As a final note, the *in situ* experiments have been analysed by presenting the following types of datasets:

- **CW spectra**, which are often separated into different temperature regions to look at intensity trends
- **Normalised CW spectra**, which are included to show how spectral profiles change with temperature
- **Analysis of peak intensity and position as a function of temperature**, included in graphical form to visualise trends, and in tabulated form to quantify changes more easily
- **Gated spectra**¹², to see how the emission dynamics might change as a function of time

¹¹ Note that SSZ-13 is not necessarily the most efficient catalyst for use in this reaction. Instead, SAPO-34, a silicoaluminophosphate zeolite based on the same CHA topology, is generally acknowledged as the catalyst of choice for MTO. However, SSZ-13 is used from the point of view of continuity, given that its emission behaviour has been well-studied up to this point in the thesis and that any further changes observed *in situ* may be more accurately assigned to the progression of the catalytic reaction.

¹² Gated spectra were not acquired for all experiments owing to the time required to record this data, which did not always conform to the time constraints associated with *in situ* experimentation.

Part A: Temperature-Induced Emission Mechanism in Framework

2 Experimental Section

2.1 *In situ* Setup

The time-resolved photoluminescence spectroscopy setup described in Chapter 3 was used in this set of experiments. Samples were loaded into a Linkam CCR1000 reaction cell fitted with quartz windows. An Oasis 3 water cooler (Solid State Cooling Systems, New York) was connected via 1/8" tubing and push-fit connections to cool the Linkam cell when being operated at temperatures over 200 °C. An EcoSys-P mass spectrometer (European Spectrometry Systems, Northwich) was used to monitor products travelling from the exhaust line.

Inert He gas and synthetic air (pre-mixed 20 % O₂ in N₂) were used in this experiment. He was used to flush lines or provide an inert sample environment, and synthetic air was used for active detemplation experiments. Figure 38 shows the gas schematic diagrams. 1/16" PTFE tubing with Swagelok connections were used throughout. Gases were modulated via mass flow controllers (Brooks Instrument, Pennsylvania) and connected to the reaction cell via a three-way valve, with only one gas source able to flow through the cell at any given time. An on-off switch (not shown) was also installed in each gas line to prevent leakage through the system. Due to the small cell and sample volume, all outgas flow from the reactor was directed into the mass spectrometer to maximise signal. A non-return valve was installed in the vent line coming out of the mass spectrometer to prevent exhaust gas reuptake. For the methanol-to-olefins experiment (see Figure 38B) a syringe pump was installed into the line with a T-piece.

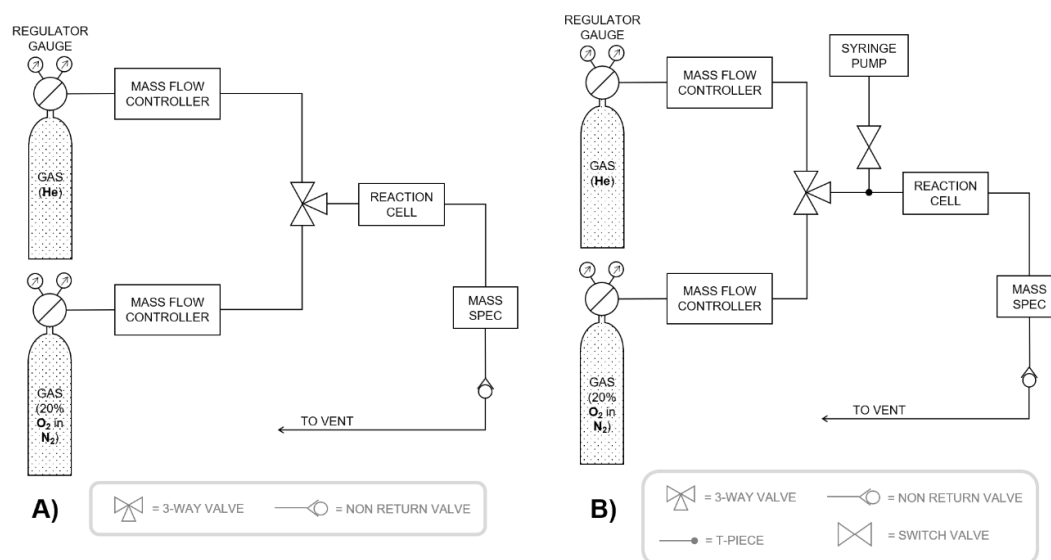


Figure 38 **Gas schematic diagrams** for A) basic setup used in detemplation and temperature studies, and B) methanol-to-olefins setup

2.2 Temperature Protocol

Three different type of temperature protocol were used for *in situ* experiments. They were continuous temperature ramping, quenching, and temperature ramp reversal. These are summarised in Figure 39. Fresh sample was used for all experiments with as-synthesised material for studies related to detemplation and pre-calcined material for the MTO reactions.

In continuous temperature ramp studies, the sample was slowly ramped up to a target temperature. The aim of this study was to mimic a catalytically relevant environment *in situ*, using similar heating gradients, to see how photoluminescence signal changes throughout the course of a reaction. For the detemplation study, this involved heating at a rate of 2 °C/min with at least 30 mL/min gas flow. The samples were held for a period of time at 100 °C. This was to ensure the zeolite was gradually dehydrated to prevent framework steaming, a process known to damage the sample, at higher temperatures. Two repeats of this study were conducted, one where the laser position was fixed and another where the laser was rastered across the sample between measurements. An increased oxygen flow rate was also used in the second repeat to reduce the rate of sample darkening.

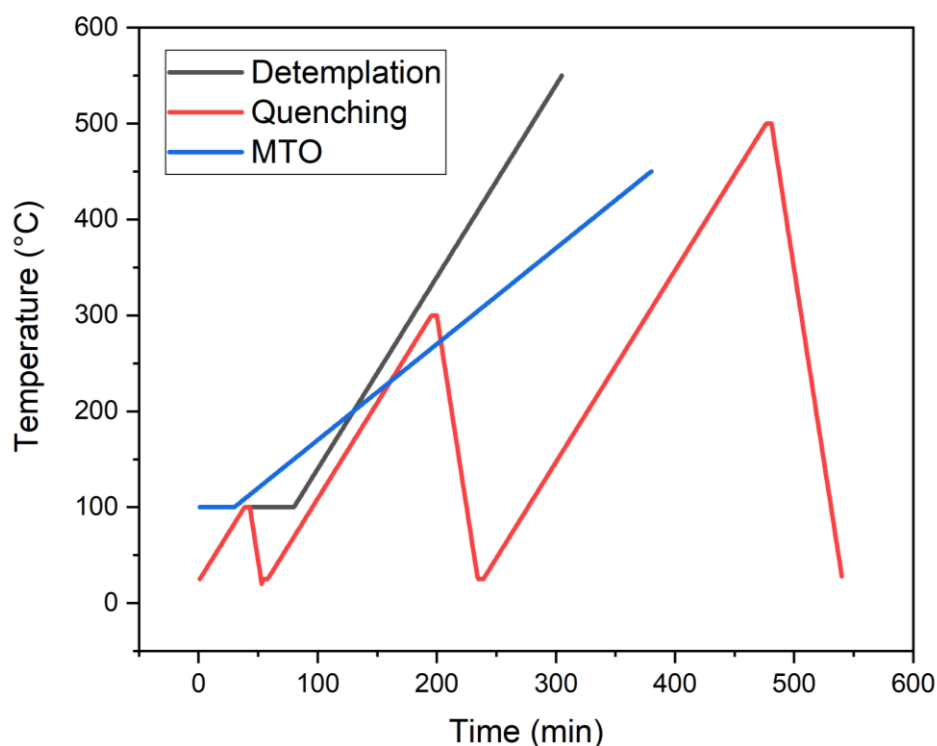


Figure 39 Temperature protocol for different experiments: A) Continuous temperature ramp study of detemplation, B) quenching study, C) continuous temperature ramp study of MTO reaction. Note that times are representative and actual experiment times were longer in some cases to accommodate acquisition times. The MTO experiment also featured an additional activation period at 550 °C prior to methanol injection

In the quenching study, the sample was brought to 100, 300, and 500 °C and then quenched back to room temperature each time (see Figure 39). The aim of this study was to determine whether the spectra observed were affected by temperature. Detemplation was chosen, as the changes in the photoluminescence at different stages of the process have previously been established (see Chapter IV). If elevated temperatures were seen to be affecting the spectral profile of the emitted signal, it was expected that there would be a difference between the spectra at high temperature and following a rapid quench to room temperature. The sample was cycled through three different temperatures, being first brought to 100 °C at a rate of 2 °C/min and then quenched to room temperature at a rate of 8 °C/min, then being reheated to 300 °C and quenched at the same rate, and finally brought to 500 °C and back down to room temperature. The sample was held at each target temperature for 15 min before being quenched.

In the temperature reversibility study, the sample was ramped continuously through a range of temperatures to reach a target temperature of 500 °C, and then slowly brought back to room temperature. The aim of the study was to determine whether temperature effects behave in a reversible fashion or not. Determining whether temperature effects are reversible or not may provide insight into the mechanism of high temperature photoluminescence. This study was conducted on a calcined chabazite sample (SAR=15) and a calcined silicon only chabazite sample. Although similar in principle to the quenching study, the temperature reversibility study was

conducted on pre-calcined zeolites under non-reactive gas conditions. It was not expected that the sample would show significant chemical changes in the way a zeolite undergoing detemplation would, therefore it was decided that continuously ramping the temperature up and down would be the most time-efficient experiment.

2.3 Si-only SSZ-13 Characterisation

A silicon-only SSZ-13 sample is studied in Section 3.2. The sample was synthesised in the same manner as described previously in fluoride media but without aluminium feedstock. XRD data in Figure 40 confirms the CHA structure, with characteristic bands at 9.58, 13.00, and 20.86 corresponding to the (100), (-110), and (-210) reflections⁸. A slight difference in the position of the bands is seen, which are shifted to higher angles, and can be attributed to the lack of Al stressing the framework.

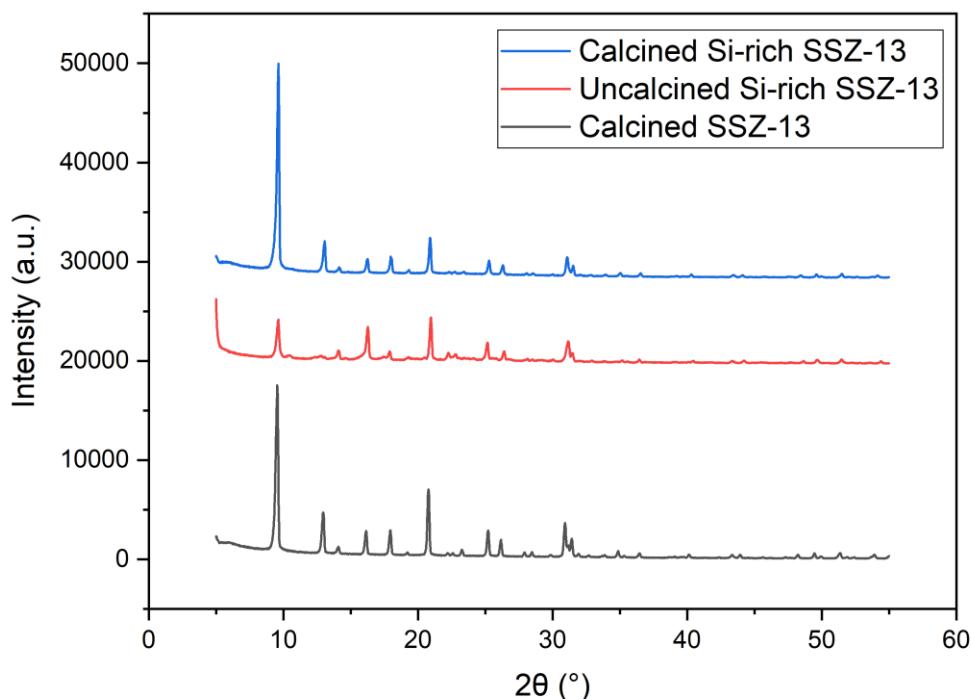


Figure 40 **Powder XRD data** of calcined Si-rich SSZ-13 (blue), uncalcined Si-rich SSZ-13 (red), and calcined Al-containing SSZ-13 (SAR=15; black). Acquired by Dr Miren Agote Aran.

NMR data in Figure 41 confirms the absence of Al from the Si-only sample. In the ^{27}Al solid state NMR spectrum, the line at around 60 ppm corresponds to tetrahedrally co-ordinated AlO_4^{2-} . A small amount of extraframework Al can also be seen in this sample at around 0 ppm, which would have an octahedral AlO_6 co-ordination. In contrast, the Si-only sample shows no lines, highlighting the lack of Al present. In the ^{29}Si solid state NMR trace both samples exhibit a band at -111 ppm, which corresponds to a tetrahedrally co-ordinated Si atom $\text{Si}(\text{OSi})_4$. This band is more intense in the Si-only sample as this form of silicon environment vastly dominates.

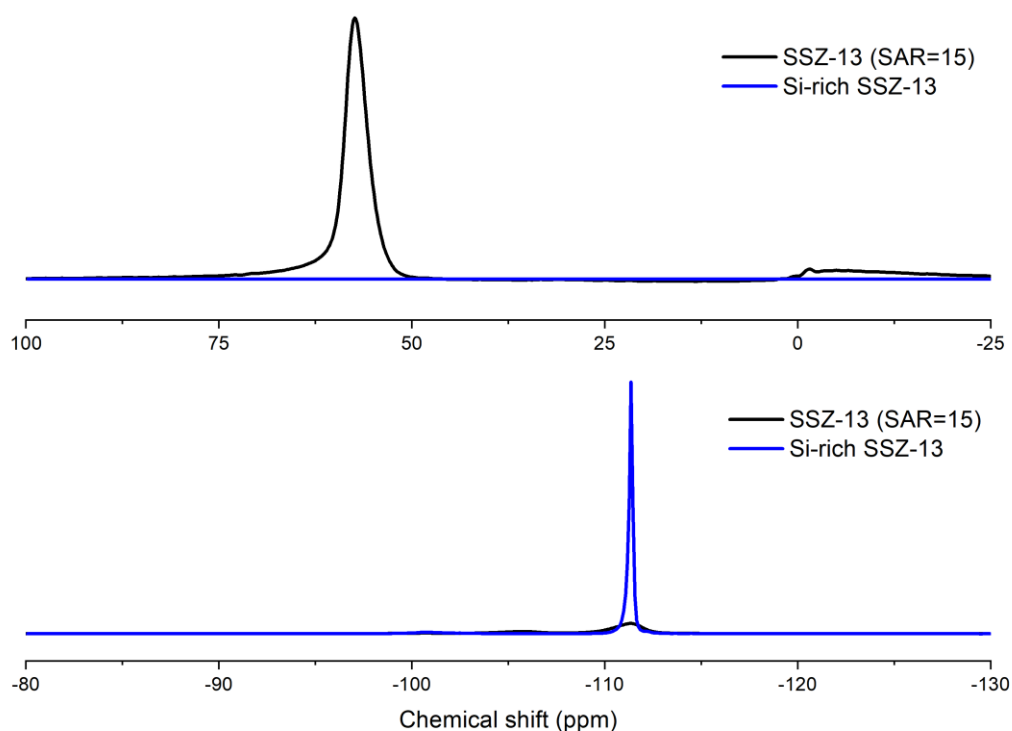


Figure 41 **²⁷Al (top) and ²⁹Si (bottom) solid state NMR** of Si-rich SSZ-13 sample compared to Al-containing SSZ-13 (SAR=15). Spectra were acquired with a Bruker Avance III unit with a widebore BB/1H WVT probe (tuned to 104.27 MHz for ²⁷Al and 79.49 MHz for ²⁹Si) at a magnetic field strength of 9:4T. Acquired by Dr Miren Agote Aran.

Additional IR spectroscopy in Figure 42 also demonstrates the absence of Al in the Si-rich sample. Al-containing SSZ-13 features a band at 3730 cm⁻¹, which is attributed to the OH stretching of isolated silanol groups, as well as two Brønsted acid sites at 3600 and 3580 cm⁻¹¹⁶¹. The high frequency site at 3600 cm⁻¹ has been attributed to Brønsted acid sites sitting in the eight-membered ring windows of the CHA structure, whereas the low frequency site at 3580 cm⁻¹ are acid sites that are not directly exposed to the eight-membered rings²¹⁵. While the Si-only sample exhibits the isolated silanol group band at 3730 cm⁻¹, there is no evidence of either the high or low frequency Brønsted acid sites, which is to be expected given the lack of Al.

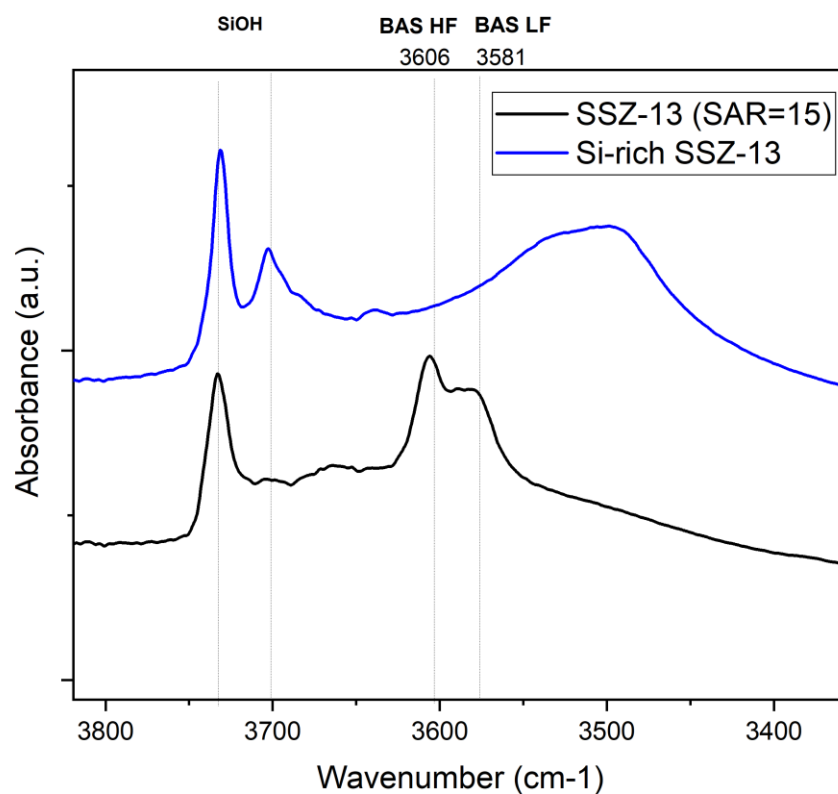


Figure 42 **FTIR data** of Si-rich SSZ-13 (blue) and Al-containing SSZ-13 (SAR=15; black). Acquired on Nicolet iS10 spectrometer under inert He gas conditions at 150 °C. Acquired by Dr Miren Agote Aran.

3 Results

3.1 Uncalcined SSZ-13





3.1.1 *In situ* Detemplation

3.1.1.1 Visual Changes

Visual changes in the sample are documented in

Table 13. Over the course of a detemplation it is expected that the white synthesised sample may turn black as a result of acid promoted hydrocarbon pool chemistry followed by incomplete combustion of the aggregated products, which are in turn decomposed and removed rendering the sample white again¹⁴⁵. The *in situ* experiment here represents the first half of the detemplation process. To stem the production of combustion products, oxygen availability was increased by doubling the rate of synthetic air flow in the second experimental repeat.

Table 13 Visible changes in sample as a function of temperature during detemplation for two experimental repeats under different air flow conditions with photos at select temperatures showing sample packed inside Linkam CCR1000 cell and crucible edge

Temperature (°C)	Visual changes	
	30 mL/min air flow	60 mL/min air flow
Room temp to 350	White powder	
		
375	No notes recorded	Sample slightly yellow around edges of crucible edge
		
450	Yellow around the edges	Ring of black around the crucible edge, yellow spreading across centre
		
475	No notes recorded	
500	Coking visible on edges	Sample is no longer white. White areas are pale yellow, and there is a fine ring of black around the edge.
		
550	Coke ring extending to almost halfway across the sample	Border of coke increasing. Yellow colour becoming darker.



3.1.1.2 Continuous Wave Spectra

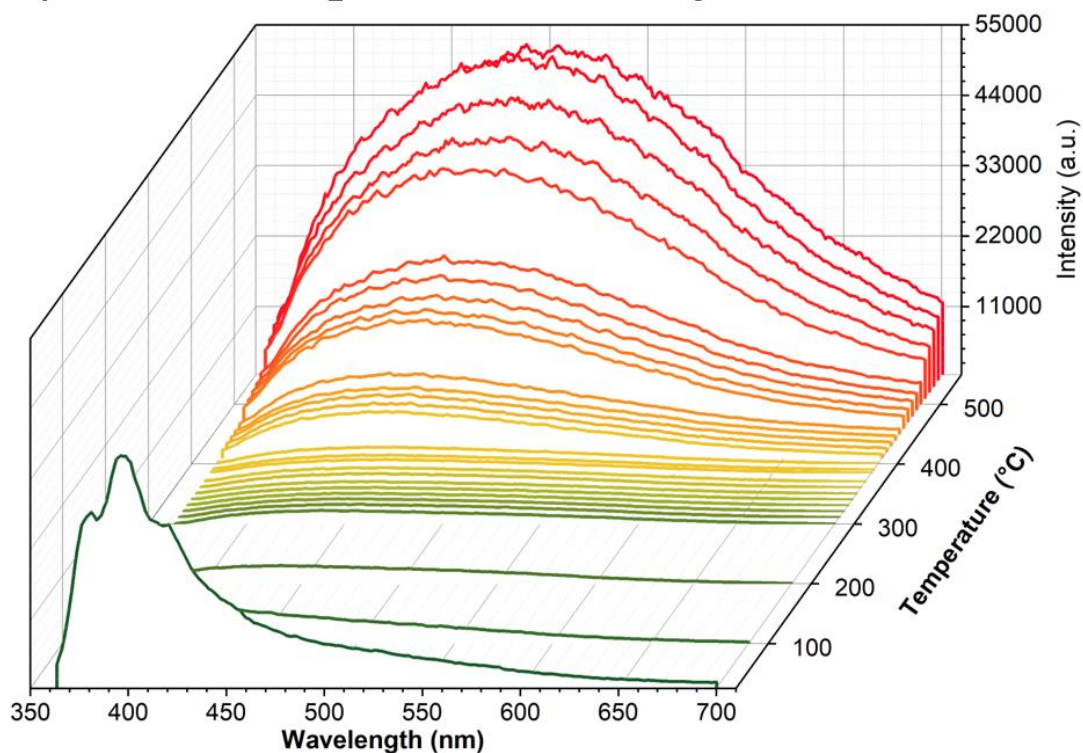
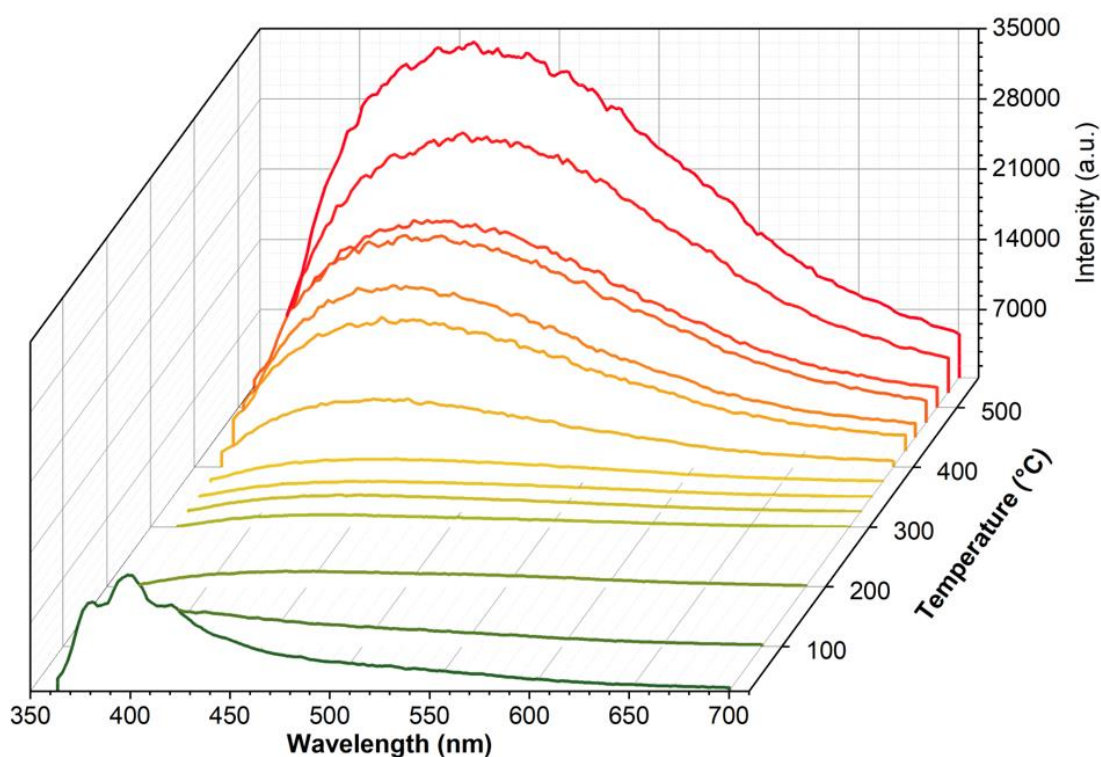
A) 30 mL/min O₂ flow, fixed laser position**B) 60 mL/min O₂ flow, moving laser position**

Figure 43 CW fluorescence emission spectra tracking the detemplation process of uncalcined H-SSZ-13: A) 30 mL/min oxygen flow with fixed laser position B) 60 mL/min oxygen flow with moving laser position.

The detemplation experiment was repeated twice (see Figure 43). In the first, spectra were measured from the same fixed laser position and in the second the laser was moved to a new spot prior to each measurement. These are also referred to as experimental repeat 1 (fixed laser) and experimental repeat 2 (moving laser). For both experiments, trends in peak intensity and spectral shape were subdivided into four sections as shown in Figure 44.

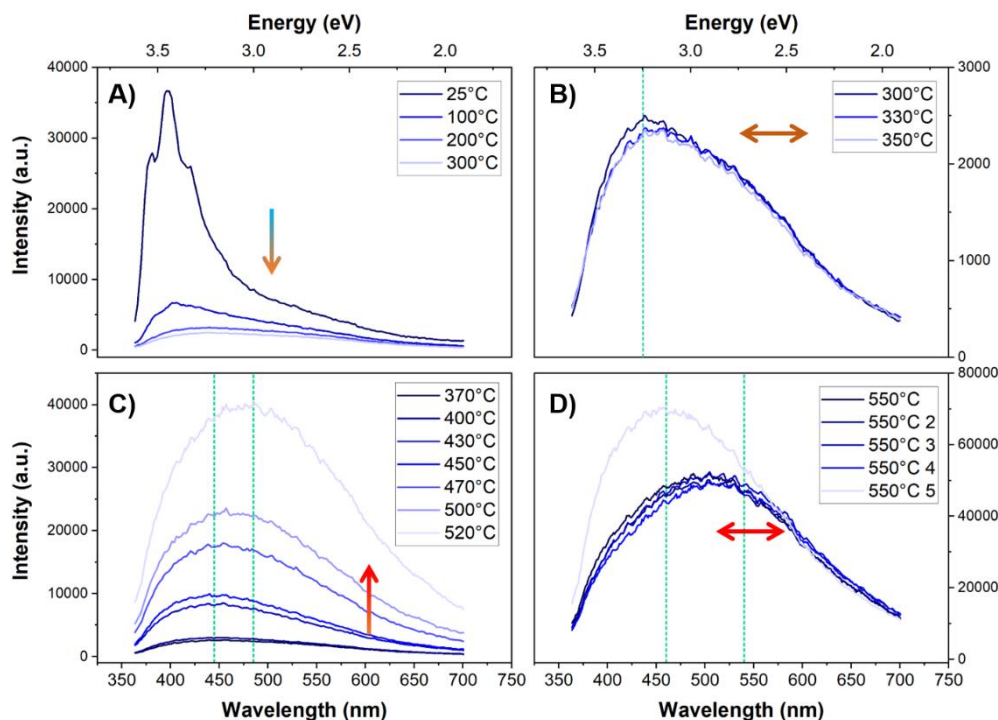


Figure 44 Proposed regions of activity in the detemplation process for moving laser experiment: A) Room temperature to 300 °C B) 300 to 350 °C C) 375 to 525 °C, and D) 550 °C

The first region of interest is from room temperature to 300 °C, shown in Figure 44A. At room temperature a triple peak is visible in the spectrum. The central peak at 399 nm (3106 cm^{-1}) partly encompasses the region for the O-H Raman stretch of water, indicating the sample is hydrated. That the 399 nm peak is associated with the presence of water is further confirmed by its diminishment from 100 °C onwards, indicating that the sample is dehydrating. Throughout this early dehydration period, peak intensity reduces to less than 2 % of the original hydrated intensity, and is tracked in Figure 46C. Normalised spectra in Figure 45 show that the biggest changes to the spectral profile occur between 100 and 300 °C.

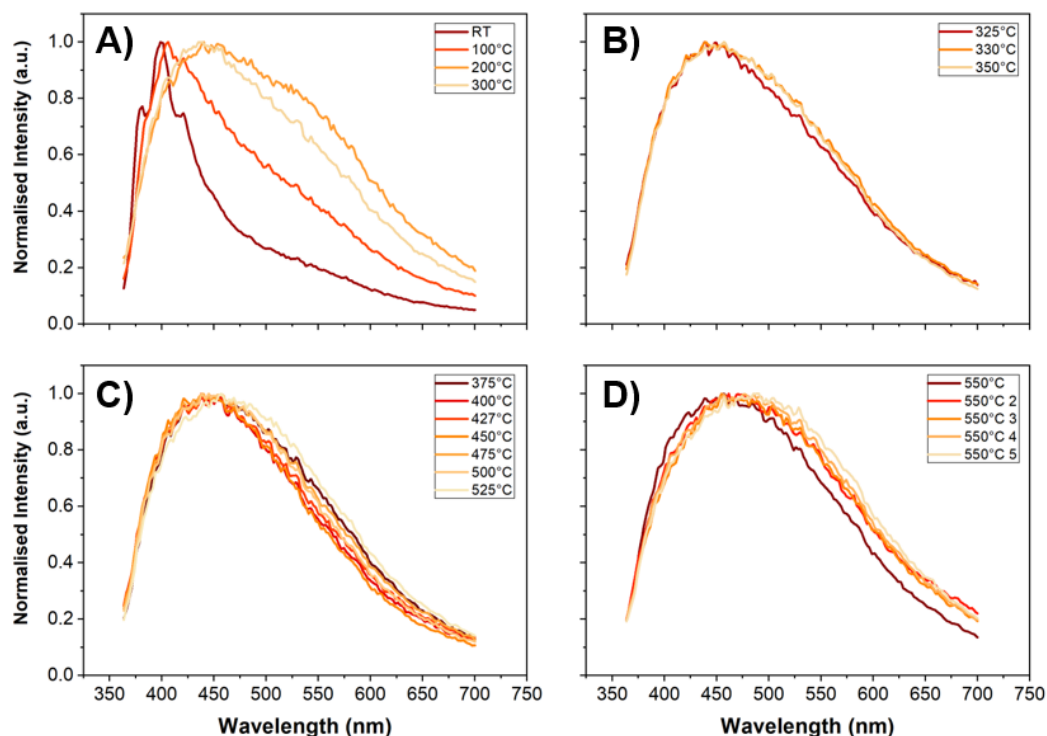


Figure 45 **Normalised CW of detemplation at representative temperatures for moving laser experiment:** A) Room temperature to 300 °C B) 300 to 350 °C C) 375 to 525 °C, and D) 550 °C

Figure 44B shows the second region of interest from 300 to 350 °C. This region is characterised by relative stability in the spectral shape and intensity. The raw data presented here show that the fixed laser experiment appears to have a higher emission intensity than the moving laser experiment with spectral profiles that appear to almost overlay in this temperature region. Conversely, the moving laser experiment seems to show a small degree of intensity evolution with increasing temperature. However, in the scheme of the whole experiment, peak intensity in this temperature region appears relatively stable until 375 °C (best visualised in Figure 45C) with the variation in the moving laser experiment perhaps attributable to sample heterogeneity. Further to this, the normalised dataset in Figure 45 shows that even the spectral profile of the moving laser experiment in this temperature region appears the same, with the peak position centred at 445 nm for both repeats of the experiment.

The third region of interest in Figure 44C covers the temperature range between 360 and 525 °C. In this region, the sample exhibits a dramatic increase in peak emission intensity. Normalised spectra in Figure 45C show that the peak position of 445 nm remains fixed and there is little to no evidence of peak broadening. Figure 43 shows that the highest intensity recorded is in the fixed laser experiment at around 500 °C, implying that the laser itself may be contributing to the emission mechanism.

The final proposed region of interest encompasses spectral variations viewed after holding the sample at 550 °C for some hours. At 550 °C the peak centre has red-shifted to from about 450 nm at 525 °C to around 500 nm.

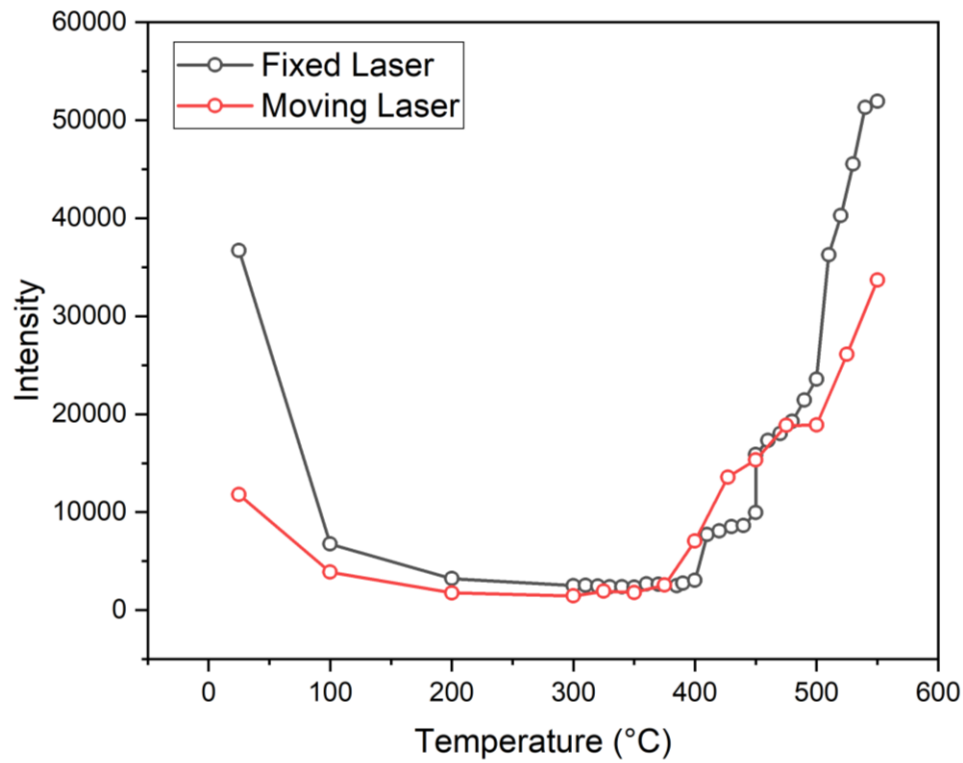


Figure 46 **Peak intensity plotted as a function of temperature for in situ detemplation** for fixed laser experiment (black) and moving laser experiment (red)

Table 14 Values of maximum peak intensity for in situ detemplation experiment for two experimental repeats. A single value taken from peak intensity of each spectrum was selected to denote the increasing intensity. Peak position (i.e. wavelength) was not taken into account. Peak intensity is also formulated as percentages of the maximum intensity of the original room temperature measurement and as a percentage of the maximum intensity of the previous measurement to show evolution.

Temperature (°C)	Max. Peak Intensity (a.u.)		Max Peak Position (nm)		Peak Height % of Initial RT Measurement		Peak Height % Difference of Previous Measurement	
	<i>Moving</i>	<i>Fixed</i>	<i>Moving</i>	<i>Fixed</i>	<i>Moving</i>	<i>Fixed</i>	<i>Moving</i>	<i>Fixed</i>
25	36715	11797	396	399	-	-	-	-
100	6744	3892	403	405	18	33	18	33
200	3213	1776	436	449	9	33	48	46
300	2501	1455	436	436	7	12	78	83
310	2531	-	447	-	7	-	101	-
320	2449	-	446	-	7	-	97	-
325	1931	1931	-	447		16	-	106
330	2374	-	446	-	6	-	97	-
340	2371	-	448	-	6	-	100	-
350	2353	1803	448	447	6	15	99	93
360	2673	-	447	-	7	-	112	-
370	2649	-	447	-	7	-	99	-
375	-	2551	-	447		22	-	105
385	2510	-	449	-	7	-	95	-
390	2737	-	447	-	7	-	109	-
400	3044	7060	447	447	8	60	111	277
410	7706	-	445	-	21	-	101	-
420	8074	-	442	-	22	-	105	-
427	-	13569	-	448		115	-	137
430	8521	-	448	-	23	-	106	-
440	8640	-	447	-	24	-	101	-
450	9971	15345	445	449	27	130	115	113
460	17323	-	450	-	47	-	109	-
470	18011	-	453	-	49	-	104	-
475	-	18850	-	446		160	-	151
480	19283	-	456	-	53	-	107	-
490	21452	-	457	-	58	-	111	-
500	23586	18891	457	448	64	160	110	100
510	36266	-	464	-	99	-	110	-

520	40264	-	475	-	110	-	115	-
530	45539	-	484	-	124	-	116	-
540	51318	-	485	-	140	-	120	-
550	51930	33675	500	457	141	285	110	129
550	50102	1584	504	473	136	13	96	5
550	52397	24955	505	473	143	212	105	1576
550	49536	27651	509	472	135	234	95	111
550	59128	30083	545	485	161	255	119	109

3.1.1.3 Gated Spectra

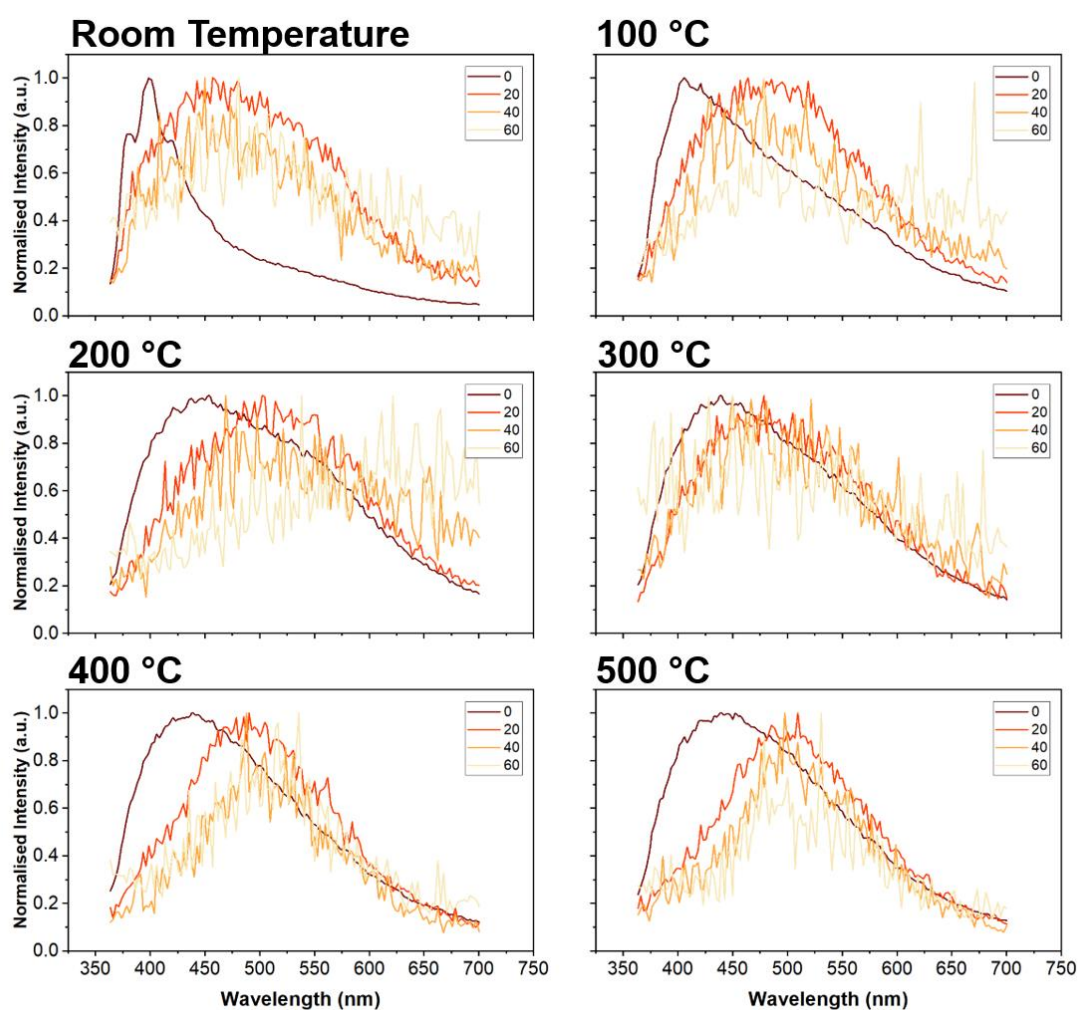


Figure 47 **Gated spectra of moving laser detemplation experiment** with time gates at 0, 20, 40, and 60 ns grouped by temperatures ranging from 25 to 500 °C

Gated spectra in Figure 47 at room temperature show a lifetime dynamic consistent with that discussed in Chapter IV. Up until 400 °C, there appears to be evolution in the gated spectra. At 100 °C, the 20 ns gate shows similarity to the room temperature ensemble with a peak at 408 nm

and a second component with a peak at 470 nm. At 200 and 300 °C the fast-lived component in the first window has a peak at around 440 nm and an additional shoulder at around 530 nm. The longer-living component at these temperatures also appears to have shifted to around 505 nm.

From 400 °C onwards, the gated spectra show the greatest similarity. The first time-window features a peak centred at 440 nm. From 400-550 °C, this peak position no longer changes. All temperatures also show a second longer lived component with a peak at 505 nm. This peak also does not change position across this temperature range. Notably, the spectral profile of the longer living component in this temperature region changes to a more symmetric shape than what was observed at lower temperatures. It is interesting to note that the sharp increase in emission intensity at 400 °C also appears to be associated here with a different lifetime dynamic in the gated spectra that interestingly does not appear to evolve with further temperature elevation. This spectral ensemble may tentatively be ascribed to a different emission source than the low temperature measurements.

Additionally, from 400 °C the spectra in the 60 ns gate is more clearly defined than in the datasets from room temperature to 300 °C, where the signal in the 60 ns gate appears as a background signal. This indicates that between 300 and 400 °C a longer living emission pathway appears to have formed.

3.1.2 Quenching Study

Figure 48 shows all emission spectra for this experiment. Most notable from this plot is once again the dramatic increase in intensity observed beyond 350 °C. A plot tracking the peak intensity is included in Figure 49.

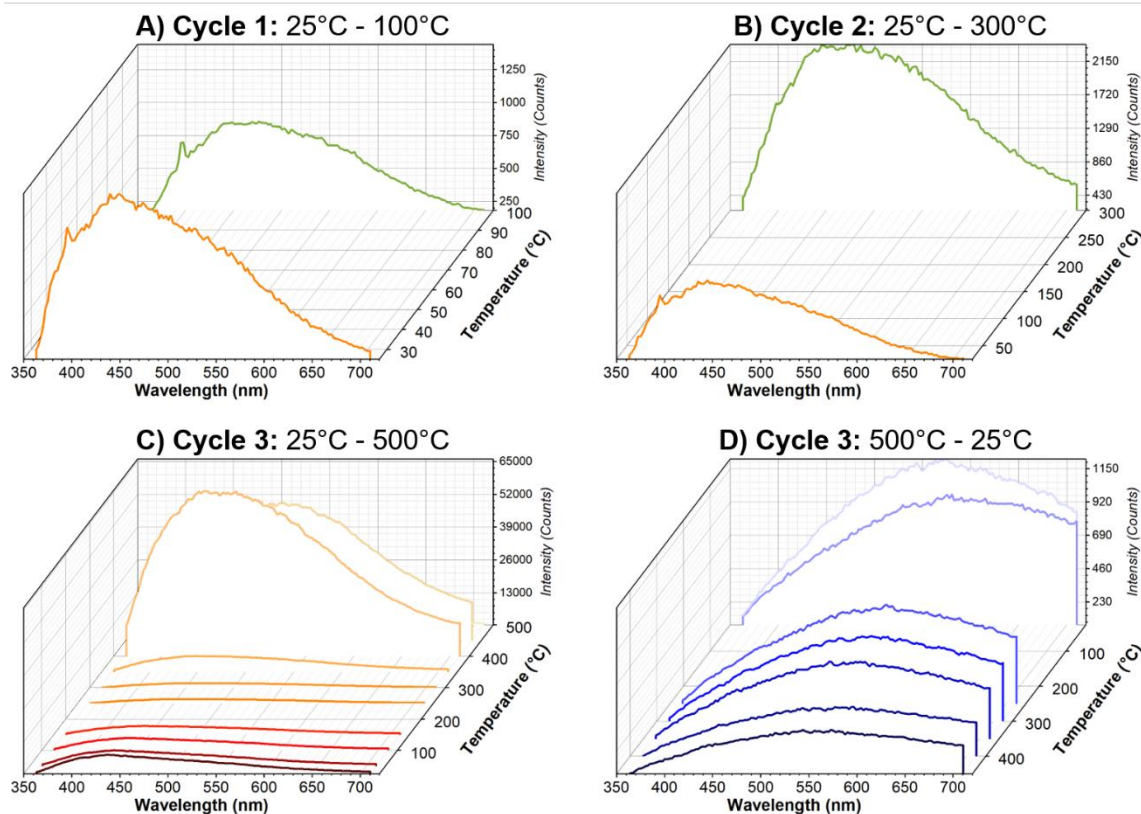


Figure 48 CW fluorescence emission spectra tracking the heating and quenching of an uncalcined H-SSZ-13: A) Cycle 1, where sample is ramped from 25 to 100 °C; B) Cycle 2, where sample has been quenched back to 25 °C and is then ramped to 300 °C; C) Cycle 3, where sample has been quenched back to 25 °C and is then ramped up to 500 °C; D) Cycle 3 continued, where the sample is quenched back to 25 °C.

Figure 48A shows initial room temperature emission spectra. This spectrum is like previous spectra acquired from uncalcined SSZ-13 framework zeolites (see Chapter IV and V) and exhibits a primary peak at 440 nm and a shoulder feature at around 550 nm. In Chapter IV, this spectrum was attributed to emission from the sterically confined organic structure directing agent. The spectral profile appears the same for each of the three repeats. Slight differences in peak emission intensity can be attributed to inhomogeneity across the sample.

Figure 48A also shows the first temperature cycle. Upon heating to 100 °C, the intensity of the emission spectrum decreases to 57 % of the original room temperature signal (see Table 15). This is in line with what has been observed previously (see Section 3.1.1). Quenching the sample back to room temperature sees the emission intensity increase, but to only 84 % of the original room temperature measurement. The spectral profile in all room temperature measurements even after quenching from 100 °C are the same implying that the sample has not experienced any change.

In terms of the detemplation process, this is to say that there does not appear to be any major compositional changes (i.e. template decomposition) that have happened yet. However, at 100 °C there is some peak broadening in the red, indicating the emission pathways at this temperature are perhaps different.

Figure 48B shows the second temperature cycle where the sample is heated again from room temperature to 300 °C. Upon heating, the spectrum intensity increases to almost 3 times the last room temperature measurement, but shows a 6-fold increase in peak intensity upon quenching back to room temperature as shown in Figure 49. Although the elevated temperature spectra at 100 and 300 °C share a similar shape, upon quenching back to room temperature the spectrum appears changed compared to previous room temperature measurements. Following elevation to 300 °C, the shoulder previously described at around 550 nm appears to have decreased, although the peak position is in a similar place. This observation is reasonable, because at 300 °C one would expect to start seeing structural changes to the occluded template material. Unpublished *in situ* NMR studies have shown that 300 °C is the temperature at which the adamantane cage begins to separate from its functional group¹³. Given that the 550 nm shoulder feature has previously been ascribed to the occluded template material, depletion in this region is consistent with changes to either the structure or concentration of the template material. Interestingly, in the transition from 300 °C back to room temperature, an increase in emission intensity is observed, indicating that in this zeolite system at 300 °C, temperature appears to be acting as a quenching mechanism.

¹³ Conducted in proprietary studies by Johnson Matthey

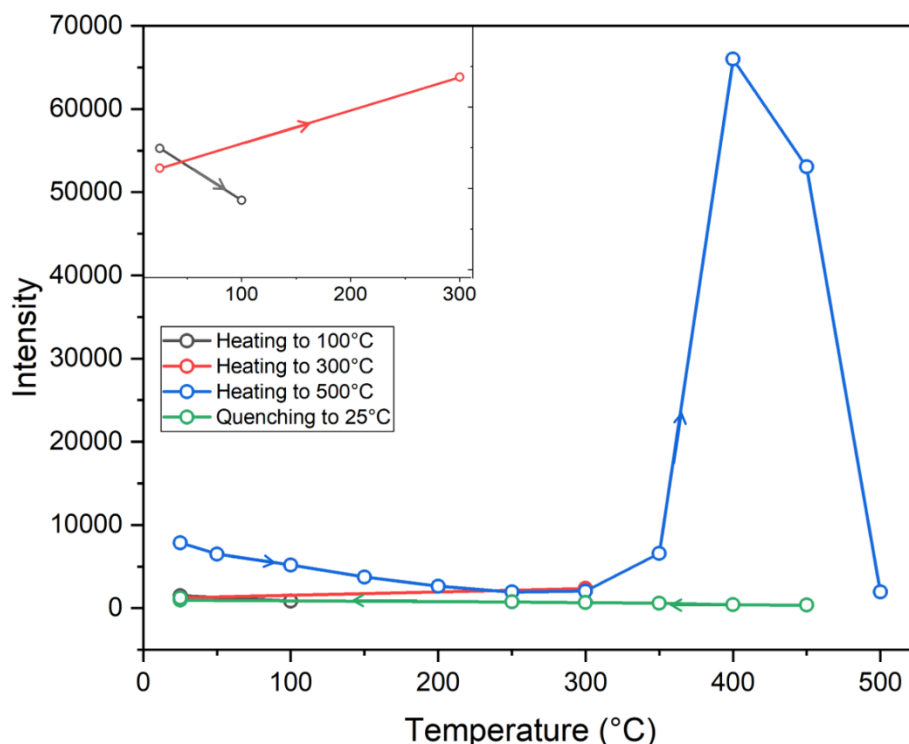


Figure 49 **Peak intensity plotted as a function of temperature of quenched uncalcined chabazite** for sample being heated to 100 °C (black), heating up to 300 °C after being quenched to room temperature from 100 °C (red), heating up to 500 °C after being quenched to room temperature from 300 °C (blue), and quenching back down to room temperature from 500 °C (green)

Figure 48C & D shows the spectral behaviour during the final temperature cycle from room temperature to 500 °C and back to room temperature. Figure 49 shows how the peak intensity changes with temperature. During the ramp up to 500 °C, the emission intensity gradually decreases with temperature up until 300 °C. Interestingly, in the previous temperature cycle, 300 °C appeared to have a quenching behaviour on the emission as is replicated in this temperature cycle.

From 350 °C, the sample appears to reach an inversion point where the peak intensity suddenly increases, with temperature no longer appearing to quench, before again significantly dropping in intensity again at 500 °C. From 400 °C, a different spectral shape is observed with the peak position red-shifting to 515 nm. It is postulated that the significant change in emission intensity and broadening of spectral profile from 350 to 450 °C is evidence of a wholly different emission mechanism.

At 500 °C the peak shifts again to 560 nm and is additionally accompanied by a significant drop in emission intensity. This spectral profile is maintained throughout the quench back down to room temperature. Figure 49 shows that during the quench back to room temperature, the emission intensity first drops at 450 °C. However, following this the emission intensity begins to increase again as the temperature continues to drop. When the sample reaches room temperature

for the final time, the peak emission intensity is 44 % of the original recorded room temperature emission intensity and is shifted by around 150 nm. The same sample measured 24 h later at room temperature shows the same spectral profile with some increase in emission intensity, indicating that the peak shift represents a permanent change in the sample.

At 500 °C it is expected that further changes are being made to the occluded template material, with a higher degree of template degradation and perhaps formation of template derivative molecules as previously indicated in Chapter IV. It is already known from a study of a sample quenched halfway through the detemplation process (i.e. the ‘intermediate sample’) in Chapter IV that the emission spectrum becomes significantly red-shifted with decreased intensity due to the proliferation of new hydrocarbon species with different emission characteristics. The darkening of the sample is partially responsible for the decreased intensity due to self-absorption.

Table 15 Values of maximum peak intensity for quenched detemplation experiment formulated as percentages of the maximum intensity of the original room temperature measurement and as a percentage of the maximum intensity of the previous measurement

Temperature (°C)	Comment	Max. Peak Intensity (a.u.)	Max Peak Position (nm)	Peak Height % of Initial RT Measurement	Peak Height % Difference of Previous Measurement
25	<i>Original room temp</i>	1492	446		
100		854	466	57	57
25	<i>Quenched from 100°C</i>	1248	441	84	74
300		2367	474	159	277
25	<i>Quenched from 300°C</i>	7853	436	526	629
50	<i>Ramping up to 500°C</i>	6509	439	436	275
100	<i>Ramping up to 500°C</i>	5185	440	347	66
150	<i>Ramping up to 500°C</i>	3753	440	251	58
200	<i>Ramping up to 500°C</i>	2630	445	176	51
250	<i>Ramping up to 500°C</i>	1933	472	130	52
300	<i>Ramping up to 500°C</i>	2039	475	137	78
350	<i>Ramping up to 500°C</i>	6590	447	442	341
400	<i>Ramping up to 500°C</i>	65980	460	4422	3235
450	<i>Ramping up to 500°C</i>	54796	513	3672	832
500		52784	556	3537	80
450	<i>Quenching to RT</i>	53036	561	3554	97
400	<i>Quenching to RT</i>	1930	560	129	4
350	<i>Quenching to RT</i>	375	562	25	1
300	<i>Quenching to RT</i>	414	569	28	21
250	<i>Quenching to RT</i>	606	568	41	162

25		662	580	44	160
-----------	--	-----	-----	----	-----

3.2 Silicon-only SSZ-13

Figure 50 shows the heating and quenching of a siliceous (i.e. Si:Al ∞) pre-calcined chabazite sample. Compared to other *in situ* experiments so far, this experiment is unique in that the zeolite sample does not experience any huge increase in emission intensity with different temperatures, with all spectra scaling onto a more limited y-axis. It is interesting to note that the absence of this phenomenon is accompanied by an absence of aluminium in the framework.

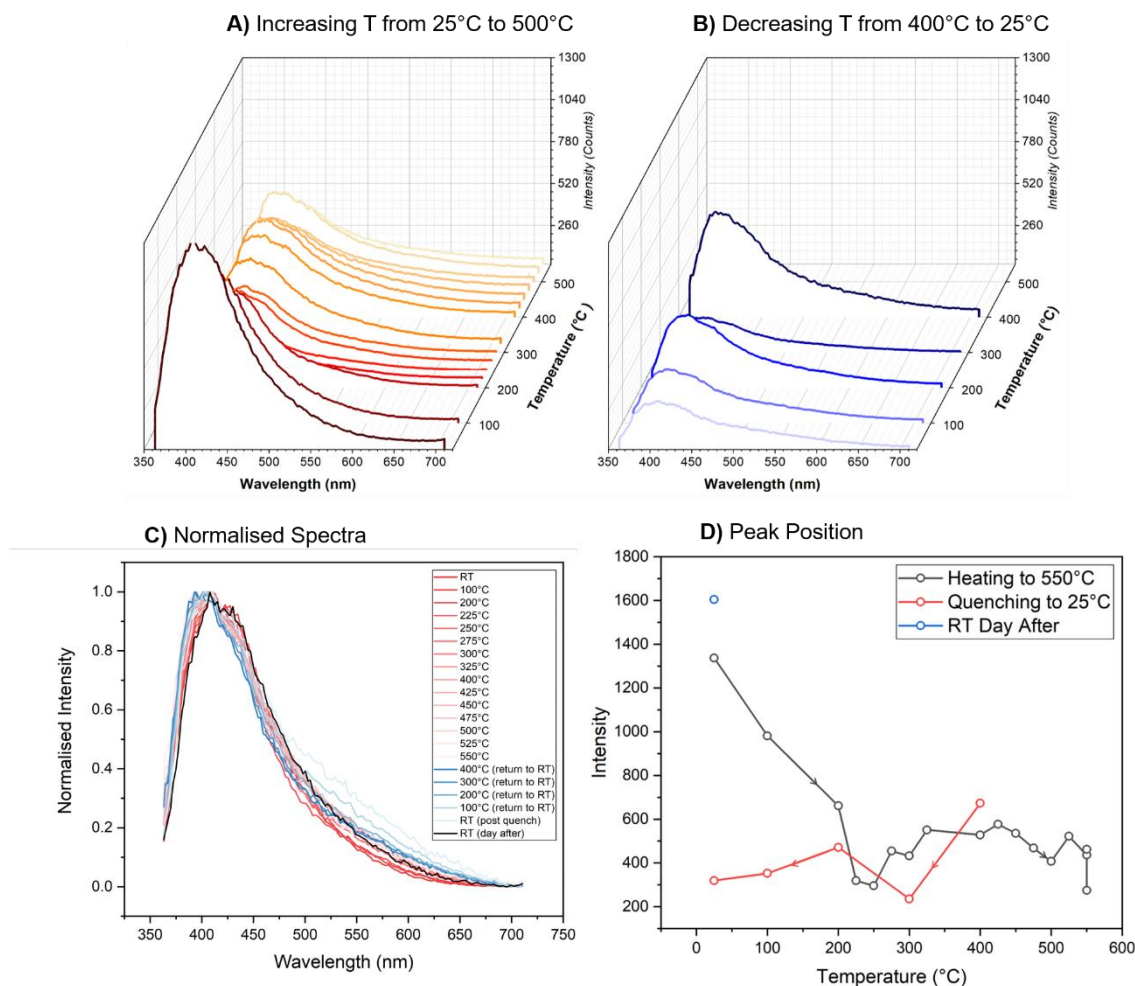


Figure 50 CW fluorescence emission spectra tracking the heating and quenching of a calcined silicon-rich SSZ-13 sample for A) sample heating from 25 to 550 °C, B) sample cooling from 550 to 25 °C, C) normalised spectra, and D) peak emission spectrum intensity plotted as a function of temperature for sample being heated to 550°C (black), quenched back to room temperature (red), and at room temperature one day after experimentation (blue) to demonstrate overall changes in emission intensity with evolving temperature.

A view of all normalised spectra in Figure 50C shows that most spectra overlay in a similar fashion, especially during the heating process where the room temperature and high temperature emission profiles occupy a similar position. The peak position does not shift dramatically except upon cooling where a small blue-shift of around 10 nm is evident. During the quenching process, the tailing edge of the spectrum appears to experience broadening, however at room temperature following quenching the spectra appears very similar to the original room temperature spectrum.

Compared to previous experiments, the emission spectra for silicon-only chabazite appears relatively narrow and is most similar to the calcined SSZ-13 sample studied in Chapter IV.

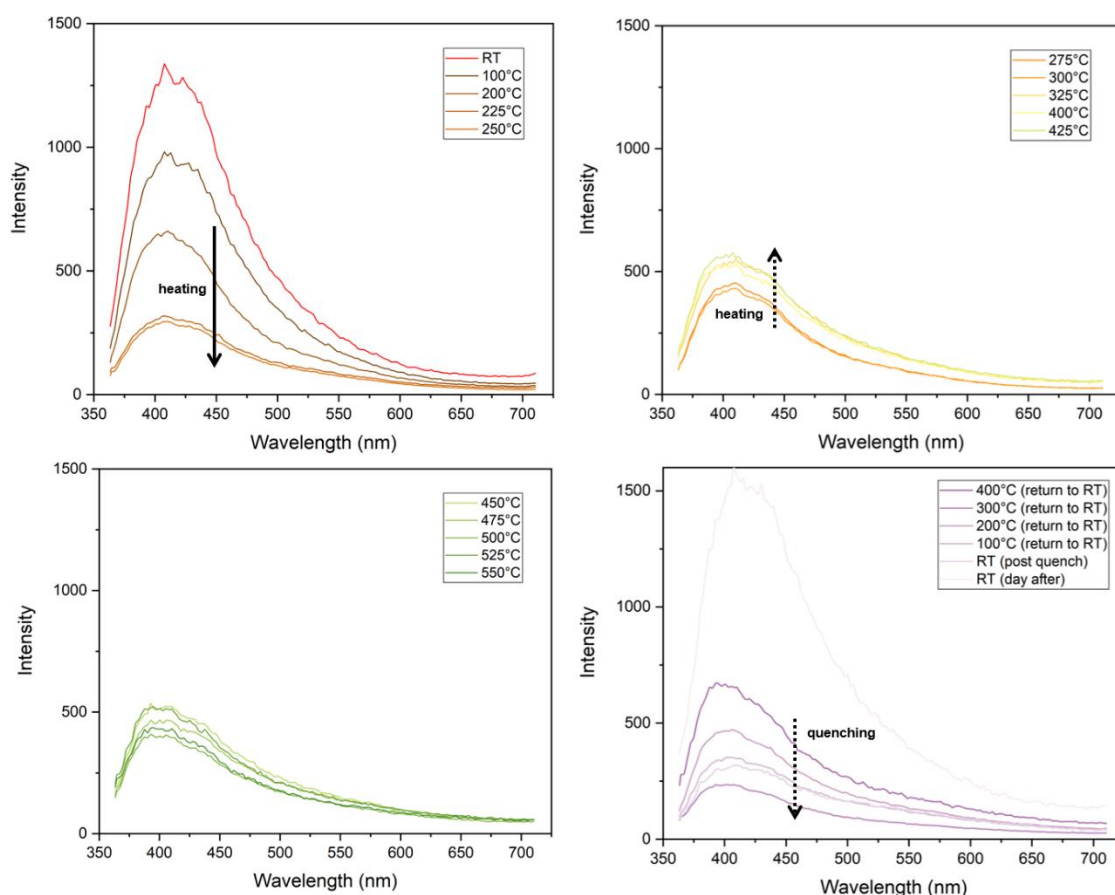


Figure 51 **Regions of activity**: A) Room temperature to 250 °C, B) 275 to 300 °C, C) 325 to 400 °C, and D) 450 °C

Figure 51A shows that between room temperature and 250 °C the peak intensity decreases in a similar fashion to what was observed in Section 3.1 and Section 3.2. Overall, it appears the dehydrating the sample reduces the emission intensity. Between 275 and 425 °C the emission intensity appears to increase slightly, and between 450 and 550 °C there does not appear to be any appreciable relationship between the change in temperature and change in emission intensity. Similarly, when quenching the temperature from 550 °C back to room temperature although there is generally a slight trend of decreasing emission intensity with decreasing temperature. A room temperature experiment acquired one day later after the sample had been exposed to atmosphere showed an increase in emission intensity comparable to the original room temperature measurement. Increase in emission intensity at room temperature here is likely related to hydration, given that zeolite frameworks are highly hygroscopic.

More so than any other *in situ* experiment, the silicon-only chabazite showed the greatest amount of reversibility in its emission behaviour following a heat treatment. This is particularly clear from the minimal change in the normalised spectral shape from the beginning to the end, and restored emission intensity. Additionally, during heating the sample exhibited the least number of

discernible trends with non-variable spectral shape and seemingly temperature-independent intensity behaviour. Further to this, between 350 and 450 °C there was no obvious jump in emission intensity like what has been recorded in other *in situ* experiments.

Table 16 Values of maximum peak intensity for Si-CHA heating experiment formulated as percentages of the maximum intensity of the original room temperature measurement and as a percentage of the maximum intensity of the previous measurement

Temperature (°C)	Comment	Max. Peak Intensity (a.u.)	Max Peak Position (nm)	Peak Height % of Initial RT Measurement	Peak Height % Difference of Previous Measurement
25	Original room temp	1337	412		
100		981	412	73	73
200		661	407	49	67
225		319	410	24	48
250		296	408	22	93
275		455	406	34	154
300		432	406	32	95
325		551	406	41	127
400		528	400	39	96
425		577	403	43	109
450		536	403	40	93
475		468	401	35	87
500		407	400	30	87
525		522	397	39	128
550		436	400	33	84
400	Quenching to RT	673	400	50	146
300	Quenching to RT	236	401	18	35
200	Quenching to RT	472	402	35	200
100	Quenching to RT	353	402	26	75
25	Quenching to RT	319	408	24	91
25	Day after	1604	412	120	502

4 Discussion

4.1 Initial Observations

Three *in situ* experiments monitoring the photoluminescence spectra of as-synthesised chabazite undergoing detemplation, as-synthesised chabazite undergoing a cyclic heating-quenching program, and a previously calcined silicon-rich chabazite sample undergoing heating. Figure 50 attempts to broadly compare these experiments by taking the peak emission intensity from each spectrum measured at each temperature and then plotting them together. Most striking in the comparison is the dramatic increase in emission intensity seen beyond 350 °C in the as-synthesised heating and quenching experiments. The effect is incredibly pronounced, with the peak intensity at these elevated temperatures reaching over 10 times that which is observed in spectra acquired at room temperature.

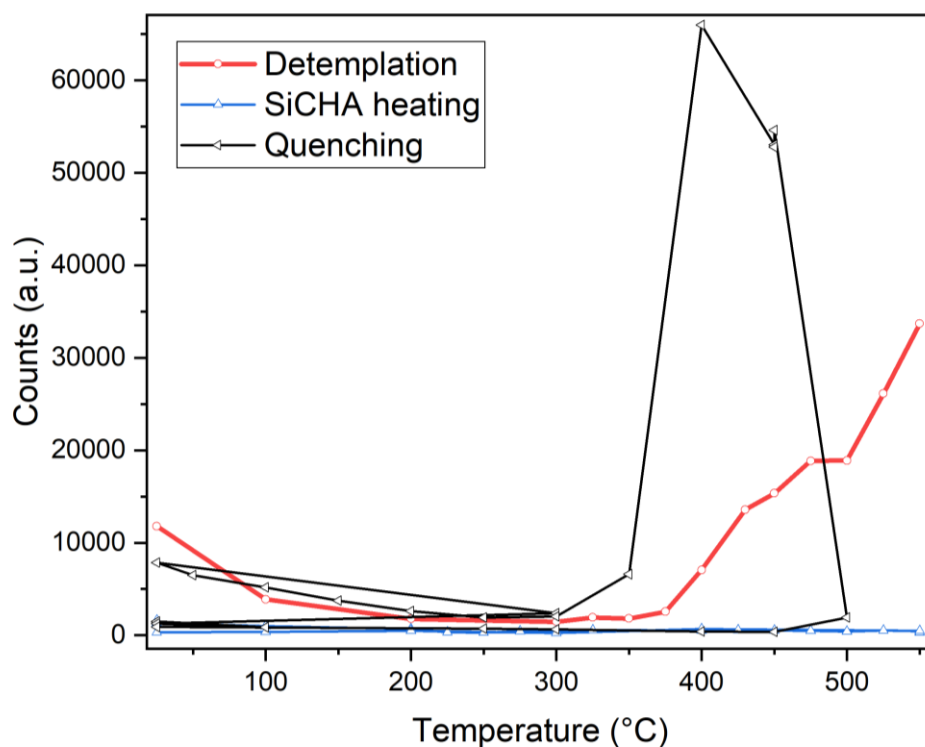


Figure 52 **Comparison of peak emission intensity** for detemplation of as-synthesised chabazite, cyclic *in situ* quenching of as-synthesised chabazite, and heating of silicon-rich chabazite

At first glance, it is reasonable to consider that most obvious difference between the samples exhibiting this high temperature response and the sample that does not is the presence of an occluded OSDA. In the previous chapter, the evolution of this OSDA following a period of pyrolysis has been shown to result in a changing emission spectrum. 350 °C might then be identified as the point at which emissive OSDA-derived PAHs and the like begin to proliferate, which in turn manifests as an increase in visible emission.

This course of reasoning is confounded, however, by the fact temperature is typically considered to be a significant collisional quenching mechanism⁹⁴ (see Chapter II). This has been shown to be the case irrespective of the origin of emission²¹⁶. Temperature is considered to be such a powerful quenching mechanism that 250 °C²¹⁷ frequently represents the upper extremity of the term ‘high temperature’ in the context of photoluminescence experimentation, with molecular origin fluorescence having been evidenced to quench at temperatures below even 100 °C^{218,219}. This is in stark contrast to the conventional understanding of ‘high temperature’ in the field of catalysis, which routinely subjects samples to thermal treatments in excess of 500 °C during the final step of preparation (i.e. detemplation), pre-catalytic activation, and catalyst regeneration. It is quite unexpected, therefore, to see such a pronounced photoemissive response in zeolite samples from 350 °C onwards, a temperature environment that would certainly be considered extreme from a fluorescence standpoint. Despite the focus on molecular origin luminescence from occluded template material in Chapter 3 at room temperature, it is not likely that the proliferation of carbonaceous species in the zeolite is solely responsible for the elevated emission observed during *in situ* experimentation²²⁰.

Our attention turns to the other significant difference between the two sample sets, which is the aluminium content of the framework. While the as-synthesised samples both have an SAR of 15 (see Chapter III), the silicon rich sample has an SAR of ∞ . The following section considers the implications of the presence of Al and discusses the possibility of high-temperature emission originating from the framework itself.

4.2 High Temperature Photoluminescence and Formation of Point Defects

4.2.1 Previous Evidence of High Temperature Photoluminescence in Zeolites

High-temperature proliferation of photoluminescence in silica-based materials has previously been reported, although in zeolite samples¹⁴ specifically the studies available are on this phenomenon are extremely limited. The most immediately relevant example is a paper by Bai et al.²²¹, which reports a strong broadband luminescence from zeolite samples subjected to high-temperature annealing, data of which is reproduced in Figure 53A & B. This experiment measured NH₄-FAU zeolites annealed at a series of high temperatures at room temperature with a 325 nm excitation source and showed an increasing photoluminescence signal between 500 and 550 nm from 100 to 500 °C. The plot tracking peak position with temperature in Figure 53B are similar to data collected in Figure 49. The emission is assigned to oxygen defects such as neutral oxygen vacancies, non-bridging oxygen hole centres, and interstitial defects. Of all the related studies,

¹⁴ Most photoluminescence studies of zeolites focus on photoluminescence arising from metal ion-exchange and pore-confined metal clusters.

this work bears the greatest resemblance to the data generated in this thesis; most specifically because of the use of a UV excitation source, the relatively featureless nature of the emission recorded, the peak position being still within the visible rather than NIR, and the intensity ratio as a function of temperature.

Mech et al.²²² also report a temperature-induced photoluminescence in their studies of Er³⁺ exchanged zeolite L whose emission spectrum is again attributed to the supposed introduction of oxygen vacancies, achieved by a three-step anneal at 200, 400 and 600 °C. The study includes the emission spectrum of an oxygen vacancy enhanced zeolite L recorded at 355 nm, which appears broadband and centred at 550 nm, and additionally claims that zeolite without induced oxygen vacancies do not exhibit photoluminescence. Although the similarity between the broadband emission spectrum presented and the data obtained in this thesis is notable, the paper itself is perhaps problematic in that it only presents samples borne of one type of annealing process and no emission dynamic from other sample preparations to compare against. There are also a few room temperature studies of zeolite films that, in a similar line of reasoning, attribute the photoluminescence observed to structural defects^{171,223}.

High-temperature photoluminescence is slightly more widely reported in non-zeolite silica-based materials^{195,224,225,226}. One noteworthy example is a study by Nakamura et al.²²⁷ who observe a similar behaviour in their study of annealed porous silicon powder. This study also captures a quenching behaviour at low temperature (see Figure 53D) similar to what is seen in the early stages of the detemplation and quenching experiments presented in this thesis (see Figure 46 & Figure 49). A similar trend is also reported by Li et al.²²⁸ and Cullis et al.²²⁹ This trend is attributed by Nakamura et al. to the formation of surface defects generated by hydrogen atom desorption, with re-emergent emission intensity at high temperature arising as a result of suppression of surface defects by oxygen passivation. In contrast to the results presented in this thesis, the peak intensity following annealing in these samples never exceeds the original room temperature intensity. This discrepancy may be related to the non-zeotypic nature of the silicon-based sample studied.

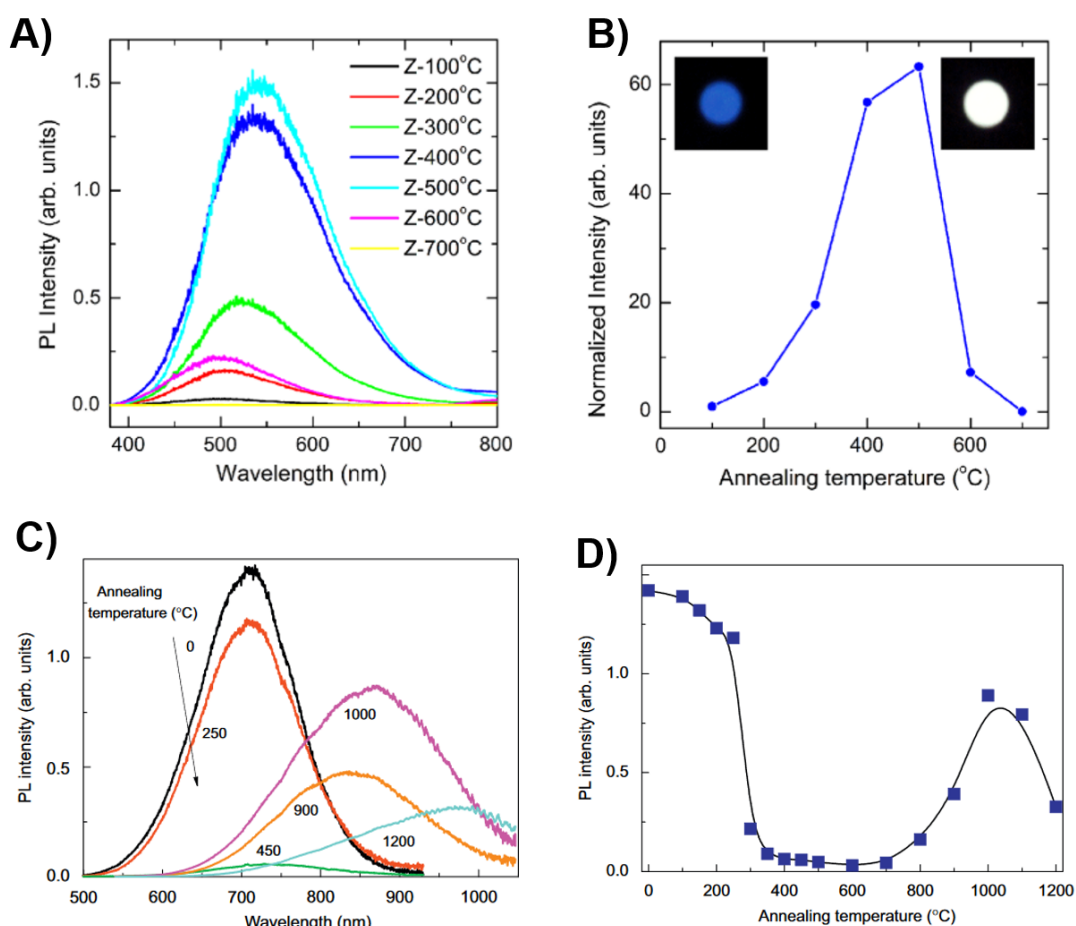


Figure 53 Photoluminescence spectra of annealed silica-based samples reproduced from literature: A) Photoluminescence spectra of zeolites annealed at temperatures from 100 to 700 °C and B) Peak position plotted as a function of annealing temperature. Reprinted from *Journal of Photoluminescence*, 145, Zhenhua Bai, Minoru Fujii, Kenji Imakita, Shinji Hayashi “Strong white photoluminescence from annealed zeolites”, 288-291 (2014) with permission from Elsevier²²¹; C) Photoluminescence spectra of porous silicon powder annealed at various temperatures and D) Peak intensity plotted as a function of annealing temperature. Reprinted from *Journal of Photoluminescence*, 4/6, T. Nakamura, T. Ogawa, N. Hosoya, S. Adachi, “Effects of thermal oxidation on the photoluminescence properties of porous silicon”, 682-687 (2010) with permission from Elsevier²²⁷

Another related effect is photoluminescence in crystalline silicon that is attributed to quantum size effects of the silicon structure itself rather than defect sites. Efficient visible light emission has previously been reported in crystalline silicon samples etched to achieve different structural features such as wafers preferentially oriented along particular crystal planes and quantum-confined silicon wires²³⁰. Tanaka et al.²³¹ considered this as a possible source of photoluminescence in their study of Si species trapped in zeolite pores alongside the contribution of aforementioned oxygen vacancies. Additionally, they collate numerical values for the photon energy values of different types of emission components, with 2.6 eV being assigned to oxygen defects, 4.0 eV to polysilanes in supercages, and 1.6 eV for silicon nanoparticles.

Defect formation, a common theme in the previous literature discussed here, presents itself as an interesting mechanism for high-temperature luminescence and its theoretical basis is explored further in the proceeding section.

4.2.2 Types of Oxygen Point Defects in Zeolites

In Chapter 1, a crystal was defined as a repeating structure based on a lattice with specific geometric requirements. In zeolites the lattice is defined by the tetrahedral co-ordination of Si^{4+} and O^{2-} atoms. A point defect occurs when there is an irregularity on a lattice point. Theoretically it is possible to have three types of point defects: vacancies, substitutions, and interstitials (see Figure 54). Further to this, defects can be considered as either intrinsic or extrinsic, intrinsic involving atomic species native to the material and extrinsic involving those that are chemically different to the host. Point defects influence the local energy arrangements of the regular host lattice through strain and the framework mutually exerts a stress on the defect. Due to the porosity and semi-ionic nature of zeolite bonding, a zeolite framework should be able to accommodate a relatively high number of point defects.

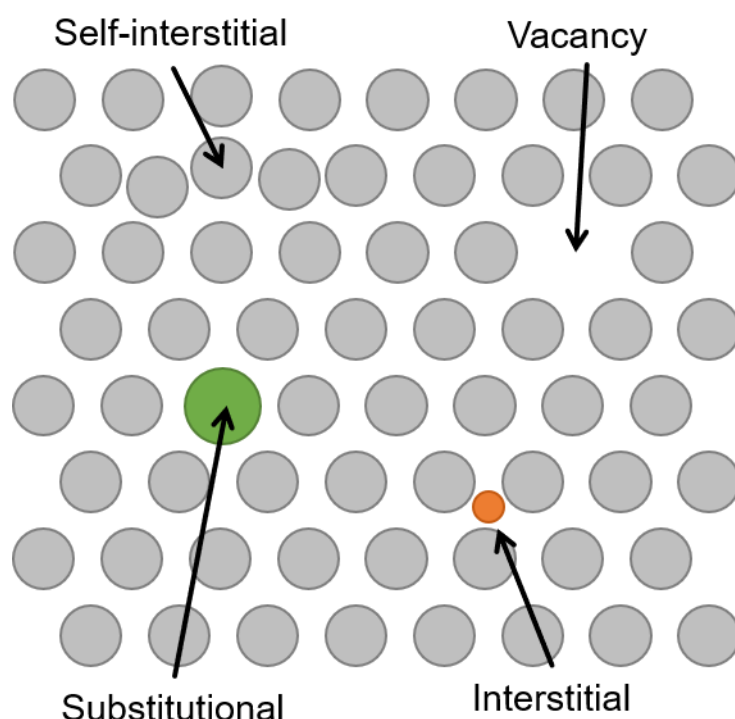


Figure 54 Point defect structures in solid crystalline materials including self-interstitials, which is termed as a Frenkel or Schottky defect in ionic structures when paired with a vacancy, substitutional defects, vacancies, and interstitial defects

Perspective depending, many aspects of zeolites could be considered point defects. For example, Al^{3+} could be considered an extrinsic substitutional defect on the Si site but is not always viewed as such as its presence is considered fundamental to the definition of a zeolite. Defects in SiO_2 have been studied since the 1950s and have been recognised to drastically alter electronic and optical properties of the material²³². Despite the commonalities between their structures, this is not so much the case in zeolites where the relationship between oxygen defect formation and optical properties has been shown thus far to be relatively under-discussed topic. This section will attempt to outline the types of possible oxygen point defects in zeolites, taking into account the

defect classification that has already been defined for SiO₂. Industrially applicable zeolites tend to feature higher Si:Al ratios, so due consideration of the SiO₂ defect model is not unwarranted.

Oxygen point defects are complex and usually formed via a combination of vacancies, interstitials, and substitutions. Five types of oxygen defects are summarised in Table 17 and Figure 55: the E' centre, non-bridging oxygen hole centres (NBOHCs), oxygen deficient centres (ODCs), self-trapped excitons (STEs), and interstitial oxygen. These features have all previously been detected as unique structures using electron paramagnetic resonance (EPR) or electron spin resonance (ESR) spectroscopy²³³. Most importantly, these selected defect structures, of which in practice there are more, are of interest for their visible photoluminescence properties. Formation of any of these vacancies is complex and will often happen in a multi-step process requiring defect precursors that is not always well understood. Some of these formation steps rely upon exposure to a highly energetic source of irradiation or elevated temperature.

Table 17 Summary of different types of oxygen point defects occurring in silica structures

Defect Type	Description	Notation	Dia-/Para-magnetic	Optical Bands
E' Centre	Unpaired spin in a dangling tetrahedral orbital of an under-coordinated Si atom. Variants of the defect type exist depending on the annealing process, nature of irradiation, and water content ²³⁴ .	$\equiv\text{Si}\bullet$	Para	<i>Absorption:</i> 5.85 eV or 211 nm ²³⁵ <i>Emission:</i> None
NBOHCs	Hole trapped on oxygen. May form from fission of a strained Si-O-Si bond or when H is radiolytically liberated from OH groups in wet silica ²³⁶ .	$\equiv\text{Si}-\bullet$	Para	<i>Absorption:</i> 1.97 and 4.8 eV ²³⁷ <i>Emission:</i> 1.91 eV or 649 nm ($\tau=20\ \mu\text{s}$) ^{237,238} 2 eV or 619 nm ^{237,238}
ODCs	Oxygen monovacancy when a bridging oxygen is missing. These are separate to E'-centers, which are also forms of ODCs. ODC(I) is a neutral vacancy formed of relaxed Si-Si bridge and ODC(II) is an unbonded, unrelaxed Si bridge. The origin of ODC(II) is unknown.	$\equiv\text{Si}-\text{Si}\equiv$ (I) $=\text{Si}\bullet\bullet$ (II)	Dia	<i>Absorption:</i> 5, 6.9, and 7.6 ^{239,240} eV <i>Emission:</i> 2.7 eV or 459 nm ($\tau=4\ \text{ns}$) ²⁴¹ 4.4 ²⁴² eV or 281 nm ($\tau=10.4\ \text{ms}$) ²⁴¹
STEs	When an exciton (i.e. bound state of an electron-hole pair) interacts with phonons suppressing the ability of the exciton to move through the crystal; a deformation of the lattice around the exciton. Potentially formed when Si-O bond ruptures and forms $-\text{O}-\text{O}^{233}$.	-		<i>Emission:</i> 2-3 eV or 619-413 nm ¹⁹⁸
Interstitial oxygen	Interstitial oxygen can occur naturally in high purity silica or can be generated by expelling	-		<i>Absorption</i> 4.8 eV or 258 nm <i>Emission:</i>

	O atoms from their usual sites into the lattice. Indications that atomic O is mobile at 400 °C ²⁴³			1.8-2.0 eV or 688-620 nm (depending on excitation λ) ²⁴⁴ 2.0-2.5 eV or 620-495 nm ²⁴⁵
--	---	--	--	---

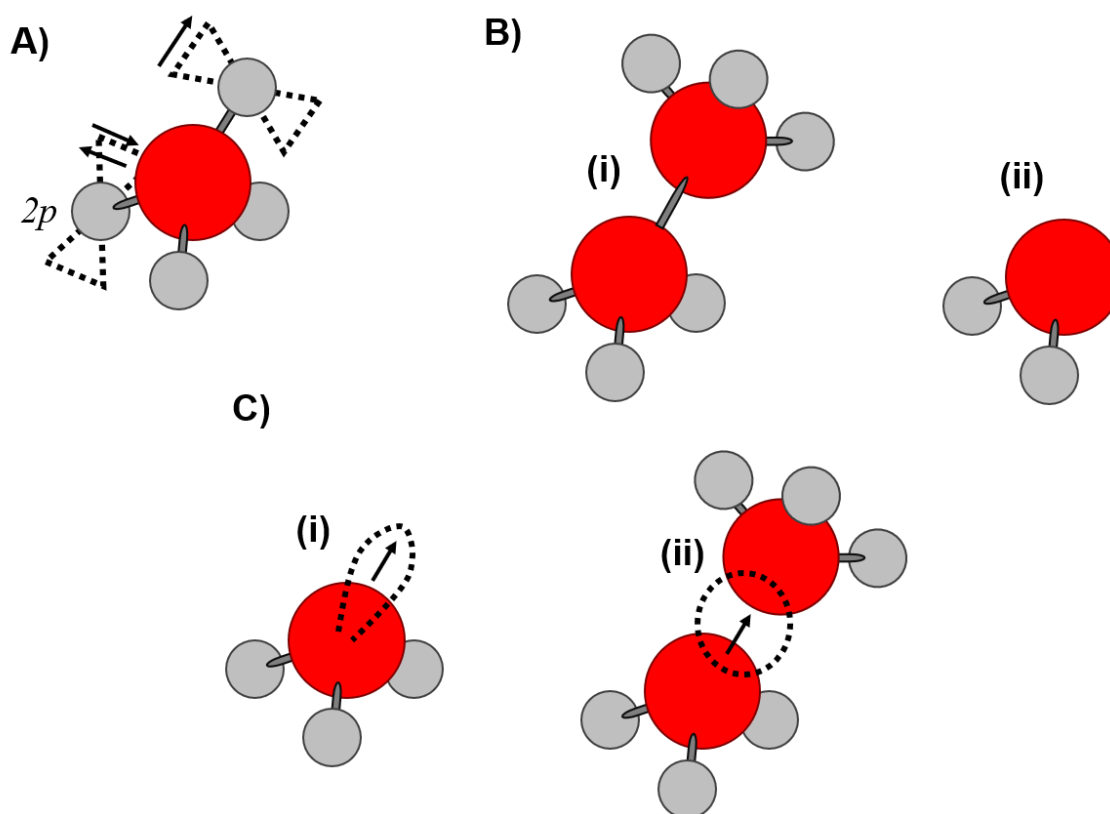


Figure 55 **Examples of different oxygen point defects in silica** where red atoms represent Si and grey atoms represent O, including a) non-bridging oxygen hole centres (NBOHC), b) oxygen deficient centres, and c) (i) E' and (ii) E' centres

4.2.3 Characterisation of High Temperature Point Defect Formation

Point defects, many of which have shown to be paramagnetic in the preceding section, have traditionally been best studied using techniques capable of discerning spin properties. The commonest example is nuclear magnetic resonance (NMR) spectroscopy as well as electron spin resonance (ESR) and infrared (IR) spectroscopy. Similar to data showing high-temperature photoluminescence, there are few studies relating directly to oxygen vacancy formation in zeolites although these studies exist extensively in the context of silica materials.

Density functional theory (DFT) modelling by Catlow et al.²⁴⁶ as shown in Figure 56 predicted that calcination could transform Brønsted acid sites into oxygen vacancies coupled with Al impurities in cluster model calculations based on siliceous chabazite. It was thought that two types of paramagnetic centres may form: one being an electron bound to Si next to the oxygen vacancy (i.e. E' centre) formed upon removal of OH⁻, and another being an electron hole localised on oxygens at the dehydrogenated Brønsted site. Pinpointing hole localisation was noted to be

challenging with simulations over one, two, three, or even four oxygen sites (both bridging and non-bridging) appearing to yield different types of electronic defects with a global energy minimum characterised by a three- or four- centre hole configuration. It was also implied that vacancy migration could lead to the formation of an ODC(II) defect.

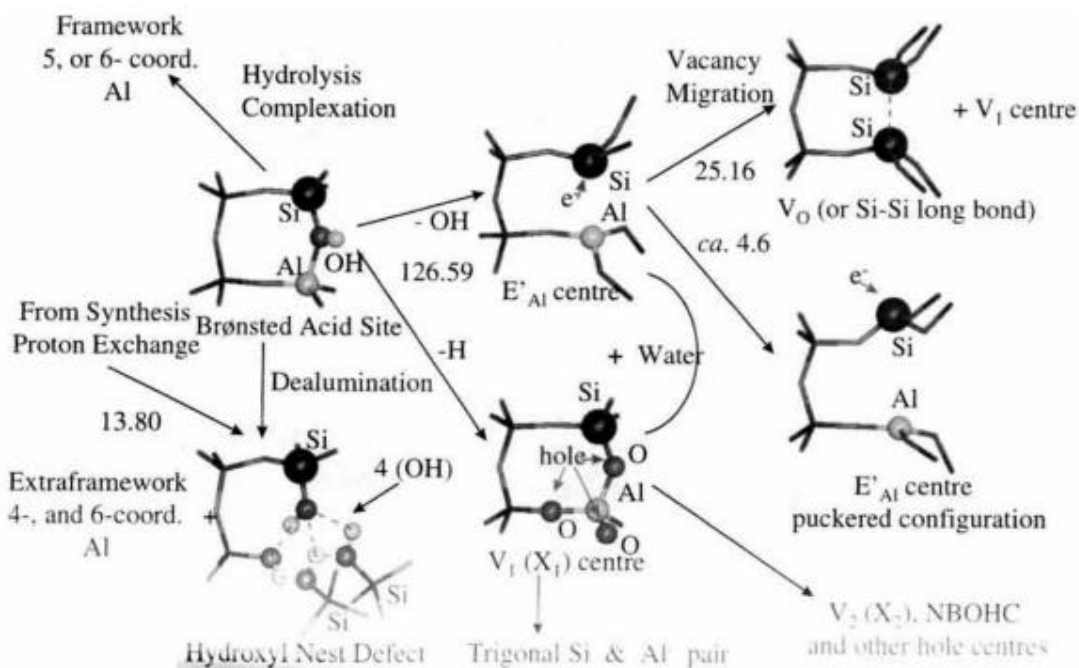


Figure 56 **Transformation of Brønsted acid sites.** Reprinted from Catlow *et al.*²⁴⁶ with permission from Taylor & Francis.

It is known that certain frameworks with particular silicon-to-aluminium ratios have been shown to be crystallographically stable up to 900 °C^{247,248}. However, a relevant question arising from theoretical modelling is whether the presence of oxygen point defects is even possible given that many of the bridging oxygen sites in question are critically important to the structural integrity of the framework. The possibility of a stable three-coordinate aluminium configuration within a zeolite has been proposed by Al K-edge XANES of mordenite and zeolite beta²⁴⁹. This study stated that at temperatures above 400 °C a portion of tetrahedrally coordinated aluminium converted to a three-coordinate species, which remained stable to room temperature, but converted back to tetrahedral aluminium after exposure to ambient atmospheric conditions. Al-EXAFS has also been used to show that aluminium maintains its position within the framework following thermal treatment²⁵⁰.

Dehydroxylation, the process by which Catlow *et al.* propose E' centre formation may occur in zeolites, has been shown to occur by FTIR studies²⁵¹. Yun *et al.*²⁵² summarised the following two pathways for dehydroxylation: heterolytic dehydroxylation by dehydration, and homolytic dehydroxylation by dehydrogenation. Similar to DFT modelling, they too propose that dehydrogenation leads to the generation of a hole localised over one of the aluminium-associated

oxygen sites²⁵³ using a combination of mass spectrometry-temperature programmed desorption (MS-TPD), electronic structure calculations, and XRD in SSZ-13.

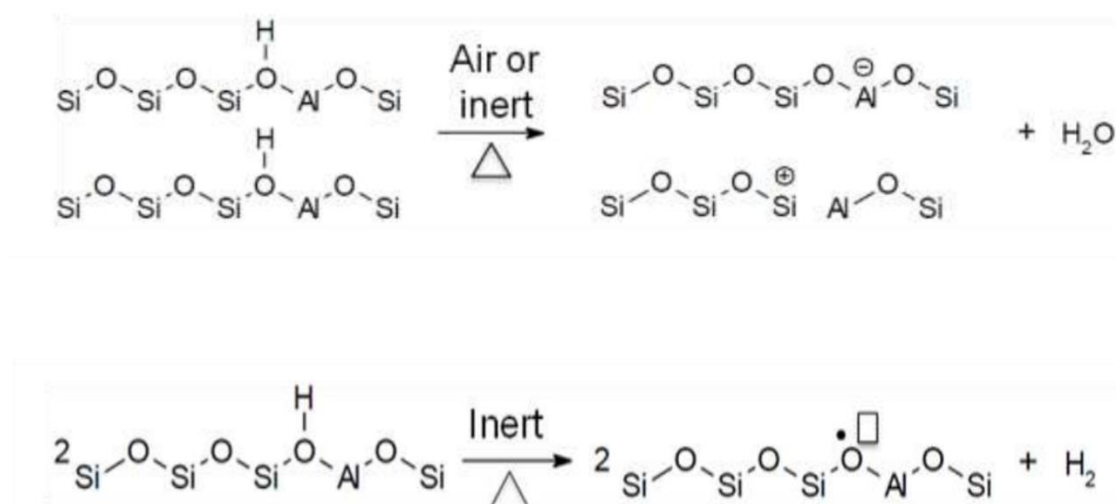


Figure 57 **Heterolytic (top) and homolytic (bottom) dehydroxylation pathway** reproduced from Yun et al.²⁵²

In situ experimental work by Balint et al.²⁵⁴ claimed to provide evidence for oxygen vacancy in MFI-type zeolite using ¹²⁹Xe-NMR and ac-conductivity studies. They too suggest that oxygen vacancies form in H-ZSM-5 via dehydroxylation at temperatures above 400 °C, although Bai et al. claim from their assignment of photoluminescence signal solely to oxygen vacancies that this defect formation is visible from as low as 100 °C. Their ¹²⁹Xe-NMR are corroborated with previous NMR studies that also conclude the formation of paramagnetic vacancies at high temperature²⁵⁵. Notably, they propose a kinetic model for the rate of vacancy formation during heating in an oxygenated environment, which is summarised in Figure 58. Up to 400 °C where dehydroxylation is low, a negligible rate of defect formation is assumed. From 500 to 600 °C, where dehydroxylation is thought to be occurring, they assume the formation of a diamagnetic oxygen deficient centre and propose the following rate constant for oxygen vacancy formation using Krogner-Vink notation:

$$K_{V_o^{\bullet}} = \frac{[h']^2}{\frac{1}{2} [Al'_{Si}] P(O_2)^{1/2}}$$

The aluminium ratio is used as a fixed rate limiter, which additionally implies that the concentration of holes is directly proportional to the rate of dehydroxylation (i.e. temperature).

At higher temperatures from 700 to 900 °C, they propose that the oxygen vacancies formed are re-incorporated with gas-phase oxygen to form paramagnetic oxygen sites with labile holes. Their model is interesting given that it is based on dynamic *in situ* data.

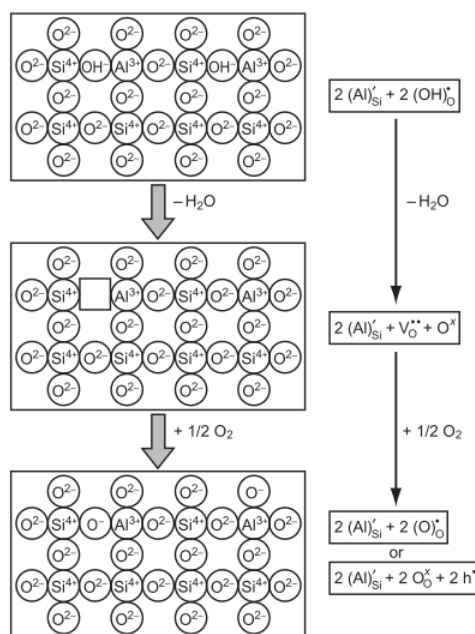


Figure 58 **Model describing formation of oxygen vacancies**²⁵⁴. Reproduced from Ref. 250 with permission from the PCCP Owner Societies.

4.2.4 Interpretation of Data Generated

The proliferation of emission intensity at high temperatures is thus attributed to the formation of oxygen point defects. The correlation is drawn based on the following arguments.

Firstly, a previous body of literature has demonstrated that lattice defects associated with oxygen sites in SiO₂ are capable of augmenting the optoelectronic response of the material. In particular, NBOHCs, ODCs, STEs, and interstitial oxygen all exhibit photoluminescent emission between 413 and 688 nm (see Table 17). It is interesting to note that the peak position recorded in high temperature spectra is 450 nm or greater, and that in the case of the detemplation experiment in Figure 48, with increasingly high temperatures (i.e. 500 °C and greater) the peak position is red-shifted to almost 550 nm. It should also be noted that photoluminescence spectra alone are not enough to discriminate between different types of defect structures as certain emission bands outlined in Table 17 have similar energies (e.g. NBOHCs and interstitial oxygen), and EPR or ESR are required for more detail.

Secondly, the existence of oxygen point defects within a zeolite structure has been shown to be feasible, and that dehydroxylation²⁵⁶ is at least one reasonable mechanism by which this might occur. Studies from a broad range of research areas all tend to support the idea that E' centres and oxygen deficiency centres are likely to preferentially form out of the dehydroxylation process. However, even with modelling and evidence of defects, it is still very difficult to know what the actual pathway of defect formation is.

Thirdly, the gated spectra confirm a definite evolution in the emission dynamics of the sample; namely that the longer living component undergoes both a red-shift and a lengthening of the

lifetime (see Figure 47) between 300 and 400 °C, indicating a new emission pathway is being established. Cross-referencing back to previous chapters, this is consistent with what was observed in Chapter 5's Figure 36 where the same behaviour was observed in both calcined and uncalcined (i.e. organic-rich) material.

Finally, the results of the Si-chabazite provide an interesting support to the idea that high temperature photoluminescence is generated by oxygen vacancies. Critical to models explaining oxygen vacancy formation is the negative charge of substituted Al^{3+} , which may be compensated by protons located on O^{2-} sites, oxygen vacancies in the absence of gas-phase O_2 , and O^- holes in the presence of a gas phase. OH^- groups are predominantly extant in the framework as a result of Al^{3+} requiring charge compensation, meaning that vacancy concentration is generally related to the Si:Al ratio of the zeolite. The absence of Al^{3+} in silicon-only chabazite therefore means many of the preferential oxygen vacancy sites are no longer available, partially explaining why at high temperature the silicon-only chabazite experiences minimal changes in emission intensity and spectral shape. As demonstrated in Figure 50, the silicon-only sample only really experiences significant emission intensity changes in the early stages of the heating process and at 24 hours after the experiment following exposure to the atmosphere. More clearly evident in the comparison in Figure 59, the silicon rich sample also does not experience a change in peak position with increasing temperature, and retains a similar profile to its room temperature spectrum, compared to the higher aluminium-content sample, which experiences a change in spectral profile at high temperature.

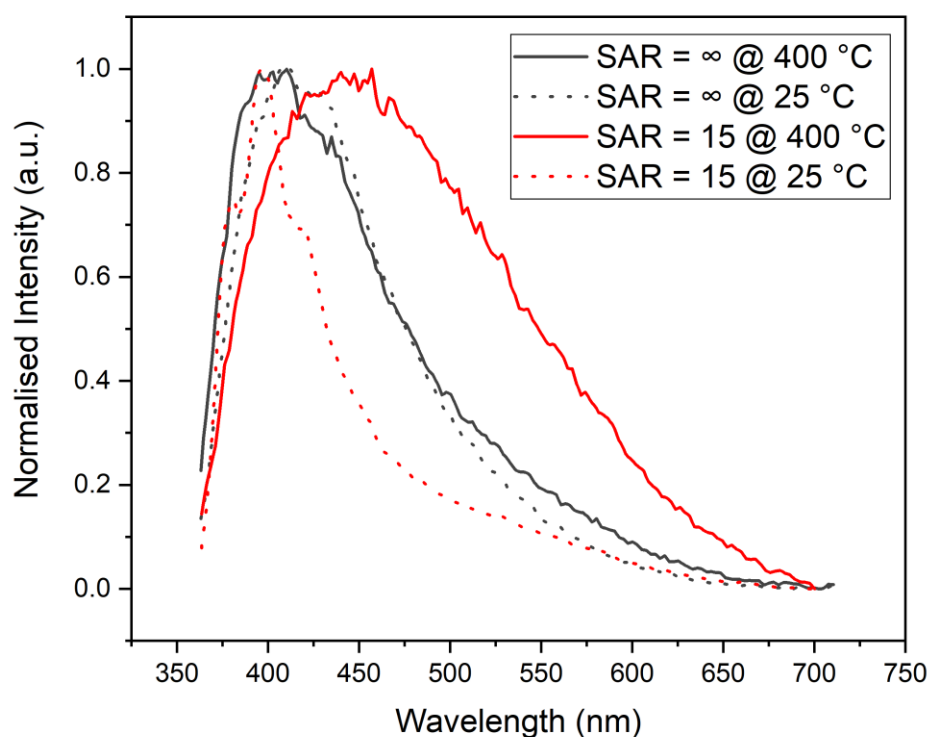


Figure 59 **Comparison of high temperature spectra recorded at 400 °C** for silicon-rich SSZ-13 (black) and as-synthesised SSZ-13 with an SAR of 15 (red)

Thus, high temperature experimentation may be providing direct evidence of point defect formation. Table 17 identified that oxygen deficiency centres, non-bridging oxygen hole centres, self-trapped excitons, and interstitial oxygens feature photoluminescence bands in the same region as exhibited in the recorded spectra. Up till 200 °C, it is not expected that the emission spectrum generated is arising as a result of oxygen defects. This is because the spectral features have previously been analysed and assigned to the presence of occluded organic template material. Additionally, from the discussion preceding this, previous studies on oxygen point defects tend to identify 400 °C as the temperature at which oxygen point defects are likely to form, whether by dehydroxylation, annealing or otherwise. Based on the intensity dynamic in Figure 46, it could be argued that the first emission spectrum with contribution from oxygen defect emission is not visible until 400 °C when the peak intensity starts to rise. Additionally, gated spectra from 400 °C onwards have the greatest amount of similarity with each other compared to gated spectra measurements from room temperature to 300 °C, which still appear to have varying components. Between 400 and 550 °C, the emission intensity appears to rise almost linearly in line with Balint et al.'s prediction that vacancy formation increases linearly with increasing temperature. In combination, this could reasonably be interpreted to mean that the emission spectrum for 400 °C onwards is depicting the presence of oxygen point defects.

The silicon-only chabazite experiment raises interesting considerations regarding the nature of an ‘intrinsic’ framework photoluminescence signal. With its peak position unwavering at around 410 nm or 3.0 eV, perhaps this is simply photoluminescence somehow arising as a result of the complex structural configuration of the framework itself, or perhaps it is arising as a result of a different type of point defect^{257,258} formed with statistical inevitability in the siliceous framework during synthesis rather than by high temperature heating. Either way, the more practically inclined may be satisfied to accept simply that the framework itself practicably carries an intrinsic photoluminescence that may require due acknowledgment in spectroscopic studies.

High temperature emission mechanisms provide interesting avenues of thought in further *in situ* experimentation. Certainly, greater understanding of these proposed defect structures would be gleaned with complimentary ESR studies. Beyond this, the lifetimes associated with these structures, which can be long in the case of singlet-triplet transitions, could be used to monitor the formation of defects during *in situ* lifetime analysis studies.

4.3 Quenching Effects

4.3.1 Dehydration

One of the most consistent observations across all experiments is the decrease in emission intensity at low temperatures¹⁵, and its reversible increase in emission intensity following exposure to atmosphere. That this phenomenon appears to be reversible with exposure to atmosphere implies that dehydration may be partially responsible. At first, this may seem counter-intuitive as it is generally assumed that water acts as a quencher reducing the photoluminescence efficiency of a system^{259,260}, although admittedly, this is only a generic summation, the veracity of which may not necessarily hold true in all environments.

In the study of reversible hydration photoluminescence behaviours in inorganic materials, there are studies in similar systems that report the opposite effect (i.e. an increase in photoluminescence following dehydration). This is the case in a study of Zn/Al layered double hydroxide nanoplatelets²⁶¹, a historical study of Cu- and Ag- exchanged zeolites¹³⁹, and a study of terbium-exchanged MFI zeolite²⁶², among others.

However, there also exist studies on Ag-exchanged zeolites that seem to show a similar photoluminescence response to dehydration as what has been observed here. A study of LTA(Li)-Ag zeolites showed an intense blue emission in its partially hydrated state and a green emission in its fully hydrated state²⁶³. Perhaps most relevant is a study by Lin et al.²⁶⁴, which discusses the illumination mechanism of Ag⁺ clusters in relation to a hydrated/dehydrated zeolite environment

¹⁵ Note that in the MTO experiment between room temperature and 550°C in Figure 63 the emission intensity appears to increase. This is rather due to the high temperature phenomenon discussed in Section 4.1.1.

and reports that dehydration is responsible for the decrease in emission intensity and the formation of a new peak at a different wavelength. The emission intensity is recovered once the sample is rehydrated. An important difference here is the inclusion of Ag, which are well known luminophores and will follow a very different emission pathway to the samples presented here. However, they postulate that H₂O molecules may be co-ordinating with Ag⁰ atoms and the zeolite framework to participate in the emission process and yield a unique photoluminescence spectrum. Although metal-ions are not present in any of these samples, organic adsorbents are and it may also be postulated that in a framework noted for its abundance of negative charge centres, H₂O is also participating by acting as a pathway through which charge transfer process may be facilitated.

4.3.2 *Thermal Quenching*

An alternative explanation to dehydration-related quenching may also be thermal quenching. This may be the case where the original room temperature signal appears to be convoluted with the Raman feature of water as is the case in Section 3.1.1. The depletion of the water Raman band with dehydration initially gives the appearance of a much more drastic emission decrease. Further decrease in emission intensity at 200 and 300 °C may then instead simply be arising as a result of thermal quenching, which is still the traditionally expected emission response to temperature (in spite of the discussion in Section 4.1.1), rather than the loss of a water facilitated emission pathway. This may be further supported by the quenching experiment in Section 3.2 where the measurements at room temperature and 100 °C feature presence of a water Raman peak at 396 from where the sample has not been held at 100 °C long enough for water to be removed. In this case, changes in emission intensity are still visible, implying that here these might be only temperature dependent.

Part B. Methanol-to-Olefins Reaction

5 Method

The calcined zeolite was first activated at 550 °C prior to experimentation. This is a standard procedure to remove adsorbed organics and water from the sample. Activation was achieved by starting a flow of synthetic air at 60 ml/min to the sample and ramping the sample to 150 °C at 2°C/min and holding it for 30 minutes. The sample was then brought up to the target temperature of 550 °C at a rate of 3 °C/min and held at temperature for 1 hour. After activation, the sample was brought back down to 100 °C. Synthetic air flow was stopped, and inert gas flow was begun at 30 ml/min, leaving the system for another 30 min for inert gas to equilibrate in the lines.

To begin the MTO reaction, the methanol syringe pump was switched on, injecting methanol at a rate of 1.6 g MeOH/ g cat. h into the system alongside inert gas flow. The system was maintained at 100 °C to allow methanol to equilibrate for 30 minutes. Temperature was ramped up to 450 °C at 1 °C/min. An EcoSys-P mass spectrometer (European Spectrometry Systems, Northwich) was used to monitor products travelling from the exhaust line.







6 Results

6.1 Visual Changes

The methanol-to-olefins experiment was repeated twice (see Figure 60) under the same conditions (see Section 2.2.2). Visual changes in the sample are recorded in

Table 18. For both experiments, trends in peak intensity and spectral shape were roughly subdivided into three regions of activity as shown in Figure 61 and Figure 62.

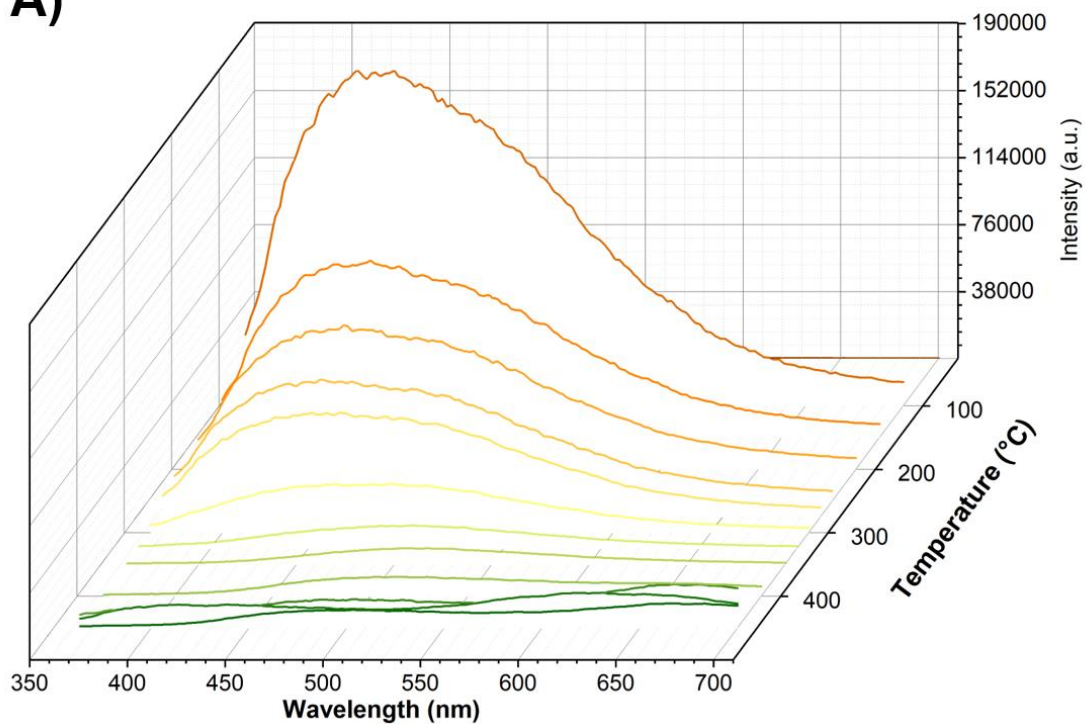
Table 18 **Visible changes in sample as a function of temperature during methanol-to-olefins reaction** for two experimental repeats under same experimental conditions including photographs

Temperature (°C)	Visual changes	
	Repeat 1	Repeat 2
Room temp to 200	White powder	
		
250	Sample starting to turn green	Sample light green around edges
		
300	No notes recorded	Light green across whole sample
		
350	Sample darkening to olive yellow	Olive green
		
375	No notes recorded	Olive green with dark ring around edge
		
400	Rapid colour change beginning	

450	No notes recorded	Very dark green with black ring around edge
550	Very dark green	Very dark green/black across sample

6.2 Continuous Wave Spectra

A)



B)

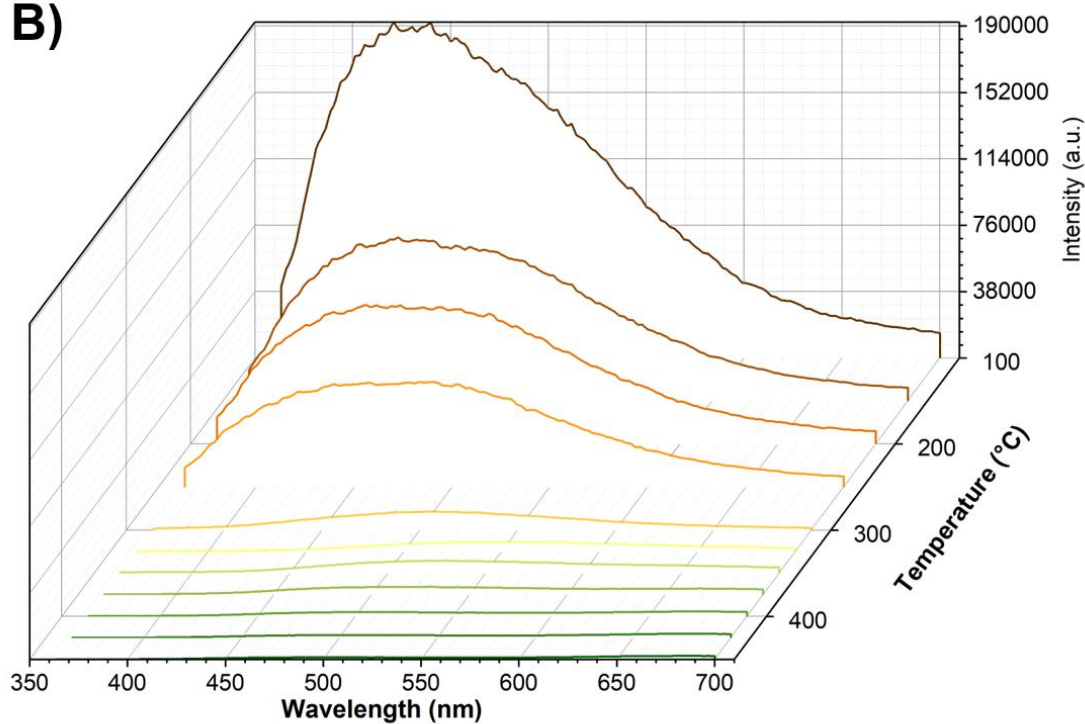


Figure 60 CW fluorescence emission spectra tracking the methanol-to-olefins reaction over activated H-SSZ-13 for A) experimental repeat 1, and B) experimental repeat 2

Figure 61A shows the sample at room temperature prior to activation and at 550 °C after 2 hours of activation. The 550 °C spectrum is similar to the high temperature spectra presented in the *in situ* detemplation experiment in Section 3.1.1. Most similar is the large increase in emission intensity demonstrated between the room temperature and high temperature measurement, in this case a 4-fold increase (see Table 19), and the significant broadening of the spectral profile.

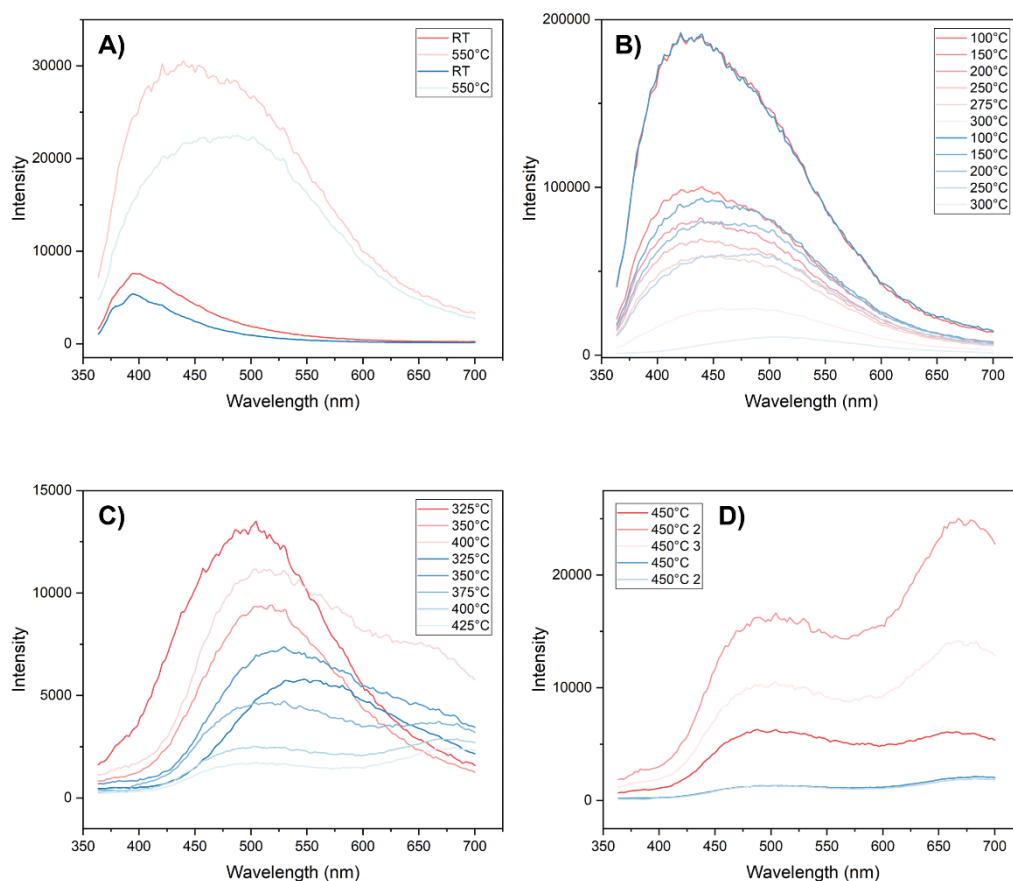


Figure 61 **Three proposed regions of activity in the MTO process** for experimental repeat 1 (red) and 2 (blue): A) Sample activation, B) 100 to 300 °C, C) 325 to 400 °C, and D) 450 °C

Figure 61B shows the first proposed region of interest during the MTO reaction. This region is characterised by a broad spectral profile and a general trend of decreasing emission intensity. Upon dropping the temperature to 100 °C and introducing methanol the emission intensity increases to a peak value over 9 times that of the emission intensity at 500 °C. As the temperature is increased through to 300 °C, the intensity decreases again to a level comparable with the original 550 °C pre-methanol spectrum.

The second proposed region of interest between 325 and 425 °C is shown in Figure 61C. Compared to the previous region of interest, the overall emission intensity is much lower, which corresponds with the overall darkening of the sample (see

Table 18). The main peak has also further red-shifted with increasing temperature from around 464 nm at 300 °C to around 500 nm at 350 °C in experimental repeat 1. This region of interest features the emergence of a second emission band in the red. In both experimental repeats, the average position of this second band appears at around 670 nm (see Figure 62C). In the first experimental repeat, the band does not appear until 400 °C but in the second experiment evidence of the band can be seen from 325 °C.

It is likely that this band can be explained by the formation of new reactant products in the MTO reaction.

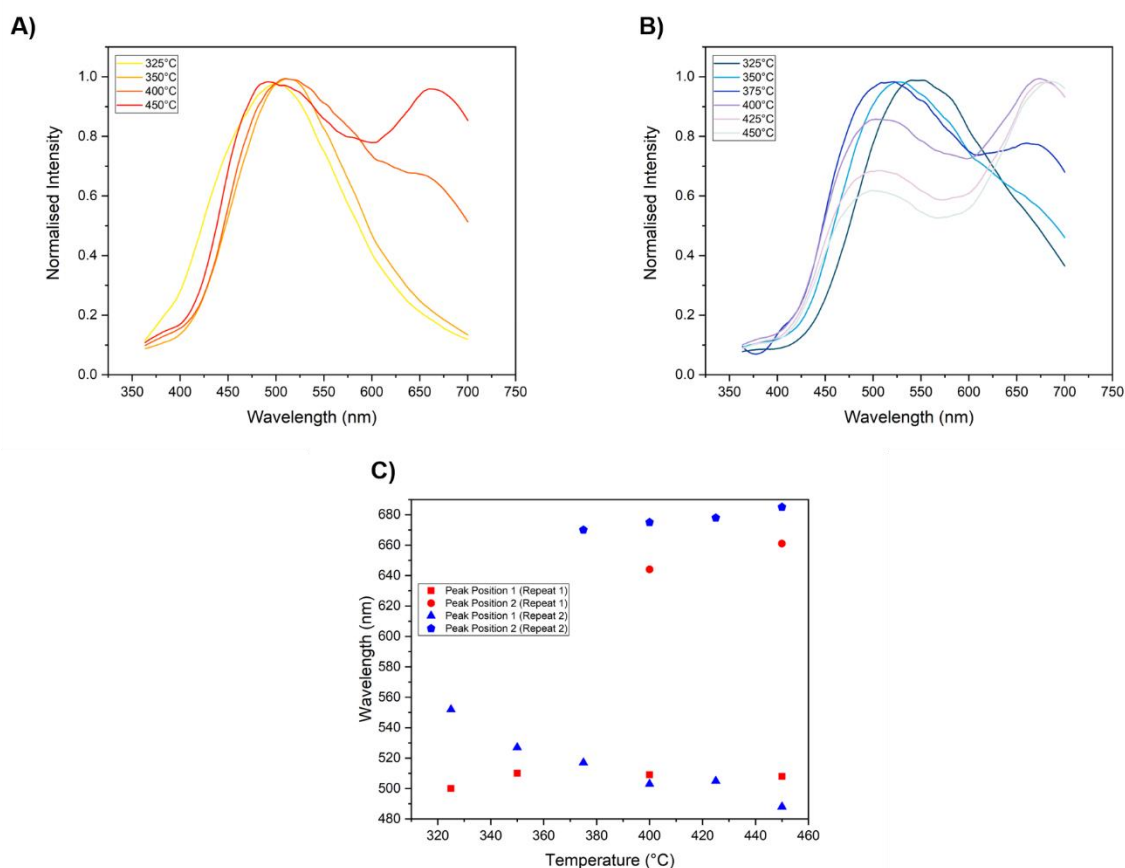


Figure 62 **Data analysis for MTO spectra between 325 and 450 °C:** A) Normalised spectra smoothed with a 30-point Savitsky-Golay filter; B) Changing peak positions with temperature

The final proposed region of interest is at the target temperature of 450 °C, as shown in Figure 61D. Although there is significant similarity in the normalised spectra at this temperature (see Figure 62A & B) there is a discrepancy in the emission intensity, with experimental repeat 1 showing a maximum intensity almost three times that of experimental repeat 2 (see Table 19). That being said, in terms of an overall trend both repeats show that the intensity at 450 °C relative to previous temperatures is behaving similarly, with the experiment appearing, overall, to be quite reproducible (see Figure 63). Differences can be reasonably attributed to the heterogenous nature of catalysis, and the fact that it is almost impossible to perfectly replicate any catalytic reaction.

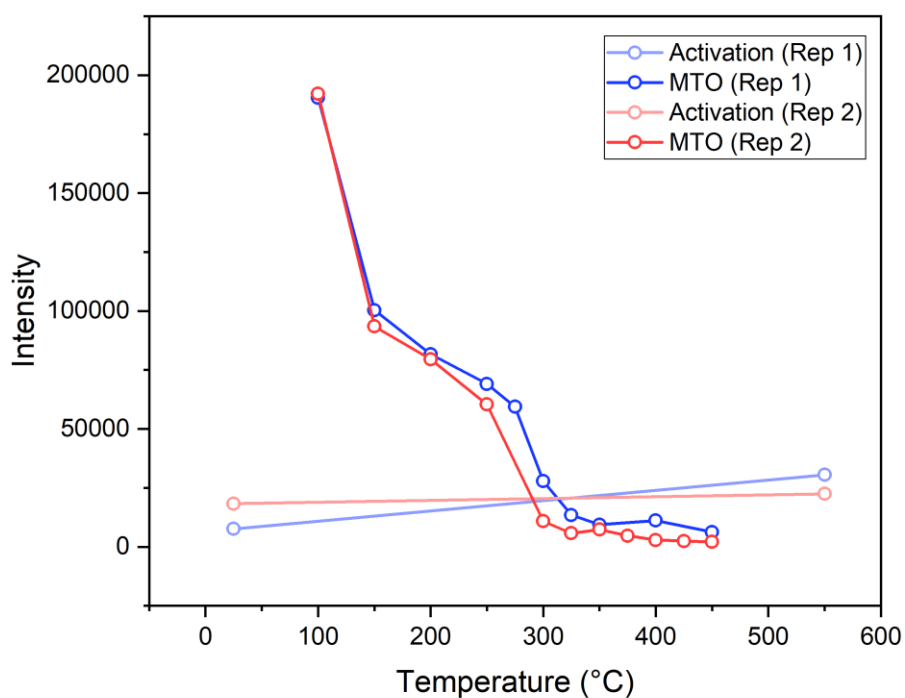


Figure 63 **Peak intensity tracked as a function of temperature for MTO reaction** for experimental repeat 1 (blue) and repeat 2 (red)

Table 19 **Values of maximum peak intensity for in situ MTO experiment** formulated as percentages of the maximum intensity of the original room temperature measurement and as a percentage of the maximum intensity of the previous measurement. Asterisk (*) refers to position of the secondary non-maximal peak emergent at higher temperatures.

Temperature (°C)	Max. Peak Intensity (a.u.)		Max Peak Position (nm)		Peak Height % of Initial RT Measurement		Peak Height % Difference of Previous Measurement	
RT	7579	5370	395	395	-	-	-	-
550°C	30536	22491	445	475	403	419	403	419
100°C	190456	192199	430	427	2513	3579	624	376
150°C	100337	93523	432	444	1324	1742	53	55
200°C	81663	79581	435	444	1078	1482	81	55
250°C	69072	60395	435	480	911	1125	85	53
275°C	59400	-	435	-	784	-	86	-
300°C	27825	10883	477	508	367	203	47	12
325°C	13503	5802	500	548	178	108	49	51
350°C	9407	7363	514	525 (664*)	124	137	70	56
375°C	-	4711	-	515 (667*)	-	88	-	43

400°C	11164	2884	500 (663*)	670 (514*)	147	54	119	53
425°C	-	2462	-	678 (505*)	-	46	-	55
450°C	6293	2125	674	678 (504*)	83	40	56	86

6.3 Mass Spectrometry

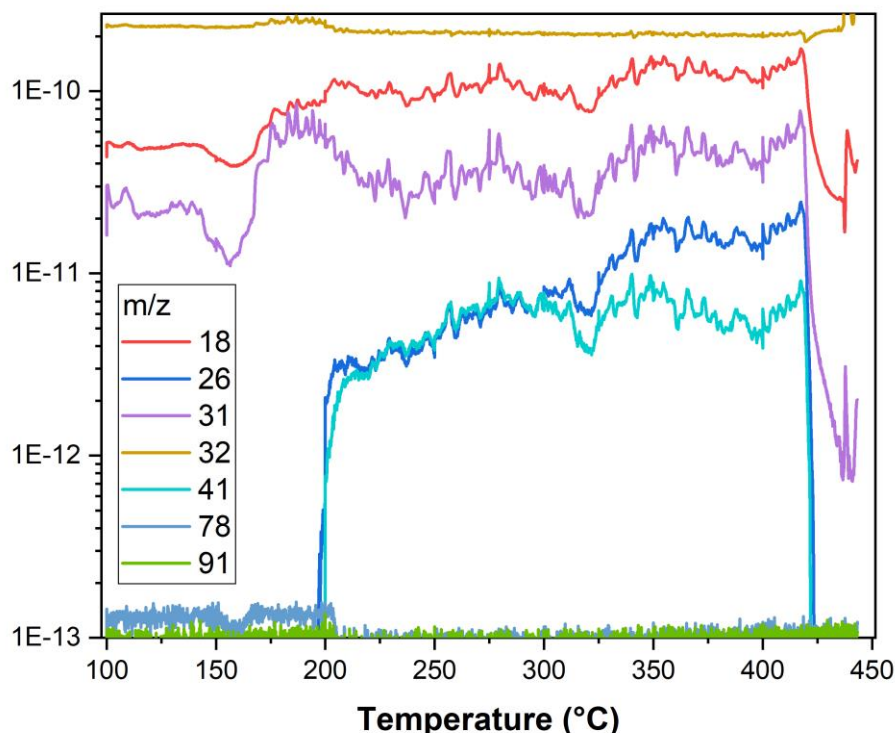


Figure 64 **Mass spec trace from in situ MTO experiment** monitoring chemical species present in the exhaust line from the Linkam cell

Figure 64 shows mass spectrometry data presented from the point at which methanol was introduced into the system, evidenced by the trace for $m/z=32$. Data collection was compromised prematurely at 425 °C. Formation of heavier products including masses 26 corresponding to C_2/C_3 hydrocarbons and 41 were seen to emerge at 200 °C and grow with increasing temperature. Formation of benzene ($m/z=78$) and toluene ($m/z=91$) were not observed in significant amounts.

7 Discussion

7.1 Product Formation Leads to Quenching at High-Temperature

In the previous section, a proliferation in emission intensity and a pronounced band in the red region at high temperature were attributed to the formation of point defects. In these studies, a

different relationship between emission intensity and temperature is observed. Rather than continuing to increase with temperature, in the MTO experiments the peak emission decreases with temperature and begins to exhibit an evolution in the emission structure as shown in the comparison in Figure 65.

In this system, it is known that organic species are actively forming as a result of a catalytic reaction that is being fed ample volumes of methanol. It follows that changing colour of the sample is accompanied by a decrease in emission intensity.

Quenching due to the adsorbed organic phase could be due to collisional quenching, from an increased concentration of product, or self-absorption due to the darkening of the sample.

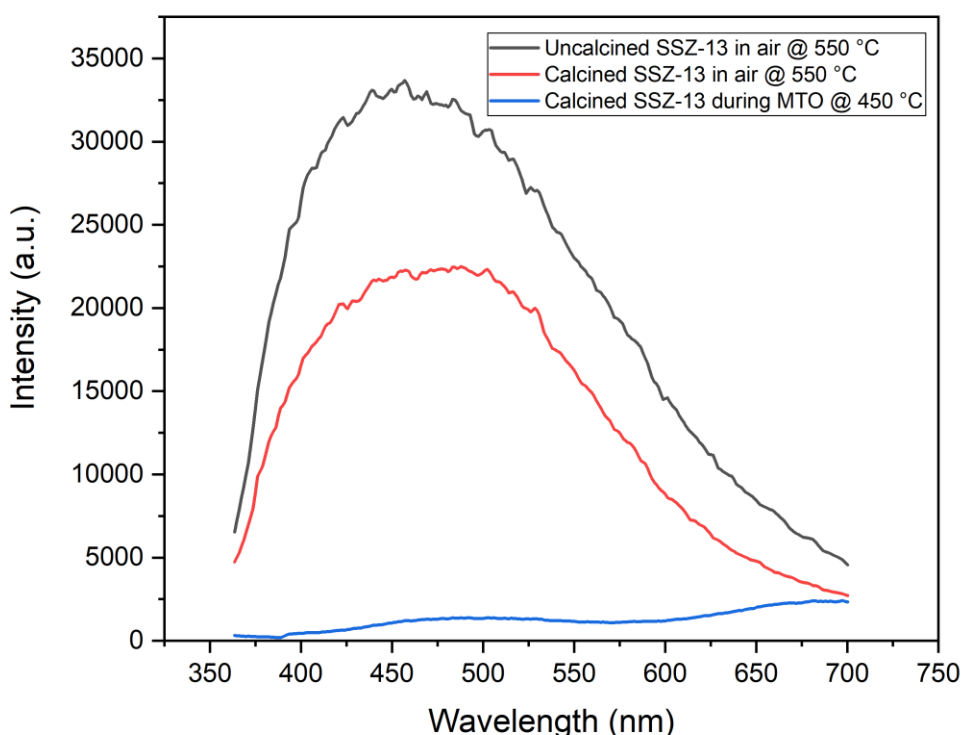


Figure 65 **Comparison of photoluminescence spectra acquired at high temperatures** including uncalcined SSZ-13 in air at 550 °C (black; from detemplation experiment in Part A), calcined SSZ-13 in air at 550 °C (red; from the activation period of the MTO reaction), and calcined SSZ-13 during the MTO reaction at 450 °C (blue)

7.2 Evolution of Band Structure due to Product Formation

In the MTO reaction it is expected that new products will be formed throughout the reaction. The compositional change of the adsorbed species appears to be responsible for both quenching and increasing the emission intensity at different stages of the reaction. Table 20 broadly summarises the different stages of the MTO process, listing products that are expected to form at certain temperatures when performed over a CHA topology zeolite. These products have been confirmed in spectroscopic *operando* studies using UV-vis, Raman, and IR spectroscopy^{203,265}.

Table 20 Summary of the different stages of the MTO reaction in CHA topology zeolites including what products are expected to form with approximate temperature ranges²⁰³

Stage		Description	Products Expected
1	Equilibration & Induction (<250 °C)	Following methanol adsorption at 100 °C, dimethyl ether (DME) forms. Dehydration	DME
2	Autocatalysis (250-300 °C)	Period of active hydrocarbon pool catalysis. Secondary reactions diversify initial olefinic product into more hydrocarbon types.	250-260 °C: Olefinic species, minor amount of aromatics 270-280 °C: Alkyl-substituted benzenium ions, naphthalenes, dienyl carbocations, ethylene, propylene, butylene 290-300 °C: Polyenes Methylbenzenes
3	Deactivation (300 °C<)	Catalyst begins to deactivate (i.e. reduced methanol conversion)	320-450 °C: Polycyclic aromatic carbocations*, methylbenzenes, methyladamantanes, methylnaphthalenes Phenanthrene derivatives Pyrene Graphitic coke

Below 300 °C, the emission spectrum still bears some shape similarity to that recorded in the experiments of Part A. For this reason, the spectra in this temperature range are disregarded, as it is not certain whether these are due to catalytic product formation. Additionally, the main $\pi \rightarrow \pi^*$ absorption for simple alkenes is at wavelengths below 200 nm. Therefore, it is not expected that characteristic photoluminescence spectrum for any early olefinic species would be observed. From 300 °C, however, the fluorescence intensity appears to be quenched, demonstrating a new behaviour to what was observed in Part A. From this point onwards, the emission signature is therefore primarily attributed to product speciation. At 300 °C, a single peak is visible at 500 nm and a secondary emission peak at 650 nm emerges after 350 °C. By 450 °C, a visible peak at 675 nm is extant. These temperatures correlate with the middle of the active hydrocarbon pool process and proceed into the deactivation stages of the overall reaction.

As discussed previously, it remains the case that the emission properties of fluorophores forming during the reaction will be affected by the chemical environment posed by the framework. It is not possible for us to experimentally reproduce zeolite material loaded with only one type of confined fluorophore with the view to create a control or comparator, for example, as it is sterically impossible to force them into the framework. Therefore, direct comparisons should not necessarily be made between literature measurements of chemical standards and those measured from within the zeolite. Of the list of products expected to form around 300 °C, methylbenzene (or toluene) excited at 266 nm has a fluorescence maximum at 280 nm, which has been shown to shift to the red with elevated temperatures at a rate of around 2 nm per 100 K^{266,267}. Polycyclic

aromatic hydrocarbons, which are known to form at temperatures in excess of 350 °C, are well known to be fluorescent. Assignments are on this topic discussed in greater depth in Chapter VII. It is likely that the band at 650 nm is due to PAHs.

As an example, the proliferation of graphitic or amorphous carbon species, for example, is likely to cause a degree of quenching as they are generally not emissive and will also cause self-absorption owing to their dark colour. Raman spectra of a zeolite quenched partway through the detemplation process shows evidence of D and G bands (see Chapter IV Figure 28), meaning it is not unreasonable to consider the presence of such quenching products during coke-forming catalytic processes.

7.3 Active Reaction Sites

Based on the discussion in Section 4.1.1, it is likely that oxygen sites are forming during high-temperature treatment of the zeolite samples. Further to being responsible for interesting emission dynamics, oxygen vacancies are also of interest for their potential as active sites in reactions such as MTO. There have been previous catalytic studies in oxide materials that indicate oxygen vacancies play a role as activation sites for different molecules (e.g. CO over Cu-Y₂O₃-stabilised ZrO₂²⁶⁸, CH₂O over TiO₂²⁶⁹, high-temperature CH₄ activation over lithium-doped MgO²⁷⁰, CH₄ activation is unambiguously mediated by oxygen vacancies over CeO₂^{271, 255}). It might be reasonable to consider that like CH₄, CH₃OH may also be activated by either oxygen vacancies.

The data presented show that from 100 °C the peak photoluminescence emission intensity progressively decreases. Prior to this, an activation was conducted at 550 °C under oxygen flow, which was not characterised in detailed temperature steps but may have feasibly allowed for the introduction of both total oxygen vacancies or paramagnetic O⁻ sites, effectively ‘pre-loading’ the zeolite with defects. Based on the detemplation experiment, during a further temperature ramp we may expect to see a further increase in vacancies with temperature. Conversely, what is observed is a decrease in intensity from 300 °C onwards, which could be related to quenching either in the form of self-quenching from changing colour or from the growth of more non-emissive components like graphite. These seem unlikely, however, because at this early temperature, it is neither likely for graphite to be forming nor was any significant colour change observed (see

Table 18).

An alternative explanation could be that assuming high temperature emission relates to defects, the formation of catalytic products is interfering with the defect emission. If this is the case, we know that from detemplation study, we don't expect to see an emission increase again until > 300 °C. However, this dynamic is not observed, with the emission intensity instead being lowest between 300 and 450 °C. The spectral changes in this temperature region indicate that evolution in the reaction products is being observed. Therefore, it is postulated that the oxygen vacancies are acting as active sites in the MTO reaction, being filled as activation takes place over them. This offers an explanation for the continued diminishment of the characteristic oxygen vacancy signal. If so, this could be a powerful method for seeing when changes in reaction rates might happen during *in situ* experimentation. Additionally, it might also be postulated that the oxygen vacancies provide an alternative activation pathway in addition to standard MTO mechanisms.

8 Conclusion

While it was first presumed that *in situ* work would yield spectra that directly reflect the changing chemical speciation within the framework at different points in the detemplation process and the methanol-to-olefins reaction, the results instead demonstrated that the zeolite framework itself begins to contribute more significantly to the emission spectra at high temperatures (i.e. 350 °C+). In the absence of a growing proportion of organic phase being fed by a constant supply of reactant, as is the case in the MTO reaction, the emission spectrum of the zeolite at high temperature exhibits a broadband emission with an extremely pronounced increase in intensity. In the discussion presented, it was postulated that the elevated temperatures provide the energy required for oxygen point defects to form within the framework, either in the form of deficiency centres or interstitials. This supports earlier DFT work that predicted the presence of oxygen vacancies. As such, it is demonstrated that *in situ* photoluminescence spectroscopy may actually be used in certain zeolitic systems to monitor the presence of framework aberrations at high temperature. This would certainly warrant further studies as the phenomenon of defect formation is very difficult to capture in other modalities and may otherwise go undetected as the window to 'see' such effects has been shown to be relatively small, in this case requiring high temperatures. This technique presents itself as an attractive option to accompany existing techniques like ESR or EPR, which are already used to probe defects, by acting as a bulk characterisation technique for point defects.

By contrast, in the MTO reaction *in situ* data produced spectra that seemed to evolve in a manner more representative of the changing chemistry occurring within the sample. The general intensity quenching exhibited at higher temperatures with greater product formation lends greater weight to the argument that increases in intensity at high temperature in the first set of experiments are

due to an alternative emission mechanism pathway such as framework defects. This highlights the broad scope of the technique, which in this context monitored the formation of hydrocarbon pool products. In the right catalytic system, the setup could be used alongside fingerprinting methods like Raman as a technique utilised for its sensitivity in detecting the presence of species of interest. It is still unclear what the significance of potential defect sites on catalytic performance might be. A recent study by Yarulina et al., for example, postulated that silanol defects were of utmost importance being associated with a faster rate of coke formation and therefore deactivation during MTO over DDR-type zeolite catalysts⁴². Equally, a study by Liang et al. claimed that silanol or framework defects did not aggravate catalyst deactivation in an MTO study using MFI zeolites prepared using different synthesis methods²⁷². Future *in situ* studies that evaluate the relationship between catalyst structure and functional performance are necessary, particularly those that more widely appraise different frameworks in the same reaction.

Consequently, there are a multitude of avenues for future work utilising this technique. On the topic of defect formation, further studies utilising zeolites with different topologies, SARs, synthesis methods, and post-processing methods could be characterised to identify any trends. Taking full advantage of the technique's flexibility in accommodating *in situ* apparatus, further catalytic reactions could be performed such as MTO over different topology or metal-exchanged frameworks. In future work, the setup used here could be modified to include additional excitation lines or detection probes (e.g. UV-vis) to yield even greater amounts of simultaneously acquired data.

Chapter VII

Multimodal Imaging of Emissive Sites in Partially Detemplated Crystals

In collaboration with the Central Laser Facility

Submitted to Angewandte Communications as Omori N, Candeo A, Mosca S, Lezcano-Gonzalez I, Robinson I, Greenaway A, Collier P, Beale A. (2020) Multimodal Imaging of Autofluorescent Sites Reveals Varied Chemical Speciation in SSZ-13 Crystals.

1 Introduction

The internal landscape of a zeolite is exceedingly chemically complex. Being not only compositionally and structurally varied over a micron length scale, the results of the last few chapters have also highlighted the propensity for localised variability on a micro- to nanometre length scale. High-temperature spectroscopic studies in Chapter V expressed the possibility that the aluminosilicate framework, far from being a perfect crystalline structure, has the capacity to accommodate an appreciable number of point-defects. Similarly, it is also well acknowledged that where catalysis is concerned, the internal volume plays host to a variety of different hydrocarbon products, the content of which likely varies compositionally from pore to pore depending on its proximity to the crystal surface^{203,273}. Were it possible shrink in size and hop from lattice point to lattice point, looking around, the surrounding chemical environment would appear appreciably different with each step through the zeolite²⁷⁴.

Within the field of catalysis, however, the nanoscale complexity of these materials is often overlooked in favour of a more top-down summation of their properties. This is primarily related to the predominant use of bulk average characterisation techniques, which by their nature actualise a broader understanding of the samples. Structural and compositional parameters like crystallinity (XRD), silicon-to-aluminium ratios (digestion followed by ICP-MS or EDXRF), and cation loading are all considered in terms of averaged values that are correlated with bulk catalytic performance metrics like conversion efficiency and selectivity of a batch of material. In an industry that commercially uses hundreds of kilograms of zeolites to catalytically convert many cubic metres of gases²⁷⁵, a bulk average characterisation approach is highly applicable and certainly not remiss. However, with growing needs for more exacting catalytic design in systems such as standard catalytic reduction (SCR)²⁷⁶ and methanol-to-olefins (MTO)²⁷⁷, garnering a deeper understanding of the real microstructural characteristics of a zeolite may provide the answers required for next-generation catalyst development. Single crystal imaging and mapping techniques provide the spatial resolution required to achieve this.

Atomic imaging methods are able to provide highly detailed structural information due to their unparalleled resolution. Transmission electron microscopy (TEM), high-resolution transmission electron microscopy (HRTEM), and scanning tunnelling electron microscopy (STEM) techniques are now able to provide 2D and 3D atomic-scale structural information²⁷⁸. Traditionally these techniques have struggled to provide spatial and chemical information of adsorbed organic phases²⁷⁹, although in more recent advancements, atomic methods such as atom probe tomography (APT) have also been able to provide carbon-sensitive chemical information by creating 3D compositional reconstructions of coked ZSM-5 crystals²⁸⁰. These techniques may also necessitate significant sample modification (e.g. wafer formation for TEM, gold coating for

SEM) and require high vacuum sample chambers, meaning that the scope for imaging zeolites in a catalytically representative environment can be limited.

The previous chapters have demonstrated the relevance of photoluminescence spectroscopy from a chemistry perspective. Although this technique is also a bulk average technique, an extension of this laser-based characterisation technique that does provide spatial resolution is confocal laser scanning microscopy (CLSM) and its advanced derivative fluorescence lifetime imaging (FLIM). CLSM generates fluorescence intensity images, whereas FLIM generates maps containing pixel-by-pixel information of fluorescent decays. Sharing the benefits of its spectroscopic counterparts, these imaging techniques are also non-destructive and can be acquired under ambient conditions, inviting the possibility of *in situ* imaging studies.

Similar to early discussions on the nature of photoluminescence spectroscopy research, fluorescence imaging studies can be divided into two categories: those that utilise a fluorescent dye, and those that utilise an intrinsic auto-fluorescence signal. The majority of work today focuses on imaging a distribution of dye particles to gain further insight into structural domains, or to comment on catalytic activity based on the behaviour and interactions of the dyes used.

Early studies simply stained zeolite samples with dyes to see where the structure was able to uptake it, such as Bonilla et al.'s confocal study of grain boundaries in MFI-type zeolite membranes²⁸¹. More selective staining has also been conducted by Weckhuysen et al. who have used thiophene to tag Brønsted acid sites^{282,283}. Thiophene is a particularly useful dye for zeolite imaging studies, as it is non-emissive in its monomer form, only becoming fluorescent after it oligomerises in the presence of Brønsted acid sites. They have also identified furfuryl alcohol as a molecule that can behave similarly as a tag by becoming emissive only upon oligomerisation onto an active site, using it to develop a 3D imaging²⁸⁴ and single-molecule imaging method called nanometre accuracy by stochastic chemical reactions (NASCA)^{130,132}, a technique similar to super-resolution stochastic optical reconstruction microscopy (STORM)²⁸⁵.

Metal doping, which is known to induce luminescence in zeolite samples, has also been imaged in lanthanide(III)-doped zeolites to show dopant distributions across films with the view to use the emissive behaviour in optical authentication systems⁶¹. Less work has been conducted on imaging the autofluorescence of zeolites. Karwacki et al.^{143,145} have focused on imaging the growing fluorescence that arises from large ZSM-5, SAPO-34, SAPO-5, and CrAPO-5 crystals during the detemplation process, attributing the emission observed to the proliferation of fluorescent intermediate products. Further, they use the images to comment on the intergrowth structure of large zeolite crystals.

FLIM has so far only been used to study tagged crystals. It has previously been demonstrated in zeolite L to show J-aggregate coupling between pyronine dye molecules inside nanochannels²⁸⁶. Bulk FLIM studies of pyronine inside zeolites have indicated multiexponential decays, which

implies that molecules interact with each other inside the pore structure²⁸⁷. Multimodal lifetime imaging studies were able to show an increase in lifetimes towards the centre of the zeolite L crystals, which were correlated with aggregate formation. FLIM has also been applied to metal-organic frameworks²⁸⁸ (MOFs) to study the incorporation of fluorescein isothiocyanate and rhodamine B isothiocyanate into a UiO-67 framework. Changes in lifetime were attributed to nanoscale defects and regions of higher dye concentration, all of which were visually mapped to show spatial distributions.

This chapter presents a multimodal imaging study of partially detemplated chabazite. The results show a spatial distribution of template derivatives, but moreover is able to identify three unique types of emissive products. Building upon the spectroscopic understanding of these samples from Chapters 4²⁸⁹ to 6, the capabilities of optical microscopy are pushed to interrogate the relationship between catalyst structure and function.

The study is differentiated from the prior art on zeolite imaging in three critical ways. Firstly, the imaging performed is label-free. This is thanks, in part, to a unique set of 30 μm chabazite crystals that are large enough to image while maintaining satisfactory resolution. Although they are arguably larger than typical industry-sized chabazite catalysts, they are more than just model systems being only 3-4 times larger than those synthesised and applied in catalytic studies²⁹⁰, meaning the results shown here have a more direct catalytic relevance. Secondly, it uses a multimodal combination of CLSM, FLIM, and Raman mapping. The use of FLIM in a label-free zeolite study may thus far be considered a novel contribution to the field. Finally, the results of the study are able to begin to comment on the chemical speciation throughout the crystals. This represents an important advancement in the chemical relevance of optical microscopy to the field of catalytic chemistry, as this characterisation technique has predominantly been used to comment on either crystal structure or the distribution of active sites throughout the crystal structure.

2 From Spectroscopy to Imaging

It is important to consider that imaging brings its own set of technical challenges when compared to spectroscopy, which should be considered prior to mounting the samples into a commercial confocal microscope. Commercial microscopes refer to pre-built imaging systems that are purchased as a whole unit, typically inclusive of the laser source, and offer minimal scope for customisation when compared to home-made setups. Two points of consideration are: the wavelength of excitation and signal-to-noise.

2.1 Wavelength of Excitation

UV irradiation is often favoured in spectroscopy because the higher energy beam is able to induce photoexcitation in a wide range of organic molecules and semiconductor materials. In the free-coupled spectroscopy setup used, alignment of a light source that is invisible to the naked eye through UV-appropriate fused silica optics is feasible. UV optics can be extraordinarily expensive as they require material components like glue that do not luminesce or degrade with UV excitation, and mounting these into commercial microscopes can be challenging. For this reason, the lowest wavelength available on the commercial microscope used in this experiment is 405 nm. In the case of fluorescence lifetime measurements, the lowest wavelength available is 488 nm.

As spectroscopy data so far has been obtained at 355 nm, emission intensity of TMAda at 405 nm is assessed with two different fluorimeters (see Figure 66). Emission intensity at 405 nm is significantly lower in both cases as the peak emission intensity appears to be deeper in the UV. Therefore, it is unlikely that imaging will be able to directly observe template material. Instead, it is more likely that imaging will provide information on template derivatives or other catalytic hydrocarbon products.

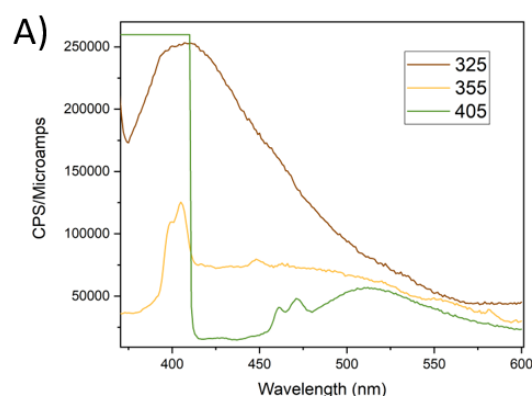


Figure 66 **Fast fluorimeter scans of TMAda in solution with water** on Horiba fluorimeter acquired with lamp at 325, 355, and 405 nm (detector = 800 V, scan speed = medium)

2.2 Signal-to-Noise

A sufficient signal-to-noise ratio is necessary in confocal imaging to ensure the axial and transverse resolution is good enough. It is worth considering that autofluorescence from zeolites is not as strong as emission from dyes, which is why the spectroscopy setup utilised an intensified camera with minimised optical components to reduce signal loss. They are also a highly scattering material. Scatter is handled in the spectroscopy setup through the use of angular offset between the excitation and detection pathways¹⁷⁴. It is generally easier to tell when scattered light is entering a time-resolved spectroscopy system as it will have no lifetime (or a measured lifetime so fast it encroaches on the instrument response function (IRF)).

Commercial imaging systems typically house a higher number of optical components and signal loss through reflection or absorption can be more significant. They also tend to use a co-linear arrangement of the excitation and detection pathway, which can allow for a significant amount of scattered light to leak through to the detector. In a confocal microscope it is possible to generate images made up almost entirely of scattered laser light rather than ‘real’ emission, which is actually of a relatively low intensity. For basic imaging systems that don’t have lifetime functionality, it can be difficult to recognise when images are being constructed out of scattered light.

Where autofluorescent imaging is concerned, there is not a lot that can be done if meaningful signal-to-noise ratio cannot be obtained from the zeolite when loaded into a microscope. Success is equally dependent on selecting samples that lend themselves towards imaging at a particular wavelength.

3 Method

3.1 Sample Preparation

Parent chabazite material was synthesised as described earlier in Chapter III. The following four samples were analysed in this study:

1. as-made uncalcined chabazite,
2. partially calcined chabazite quenched at 275 °C (i.e. halfway through a temperature ramp to 550 °C),
3. chabazite calcined twice at 550 °C, and
4. chabazite calcined at 630 °C.

Calcination in all cases involved placing the sample in a ceramic dish in a static oven and heating in air to 120 °C at 1 °C/min and holding at temperature for 2.5 h, then heating to the target temperature (i.e. 550 or 630 °C) at 4 °C/min and holding at the nominated temperature for 10 h.

3.2 Imaging

3.2.1 Scanning Electron Microscopy (SEM)

SEM images were obtained on a JSM-6701F Field Emission Scanning Electron Microscope (JEOL, Tokyo) using the equipped secondary electron (SE) detector. Images were obtained under high vacuum (5.15×10^{-7} torr/ 6.87×10^{-5} Pa) at 10 kV with scan speed of 735. All samples were coated with gold for 35 s, but actual thickness is unknown.

3.2.2 Confocal Imaging

Confocal images were obtained on a Leica SP8 microscope (Leica Microsystems, Germany) at 405 nm excitation with a continuous wave diode laser (NKT Photonics, Denmark) that delivered a maximum power of 7 mW to the sample. A 63x water-immersion objective (Leica, HC Pl Apo, 63x/1.4) was used to collect images with a resolution of 1024 x 1024. Images were averaged across the whole acquisition frame 3 times.

Single-colour images were collected using a single hybrid detector with a detection window set from 450 to 650 nm. Two-colour images were collected using two hybrid detectors, the first detection window spanning from 450 to 550 nm and the second detection window spanning from 550 to 650 nm. Z-stacks were collected with a z-step of 0.4 – 0.8 μm^{xvi} .

^{xvi} Exact z-step is specified in results section.

3.2.3 Fluorescence Lifetime Imaging Microscopy (FLIM)

FLIM images were obtained on a Leica SP8 microscope at 488 nm with a pulsed supercontinuum laser (NKT Photonics, Denmark) featuring a variable repetition rate (10-80 MHz) that delivered a maximum power of 50 mW to the sample. The repetition rate was selected on a sample-by-sample basis. A HC Plan Apo 63x water objective (Leica Microsystems, Germany) was used to collect images with a resolution of 1024 x 1024. Integrated photon counting hybrid detectors were used in conjunction with the PicoQuant TCSPC system (PicoQuant GmbH, Germany).

Fitting was performed in SymPhoTime 64 software (PicoQuant GmbH, Germany) using an exponential reconvolution^{291,292}. Images are spatially binned by 2^{xvii} and fit to either a biexponential or triexponential function depending on the χ^2 value^{xviii}. In some cases, a truncated tailfit was used between 1.45 ns to the end of the time window, which is dependent on the repetition rate and typically at 95 ns. The nature of the fit is specified on an image by image basis. A 100 nm smoothing filter was used in the FLIM maps.

3.3 Raman Spectroscopy

Raman spectra were obtained from an InVia confocal Raman microscope (Renishaw, Wotton-under-Edge, UK) equipped with a 50x objective lens (Nikon, L Plan Apo, 50x/0.45, WD17) and Peltier cooled CCD. The sample was irradiated with either an 830 nm diode laser with 34 mW maximum power output, or a 514 nm Stellar PRO argon laser (Modu-laser, USA) with 10 mW maximum power output. Attenuated laser power at the sample was achieved using neutral density filters. A grating with 1200 lines/mm was used, yielding an overall spectral resolution of 1 cm⁻¹. Raman maps were acquired using an x-y motorised stage, which was moved in 1.5 μ m steps to raster across a region of interest. At each point, Raman spectra were collected in the spectral region 1015 to 1472 cm⁻¹ with an acquisition time of 20 s and 10 accumulations totalling an overall acquisition time of 18-20 hrs per map, and an irradiance of 5000 W/cm².

The spatial distribution of the most significant Raman bands were reconstructed by calculating the correlation of a triangular template (cantered at the frequency ν with a base width $\Delta\nu$ of 20 cm⁻¹) with the Raman spectrum detected in each analysis point in the spectral band $\Delta\nu$. The following method, quoted as TC descriptor^{293,294}, is more selective than other mapping methods²⁹⁵. Since 830 nm was used with a long working distance objective lens, the nominal spot dimension is around 5 μ m and the depth of field is at least 10 μ m. The entire z-depth is likely to be excited

^{xvii} Spatial binning involves taking two or more pixels and combining their information with the view to increase signal. Here, the binning was performed after the data was acquired; it is also possible to bin CCD pixels prior to readout. Binning in this manner decreases the spatial resolution but not temporal resolution, and instead improves signal-to-noise. In the case of 2x2 binning, this would mean a 1024x1024 image would effectively become a 512x512 pixel image.

^{xviii} As the fitting procedure is purely numerical, multiexponential fits beyond three exponents is usually not performed as the fourth, fifth, and higher exponents generally have increasingly smaller contributions to the overall fit.

as the spectra were acquired without a pin hole, relatively high laser power, and the crystal medium's low absorption and tendency to scatter allows for greater photon propagation through the volume.

4 Results

4.1 SEM Imaging^{xix}

4.1.1 Uncalcined Chabazite

The widefield SEM image in Figure 67 show that the synthesis process is effective in producing regular cubic crystals with a relatively uniform size distribution of 20-30 μm cubes. The cluster views at x1900 magnification demonstrates a reasonable average representation of the sample. There appear to be some instances of planar defects on the external surfaces, also visible in the x1000 magnification image but overall there don't appear to be major synthesis problems. Bright areas on the crystal surfaces are attributed to charging effects, which still arise despite the gold coating.

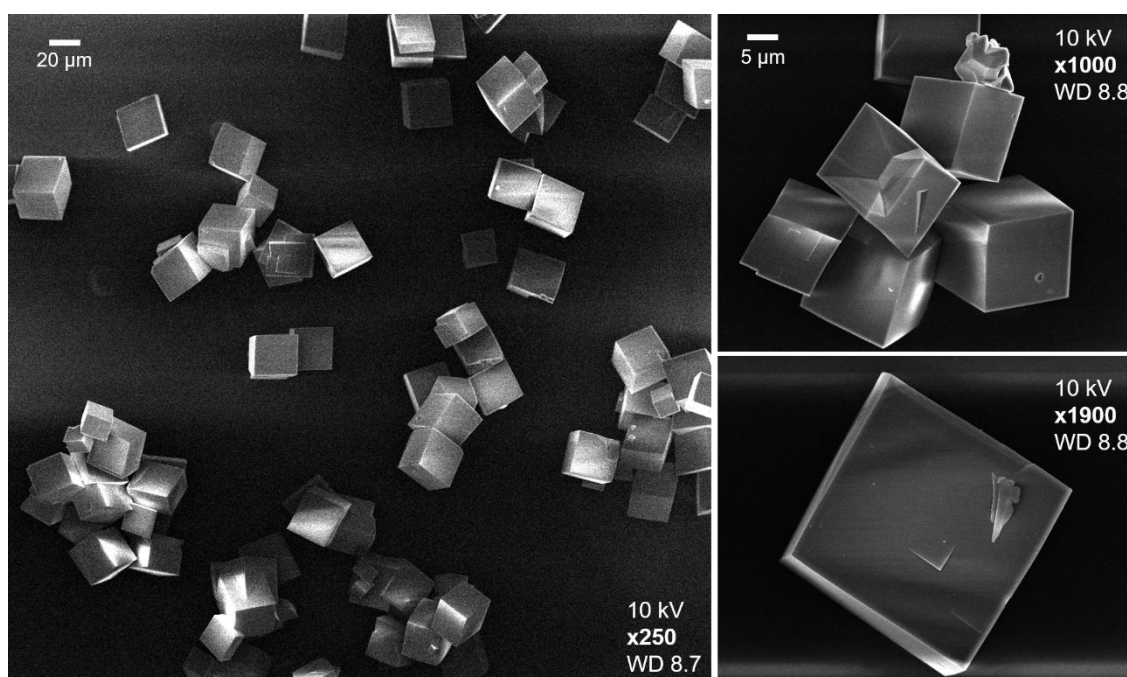


Figure 67 **SEM images of as-synthesised uncalcined chabazite crystals** including widefield image (left), x1900 magnification cluster view and x1000 single crystal zoom (right)

^{xix} SEM images have not been acquired for the partially calcined sample.

4.1.2 Chabazite Calcined twice at 550 °C

Based on the widefield image and x1000 magnification SEM image in Figure 68, two calcination treatments do not appear to adversely impact the external appearance of the crystals, which don't look appreciably different to the as-synthesised uncalcined sample shown in Section 4.1.1. The surface defects that are present look similar to the uncalcined sample. Some crystal intergrowth is visible in the cluster image at x1000 magnification, however this is a product of the synthesis process rather than the calcination. The image acquired at x3700 magnification shows a broken crystal with a series of shear planes perpendicular to the cubic axes of the crystal. This likely indicates some crystals have experienced cracking as a result of thermal stress.

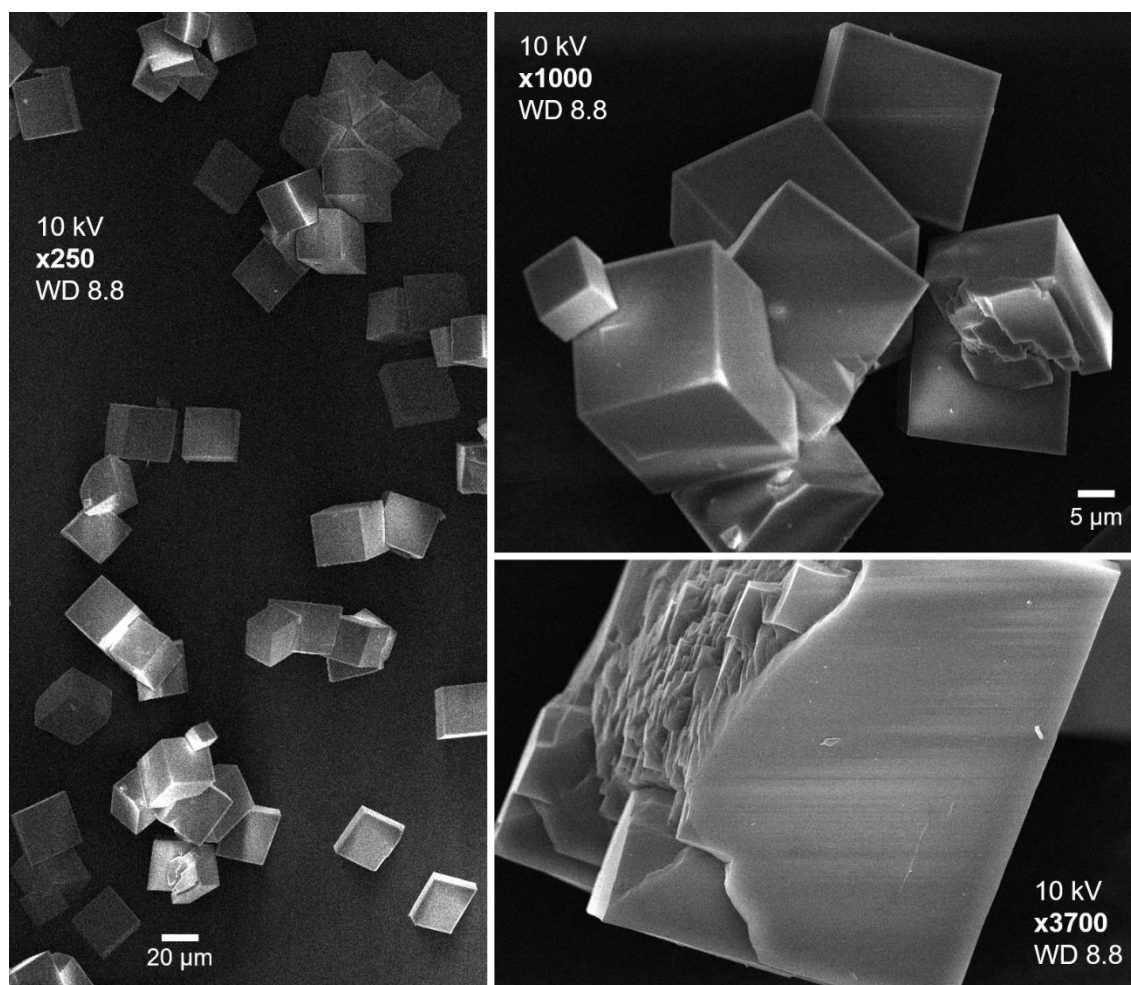


Figure 68 **SEM images of chabazite crystals calcined twice at 550 °C** including widefield image (left), x1000 magnification cluster view and x3700 single crystal zoom (right)

4.1.3 Chabazite Calcined at 630 °C

The widefield image in Figure 69 shows that the overall cubic structure appears to be maintained. Magnified images show the same kind of planar defects visible in the uncalcined material, as well as some evidence of crystal breaking with fracture planes similar to what is seen in the twice calcined sample in Section 4.1.2. Some amount of cracking due to high temperature is understandable, meaning the morphologies visible in Figure 69 are in line with expectations. Although some thermal damage is evidenced, it is not substantial in that the overall structure of the samples are maintained.

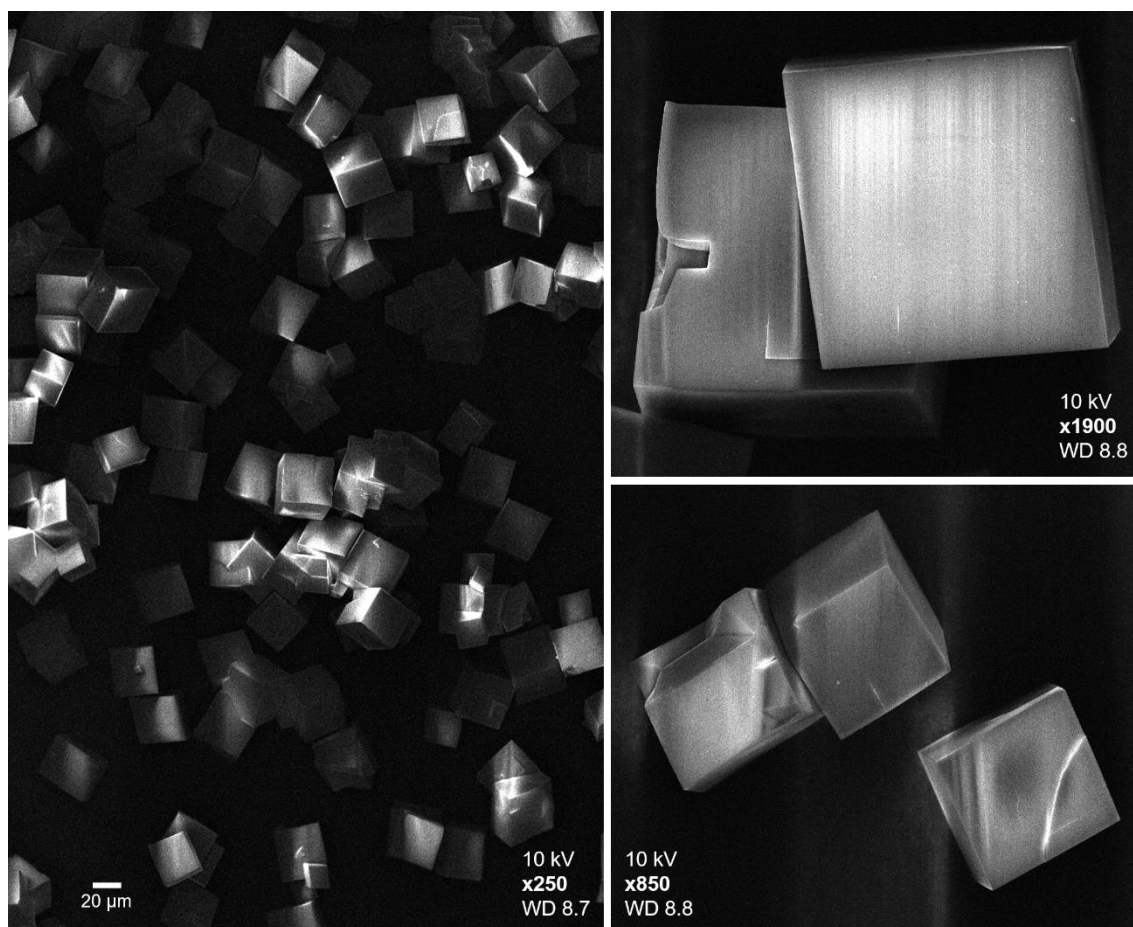


Figure 69 **SEM images of chabazite crystals calcined once at 630 °C** including widefield image (left), and cluster views (right)

4.2 Confocal and Fluorescence Lifetime Imaging (FLIM)

4.2.1 Uncalcined Chabazite

Figure 70 shows single-channel confocal images of uncalcined chabazite. Overall, the samples do not exhibit significant emission. Bright regions demarcating the crystal edges and across the faces of the crystals may be attributed to some form of impurities. In all cases, the intensity of the bright spots is heavily overstated by the use of z-stack summation, maximised detection window and brightness control, which have been optimised to best elucidate the structure of the crystals.

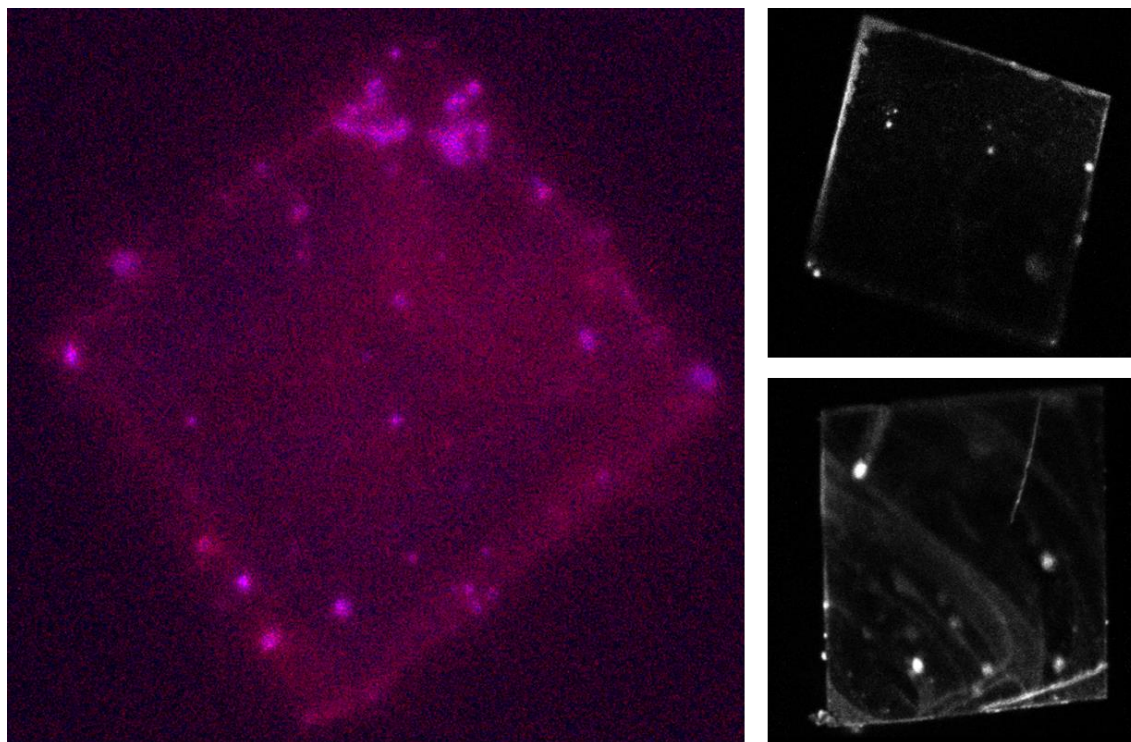


Figure 70 **Single-channel confocal images of uncalcined chabazite** including a summed projection of a z-stack (left) and single-plane images (right top and bottom) obtained from three different crystals.

FLIM was attempted on the uncalcined chabazite but an appreciable number of photon counts could not be detected from the samples to generate a lifetime map. It was established in Chapter IV that the primary signal detected in spectroscopic studies of the uncalcined chabazite material was originating from the framework-encapsulated organic structure directing agent. While this structure was excitable at the higher energy wavelength of 355 nm, it is not expected that imaging at a lower energy of 405 nm can yield meaningful maps of template distribution. As FLIM is restricted to 488 nm, successful TCSPC FLIM is pushed even further out of the realm of probability. With the assumption that as-synthesised chabazite is the most compositionally predictable sample analysed here, being comprised of only aluminosilicate framework and an adsorbed organic phase of known composition (i.e. template) there remains no further component of the material that imaging is expected to elucidate. In the spirit of rigour, FLIM was also unsuccessfully attempted on the template material (i.e. 25 % TMAda in water), confirming that

the combination of the excitation wavelength and detection system used are not able to probe the methylated adamantane molecules. The results of this sample also imply that the framework itself is optically transparent at this wavelength, which is consistent with the observations of previous studies¹⁴⁵.

4.2.2 *Partially Calcined Chabazite*

Figure 71 shows a single-channel z-stack of partially calcined chabazite acquired every 0.4 μm . Overall, a greater emission signal is visible compared to the uncalcined chabazite in Section 4.1.1, with luminescence generically visible across the whole crystal face implying that new emissive species excitable at 405 nm have formed during the calcination process. Consistent with SEM images, the overall cubic structure is maintained, although the luminescence also unveils evidence of internal cracking predominantly along (h00) and (0k0) planes through the crystal.

The z-stack, which first acquires images from the upper outermost plane of the crystal and then moves down through the bulk of the crystal, also highlights two regions of photoluminescence: the first being a roughly 5 μm thick border around the edge of the crystal that appears to be an evenly distributed luminescence of the crystal itself; and the second being a central region of emissive dots that rather than being uniform across the crystal as the first region is, appear to have more localised, deposit-like morphologies. This central region of emissive deposits is also, according to the z-stack, localised towards the surface of the crystal, being visible only within 2.2 μm from the uppermost surface. Although it is not expected that z-stack imaging would be possible through the totality of the crystal volume due to the highly scattering nature of the material, the homogenous region of luminescence is still visible from the edges of the crystal for a further 3 μm (up to image J), indeed implying that the two different presentations of luminescence have different distributions throughout the crystal.

Figure 72 shows a two-channel image of the top plane of the crystal. Here, it is visible that the evenly distributed photoluminescence is predominantly emissive between 450 to 550 nm, whereas the localised emission from the deposits in the centre is centred between 550 to 650 nm. The contrast between the two detection windows is highlighted in the channel overlay image. This further implies, alongside the differing distribution patterns throughout the bulk of the crystal, that the different morphologies of the two emissive regions should correspond to different types of chemical speciation.

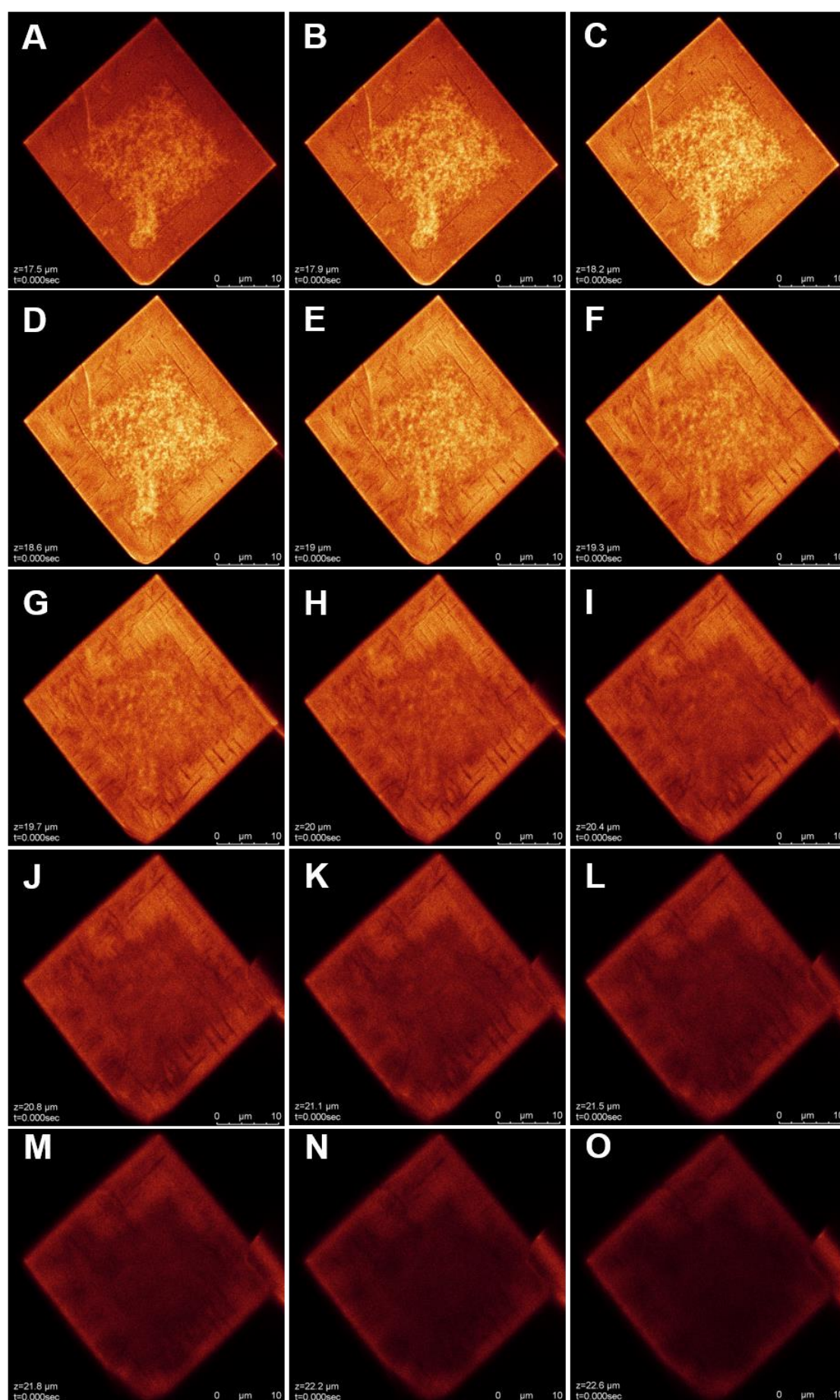


Figure 71 **Single-channel confocal z-stack images of a partially detemplated chabazite** acquired with a 0.4 μm z-step size at 405 nm.

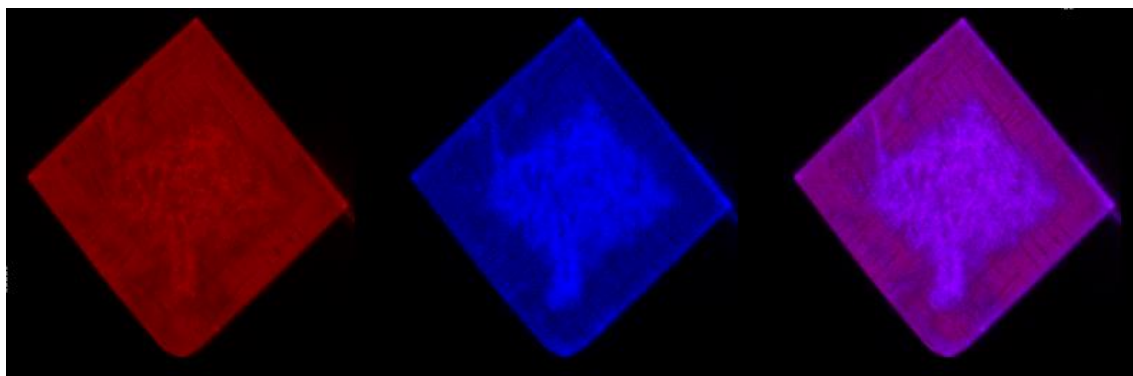


Figure 72 **Two-channel confocal imaging of partially detemplated chabazite** including 450 to 550 nm (left), 550 to 650 nm (centre) and channel overlay (right) acquired at 405 nm

Figure 73 shows confocal imaging of the partially detemplated chabazite acquired at 488 nm. The frequency histogram shows that the average lifetimes are generally quite short, being centred at 2 ns. The lifetime map shows the lifetimes of the edge region are slightly longer, however on balance the emission is generally fast throughout.

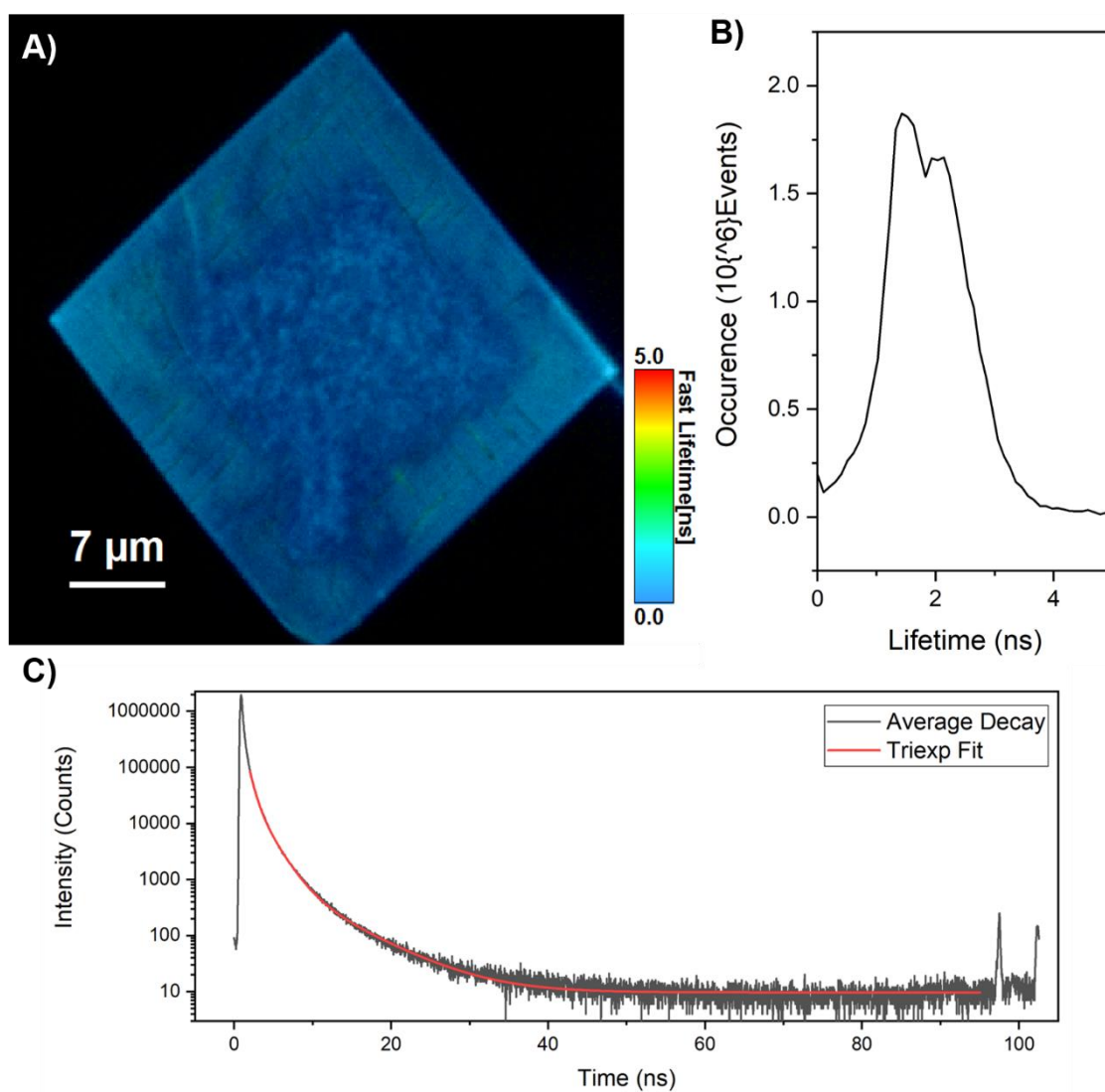


Figure 73 Single-channel fluorescence lifetime imaging ensemble of the top surface of a partially detemplated chabazite crystal acquired at 488 nm: A) Average lifetime map, B) average lifetime distribution histogram, and C) average decay with truncated triexponential tailfit

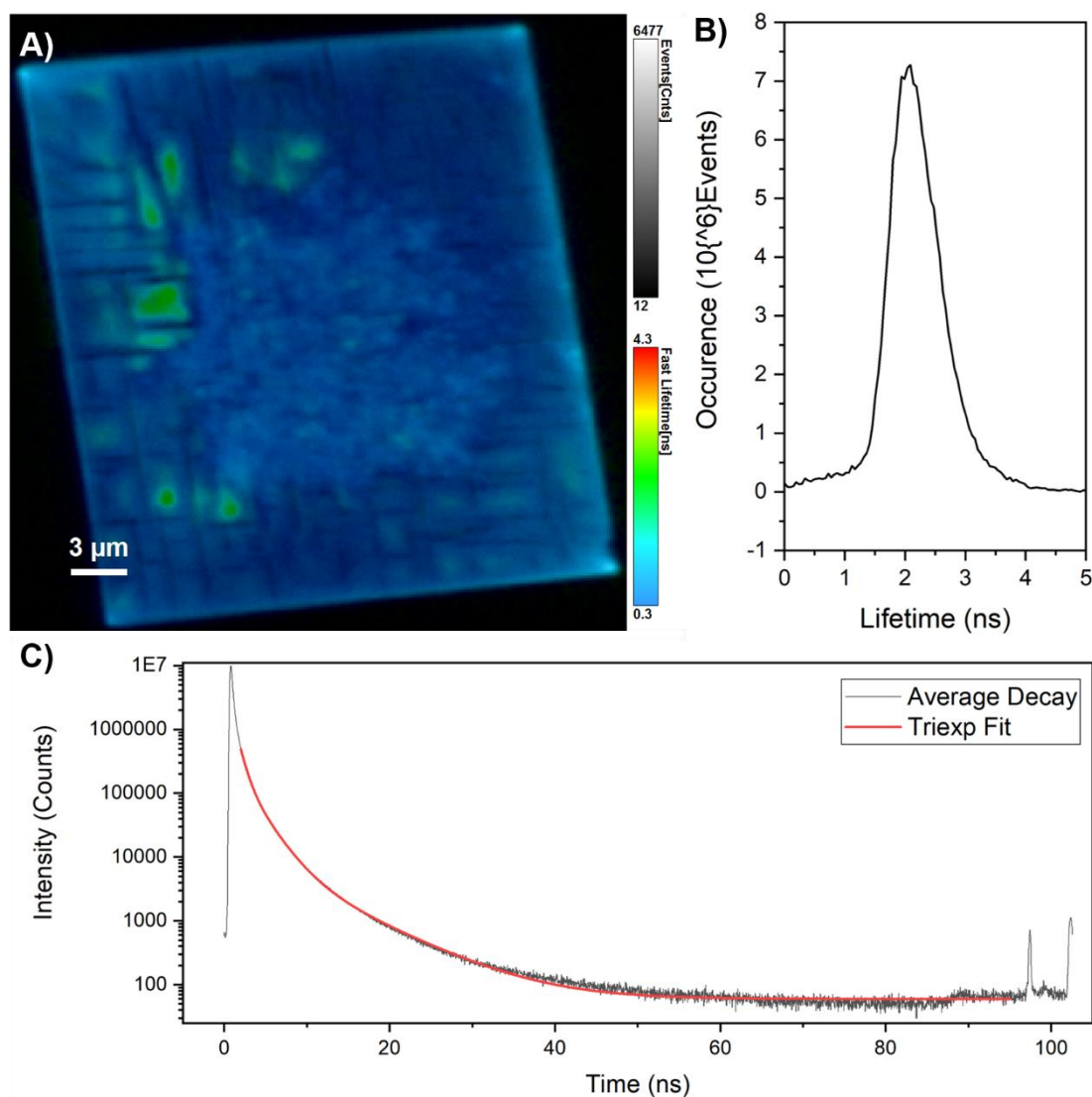


Figure 74 **Single-channel fluorescence lifetime imaging ensemble of an inner plane of a partially detemplated chabazite crystal acquired at 488 nm:** A) Average lifetime map, B) average lifetime distribution histogram, and C) average decay with truncated triexponential tailfit

Table 21 **Table of lifetimes and amplitudes for partially calcined chabazite**

Sample	A ₁ [kCnt s]	A ₂ [kCnt s]	A ₃ [kCnt s]	T ₁ [ns]	T ₂ [ns]	T ₃ [ns]	T _{Av} A [ns]	χ ²
Top Plane (Figure 73)	2.93	0.07	1.4	0.6	5.9	1.7	1.01	1.61
Inner Plane (Figure 74)	334.7	10.3	155	0.7	6.9	2.0	1.24	3.15

Figure 73, Figure 74 and Table 21 shows the single-channel FLIM dataset including the average lifetime map, lifetime histogram, decay, and table of lifetimes for a surface plane and inner plane of a crystal. The amplitude weighted average lifetime is 1.01 ns for the top plane and 1.24 ns for the inner plane, sampled 3.5 μm from the surface, constituting a reasonably fast overall lifetime dynamic in this sample when compared to other samples. The longest component of the triexponential fit is only 5.9-6.9 ns and appears to be concentrated on the outer edges of the crystal. In the inner plane FLIM image the regions of longer lifetime, denoted in pale green, patched in between the cracks are more visible, perhaps indicating that a different species or environment is present in these areas. The central region that features globular deposits has a much faster average lifetime. The fast average lifetime is in-line with previous postulates made regarding this sample; namely that its dark colouring and strong emission background in Raman spectroscopy indicate it has the most significant build-up of organic material of all samples studied here and is therefore consistent with findings in Chapter IV that carbonaceous species exhibit fast lifetimes of only a few nanoseconds.

4.2.3 Chabazite Calcined Twice at 550 °C

Figure 75 shows confocal images of chabazite calcined twice to 550 °C. In a widefield view, it appears that a number of crystals display a strong emission from the centre of each crystal face. Consistent with SEM imaging again, the cubic structure is well maintained, but similar to the partially calcined chabazite there is evidence of significant internal cracking. Compared to the partially calcined chabazite, the fractures along (h00) and (0k0) planes are more pronounced with some crack apertures being larger than 500 nm.

Zooming into one crystal, the emission pattern in this sample set is characterised by a distribution of what appears to be well-defined circular agglomerates concentrated at the centre of the crystal faces. The deposit-like nature of the central region of these crystals is similar to the partially calcined sample in Section 4.2.2, where crystals appeared to exhibit a homogenous emission across the crystal edges as well as a series of deposits towards the centre. Dissimilar to the partially detemplated samples, however, is the fact that: a) emissive deposits in the twice calcined sample appear to span further across the samples in some cases encroaching on the edges of the crystal, being overall less confined to the centre of the crystal than in the partially detemplated sample; and b) the homogenous region of emission visible around the edge of the partially detemplated sample does not appear as evident in the twice calcined sample, with the crystal itself appearing comparatively less emissive than the discrete deposits. Towards the edges, there are instances where the agglomerates appear to be aligning themselves in lines parallel to the cubic axes of the crystals. This is more clearly visible in the second zoomed in view which also shows the approximate size of the emissive deposits to be around 400 nm.

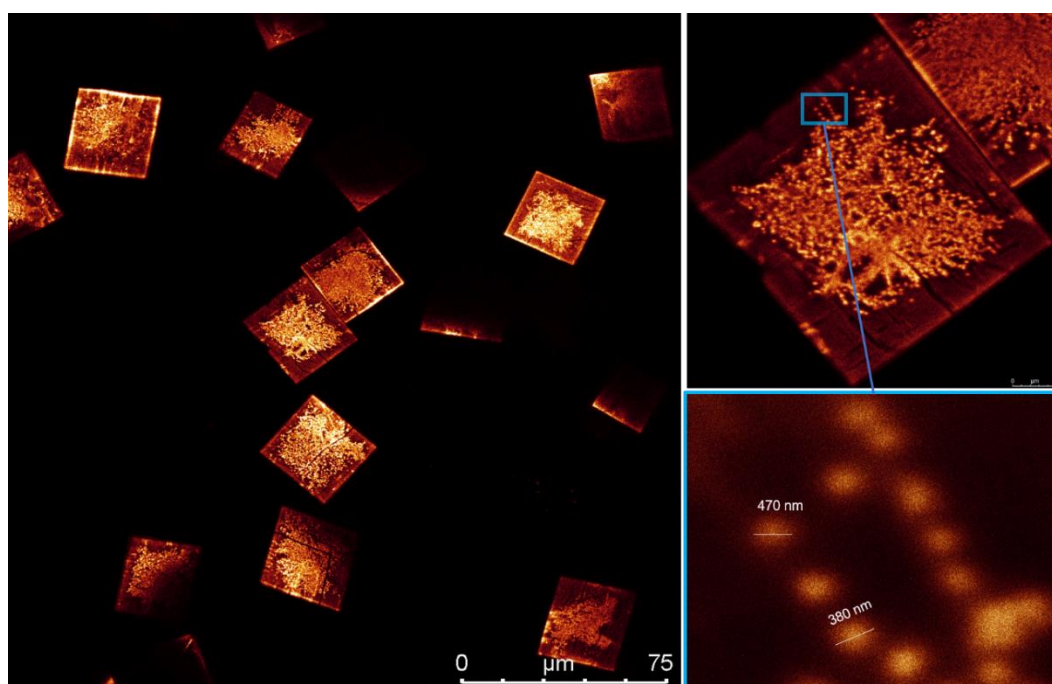


Figure 75 **Single-channel confocal images of chabazite calcined twice at 550 °C** including widefield (left) and two zoomed-in views (right) acquired at 405 nm

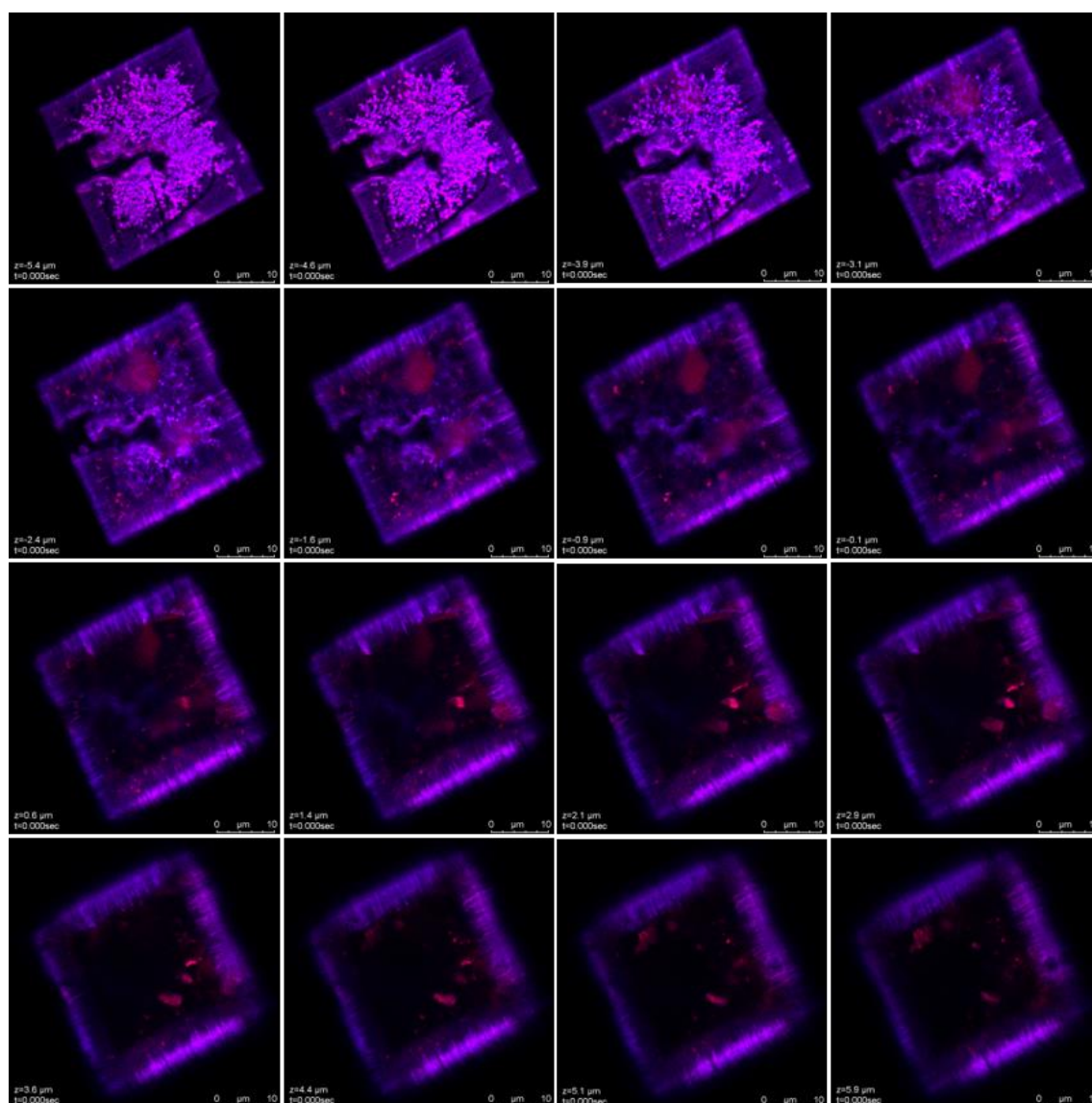


Figure 76 Two-channel confocal z-stack images of chabazite calcined twice at 550 °C acquired with a 0.8 μm z-step size at 405 nm. Stack images from the uppermost plane (first frame) and then moves down through the bulk of the crystal, explaining the poorer signal from the centre of the crystal in later frames.

A two-channel confocal z-stack displayed in Figure 76 provides even further information regarding the nature of emissive deposits in these samples. The agglomerated deposits appear to be predominantly localised within 3 μm of the crystal surface. This is evidenced by the changing distribution of emissive sites through the first five frames^{xx} of the z-stack, as well as the evidence of fringing around the edge of the crystal at deeper z-stack slices that also measure approximately 3 μm thick, which can be rationalised as an orthogonal view of emissive deposits that are likely to be agglomerated on the other faces of the crystal based on their consistent intensity through the z-slices.

From around 2 μm into the z-stack, there is also evidence of a different type of sub-surface emissive region that features stronger emission between 550 to 650 nm, rather than the surface

^{xx} Corresponding to a z-stack depth of around 3 μm .

deposits that are mainly emissive from 450 to 550 nm. These larger regions, which appear with a reddish hue in the z-stack, are shaped and distributed in a way such that they do not immediately appear to be governed by pore structure or crystallographic geometric restrictions. 3D rendering additionally shows how these regions are positioned at different depths within the centre of the crystal volume.

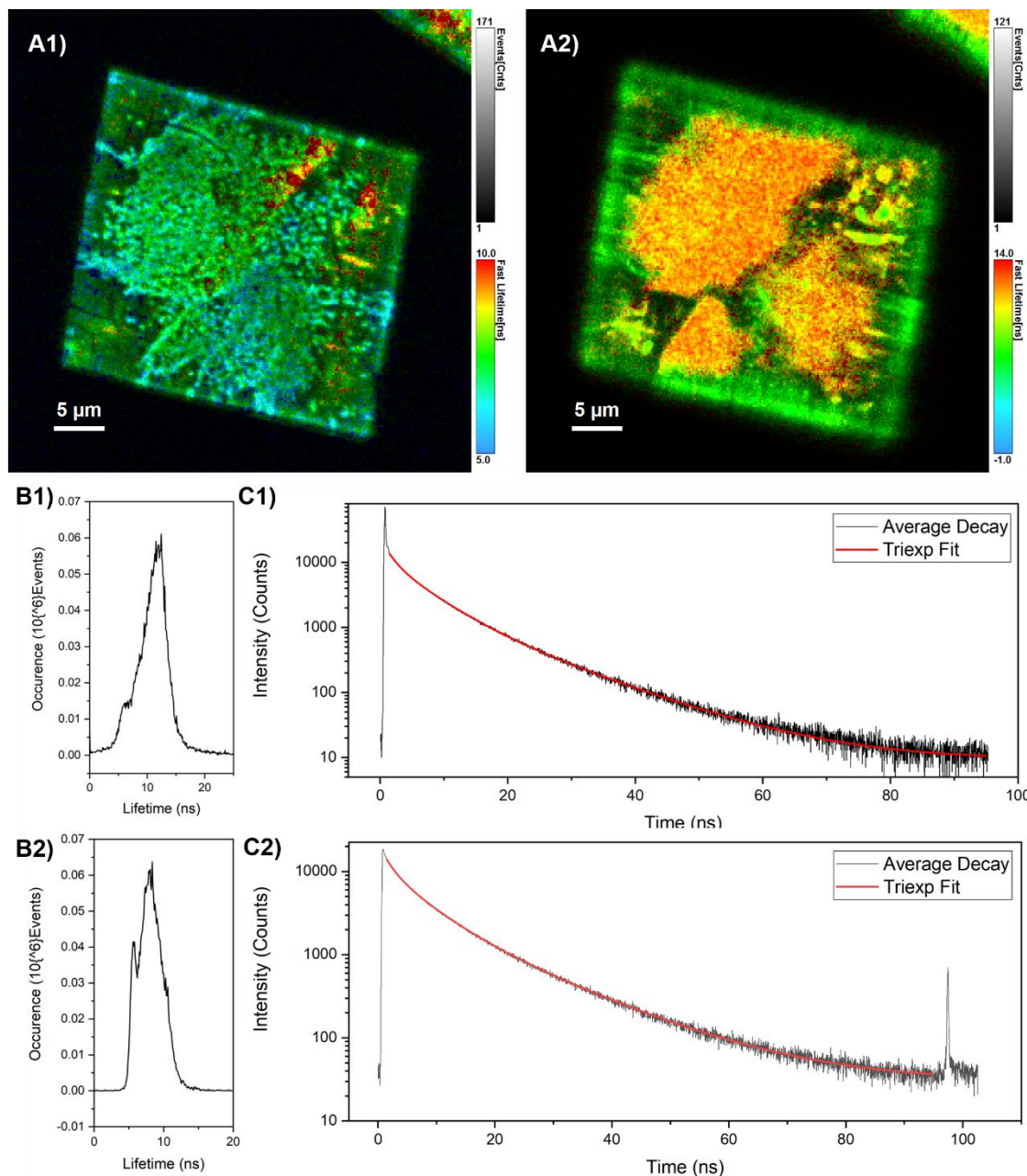


Figure 77 Single-channel fluorescence lifetime imaging ensemble showing uppermost (1) and inner (2) plane of chabazite calcined twice at 550 °C acquired at 488 nm: A) Average lifetime map, B) average lifetime distribution histogram, and C) average decay with truncated triexponential tailfit. Spikes in the decay curve at around 98 ns are scatter-related and are trimmed out of the fitting.

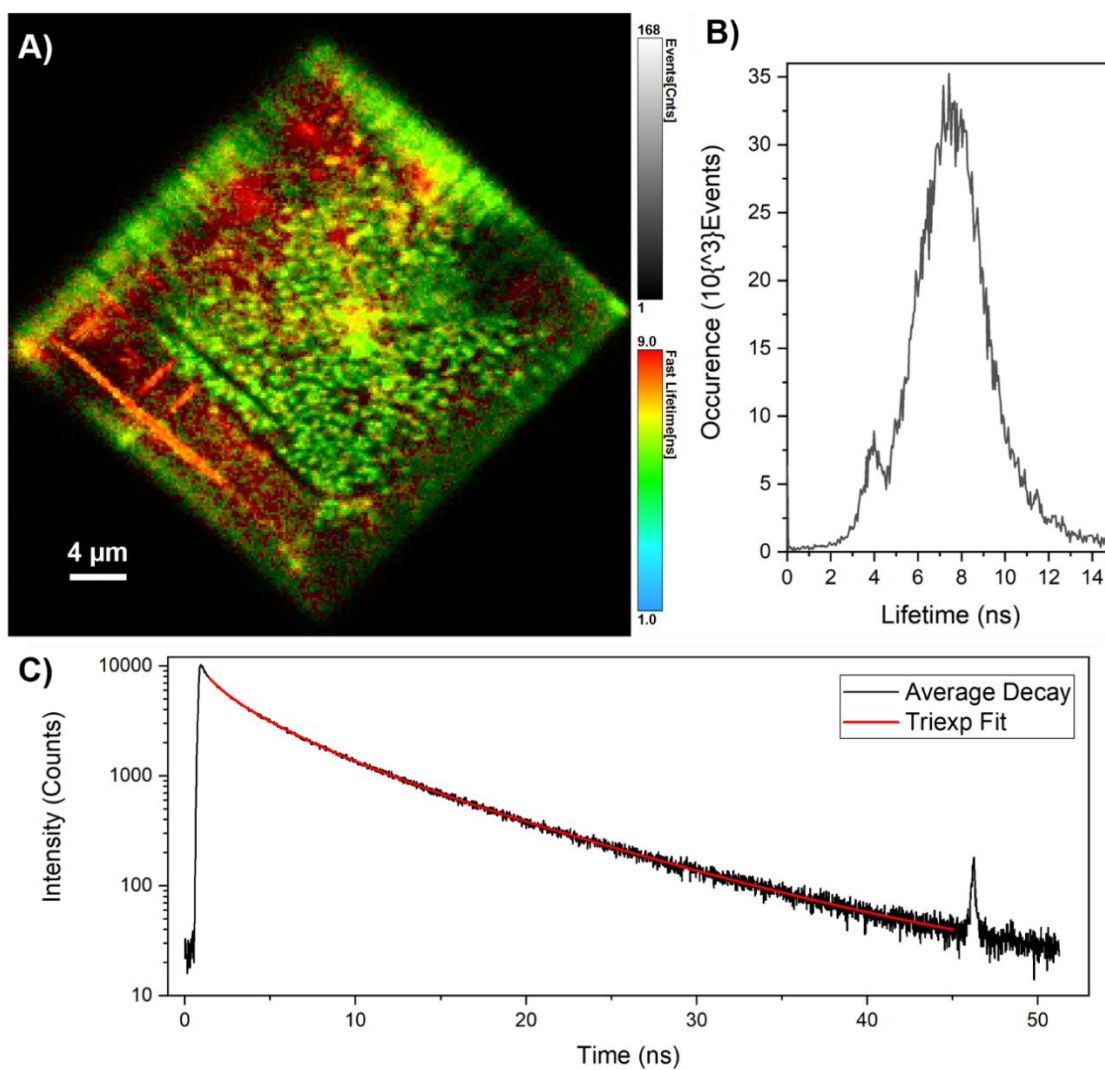


Figure 78 **Single-channel fluorescence lifetime imaging ensemble of chabazite calcined twice at 550 °C acquired at 488 nm:** A) Average lifetime map, B) average lifetime distribution histogram, and C) average decay with truncated triexponential tailfit. Spikes in the decay curve at around 98 ns are scatter-related and are trimmed out of the fitting.

Table 22 **Table of lifetimes and amplitudes for chabazite calcined twice at 550 °C in Figure 77 and Figure 78**

Sample	A ₁ [kCnt s]	A ₂ [kCnt s]	A ₃ [kCnt s]	T ₁ [ns]	T ₂ [ns]	T ₃ [ns]	T _{Av} A [ns]	χ ²
Top Plane (Figure 77)	5.02	9.21	-	9.85	2.88	-	5.34	2.32
Inner Plane (Figure 77)	3.29	7.07	3.8	14.85	5.8	1.59	6.77	1.78
Top Plane (Figure 78)	2.4	3.7	1.6	9.5	3.7	1.0	4.7	1.69

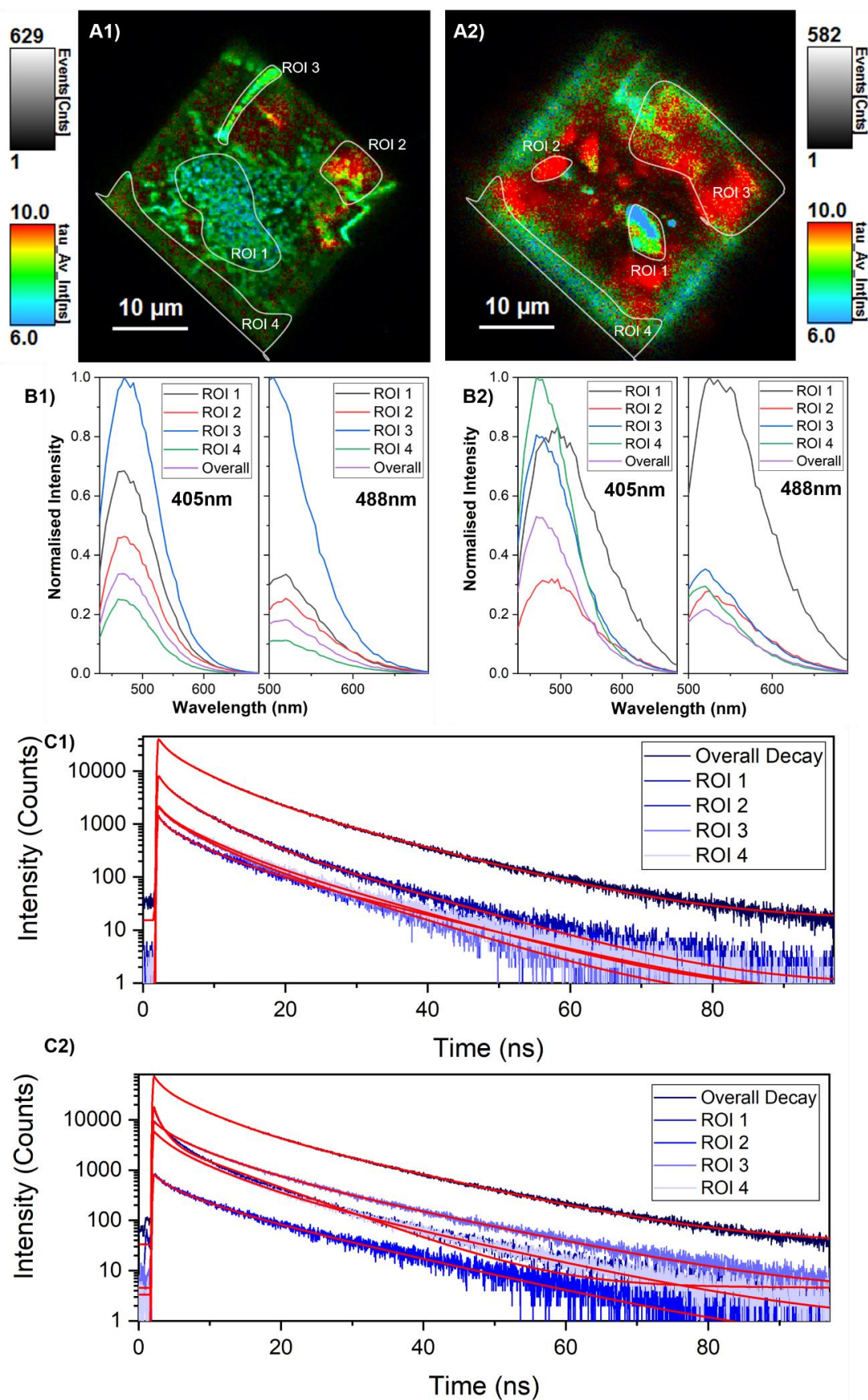


Figure 79 **Single-channel fluorescence lifetime imaging ensemble with spectral regions of interest showing uppermost (1) and inner (2) plane of chabazite calcined twice at 550 °C acquired at 488 nm:**

A) Average lifetime map, B) spectra in regions of interest, and C) decay curves for regions of interest and overall decay

Table 23 Table of lifetimes and amplitudes for chabazite calcined twice at 550 °C in Figure 79 for top plane and central plane both overall and in each region of interest. Some components are fitted to only two components based on a sufficiently good χ^2 value.

	Area	A ₁ (kCnts)	A ₂ (kCnts)	A ₃ (kCnts)	T ₁ (ns)	T ₂ (ns)	T ₃ (ns)	T _{Av} A (ns)	χ^2
Top Plane	Overall	7.2	21.1	16.4	12.4	4.7	1.0	4.6	1.594
	ROI 1	1.2	4.3	3.6	11.4	4.4	0.9	4.0	1.126
	ROI 2	0.5	0.9		11.8	2.9		5.9	1.49
	ROI 3	0.7	1.4		10.1	2.9		5.3	1.15
	ROI 4	0.8	1.4		10.3	2.9		5.6	1.58
Centre Plane	Overall	12.9	34.1	32.1	13.5	4.9	1.1	4.8	12.63
	ROI 1	3.8	12.3	7.1	8.5	1.3	0.3	2.1	11.69
	ROI 2	0.3	0.5	--	13.3	3.3	--	7.3	1.07
	ROI 3	3.1	6.1	--	12.5	3.3	--	6.4	1.9
	ROI 4	1.8	4.1	--	11.2	3.1	--	5.5	1.68

Figure 79 shows average data from fluorescence lifetime imaging of the sample. Two planes from the same crystal are depicted: the uppermost plane, and an inner plane 4 μm from the surface. Figure 79 shows FLIM data from the uppermost plane of an additional crystal. As demonstrated by the χ^2 values, the overall images as well as ROI 1 were fit to a triexponential fit, but other selected ROIs converged to a biexponential fit. The overall lifetime fitting for the central plane shows a high χ^2 value. This highlights the complexity of the decay behaviour here. This behaviour is particularly evident in ROI 1, whereas other ROIs in this plane have more stable biexponential decays. ROI 1 can therefore be pinpointed as being markedly different from other regions of the sample.

In all cases, it is evident from the decay curves alone that the overall lifetimes of these sample are longer than the previous sample, with the weighted average lifetime of this sample being approximately 4-6 times longer than the partially detemplated sample in Section 4.2.2, indicating that there has been an evolution in the nature of species present in this sample. The agglomerated deposits concentrated at the centre and along the edges still exhibit the shortest lifetimes in the map, with regions of longer lifetimes being attributed to the sub-surface emission regions visible in the two-channel z-stack. Although the average lifetime of the uppermost plane in Figure 77 appears longer than Figure 78, this is primarily attributed to the lack of a τ_3 component, as the numerical values for τ_1 (9.85 & 9.5 ns) and τ_2 (2.88 & 3.7 ns) are very similar.

The inner plane FLIM in Figure 77 shows the sub-surface deposits first seen in two-colour z-stack imaging in Figure 76. Where the two-colour stack showed that the subsurface deposits appeared to have emission in the red (i.e. 550-650 nm), the FLIM shows that these regions have a markedly longer lifetime with a τ_1 of 14.85 ns and a weighted τ_{Av} of 6.8 ns compared to the surface-bound agglomerated deposits.

Figure 79 and Table 23 show another one-channel FLIM dataset with spectral information in separate ROIs. Overall, the amplitude-weighted average lifetime of the top plane is longer than the inner plane (4.6 vs 4.8 ns), with the agglomerated deposits in ROI 1 of the uppermost plane exhibiting the shortest lifetimes in the top map at 4 ns. ROI 2 and ROI 3 exhibit longer lifetimes (5.9 and 5.3 ns respectively). However, spectral analysis at 405 nm and 488 nm exhibits minimal difference for each ROI with a common peak at 470 nm (at $\lambda_{\text{ex}}=405$ nm), indicating that the different lifetimes may be attributed to local environmental factors or morphological configurations.

The inner plane generally shows regions with longer lifetimes for sub-surface deposits. This is partially attributed to the greater degree of confinement emissive materials will experience this deep within the crystal. Particular attention is drawn to ROI 1, however, which not only exhibits a shorter average lifetime of 2.1 ns but also features a spectral peak at 495 nm rather than 465 nm (at $\lambda_{\text{ex}}=405$ nm), indicating that this emissive species is likely to be chemically distinct.

Based on morphology, lifetime, and spectra there appear to be three types of emissive deposits. The first being the well-defined agglomerates clustered on the surface, and the second and third being the larger sub-surface deposits, one of which exhibits a long lifetime and the other a short lifetime. In Chapter IV, a lengthening of lifetimes was attributed to both a decrease in organic material, and of occlusion within a pore structure. In the case of subsurface deposits in Figure 77, it is certainly likely that the greater degree of steric confinement will be responsible for their longer lifetimes. It is possible that the partially detemplated sample in Section 4.2.2 may have had shorter lifetimes due not only to its higher concentration of organic material, but due to smaller organic molecules formed from the early stages of the decomposition process^{xxi} of a larger parent entity that tended to experience less size-related confinement effects. Conversely, it is expected that this sample, which has been subjected to two high temperature heat treatments and appears predominantly white to the eye, is likely to have a different type of organic matter adsorbed; a lower concentration of molecules that are perhaps larger, remaining and in fact having been generated within the pores as a result of further hydrocarbon pool chemistry, thus experiencing more acutely the effects of spatial confinement.

^{xxi} Unpublished industrial *in situ* NMR data shows that at around 300 °C the adamantane cage loses its functional group, after which point it is presumed that each loose component begins to decompose into even smaller compounds.

4.2.4 Chabazite Calcined at 630 °C

Figure 80 shows two-colour confocal z-stack images of chabazite calcined once at 630 °C. Significant areas of the crystals appear to be optically transparent with less visible emission, as is the case in the as-synthesised samples in Section 4.1.1. This is in contrast to the partially calcined and sample calcined twice at 550 °C, which show more homogenous regions of emission all the way across the crystal. Emissive regions in this sample have a markedly different distribution characteristic to that seen in the partially detemplated and twice calcined chabazite samples. The distribution of circular deposits at the centre of the crystal face is no longer evident. Rather, there appear to be larger deposits of around 2 µm in diameter punctuating the top face. Close to the edges, some evidence of cracking is visible in these samples, although not to the extent that it is seen in the partially detemplated or the twice calcined samples.

In the inner planes, there appear to be larger emissive regions that emit more strongly in the 550 - 650 nm window. This is similar to the subsurface deposits observed in Section 4.2.3, although the regions appear 2-3 larger here.

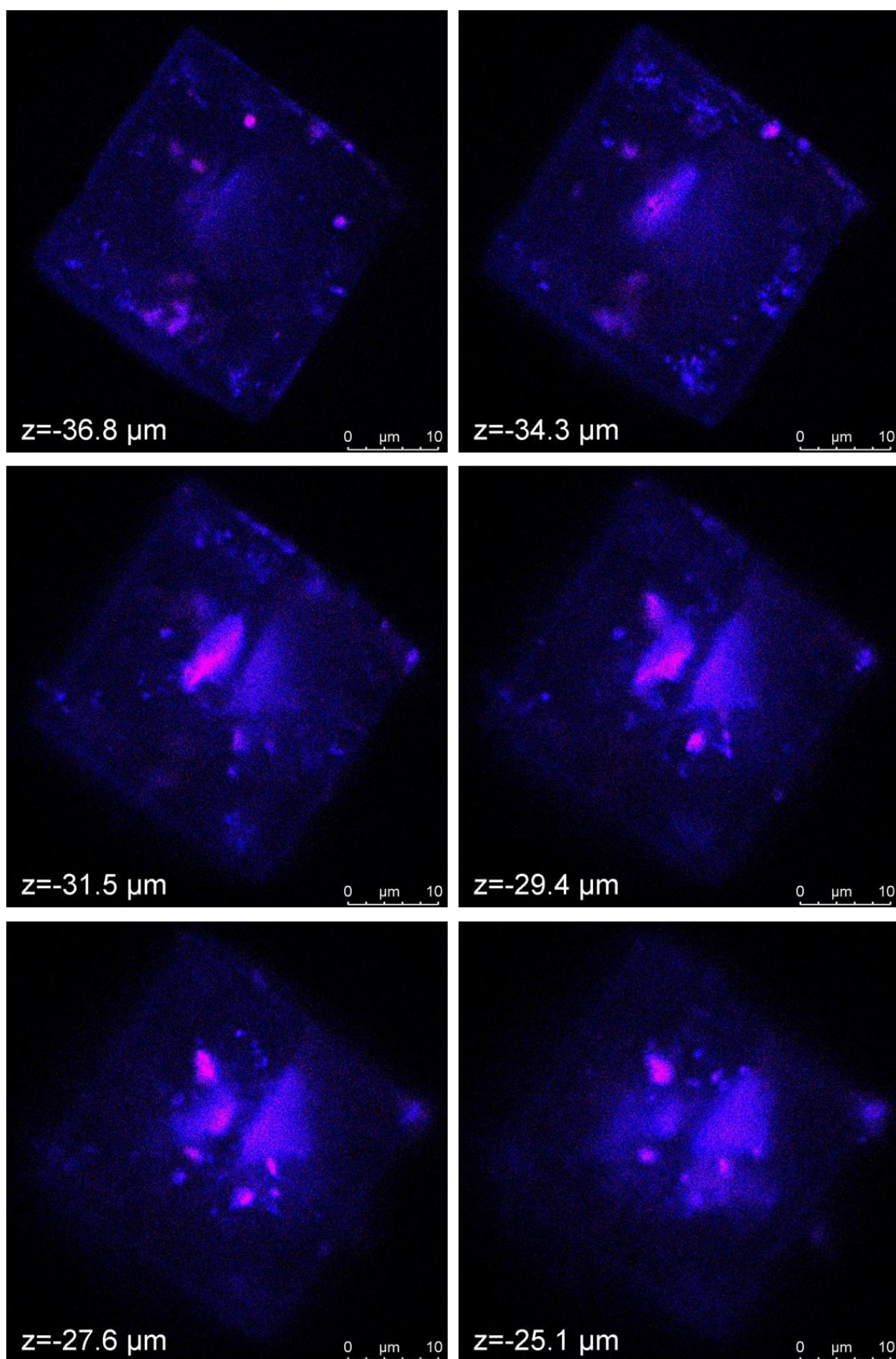


Figure 80 **Two-channel confocal images z-stack of chabazite calcined once at 630 °C acquired at 405 nm.** Blue channel is from 450-550 nm and red channel is 550-650 nm. Z values are nominal heights from stage with top plane at -36.8 μm and inner plane 11.7 μm lower at -25.1 μm .

Fluorescence lifetime imaging in Figure 81 show that this sample has the longest average lifetimes of all the samples, with the average lifetime distribution centred around 11 ns.

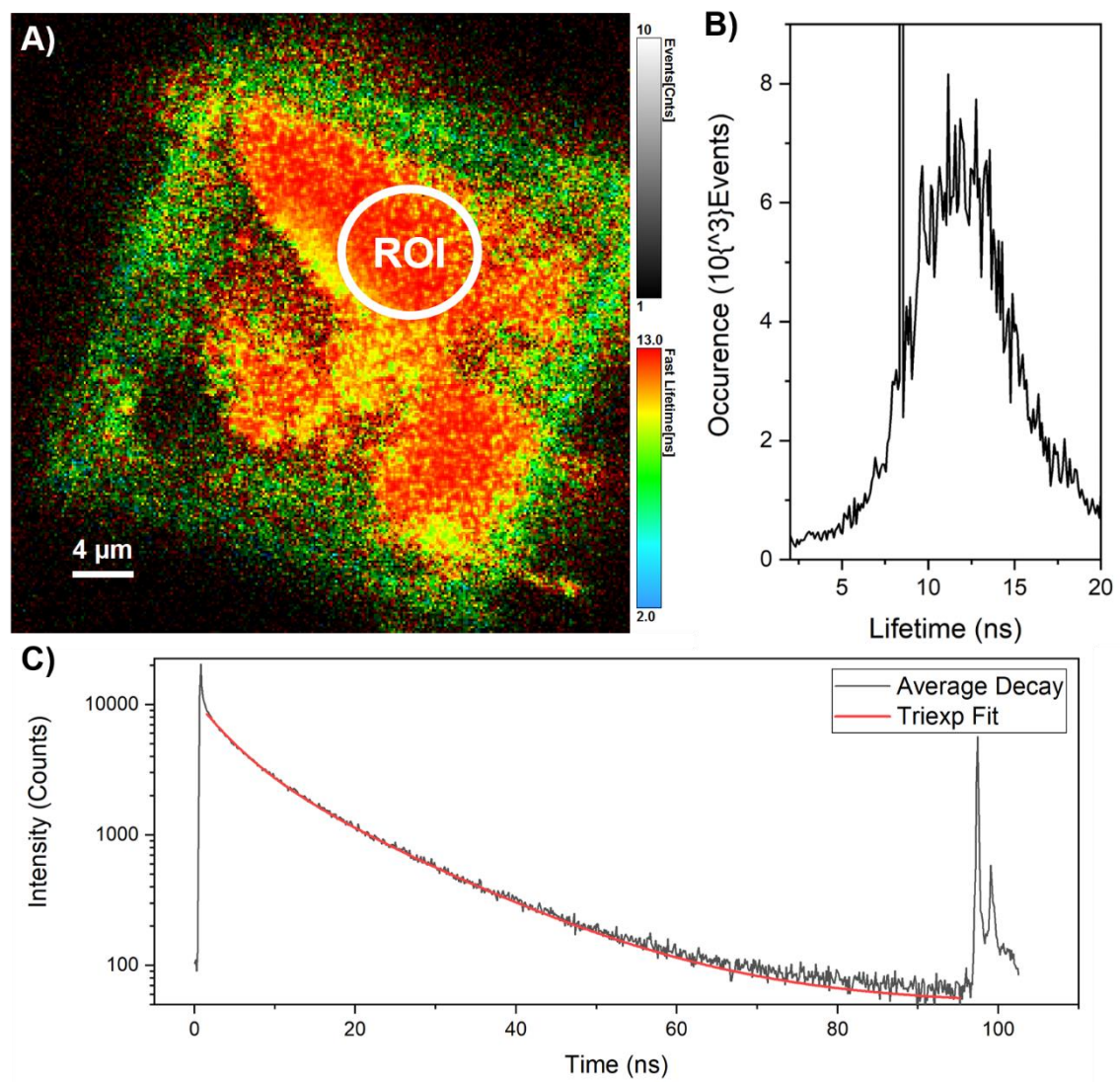


Figure 81 **Single-channel fluorescence lifetime imaging ensemble of the upper plane of a chabazite crystal calcined once at 630 °C acquired at 488 nm:** A) Average lifetime map, B) average lifetime distribution histogram, and C) average decay with truncated triexponential tailfit

Table 24 **Table of lifetimes and amplitudes for chabazite calcined once at 630 °C**

Sample	A ₁ [kCnt s]	A ₂ [kCnt s]	A ₃ [kCnt s]	T ₁ [ns]	T ₂ [ns]	T ₃ [ns]	T _{Av} A [ns]	χ ²
Average (Figure 78)	1.1	1.3	0	13.5	3.4	0	8.1	2.74
Region of Interest (marked)	3.2	4.3	1.2	14.9	3.7	8.5	8.6	1.47

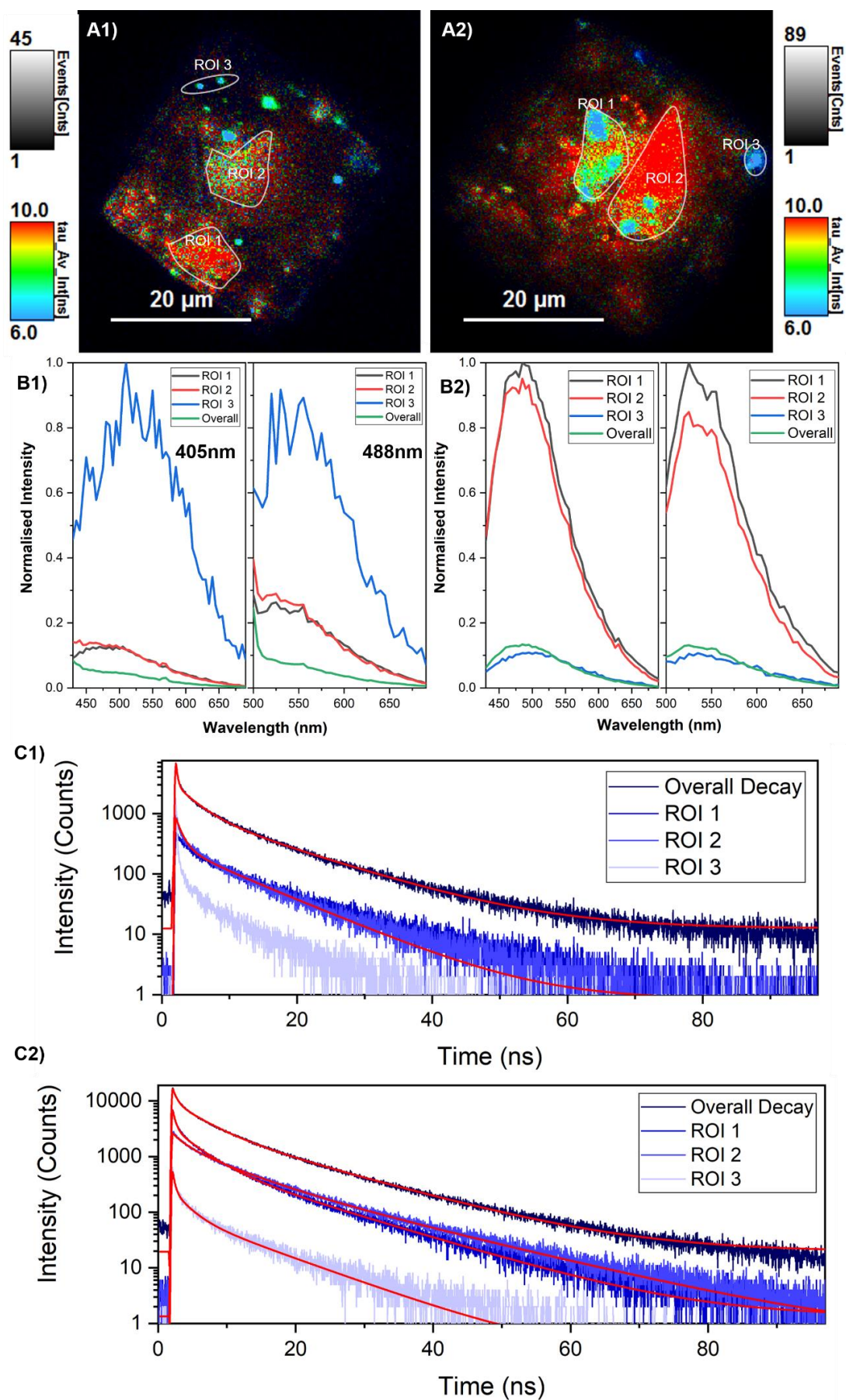


Figure 82 **Single-channel fluorescence lifetime imaging ensemble of chabazite calcined once at 630 °C acquired at 488 nm:** A) Average lifetime map and B) decay curves fit with an exponential reconvolution for regions of interest

Table 25 **Table of lifetimes and amplitudes for chabazite calcined twice at 550 °C in Figure 82 for top plane and central plane both overall and in each region of interest.**

	Area	A ₁	A ₂	A ₃	τ ₁	τ ₂	τ ₃	τ _{Av} A	χ ²
		(kCnts)	(kCnts)	(kCnts)	(ns)	(ns)	(ns)	(ns)	
Top Plane	Overall	1.1	5.9	1.9	12.0	0.3	3.1	2.3	2.36
	ROI 1	0.1	0.2		11.8	2.5		6.9	1.38
	ROI 2	0.1	0.3		10.9	2.2		5.1	1.1
	ROI 3	3.6	0.1		0.2	4.1		0.3	1.56
Centre Plane	Overall	3.6	9.3	6.4	12.7	0.6	4.0	3.9	2.43
	ROI 1	0.9	2.5	5.3	11.8	3.5	0.4	2.5	1.16
	ROI 2	1.1	1.6		12.6	3.2		7.0	1.29
	ROI 3	0.1	0.5		9.8	0.9		2.6	1.21

Figure 81 and Figure 82 shows lifetime data from the inner plane of a chabazite crystal calcined once at 630 °C^{xxii}. Based on the χ^2 values, like the previous sample the overall images were fit to a triexponential, whereas the majority of the ROIs converged to a biexponential fit. While the decay curve initially shows an extremely fast component is extant in the sample, this sample overall has the longest lifetimes with a weighted average lifetime of 8.1 ns. The edges have a shorter lifetime than the central areas, which are shown from the analysis of a region of interest to have a longer weighted average of 8.6 ns. The overall difference in lifetimes here again indicates some level of difference between the chemical speciation in this sample and previous samples, with the longer lifetimes in the centre of the crystal likely being associated with a greater confinement effect being imparted on the emissive materials.

Spectral information is also presented in Figure 82. The overall lower levels of emission can be seen in the traces. The majority of the regions of interest are predominantly emissive at 475 nm, however the concentrated blue dots in ROI 3 have a peak emission at 515 nm indicating this may be a different species.

^{xxii} There is an apparent discrepancy between the lifetime values in Figure 81 and Figure 82. Specifically, the weighted average lifetimes in Figure 81 appear longer (around 8 ns) than those presented in Figure 82. This can be explained by the nature of the algorithmic fit used. In Figure 81, an exponential tailfit is used where only the decaying portion is fitted, whereas in Figure 82 an exponential reconvolution is used where the initial portion of the decay including the IRF is synthetically fitted. As might be expected, the exponential tailfit will tend to be biased towards longer lifetimes, as extremely fast lifetimes associated with the early part of the decay are not included. Thus, even if only present in small amounts, the reconvolution fit will present comparatively shorter lifetimes as it considers all elements of the lifetime evolution. Arguably, a reconvolution might be seen as more ‘complete’, however the choice of fitting method depends on the intended outcome; a selective interest in longer lived components might, for example, justify the use of a tailfit. In either case, the comparison could be seen as an example of the subjectivity of numbers and the opacity of their meaning in the context of fluorescence studies, highlighting the need for comparative, qualitative interpretation to understand what they could mean in a non-abstracted sense.

Table 25 shows another set of one-channel FLIM data. The overall lifetime of the top plane appears very short at 2.3 ns. However, it becomes evident from an analysis of ROIs that this shortening is biased by the highly localised deposits that exhibit an extremely fast lifetime in ROI 2. In the inner plane, the overall lifetime again appears longer. Regions of longer lifetimes are concentrated at the centre of the inner plane, correlating to the lengthening of lifetimes seen due to spatial confinement. Additionally, the lifetimes, morphology and spatial distribution of the sub-surface deposits in ROI 1 appear to correlate with the sub-surface deposits in ROI 1 in Figure 2 A2. Across the chabazite calcined once at 630 °C, then, there appear to be at least two distinct types of emissive deposits, one of which may have commonality with a type also observed in the chabazite sample calcined twice at 550 °C.

4.3 Raman Spectroscopy & Mapping

4.3.1 Averaged Raman Spectra

Raman spectra were acquired at 830 nm for all samples except the partially calcined chabazite, which exhibited a fluorescence background that overwhelmed Raman signal as displayed in Figure 83. As previously assigned in Chapter 4, the Raman spectra for as-synthesised chabazite shows all the peaks of the occluded template at 777, 800, 941, 977, 985, 1103, 1200, 1283, 1305, 1368, 1444, and 1452 cm^{-1} . These are all attributed to the C-C stretching and H-C-C bending of the adamantane structural base unit of the quaternary ammonium salt¹⁸⁵.

In both calcined samples, the ensemble of OSDA assigned peaks are no longer visible, implying that significant concentrations of whole TMAda molecules are no longer present following the thermal treatment. Rather, the signal is comprised of bands at 335 cm^{-1} , 466 & 484 cm^{-1} and 803 & 831 cm^{-1} . The bands in the region 330 to 490 cm^{-1} are attributed to the aluminosilicate framework, with the 466 cm^{-1} being the well-established class A vibration of the SiO_2 unit cell^{186,187}. Further to this, the 484 cm^{-1} band is attributed to T-O-T bending in 4-membered rings and the 335 cm^{-1} band is attributed to 6-membered ring bending^{158,296}. The trio of peaks in the 330 to 490 cm^{-1} region are characteristic to the CHA topology, and absence of the 6-membered ring Raman band as well as broadening of the 4-membered ring Raman band has previously been attributed to amorphization secondary to desilication of the crystal¹⁵⁸. As such, the Raman spectra here also attest to the crystalline, compositionally stable nature of these samples.

The bands at 803 and 835 cm^{-1} have been variably reported in previous studies of Cu-SSZ-13^{297,298} samples but have not been explicitly assigned in these papers. It is suggested that the 835 cm^{-1} band may be due to extraframework Al species²⁹⁹. They have also been observed in PdOx/silicalite-1 substrates¹⁸⁸ and been assigned as symmetric $\nu_s(\text{T-O-T})$ stretches¹⁸⁹, which are nonetheless expected to be comparably weaker than the framework vibrations from 330-490 cm^{-1} . During faster, unoptimised acquisitions, this peak is not immediately visible, so it is not uncommon for this region of the calcined chabazite spectrum to appear flat.

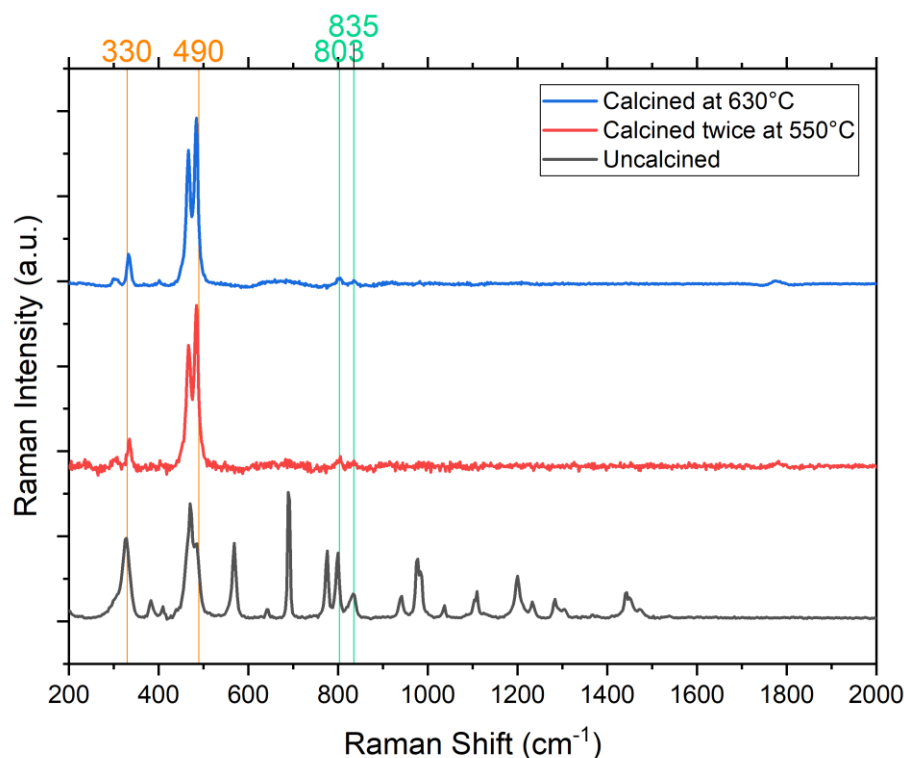


Figure 83 **Averaged Raman spectra acquired at 830 nm across ten different points**

4.3.2 Raman Mapping

Given that imaging appears to be showing visible distributions of an emissive material most likely attributable to hydrocarbon speciation, it is presumed that the lack of carbon-related Raman peaks in the averaged Raman spectra in Section 4.3.1 is due to their low concentration and subsequently weak signal. The framework peaks at 466 & 484 cm^{-1} overwhelmingly dominate the spectrum of the calcined chabazite samples. In a bid to detect the extremely low concentration of organic material believed to be present in the calcined samples, a smaller Raman detection window non-inclusive of the framework assigned peaks was selected. Knowing that carbon stretches were visible up to 1500 cm^{-1} from the uncalcined spectrum, the region between 1015-1470 cm^{-1} was selected with the view to detect residual template derivatives through extensive acquisitions.

The averaged Raman spectra for the region 1015-1470 cm^{-1} are shown in Figure 84. The peaks of the uncalcined sample are consistent with those obtained in the extended range Raman acquisition in Section 4.3.1. However, the two calcined samples show a new series of peaks not previously visible in the extended range scans. For each sample a series of maps tracking the presence of each peak are presented.

Raman mapping on the partially calcined sample was not viable due to the high fluorescence signal exhibited.

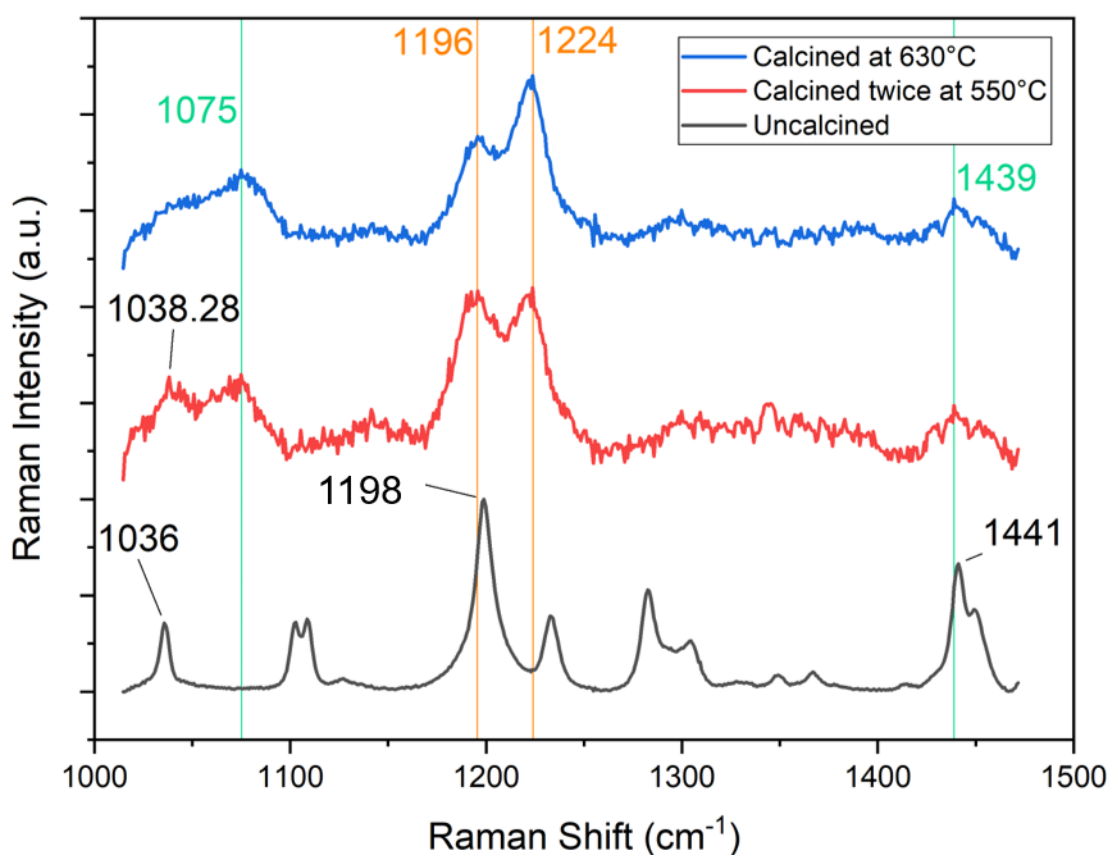


Figure 84 **Average Raman spectra from maps of each SSZ-13 sample** showing uncalcined chabazite (black), chabazite calcined twice at 550 °C (red), and chabazite calcined once at 630 °C (blue).

4.3.2.1 Uncalcined Chabazite

The averaged Raman spectrum, shown in Figure 84, features a clear signal-to-noise ratio, with peaks present at 1036, 1102, 1109, 1198, 1223, 1283, 1305, 1328*, 1349, 1367, 1414, 1441, 1450 cm^{-1} . These are consistent with peaks from the extended range scan in this region and are attributed to the occluded template material. Figure 85 shows a series of intensity maps showing the presence of selected peaks at 1035, 1102, 1198, 1223, 1282, and 1441 cm^{-1} across the crystal area. Intensity maps show that, as expected, all the peaks are broadly present all the way across the crystal face. This is due to template being relatively evenly distributed through the crystal, and the lack of z resolution given by the technique.

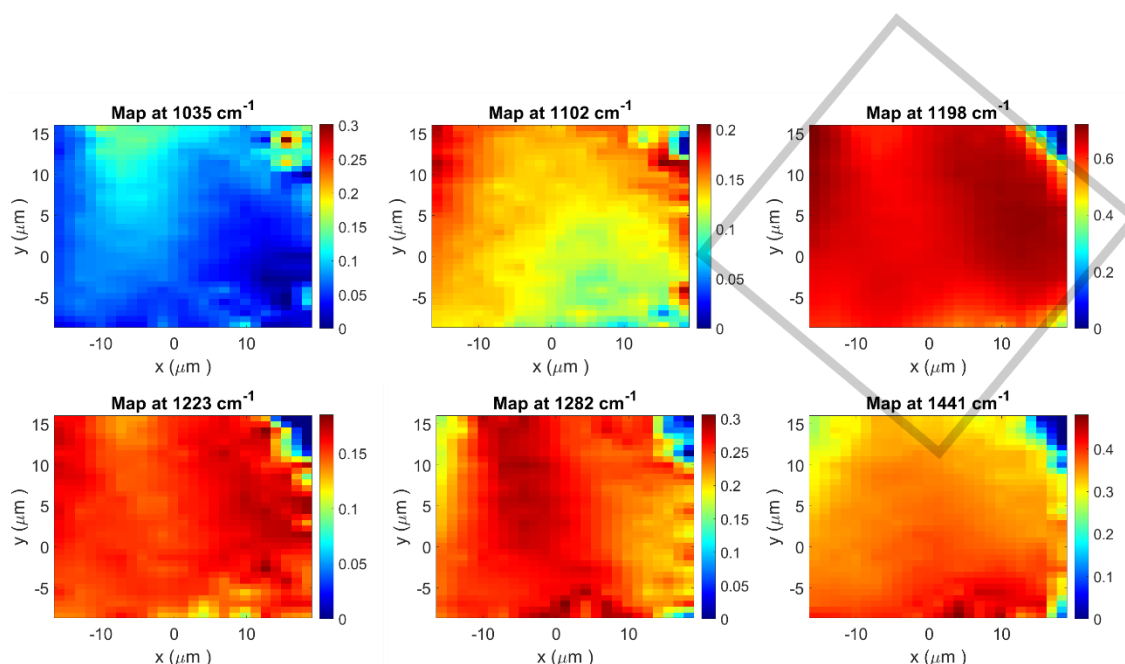


Figure 85 Raman maps of uncalcined chabazite at 1035, 1102, 1198, 1223, 1282, and 1441 cm^{-1} . Units for x and y axes are given in μm and colour scale on right indicates Raman peak intensity in counts. Outline of cubic crystal denoted by transparent grey line.

4.3.2.2 Chabazite Calcined Twice at 550 $^{\circ}\text{C}$

Figure 86 shows a series of Raman maps for chabazite crystal calcined twice at 550 $^{\circ}\text{C}$. Compared to the uncalcined sample, a different average Raman spectrum is visible in this sample. There are visible bands at 1038, 1075, 1196, 1223, 1299, 1347, and 1439 cm^{-1} . It is speculated the bands at 1196 and 1223 cm^{-1} are due to the framework^{296,300} (also marked in orange in Figure 84). It is possible to view the band at 1196 cm^{-1} as being the same as the template-assigned band at 1198 cm^{-1} in the uncalcined sample (see Figure 85). However, the corresponding distribution of 1196 and 1223 cm^{-1} perhaps indicate that the bands should be viewed as a doublet associated with the framework.

The band at 1223 cm^{-1} has previously been assigned as an asymmetric Si-O-Si stretch, potentially arising as a result of silicon enrichment at the surface of the crystal. In line with this assignment to framework vibrations, the maps for the peaks 1195 and 1223 cm^{-1} show a relatively intense distribution all the way across the crystal face. In particular, the 1223 cm^{-1} map shows the greatest intensity around the edge of the map, correlating with silicon enrichment towards the external aspects of the crystal.

Bands at 1038, 1075, 1299, 1347, and 1439 cm^{-1} are therefore assigned to vibrations from residual organic species adsorbed to the framework (also marked in aqua in Figure 84). It is challenging to assign these bands to specific vibrations given that it is not precisely known the nature of carbonaceous material extant in the sample after a two-stage heat treatment. However, it is possible to comment on the spatial distribution of some of these bands. In particular, the peak at 1038 cm^{-1} appears to be distributed towards the centre of the crystal, while the peak at 1075 cm^{-1}

appears distributed more intensely towards the edge of the crystal. In both cases, these bands are spread over a larger surface area of the crystal. Conversely, the bands at 1344 and 1439 cm^{-1} appear to be highly concentrated in a single localised area of the crystal. This would imply that in attributing the peaks to a particular chemical entity, the difference in spatial distribution would likely correlate to the presence of different molecular species. The species responsible for the band at 1439 cm^{-1} , for example, is likely to be separate to the species generating the band at 1038 cm^{-1} , however, there is arguably similarity between the maps for 1439 and 1344 cm^{-1} , meaning these two bands could be vibrational modes of the same molecule. Based on spatial distribution patterns, these maps indicate there might be as many as three types of organic molecules present (1439 cm^{-1} , 1077 cm^{-1} , and 1038 cm^{-1}).

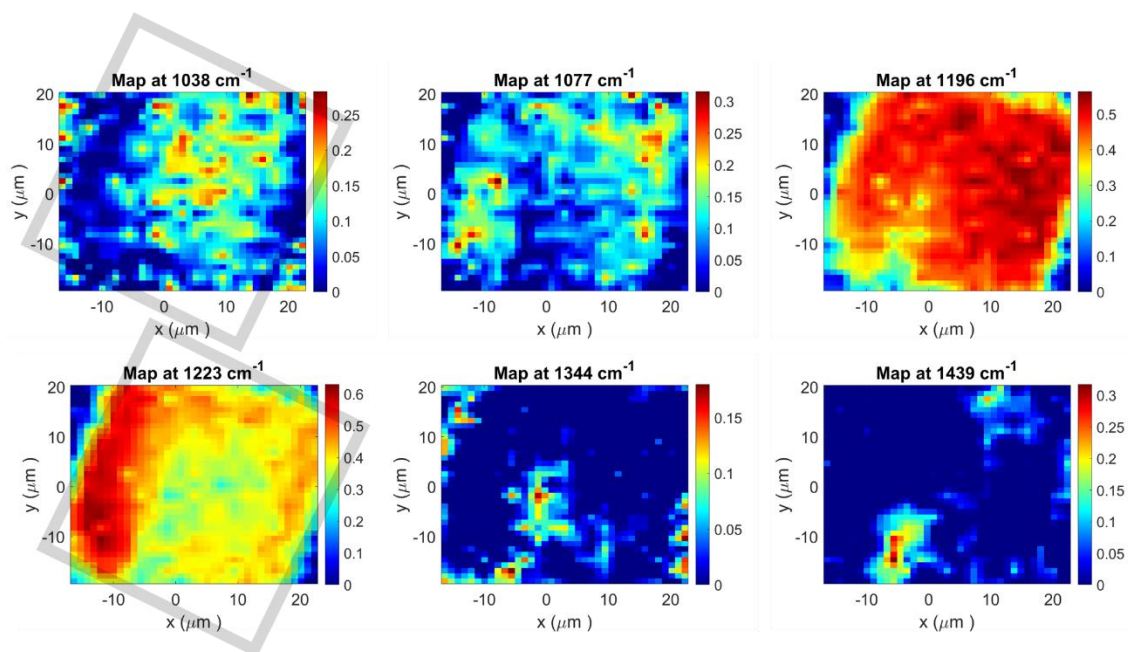


Figure 86 Raman maps of chabazite calcined twice at 550 °C at 1038, 1077, 1196, 1223, 1344, and 1439 cm^{-1} . Units for x and y axes are given in μm and colour scale on right indicates Raman peak intensity in counts. Outline of cubic crystal is shown as thick grey outline in map 1038 and 1223 cm^{-1} .

4.3.2.3 Chabazite Calcined Once at 630 °C

Figure 87 shows a two sets of Raman maps of chabazite crystal calcined once at 630 °C acquired from two crystals. Similar to the twice calcined chabazite in Section 4.3.2.2, the framework assigned peaks at 1196 and 1223 cm^{-1} are visible in the averaged Raman spectrum for both crystals. As expected, the intensity maps show peaks distributed across the whole crystal with 1223 cm^{-1} again being more concentrated around the edges.

The bands at 1038 and 1074 cm^{-1} both show characteristic distributions across the two samples. In Figure 87A, the 1074 cm^{-1} band is distributed evenly across the sample at a lower intensity than that of the framework peaks, and residual 1038 cm^{-1} is visible at the centre of the crystal with a comparable distribution pattern to the twice calcined sample. The band at 1439 cm^{-1} is also present in this sample, and like the twice calcined sample, appears to be tightly localised to a

single area. In Figure 87B, the 1038 cm^{-1} map shows a localised distribution in the centre, and the 1074 cm^{-1} map appears more broadly distributed across the crystal similar to Figure 87A. The distribution of this looks similar to the subsurface emission regions shown in Figure 82.

The averaged spectra in Figure 84 show that the region between 1299 and 1400 cm^{-1} is depleted compared to the twice calcined sample implying that this sample may have lower levels of coke present. This is reflected further in the Raman maps, which show minimal meaningful signal at 1344 or 1439 cm^{-1} .

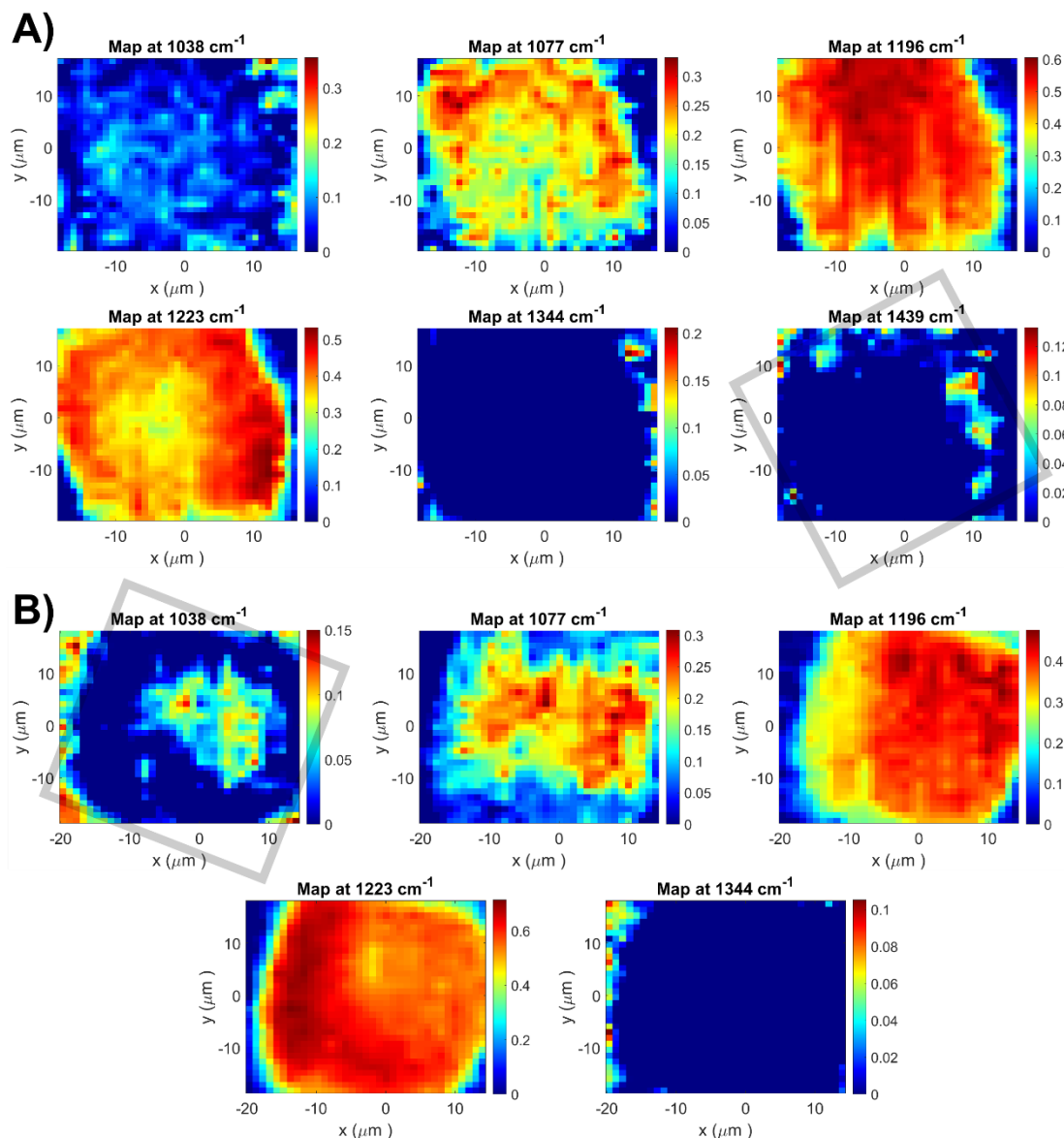


Figure 87 Raman maps of two chabazite crystals (A and B) calcined once at 630 °C at 1038 , 1077 , 1196 , 1223 , 1344 , and 1441 cm^{-1} . Units for x and y axes are given in μm and colour scale on right indicates Raman peak intensity in counts. Outline of cubic crystal denoted in transparent grey line.

5 Discussion

5.1 Ascribing Fluorescence to Chemical Speciation

Not all organic molecules are fluorescent. The following section will discuss what chemical species might be present in the samples imaged. Table 26 summarises some of the fluorescence emission properties for two broad categories of chemical species: PAHs and carbon nanostructures.

Table 26 Summary of fluorescence emission characteristics including wavelengths of emission (λ_{em}) for a given wavelength of excitation (λ_{ex}) and associated lifetime values drawn from a selection of literature sources

Type	Emissive Product	λ_{ex} (nm)	λ_{em} (nm)	Average Lifetime (ns)
PAH	Anthracene ³⁰¹	245	401	5.7 ¹⁸² (vapour phase) 5.1 ³⁰² (in methanol) 5.3 ³⁰² (in cyclohexane)
	Anthracene excimer in NaX zeolite ¹⁸⁴	370	520	10-43
	Benzo[a]anthracene ³⁰³	288	387	
	Benzo[a]pyrene ³⁰³	297	405	26.7 ³⁰⁴ (in water)
	Benzo[k]fluoranthene ³⁰³	307	403	10.2 ³⁰⁴ (in water)
	Chrysene ³⁰³	268	382	13.4 ³⁰⁵ (in cyclohexane) 30 ms ³⁰⁶ (crystalline form)
	Dibenz[ah]anthracene ³⁰¹	297	430	
	Fluoranthene ³⁰¹	281	465	44 ³⁰⁷ (crystalline form) 32 ³⁰⁴ (in water)
	Naphthalene	266	325	16.6 ³⁰⁵ (in cyclohexane) 39 ³⁰⁸ (in water) 34 ³⁰⁴ (in water)
	1-methylnaphthalene ³⁰⁹	265	340	30 (in water)
	2-methylnaphthalene ³⁰⁹	265	340	24 (in water)
	Dinapthylethane in zeolite Y ¹⁸³	275	325	-
	Dinapthylpropane in zeolite Y ¹⁸³	280	330	-
	Dinapthylpropane dimer in zeolite Y ¹⁸³	280	405	-
	Phenanthrene ³⁰³	251	366	14.6 ³⁰⁵ (in cyclohexane) 37.4 ³⁰⁴ (in water)
Carbon nanostructures	Nanodots formed in MgAPO-44 ³¹⁰	550	630	4.1-6.5 (in water)
	Nanodots formed in ITQ-29	450	525	-
	Purified SWNT in dimethylformamide ³¹¹	634	1000-1300	1.3

	SWNT produced by laser ablation dispersed in solution ³¹²	337	520	2.3
	Oxidised MWNT ³¹³	204	454	4.6
	Oxidised MWNT modified with 1,4-butanediamine ³¹³	356	442	6.1
	Oxidised MWNT modified with 1,2-propanediamine ³¹³	434	457	3.4
	Oxidised MWNT modified with 1,2-ethylenediamine ³¹³	337	410	10.9
	DNA-wrapped SWNT ³¹⁴	730	1128	12.5
Other	Graphene oxide (in water) ³¹⁵	400	620	0.03-0.14

Table 27 Comparison of principle Raman features in selected PAHs based on experimental data from literature sources^{316,317}

	Napthalene	Anthracene	Phenanthrene	Chrysene	Pyrene	Vibration type
2	513 ^S	521 ^W	551	570	595 ^S	C-C-C bending
4	765 ^S	754 ^M	715	773	-	Ring breathing
6	1021 ^M	1011 ^M	1039	1021	1067 ^W	C-C stretching
10	1383 ^S	1409 ^S	1351	1380	1407 ^S	Ring deformation & C-C stretching
12	1464 ^M	1484 ^M	1443	1436	-	C-H bending & C-C stretching
13	1578 ^M	1559 ^M	1526	1576	1594 ^M	C=C stretching (in-phase)
14	1629 ^W	1632 ^W	1573	1604	1629 ^M	C=C stretching
17	3057 ^S	3052 ^S	3075 ^S	3064 ^S	3053 ^S	C-H stretching (out of phase)

S=strong, M=moderate, W=weak

5.1.1 Polycyclic Aromatic Hydrocarbons

When initially surveying literature for information on fluorescent organic species, the most commonly discussed family of molecules are aromatic hydrocarbons or hydrocarbons containing conjugated double bonds. It has been established in Chapter 2 that fluorescence is an electronic phenomenon occurring as a result of electrons undergoing energy transitions. In the context of molecular structure, these electrons must necessarily be delocalised or ‘ π ’ electrons, or lone pair electrons. Compounds containing π -electrons are likely to fluorescence. Aromatic rings, in

particular, have smaller HOMO-LUMO gaps that correspond to $\pi \rightarrow \pi^*$ transitions. This is increasingly the case the more highly-conjugated pi systems are.

The act of substituting may also make molecules more or less likely to fluorescence depending on the parent molecule, a concept rather authoritatively examined by Williams and Bridges³¹⁸. Where a substituent tends to localise pi electrons, fluorescence will be diminished. Benzene, for example, is a weakly fluorescent aromatic compound requiring 20-25 $\mu\text{g/mL}$ to detect fluorescence with an absorption peak at 254 nm and an emission maximum at 291 nm. Substituting an ortho-para-directing group such as NH_2 to create aniline optically activates the benzene ring, enhancing the freedom of the pi-electrons and by extension its ability to fluoresce, being detectable with at concentrations of only 0.01 $\mu\text{g/mL}$. Conversely, substituting a meta-directing group like NO_2 to form nitrobenzene deactivates the ring's fluorescence. Broadly speaking, trends in ortho-, para-, and meta-directing groups tend to be relatively, but not wholly, consistent, with aromatic compounds substituted with NH_2 , OH , F , OCH_3 , NHCH_3 , and $\text{N}(\text{CH}_3)_2$ groups tending to be visibly emissive, and those with Cl , Br , I , and NHCOCH_3 tending to be less or non-fluorescent. A typical example of the effects of Br or I substitution is their quenching effect in fluorescein³¹⁹. The effect of disubstitution is less clear, although as molecules become more complex, it would appear that increased emission associated with higher orders of conjugation tend to outweigh the quenching effects of meta-directing groups. This is particularly the case in polycyclic aromatic hydrocarbons (PAHs) where the number of pi-electrons available from the increased number of rings in compounds like naphthalene or anthracene lead to significantly greater fluorescence than that observed in benzene. Luminescent PAHs have been shown to form readily in simple setups such as gas flame reactors³²⁰.

Spectroscopic studies of PAH monomers where emission is dominated by $\pi \rightarrow \pi^*$ transitions show that emission generally lies between 300-450 nm. This generally appears to be the case from the selection of literature figures presented in Table 26. Experimentally, it is not uncommon in contexts that expect to see PAH formation, such as studies of soot formation in flames, to see broadband, structureless emission extending from beyond 450 nm. One school of thought attributes higher wavelengths of emission to progressively bulkier PAHs possessing over four cyclic rings^{321,322}. More recent studies have refuted this, instead attributing emission in the region of 500-600 nm to the formation of dimers of moderate-sized PAHs³²³. Where dimers are present, it is thought that they may have longer lifetimes than monomers measured under the same circumstances^{324,325}. This is supported by studies of anthracene and bisnaphthalenes that have been loaded into zeolite frameworks and form dimers as a result of geometric confinement^{184,183}. In a potentially chicken-egg line of reasoning, the broadening of the emission profile and red shift of peak emission is attributed to PAH dimerization, although this has broadly been supported by other studies performed outside of zeolites on related molecules³²⁶⁻³²⁸.

It is also important to remember that due to the size limitations of the cage structure, there is an upper limitation on the size of PAH that might fit within the zeolite. Increasingly large structures like chrysene, which are listed in Table 26, may become prohibitively large, especially when functionalised. This is relevant when rationalising whether the lifetimes exhibited are compatible with literature values of PAH species; longer lifetimes like those seen in fluoranthene may not be seen in a zeolite as this molecule might be too large to fit in the pores.

Thus far, PAHs, highly conjugated molecules, and certain substituted derivatives of these are considered to be the primary classes of ‘natively’ fluorescent organic molecules. An additional class of organic compounds that could be considered in the context of zeolites are those that become fluorescent following a chemical process. A typical example of this from the life sciences is cortisol, which is non-fluorescent but becomes so fluorescent when dissolved in a solution of concentrated sulphuric acid and ethanol that it may be used as an assay³²⁹. Another example from the life sciences that involves an acid-induced fluorescence is 5-aminolevulinic acid (5-ALA) induced fluorescence of protoporphyrin IX (PpIX), which can be used to visualise regions of metabolic activity in tissue, such as gliomas, intraoperatively³³⁰. It is possible to consider that the acidic nature of zeolites may have the capacity to chemically induce fluorescence. This concept has indeed already been demonstrated in studies by Karwacki *et al.* where thiophene-based chemosensors were artificially introduced into zeolite frameworks to visualise acid sites¹⁴⁵.

Raman spectra for PAHs have been modelled and experimentally validated relatively comprehensively^{316,317}. Generally, the strongest Raman modes are those associated with C-C & C=C stretching as well as ring breathing, which have been summarised in Table 27, and shift with increasing conjugation as a result of changes in π -electron distributions. These modes are predominantly found between 500 and 1700 cm^{-1} at visible range excitation, although it has been noted that resonance effects dependent on the wavelength of excitation (in particular UV) will result in the preferential resolution enhancement of modes between 1400-1600 cm^{-1} ³³¹. Further to this, these vibrations can also be influenced by steric repulsion, hydrogen bonding, and the presence and location of functional groups, so it is difficult to observe definitive systematic variations in peak position as a function of PAH structure or size³¹⁷. Similarly, the weak polarisability of most functional groups makes the generally Raman inactive, so the technique cannot always specify to what extent substitution may have occurred.

Although studies exist on template removal in zeotype structures, there are none that directly relate to TMAda in CHA frameworks. Related studies on the topic utilising vibrational spectroscopy include removal of tetrapropylammonium (TPA) from MFI zeolites^{332,78,145}, 1,9-diaminononane from cobalt containing SBE aluminophosphates³³³, tetraethylammonium from zeolite β ⁸⁶, triethylamine from SAPO-5 and $\text{AlPO}_4\text{-5}$ ³³⁴, and TPA & tetramethylammonium in SAPO-37³³⁵. Geus *et al.* noted the nonuniform degradation of template due to the crystal’s internal

growth structure and use IR spectroscopy to track the diminishment of C-H bands over the course of the calcination³³².

It is likely that pyrolysis of the TMAda template molecule ($C_{13}H_{25}NO$) within the confines of a framework will see both the destruction and regeneration of derivative organic species through a mechanism called the hydrocarbon pool. It is expected that the template, which features a trimethylamine (TMA) component, will act as sufficient fodder for substituted aromatics to form. Separate studies of TMA decomposition on Pt(111) substrates using electron energy loss spectroscopy (EELS) indicate that sequential CN bond cleavage occurs, followed by the generation of dimethylamino species ($(CH_3)_2N$) from 127 °C, methylnitrene species (CH_3N), methylene amido species (CH_2N) and finally dehydrogenation at temperatures exceeding 227 °C³³⁶. Based on previous literature that studies the hydrocarbon pool mechanism in the methanol-to-olefins reaction in CHA frameworks^{203,337} and ethene to propene conversion in MSE frameworks²⁷³, some specific chemical species might be expected. In methanol conversion in CHA and MFI frameworks, these include neutral aromatics, charged monoenyl and cyclopentenyl species, charged poly-alkylated benzenes, charged alkylated naphthalenes, and complex carbenium species³³⁸. In ethene to propene conversion, substituted bicyclic aromatics, naphthalenes, and isopropylmethylnaphthalenes can be expected.

5.1.2 Graphitic Compounds

Large scale solid-state graphitic materials are not reported to have visible emission and rather, on their own, are generally considered to be efficient quenchers that quash emission from other fluorophores via long range energy transfer processes^{339,340,341}. This characteristic has been exploited in biosensing technologies³⁴². However, physically or chemically manipulating can lead to instances where fluorescence might be observed. There is limited literature that suggests as-prepared graphene oxide might exhibit fluorescence. This has been attributed to local disorder-induced states in the π - π^* gap of sp^2 sites, bond disorder-induced energy gaps, and quasi-molecular fluorophores formed by COOH and similar dangling functional groups³¹⁵. The existence of structural defects has, in turn, primarily been attributed to the generally abrasive synthesis process, which involves the oxidation and exfoliation of graphite sheets³⁴³. Graphene oxide has also been shown to exhibit ultrafast fluorescence (1 ps – 2 ns) when dispersed in water³¹⁵.

5.1.3 Carbon Nanostructures

Another class of potentially luminescent species are carbon nanostructures. These include morphologies like nanotubes, nanodots or nanoribbons³⁴⁴ that have all been shown to luminesce. The chemical composition can vary from being graphitic in the case of single or multiwalled carbon nanotubes (SWNT or MWNT) to aromatic³⁴⁵ in the case of some nanodots. They are

primarily grouped together by their size, which are generally not larger than a few tens of nanometres and is the reason for the complex 1D quantum effects are thought to contribute to some of the pathways of emission.

Carbon nanoparticles generated via nitric acid oxidation of carbon soot with a known graphitic composition were shown to luminesce at 520 nm with a 450 nm excitation source³⁴⁵. In this study, luminescence was similarly attributed to the incorporation of either nitrogen or oxygen defects in the form of dangling functional groups.

Carbon nanotubes have been shown to luminesce between 500-600nm if oxidised or functionalised^{346,312} and have lifetimes ranging from 1.3-12.5 ns (see Table 26). This is dependent on the synthesis method and functionalisation or post-processing of the tube. Their emission intensity is great enough to image³¹¹. Zeolites have been used in the past as a size-selective substrate to grow SWNTs on³⁴⁷. In these studies, metal-exchanged LTA, FAU, and SOD-type frameworks were used to catalytically decompose vapour-phase acetylene (C_2H_2) in a fixed bed flow reactor. A study of spent coked FCC FAU catalyst residue has also showed that pulsed 532 nm laser ablation can form SWNTs and silica nanowires through vapour/solid-liquid-solid self-assembly³⁴⁸.

Carbon nanodots have previously been prepared from organic templated aluminophosphate zeotypes^{310,349,350,351}. These studies are of interest because they purport the formation of emissive nanoparticles through effectively partially detemplating a sample. In a study by Mu *et al.*, an as-synthesised MgAPO-44 zeolite was heated from room temperature to 400 °C in air and held isothermally at the maximum temperature for 4 hours, during which time it is posited that carbon nanodots formed via carbonisation of the templating agent *N*-methylpiperazine³¹⁰. Nanodot-containing zeolite was then dispersed in water at different concentrations. X-ray photoelectron spectra (XPS) pointed towards the presence of C=C, C-N/C-O, and C=O bonds with approximately 22% of the content containing N-groups. The luminescence appeared to be concentration dependent, with the highest concentration (1.36 g/L) yielding $\lambda_{ex} = 550$ nm and $\lambda_{em} = 625$ nm versus a concentration of 0.92 g/L having $\lambda_{ex} = 520$ nm and $\lambda_{em} = 600$ nm. A similar study was performed in ITQ-29 (LTA) zeolite, which also claimed that fluorescent carbon nanodots could also be formed in small pore zeolite framework types ITW but not MFI or BEA³⁵¹. In all studies, the emission is generally centred at 500 nm and above, and they report some degree of dependence on the excitation wavelength.

In Raman spectroscopy, carbon nanostructures exhibit a D and G peak³⁵². The D band at 1332 cm^{-1} represents carbon atom vibrations in disordered graphite and the G band at 1582 cm^{-1} is related to electron-phonon coupling interactions of ordered sp^2 carbon atoms in a 2D hexagonal lattice. There are no clear D and G peaks visible in the Raman maps acquired, which also feature particularly long acquisition times. However, being collected at 830 nm in a bid to reduce the

overall fluorescence background of the samples, it is also the case that the spectra have been acquired at a wavelength that is not tailored or sensitive to graphitic structures, and that resonance enhancement using an excitation source such as 514 nm should probably be attempted first before ruling out the presence of carbon nanostructures on the basis of the Raman data³⁵².

5.1.4 *Additional Lifetime Augmenting Factors*

It is broadly evident from the table above that numerous other factors may affect lifetime. In the case of PAHs, the physical form and solvent are shown to dramatically change the lifetimes. This highlights the highly contextual nature of lifetime measurements, with the local environment requiring serious consideration in the interpretation of results. Beyond what is summarised in the table, there are some further parameters that might affect lifetimes.

Early spectroscopic studies exploring the effect of methyl groups on the fluorescence behaviours of aromatic molecules saw an increase in fluorescence lifetime³⁵³, although more recent in-depth studies demonstrate that while methyl groups do alter the lifetimes, it depends on where they have been substituted, how extensive asymmetry within the molecule generated by the substitution is, and what the parent aromatic is³⁵⁴. Naphthalenes, for example, were shown to have shorter lifetimes with the addition of methyl groups³⁰⁹.

Another parameter that may have an effect on lifetime is temperature. Between 500 – 1200 K (227 – 927 °C) in an inert gas environment, naphthalene, fluorene, anthracene, and pyrene were all found to decrease in lifetime with increasing temperature³⁵⁵.

The zeolite framework is likely to have an overall effect on the emission properties based on the confines of the geometry as well as the chemically active sites throughout. Generally, it is thought that confinement will serve to sterically stabilise molecules and prevent certain vibrations, which might also lead to an increase in lifetime¹¹⁷.

On a more generic level, concentration is well known to cause an effect on the lifetime of a fluorophore, although whether it induces quenching or lengthening is highly dependent on the sample. Using a classic example of common laser dyes, rhodamine B experiences quenching at high concentrations but coumarin does not³⁵⁶. Increase concentration of pyrene indicates formation of an excimer that leads to a more complex multiexponential emission with a longer component³⁵⁷. Addressing the acidity of zeolite frameworks, the effect of pH on lifetime is not globally well established. Sources in the life sciences^{358,359} and food science indicate that seemingly more alkaline conditions might increase lifetimes with studies showing dyes that are sensitive to pH changes can experience lifetime increases of 1-2 ns³⁶⁰. Based on this, it may be the case that the pH of zeolites could globally suppress lifetimes, although the extent to which this is the case is difficult to ascertain. The study of carbon nanodots generated during zeolite template

pyrolysis seemed to show that when dispersed in solution, low pH (1-5) led to a decrease in photoluminescent intensity³¹⁰.

5.1.5 Summary

So far it can be concluded that:

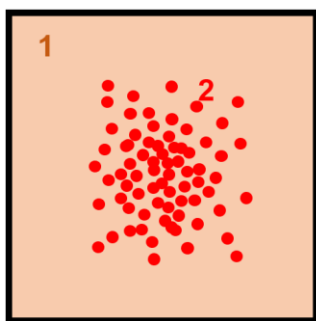
- It is highly likely and reasonable, based on literature sources, that the products being formed during the detemplation of SSZ-13 will be fluorescent
- Substituted PAHs are expected to form and comprise the bulk of emission between 400-450 nm
- The formation of dimerised PAHs is feasible based on the extensive steric confinement from the framework, and would be responsible for some emission above 450 nm
- Carbon nanostructures can be expected to form, and would be broadly responsible for emission from 450 nm and above
- Modified graphitic species may be present and would be responsible for emission from 450 nm and above
- Chemically induced fluorescence from non-natively fluorescent molecules could be reasonable on the basis that the framework imparts a chemically relevant effect

Note that for all of the trends in lifetime and emission characteristics described here, the effect of the zeolite framework has not fully been taken into account. Certainly, it is expected that the steric confinement and abundance of chemically active sites will have an additional effect on the lifetimes, although it is difficult to definitively state what these effects will be.

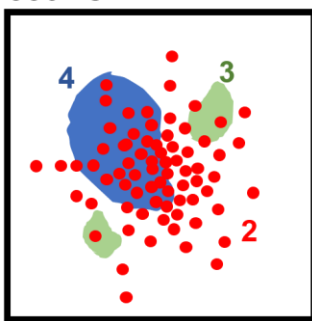
5.2 Evidence of Different Emissive Species

Based on differences in deposit shape, distribution, lifetime, and Raman mapping it is possible to speculate that confocal imaging is showing different types of emissive species in the partially detemplated chabazite, the chabazite calcined twice at 550 °C, and the chabazite calcined once at 630 °C. Five characteristic emission behaviours have been proposed in these crystals, as summarised in Table 28 and Figure 88. The morphology & distribution, emission windows, and average lifetimes have been summarised and then tentatively linked to some Raman features. In all cases, they are believed to be due to carbonaceous species rather than the framework, based on the wavelengths of visible excitation and emission.

A) Partially Calcined



B) Calcined Twice at 550 °C



C) Calcined Once at 630 °C

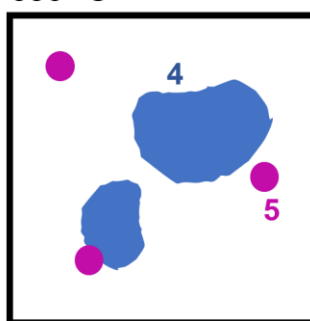


Figure 88 **Schematic diagram of five types of emissive behaviours in three samples.** Black lines demarcate the edge of the crystal.

Table 28 *Summary of different proposed chemical species based on their emissive features*

#	Sample	Morphology & Distribution	Emission Peak at $\lambda_{\text{ex}} = 405$ (nm)	Emission Peak at $\lambda_{\text{ex}} = 488$ (nm)	τ_{Av} (ns)	Raman Features	Speculated Species
1	Partially calcined	Broad emission across whole crystal face	450-500	450-550	1-2	Unknown	Preliminary template decomposition derivatives
2	Partially calcined	400 nm deposits clustered in center of the crystal	450-550	450-550	-	Unknown	Polycyclic aromatic hydrocarbons
2	Calcined twice at 550 °C	400 nm deposits clustered across center of the crystal face	470	500	4-5	-	Polycyclic aromatic hydrocarbons
3	Calcined twice at 550 °C	Medium-sized subsurface deposits, approximate $\varnothing 2\text{-}4\ \mu\text{m}$	495	535	2-3		Carbon nanonstructures
4	Calcined twice at 550 °C	Large regions of subsurface emission, $\varnothing 5\ \mu\text{m}$ or greater	485	520	6-7	1038 & 1077 cm^{-1}	Substituted or highly confined polycyclic aromatic hydrocarbons
5	Calcined once at 630 °C	Concentrated regions of emission, surface and subsurface	505	535	2-3	-	Carbon nanostructures
4	Calcined once at 630 °C	Large regions of subsurface emission	480	530	7-8	1038 & 1077 cm^{-1}	Substituted or highly confined polycyclic aromatic hydrocarbons

5.2.1 Type 1 Emission

The first type of emission behaviour (hereafter termed ‘Type 1 Emission’) is denoted in Figure 88A in orange and refers to a homogenous, structureless emission across the crystal face that doesn’t conform to any particular shape. This is seen mainly in the partially detemplated sample. It appears to have a short average lifetime of 1-2 ns and predominantly emits in the region of 450-500 nm. This emission behaviour might be explained by an even distribution of an emissive species throughout the existing pore structure of the zeolite, as pore structures exist on a length scale below Abbe’s diffraction limit. Based on studies of nanodots, which were formed after at least 4 hours of being held at 400 °C or higher^{310,349,351}, it is unlikely that these are nanostructures as the sample was only brought to 300 °C and was quenched after reaching this temperature.

Instead, these emissive products might be arising directly as a result of preliminary template pyrolysis.

5.2.2 Type 2 Emission

The second type of emission behaviour (hereafter termed ‘Type 2 Emission’) exemplified in red in Figure 88 are the clustered deposits concentrated in the centre of the crystal faces in the partially detemplated chabazite and the chabazite calcined twice at 550 °C. These deposits appear roughly circular with an average diameter of 400 nm. In the chabazite calcined twice at 550 °C, they appear more concentrated on the external surfaces of the crystal. The peak emission region is at 470 nm and the lifetime is in the range of 4-5 ns. Raman mapping suggests that a band at 1038 cm^{-1} could be assigned to this emissive product. While the morphology and distribution of these deposits is compellingly similar for both the partially calcined and the twice calcined chabazite, it is not certain that the chemical composition of these deposits are the same. It is likely that in the sample calcined to completion that the composition is an evolution of that which is present in the partially calcined sample.

Of all the regions identified, this type has the emission peak with the lowest wavelength. It should also be acknowledged that despite the weighted average being listed as 4-5 ns the τ_1 component is relatively long at around 11 ns. Based on this, it is possible that these deposits are PAHs, substituted or otherwise, formed as a result of more extensive hydrocarbon pool chemistry. In the partially calcined sample, the early indications of this deposit formation are visible, although the agglomerates are not yet fully defined. This could be evidence of the early stages of hydrocarbon pool chemistry occurring. The deposits in the twice calcined chabazite, then, are as a result of more extensive hydrocarbon pool chemistry. These products could be more extensively recycled or substituted than those seen in type 1 emission.

5.2.3 Type 3 Emission

The third type of emission behaviour (hereafter termed ‘Type 3 Emission’) observed in the chabazite calcined twice at 550 °C are the subsurface deposits represented in green in Figure 88. These regions are larger than the red deposits and measure around 3 μm across. They overall appear to be more emissive in the red (i.e. 550-650 nm) and also have a shorter lifetime compared to the type 2 emissive deposits. Raman mapping of the same sample shows that a similar localised distribution is seen in intensity maps of the bands 1344 and 1439 cm^{-1} . The distribution pattern of these bands is different to the Raman bands suspected to be associated with Type 2 emission, further suggesting that Type 1, 2, and 3 emission behaviour are arising from different chemical species.

Based on their emission peak, which is at 500 nm, and their shorter lifetimes, it is speculated that these deposits could be carbon nanodots or similar nanoscale structures. Beyond the weighted

220

lifetime presented in Table 28, these deposits do exhibit the shortest τ_1 and τ_2 values of all the emissive deposits proposed here. The shorter lifetimes in the framework would be consistent with nanostructures as these would be too small to experience significant steric confinement, unlike bulkier PAHs that might experience longer lifetimes. Modified graphitic materials in the form SWNTs or graphene oxide were also shown to have short lifetimes (see Table 26).

5.2.4 Type 4 Emission

Like type 3 emission, type 4 emission behaviour is another form of subsurface deposit present in the chabazite calcined twice at 550 °C and once at 630 °C. Unlike type 3 emission, type 4 emission regions are larger with an average diameter of 5 μm or greater and have an emission peak slightly more towards the blue region at 485 nm. These also have the longest average lifetimes at 7-8 ns. The distribution map for the 1077 cm^{-1} Raman band appears to show similarities to the confocal imaging distributions. Where type 3 emission was potentially attributed to carbon nanostructures, the longer lifetimes indicate that these might be a type of bulky, substituted PAH instead. This could make these regions compositionally similar to type 2 emission. The longer lifetimes could be as a result of similar types of PAH undergoing greater confinement effects from being trapped deeper in the framework.

5.2.5 Type 5 Emission

The fifth type of emission (hereafter termed ‘Type 5 Emission’) occurs in the chabazite sample calcined once at 630 °C. These are concentrated regions of emission that appear like bright spots both on and below the surface. The average lifetimes are 2-3 ns and the peak emission is 505 nm when excited at 405 nm, which is behaviourally very similar to type 3 emission. The distribution might be likened to the Raman map at 1038 cm^{-1} although this is not conclusive. Distinction has been drawn between type 3 and 5 emission on the basis that type 5 emission morphologically appears smaller (1-5 μm), although arguably this could be from the same source. In this case, type 5 emission might be also be attributed to carbon nanostructures as described in the earlier discussion.

5.3 Evidence of Morphological Features

5.3.1 Crack Formation

The most straightforward morphological change visible in the crystals is the formation of cracks. These cracks are most visible in the partially detemplated and the twice calcined zeolites, as they both exhibit the greatest amount of emissive background against which the cracks may contrast. The cracks themselves are not sites of emission, indicating they are acting as non-size selective diffusion pathways along which emissive products may readily escape. They also appear to be

quite abundantly distributed across the area of the crystal, concordant with the x3700 SEM image in Figure 68, which shows a view of a fractured crystal with a laminar cross-sectional topography.

Thermal stress cracking is not unexpected^{71,72,74,75,76} and may be explained by the abrupt extrusion of the adsorbed organic template phase across a large temperature differential leading to an uncontrolled increase in the internal pressure of the lattice, which results in framework damage and could also feasibly be exacerbated by the presence of water. Cracks large enough to cleave structurally analogous SAPO-34 crystals have been three-dimensionally imaged by serial block-face scanning electron microscopy (SBFSEM) and have been attributed to phase impurities (e.g. cristobalite) causing tensile strain in the crystals during crystallisation, which remains incorporated in the final crystal structure³⁶¹. Regions of tensile strain then act as preferential fracture planes when further external stress is applied.

It is difficult to assess whether hairline cracks are already present in such abundance in the uncalcined material resultant of the synthesis process, as the framework itself appears optically transparent. Although SEM does provide some evidence of planar defects on the surface of the as-synthesised crystals, it is unclear whether such an extensive network of cracks forms at this stage or after exposure to a certain level of heat. In comparing the partially detemplated chabazite, which was heated to only around 400 °C before being quenched, to the twice calcined chabazite, which was heated up to 550 °C, it does appear that although the density of cracking^{xxiii} is similar in both samples, the size of the voids appear markedly larger in the twice calcined chabazite, implying the cracking process is temperature dependent and evolves with exposure to heat. It is possible that with further heating, some of these cracks may anneal, as the chabazite calcined once at 630 °C seems to exhibit less evidence of cracking. This may partially be due to the overall lack of crystal emission, which may downplay the extent of the crack network.

It might be concluded that the heat treatment employed in these particular experiments is not ideal. This is feasible, as the primary purpose of exploring detemplation here was not to finesse the thermal process but to observe the formation emissive products. Based on the extent of cracking in these results, it would appear that heating up to 550 °C twice does not produce an ideal result, and that if a two-step procedure were being utilised, the first step should likely be performed to temperatures less than 400 °C, with the final ramp to 550 °C being performed as slowly as possible⁷². Indeed, in zeolites being synthesised for the purpose of catalysis, a much more considered calcination process is typically employed with pre-heating phases, slower ramp rates, and the introduction of oxidative gases at a later stage in the process, as previously outlined in Chapter I Section 3.2.

^{xxiii} Cracking refers in this context, of course, to the process of crystal fracturing and splitting rather than the catalytic definition.

The following conclusion might be drawn. Heat treatments are generally the preferred method of detemplation and are known to induce problems in the framework if performed hastily. The results here, which see the zeolites being treated with more haste than caution, show a network of cracks that appear to become more pronounced the longer and more frequently the sample is heated. The introduction of cracks potentially has implications for the long-term efficacy of the catalyst in its capacity as a molecular sieve, especially if the zeolites are to be used in applications that require cyclical thermal regenerative processes. It is difficult to assess whether the overall effect of this may be positive or negative, however, as though premature evacuation of incompletely converted products from size-restricted pores might seem at first negative, the newly formed crevices may also make available a larger internal surface area to a greater influx of reactant gases. Further studies that image a series of zeolites subjected to a range of permutations of thermal detemplation would be useful in assessing the relationship between thermal cracking and catalytic efficiency. It would be worth assessing the effect of heating rates, humidity, and maximum temperature on the crystals in further structured experimentation.

5.3.2 Pore Formation

The twice calcined chabazite also showed evidence of potential pore formation. Pores are channels that do not conform to the framework's microstructure being of a larger length scale, and generally exceed 50 nm in diameter³⁶². This is based on the observation that type 2 emission deposits appear to be aligning themselves in lines perpendicular to the crystal edges. This apparent tendency to self-organise implies that a diffusional limitation is being imposed on the emissive deposits, which is more consistent with the idea of macropores rather than cracks.

5.3.3 Regions of Non-specific Structural Change

A possible explanation for the sub-surface emissive behaviours visible in the chabazite calcined twice at 550 °C and once at 630 °C is if these regions correspond to a type of induced structural change such as a phase change. It is possible that if there is a kind of structural or compositional change occurring in these regions that the local chemistry promotes the formation of a different type of emissive species based on different confinement properties, which are thought to govern hydrocarbon pool mechanisms³⁶³. Alternatively, it could be that emissive products themselves are the same but the change in local environment (due to an induced structural or compositional change in this area) causes the lifetimes to change. This may be through processes such as dimer formation or interactions with the framework.

The evidence of red-shifted emission, however, indicates that it is most likely a different speciation arising in these regions. This is further supported by Raman mapping studies, which show through the tracking of peaks at 1439 and 1344 cm⁻¹ that there are regions that in the twice calcined sample that morphologically correspond to the type 3 emission, whereas in the once

calcined sample there is no such evidence of these peaks. Overall, it could still be the case that type 3 emission is corresponding to local regions of structural or compositional change (e.g. siliceous phase like quartz or cristobalite, amorphous phase, or compact aluminosilicate like labradorite³⁶⁴). These regions still occupy only a small percentage of the overall bulk volume, explaining why XRD studies may not pick up on this.

5.4 Spatial Distributions of Emissive Sites Indicate Position of Brønsted Acid Sites

Charge compensation of aluminium sites is an intrinsic feature of zeolite frameworks. As mentioned in Chapter 1, there is a certain degree of flexibility regarding the nature of the counterion. In the case of an as-synthesised framework, it is predominantly the OSDA that provides charge neutrality, but following thermal treatments and ion-exchange processes, it may be provided by protons, which result in H-form zeolites with Brønsted acid sites, or indeed any cationic species such as Na^+ , K^+ , or transition metals like Cu^{2+} , $\text{Fe}^{2+/3+}$, or Mn^{2+} ³⁶⁵. A correlation may be made between the observation that emissive deposits appear to be migrating from the centre of the crystal outwards, and fluorescence tomography imaging collected by Robinson et al. of Cu-SSZ-13 crystals in Figure 89. These samples are the same chabazite crystals studied here following a wet-ion exchange preparation method that introduces Cu(II) into the micropore network.

In the images Al signal is generally lower due to its lower concentration. Of note in these images is the zoning effect, where Cu appears uniform at the centre of the crystal but absent in the a 7-8 μm region from the outer edge. The contrast in the Si map implies silicon enrichment towards the outer aspect of the crystal. Based on the localised distribution of Cu, it is possible to speculate that by extension, charged sites are concentrated towards the centre of the crystal. Further to this, it may be speculated that emissive products emanating from the centre of the crystal may also be related to this site distribution, and that lifetimes in subsurface species may additionally be lengthened via interactions with Brønsted acid sites.

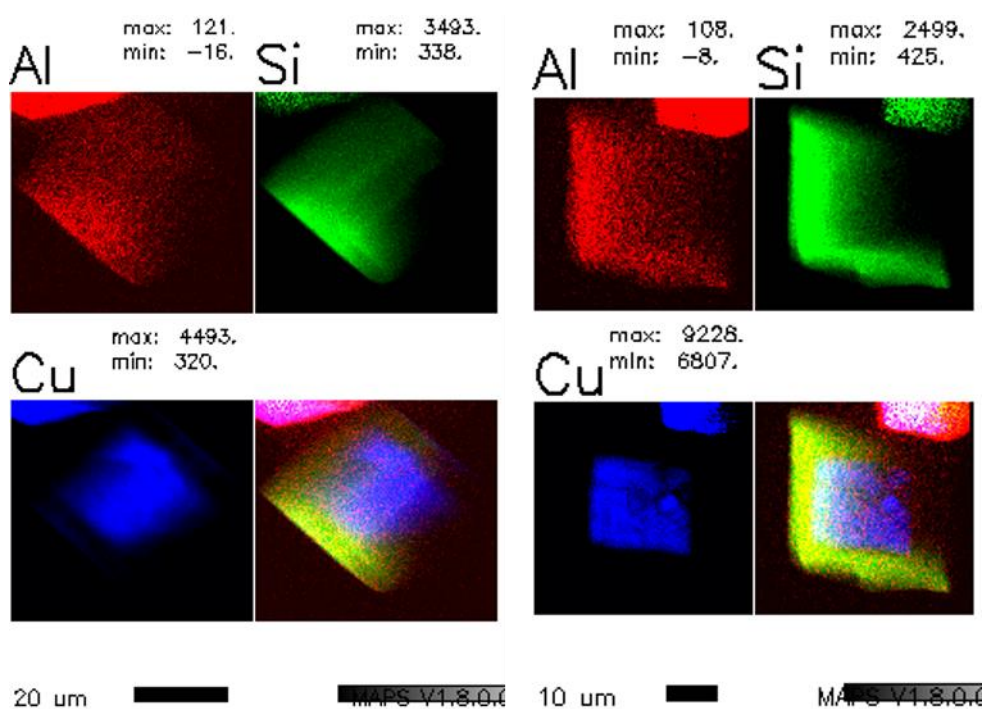


Figure 89 **XRF tomography of wet-ion exchanged Cu-SSZ-13 crystals** obtained at Argonne Sector 2ID with 10 keV showing elemental maps of Al (top left), Si (top right), Cu (bottom left), and channel overlays (bottom right). 70 projections were measured over a 210° span. Si & Al show significant self-absorption, as expected, resulting in shadowing across the right side of the crystals. *Images courtesy of Dr Lu Xi Li and Prof Ian Robinson.*

6 Conclusion

Multimodal imaging studies are presented as a promising avenue for studying the spatial distribution of emissive species across a crystal, with wavelength optimisation providing the key to probing target species with greater accuracy. In the case of imaging, a 405 nm laser for confocal imaging and a 488 nm laser for FLIM strikes a practical balance, yielding data sets bearing chemical relevance on readily available commercial imaging setups^{xxiv}. Within this near-UV to visible range excitation, maps showing the distribution of organic material associated with the detemplation process have been successfully collected. Further to this, Raman studies conducted at 830 nm makes it possible to avoid the materials' considerable fluorescence background^{xxv} and provide greater chemical specificity with maps that show an intensity distribution of particular peaks.

Across three samples taken from different stages of the detemplation process, a comparison of the morphology of emissive deposits, highlighted through confocal imaging, the lifetime of deposits, possible with FLIM, and vibrational characteristics, through Raman mapping, has demonstrated that there are likely to be at least four unique types of emissive speciation present in the samples. These include:

1. An emissive species (type 1) distributed fairly evenly throughout the zeolite matrix with a shorter lifetime, primarily seen in the partially detemplated sample and possibly associated with smaller molecules directly resulting from the template decomposition process;
2. An agglomerated emissive species (type 2) with a highly characteristic morphology and medium duration lifetime, appearing to originate from the centre of the crystal in the partially detemplated sample, and emanating towards the surface of the crystal in the twice calcined sample, possibly comprised of late hydrocarbon pool products like substituted PAHs;
3. An emissive species localised both subsurface and close to the surface, with an emission centred more towards the red but with a shorter lifetime, seen in both calcined materials (type 3/5), which is tentatively assigned to carbon nanostructures; and
4. An emissive species spanning across larger subsurface regions with a significantly longer lifetimes (type 4), and seen in both calcined materials, possibly associated with late products of hydrocarbon pool chemistry and also potentially influenced by both the local

^{xxiv} Given that UV imaging setups (<405 nm; corresponding with the excitation source used in previous fluorescence spectroscopy studies) are not usually commercially available.

^{xxv} Fluorescence background remains a challenge in Raman spectroscopy despite optimised wavelength selection, as evidenced by the partially detemplated sample whose background remained overwhelming even at 830 nm. These samples require additional intervention with technologies such as Kerr-gated Raman.

microstructural changes that promote their production and the confinement effects of the framework.

The imaging has also shown a propensity for crystals to thermally crack after repeated heating, as shown in the twice calcined material, which may have repercussions in the long term efficiency of the catalyst's use.

These images are differentiated from the existing body of imaging studies in that they are label-free, and therefore provide an exciting insight into the spatial variation of zeolitic catalysts in their native, untainted state. In particular, Raman mapping demonstrates in a compelling manner the capacity for monitoring the fingerprint of the residual organic material. There exist, however, caveats that can be addressed in future studies.

It remains that zeolites don't globally lend themselves towards imaging in commercial systems. It has been established that in these particular CHA type samples, the nature of the template used, and the relatively large size of the cages is likely to facilitate the formation of emissive products. This may not necessarily be the case across the board for all zeolite families depending on the synthesis process used and pore size. Compared to the biological samples for which these imaging systems are geared, zeolites are incredibly lowly emitting. As an example, FLIM images of biological material are comprised of thousands of counts per pixel, whereas zeolite images feature up to two orders of magnitude less counts per pixel, resulting in the need to spatially bin the images, which further compromises the overall resolution. Scatter from the crystal microstructure can also convolute the decay curves (as seen in Figure 74, Figure 78, and Figure 81) prompting the need for manual fitting interventions. The carbonaceous material is also highly subject to irreversible damage from laser power, requiring a delicate hand to balance the trade-off between excitation power and resolution during image acquisition. This is also a key limitation in the move towards techniques like multiphoton imaging using NIR lasers, which may provide access to UV range excitation, but is coupled with an increased tendency for the samples to absorb, heat, and burn. In the case of Raman mapping, extremely long acquisition times of 24 hours and longer are required to detect signal to the level demonstrated in this chapter. In the interest of total time taken, a static Raman grating is preferred although this comes at the expense of being able to offer only a limited detection window.

Further success in label-free zeolite imaging studies will likely be achieved through the development of customised imaging setups. The key points of difference between the samples the commercial systems are optimised for and inorganic zeolites are that biological samples tend to be:

- tagged to have higher quantum yield, which improves resolution and acquisition times; and
- soft, transparent materials that don't scatter, absorb, or burn as much.

To this end, a customised imaging setup will most likely require a homemade system featuring an optical pathway with greater geometric offset to deal with scatter, and significantly fewer optical components to minimise signal loss.

Ultimately, these limitations should not be seen as prohibitive factors that undermine further meaningful usage of the technique in future zeolite interrogations, but rather as a list of surmountable challenges that can be addressed with further intelligent experimentation in a future project. The truly novel potential of this technique should not be understated and is perhaps best framed in terms of the XRF images in Figure 89. XRF is an established technique that is already used to successfully analyse composition and elemental distributions in zeolite samples. In Cu-zeolite samples, Figure 89 shows a characteristic zoning distribution of copper that is concentrated at the centre of the crystal. It is interesting to note that the spatial distributions of emissive species in Figure 77, Figure 78, and Figure 81 seem to correlated similarly with a concentration towards the centre of the crystal. Given that the ion-exchange sites are associated with the distribution of Al, it follows also that template derivatives would also be able to mirror this effective Al distribution as the OSDA cations will also be preferentially located around the charge-introducing Al sites^{xxvi}. As such, on the basis of their chemical relationship to the framework, the emissive deposits are in fact able to indirectly provide information on the distribution of framework elements as well as the distribution of the organic phase themselves, providing even further insight than what XRF mapping is already providing.

Lifetime maps then are not necessarily of interest because the numerical lifetime values are independently meaningful, but rather because they become useful if they are viewed as a map representative of degrees of confinement and chemical influence from factors like silicon:aluminium concentration. The fluorescence maps in this sense can be viewed not simply as a means of viewing a distribution of hydrocarbons, where different lifetimes correlate with discrete chemical species, but as a means of seeing how the local chemical environment is different across the crystal by seeing the degree to which it influences the lifetime of a guest species. In this sense, FLIM & confocal images provide a wholly unique way of visualising a zeolite and represent perhaps the closest iteration of a chemist's ideal imaging modality as they elucidate the arguably intangible concept of a 'chemical environment'. Viewed in this manner, the appeal and potential of FLIM in an inorganic chemistry context should become relatively clear. Systematic experimentation imaging families of zeolites synthesised and reacted under strict conditions will likely yield abundantly useful datasets that provide insight into how the chemical environment changes and influences catalysis. Extending studies into other inorganic materials

^{xxvi} Although it should be noted that in the case of Cu²⁺ two negative framework charges are required, generally in close proximity, so the distribution of copper might more directly speak to the distribution of Al pairs or higher Al concentrations.

may provide similar forms of insight. Finally, conducting multi-wavelength studies will make it possible to probe different regions and forms of speciation.

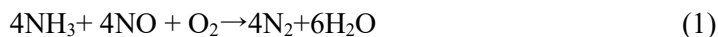
Chapter VIII

Multimodal Study of Copper: Elucidation of NO_x Species in SCR Catalysts

In collaboration with the B22 and I14 beamlines at the Diamond Light Source

1 Introduction

Selective catalytic reduction (SCR) is a process that uses a catalyst to convert nitrogen oxides in the presence of a reductant, like ammonia or urea, into water and diatomic nitrogen. It can be generally described as follows:



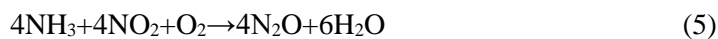
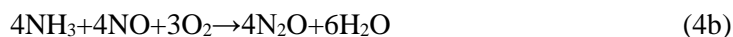
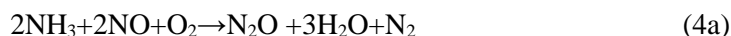
Nitrogen oxides, or NO_x gases, are a serious pollution problem that pose as a hazard to human respiratory function and environmental ecosystems³⁶⁶. Almost 50 % of NO_x emissions originate from combustion engines used in transport, with a further 20 % arising from the stationary production of energy such as thermal power plants and industrial boilers³⁶⁷. Owing to its capacity for high conversion efficiency and stability, SCR has been employed since the 1960s to purify NO_x emissions. In the automotive sector, SCR has already been commercially applied to reduce NO_x emissions in diesel cars using an exhaust fluid reductant source such as an aqueous urea solution like AdBlueTM. The majority of heavy-duty diesel vehicles use it, and some passenger diesel cars by Volkswagen and BMW utilise the technology to help vehicles meet Euro6 standards.

A range of potential catalysts can be employed in this technology. The most standard type used in cars is an extruded ceramic monolith matrix that carries catalytically active metal oxides such as titanium oxide, vanadium, and molybdenum. Base metals do not have high thermal durability. More recently, small pore Cu-zeolites have been identified as excellent catalysts in the SCR reaction, being lauded for their unrivalled NO_x conversion^{368,369,36}. Additionally, their strong performance in the highly topical³⁷⁰ low-temperature SCR (LT-SCR) region (i.e. $\leq 250^\circ\text{C}$ ³⁷¹), and durability following hydrothermal ageing³⁷² make them excellent candidates for vehicular SCR, and the current catalysts of choice for commercialized SCR in heavy goods diesel vehicles³⁷³.

This chapter focuses on one specific challenge arising in NH_3 -SCR, which is the unwanted formation of N_2O . N_2O is an unwanted by-product observed in SCR over copper- and iron-exchanged small-pore zeolite catalysts³⁷⁴, as well as Mn-Fe spinels³⁷⁵. Although historically exempt from emissions regulations due to their believed lack of toxicity, harmful indications following long-term exposure³⁷⁶ and a global warming potential almost 300 times that of CO_2 ³⁷⁷ mean that N_2O will inevitably become the subject of increasingly exacting legislation beyond Euro6. Unwanted N_2O formation in SCR is not well understood as the focus of studies is generally on the formation of N_2 .

N_2O has been observed in systems catalysed by VO_x/TiO_2 ^{378,379} as well as with Cu-ZSM-5, Cu-beta, Cu-Y, Cu-SSZ-13, and Cu-SAPO³⁸⁰. Chemically speaking, a number of different N_2O

formation pathways have been proposed in these studies, which happen alongside the primary SCR reactions described in (1) & (2). These include:



The simplest option is perhaps the oxidation of NH_3 , as expressed in reaction (3). Equations (4a) & (4b) have been of relative interest given that there is experimental evidence to suggest that NO and NH_3 are simultaneously extant in a standard SCR system and may react to form N_2O ^{381,382}. Mechanistically, this has been rationalised as a dual Eley-Rideal (ER) and Langmuir-Hinshelwood (LH) process^{383,384}, where it is thought that NO reacts with adsorbed NH_3 species via the ER mechanism^{385,386,387}. In their work on ‘fast SCR’, Tronconi and Nova proposed a nitrate route that concluded N_2O was a primary product arising from the thermal decomposition of nitrate species^{388,389} as outlined in reaction (7). This option has been explored in Cu-zeolite catalysts^{390,391,392,393} and VO_x catalysts³⁷⁹ alike. An extensive review of the mechanistic aspects of N_2O formation has been published by Brandenberger et al., which details reaction steps in a manner beyond the scope of this paper³⁹⁴. This work further explores the decomposition pathway of ammonium in the formation of N_2O .

Independent of the particular mechanism underlying the process, studies of various properties, including different catalysts and different reaction conditions, have been shown to yield different rates of N_2O formation. Some have noted trends in N_2O production as a function of the framework, with Cu-ZSM-5, Cu-beta, and Cu-Y all forming larger amounts of N_2O than Cu-SSZ-13 under the same conditions³⁸⁰. Others have observed increased formation in environments featuring an excess of NO_2 ³⁹⁵, while other focus on increased accessibility to oxygen³⁹⁶. The effects of hydrothermal ageing³⁹⁷ have also been reviewed. As yet, there is no conclusive common denominator that unites these observations.

In the work presented in this chapter, it is posited that there may be a correlation between N_2O formation and the nature of copper speciation throughout the catalyst. Working under the assumption that NH_4NO_3 acts as a source of N_2O , as broadly expressed in reaction (7), it is proposed that there may exist sites within Cu-zeolites that act as preferential sites for nitrate formation. In samples where there is an excess of such sites, it is hypothesised that N_2O formation

rates will be higher. Central to this idea is a piece of work conducted by Deka et al.³⁹⁸, which involved comparing the DeNO_x selectivity of two Cu-zeolites prepared by two different methods (i.e. wet ion exchange and vapour deposition). In a Cu K-edge XANES experiment, reproduced here in Figure 90, there was evidence to suggest that the zeolite prepared by vapour deposition contained a linear Cu⁺ species. This can be seen in the form of the pre-edge feature at 3a, which is not present in the wet ion exchanged sample and has previously been seen in systems like Cu₂O or CuAlO₂ owing to a transition from a 1s orbital to a double degenerate 4p_{xy} orbital³⁹⁹.

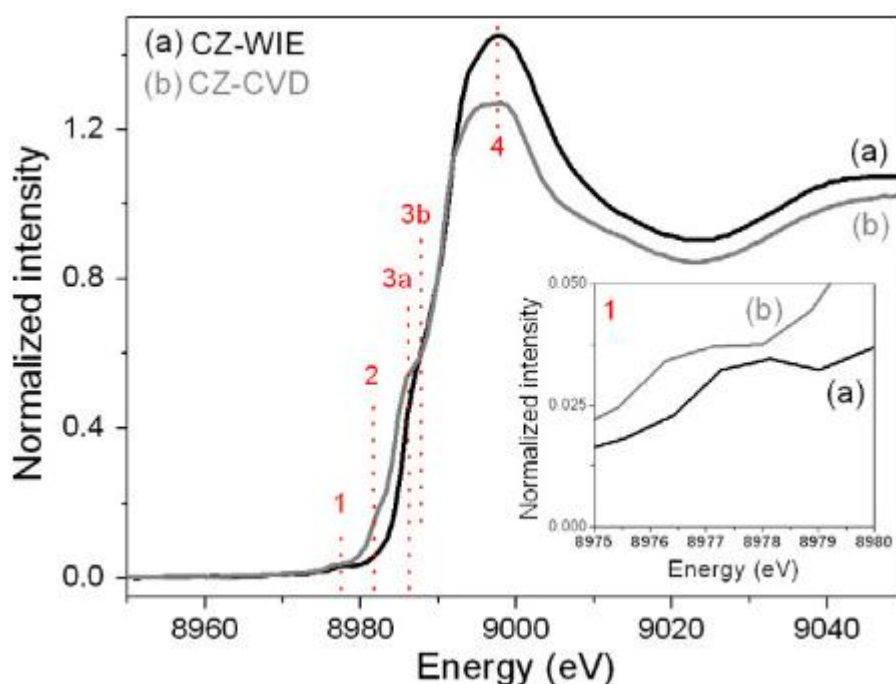


Figure 90 **Cu K-edge XANES spectra wet ion exchanged and vapor deposition prepared Cu-zeolites.** Features of interest are marked with numbered lines. *Reproduced from Deka et al.*³⁹⁸

In this chapter, the presence of copper aluminate species, which has previously been associated with the deactivation of Cu-zeolites^{400,398,401}, is identified as a site for preferential nitrate formation.

To test this hypothesis, two Cu-zeolite samples were produced. The first is an efficient and high performing Cu-SSZ-13 sample known to produce low N₂O amounts prepared through a standard wet ion exchange method. The second is a Cu-SSZ-13 sample prepared via a solid-state exchange method thought to contain varying amounts of different copper aluminate species. To verify the disparity in copper speciation between the two Cu-zeolite preparations, the samples were analysed on the hard X-ray nanoprobe at beam I14 of the Diamond Light Source (DLS) using a combination of X-ray fluorescence (XRF) and X-ray absorption near edge spectroscopy (XANES) maps. The N₂O performance of each Cu-zeolite was then monitored in an operando infrared spectroscopy study on the multimode infrared imaging and microspectroscopy (MIRIAM) B22 beamline at the DLS, differentiated from lab-based IR setups by its high brilliance irradiation source and superior signal-to-noise.

2 Methods

2.1 Sample Preparation

A parent SSZ-13 zeolite (Si/Al = 13) was synthesized using *N,N,N*-trimethyladamantammonium hydroxide as a structural directing agent in a fluoride media, under static hydrothermal conditions^{159,176}. The proton form of the zeolite was obtained by calcining the sample in air by heating at 1 °C min⁻¹ to 120 °C, held for 2.5 h and then at 4 °C min⁻¹ to 550 °C, held for 10 h. Crystals synthesised were 30 µm on average. Copper-exchanged forms of the zeolite were created via the following two preparations.

The first method was a wet ion exchange method as reported previously⁴⁰². An amount of the H-SSZ-13 was added to an aqueous solution of copper sulphate and heated at 80 °C for 2 h under stirring. The product was recovered by vacuum filtration, washed with copious amounts of water, dried overnight at 80 °C and calcined in air. This sample is hereafter referred to as Cu-Zeolite Wet Ion Exchange (CZ-WIE).

The second method was a solid ion-exchange preparation. Cu-nitrate was combined in a five-time stoichiometric excess with H-SSZ-13 framework in a mortar and pestle and mechanically incorporated. The resultant sample was filtered and dried at 120 °C overnight, before being calcined again at 550 °C with a ramp rate of 2 °C min⁻¹. The resultant sample featured a Cu loading of 3 wt%.. This sample is hereafter referred to as Cu-Zeolite Solid State Exchange (CZ-SSE).

2.2 Preliminary Zeolite Characterisation

2.2.1 UV-vis

UV-vis spectra were acquired under ambient conditions with a Shimadzu 2700 UV-vis spectrophotometer fitted with an optical integrating sphere for solid powdered samples. Zeolites were pressed into a sample holder and mounted vertically in the integrating sphere. A standard barium sulfate (BaSO₄, Sigma-Aldrich, 99%) sample was used for baseline scans. Spectra were collected from 200-1400 nm at a scan speed of 130 nm/min and a resolution of 0.5 nm.

2.2.2 Raman Spectroscopy

Raman spectra were obtained from an InVia confocal Raman microscope (Renishaw, Wotton-under-Edge, UK) equipped with a 50x objective lens (Nikon, L Plan Apo, 50x/0.45, WD17) and Peltier cooled CCD. The sample was irradiated with either an 830 nm diode laser with 34 mW maximum power output, or a 514 nm Stellar PRO argon laser (Modu-laser, USA) with 10 mW maximum power output. Attenuated laser power at the sample was achieved using neutral density filters. A grating with 1200 lines/mm was used, yielding an overall spectral resolution of 1 cm⁻¹.

2.2.3 XRD

Powder X-ray diffraction was measured using a Rigaku Miniflex X-ray instrument with a Cu tube source of 600 mW and 1D D/teX detector and divergent slits. Diffraction patterns were collected between 5-50 $2\theta^\circ$ with an increment of 0.017 ($2\theta^\circ$) and an acquisition time of 1 sec/step.

2.3 Advanced Characterisation

2.3.1 XRF and XANES

Nano-XRF and nano-XANES experiments were performed on the I14 hard X-ray nanoprobe beamline at the Diamond Light Source. Sample was suspended in isopropanol and deposited onto silicon nitride wafers, which were mounted into the beamline. The sample was then scanned across the X-ray beam, focused to a spot-size of 100 nm, to form a map with 100 nm lateral resolution. Signal was detected using a four-element silicon drift detector.

The incident nano-XRF beam energy was chosen at an energy above that of the respective Si, Al, and Cu K-edges. Nano-XANES data were obtained by compiling a series of nano-XRF maps collected at 100 different photon energies crossing the Cu K-edge. The map was then derived as the integral of the Cu $K\alpha$ emission at each energy, resulting in a stack of images. These were aligned to correct for thermal drift and analysed using principal component analysis (PCA) and clustering tools available in the freely-available package HyperSpy⁴⁰³.

2.3.2 Operando IR Spectroscopy

The infrared micro-spectroscopy experiment employed a Bruker Hyperion 3000 infrared microscope-fitted with either a $\times 36$ magnification objective & condenser-coupled to a Bruker Vertex 80V FTIR instrument at MIRIAM beamline B22 of Diamond Light Source. A slit size of 25 x 25 μm and a beam size of 10x10 μm^2 was used.

Bulk transmission IR experiments were performed on 6 mm thick wafers of catalyst particles (~ 10 mg) which were formed by pressing at a pressure of 1.5-ton cm^{-2} for 1 min. Wafers were placed onto a CaF_2 window mounted inside a temperature-controlled Linkam FTIR600 reaction cell. Gas stream inlets to the cell were controlled by a mass flow controller. Prior to experimentation, wafers were dehydrated by heating at 300 $^\circ\text{C}$ under nitrogen 100 ml min^{-1} N_2 flow. When adsorbed water bands were no longer visible in the spectrum, the Linkam cell was cooled down to the desired reaction temperature under N_2 flow at a rate of 10 $^\circ\text{C min}^{-1}$.

Spectra were recorded from selected points across the sample with 256 scans and 4 cm^{-1} resolution, equivalent to 32 s per measurement, using the Bruker OPUS software. NH_3 -SCR was performed using a base gas mixture of 500 ppm NO, 500 ppm NH_3 , and 1000 ppm O_2 (balance

N₂) at 180 °C. The outlet of the cell was connected to a mass spectrometer to provide qualitative information for reactant consumption and product formation.

3 Results & Discussion

3.1 Preliminary Zeolite Characterisation

3.1.1 UV-vis

UV-vis confirms the presence of copper species within the zeolite. An intense absorption band is visible in the CZ-WIE and CZ-SSE samples at 200-225 nm. Previous studies have assigned this feature to the charge transfer between of O²⁻ → Cu²⁺ or 3d¹⁰-3d⁹4s1 Cu⁺ transitions⁴⁰⁴, although its presence in the copper-free zeolite means it could also partly be arising as a characteristic transition of the zeolite⁴⁰⁵. The broad absorption band at 800 nm in the CZ-WIE and CZ-SSE is assigned to the d → d transition of isolated distorted octahedral hexa-aqua^{xxvii} complexes of Cu²⁺ and has been previously identified in Cu-SSZ-13⁴⁰⁶, Cu-ZSM-5⁴⁰⁷, Cu-SAPO-34³⁹³, and Cu-BEA⁴⁰⁸. As the band is broad, it is likely that the absorption band may be due to three different types of Cu²⁺ complexes including divalent complexes charge compensated by an Al pair (e.g. [Cu(H₂O)₆]²⁺), monovalent, single Al charge compensated complexes (e.g. [Cu-OH(H₂O)₅]⁺), and complexes involving organic ligands⁴⁰⁹.

^{xxvii} Measured at ambient temperature, it is assumed the samples are hydrated.

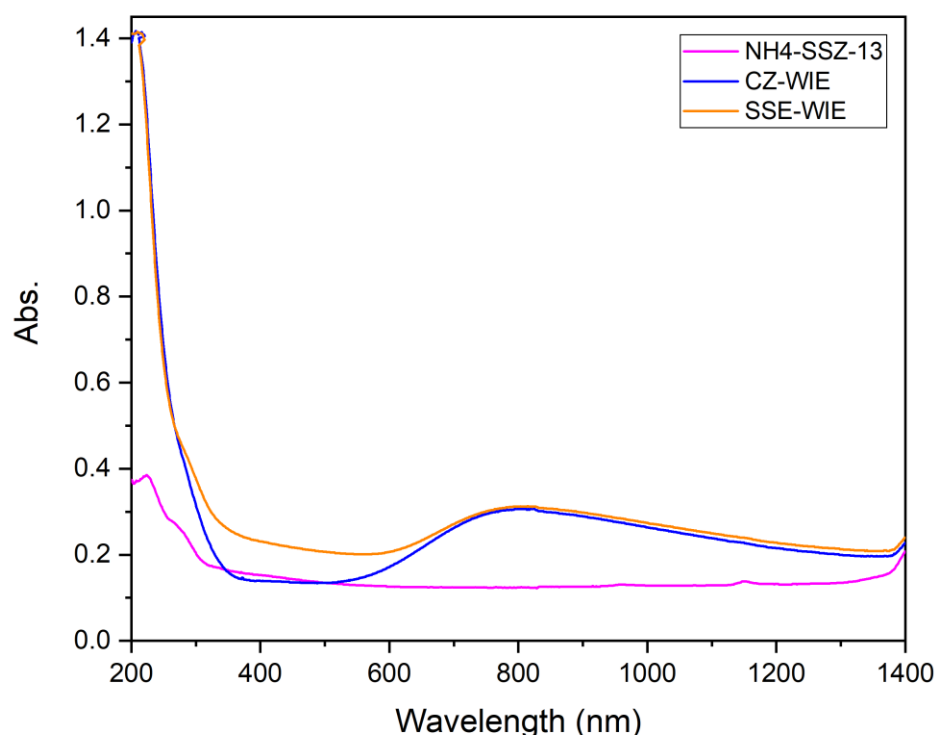


Figure 91 **UV-vis of SSZ-13** including blank framework (magenta), 4x wet ion exchanged Cu-zeolite (blue), and solid-state exchanged Cu-zeolite (orange)

The CZ-SSE exhibits increased absorption in the region between 350-620 nm, which can be assigned to charge transfer in O-Cu-O and Cu-O-Cu linear copper systems like CuO⁴⁰⁷. This is also evidenced in UV-vis studies of copper loading in zeolites where higher copper loadings are accompanied by an increase in oxidic copper species⁴⁰⁵. CZ-SSE also has a shoulder at around 300 nm that has previously been observed in optical transmission studies of CuAlO₂⁴¹⁰.

Overall, the UV-vis data indicates that both samples clearly evidence the presence of copper speciation, with the CZ-SSE exhibiting multiple copper environments.

3.1.2 Raman Spectroscopy

Raman spectra were acquired for the CZ-WIE, the CZ-SSE, and the copper-free parent zeolite of both types of copper-exchanged samples. Representative spectra from 5 different areas of the sample were acquired and then averaged to create the traces presented in Figure 92. The copper-free parent zeolite appears to be quite homogenous with the characteristic chabazite quartz peak at 484 cm⁻¹. As previously discussed in Chapter 3, bands at 803 and 833 cm⁻¹ have been assigned to $\nu_s(\text{T-O-T})$ stretches¹⁸⁹ of the silicalite structure. These bands are weak and only visible in longer accumulations.

The first batch of wet ion exchanged Cu-zeolite preparations (i.e. series AG02) show strong crystallinity of the chabazite doublet and no further meaningful bands. The second CZ-WIE batch (i.e. series AG03) has a higher background noise and two additional bands in the spectrum at 607 and 809 cm^{-1} . Additionally, the chabazite doublet appears compromised. It could be the case that this preparation may have interfered with the structure of the parent material, highlighting the need to characterise material regularly during ion-exchange processes. This batch of sample was not used in further analysis.

In the CZ-SSE sample the chabazite doublet is clearly visible indicating crystallinity is maintained. However, there appear to be two unique bands at 655 and 833 cm^{-1} . Despite previous assignment to silicate stretches, the 833 cm^{-1} peak, unaccompanied by a band at 803 cm^{-1} , appears disproportionately intense in the CZ-SSE sample. It is instead speculated that these peaks may be attributed to a unique copper environment.

Previous studies have explored the spectroscopic features of mononuclear and dinuclear Cu_xO_y complexes that might be extant in Cu-zeolite samples. A study by Pappas et al.²⁹⁷ exploring the structure-activity relationship for Cu-CHA presented Raman data for hydrated and activated Cu-SSZ-13 samples with bands at 510, 580, and 830 cm^{-1} that were assigned to $[\text{Cu}(\text{trans-}\mu\text{-1,2-O}_2)\text{Cu}]^{2+}$ species²⁹⁸. A shoulder feature is also observed at around 620 cm^{-1} , which could be associated with bis(μ -oxo) dicopper(III) and mono-(μ -oxo) dicopper(II) species^{298,411,412}. Further, Vanelderen et al. showed that such vibrational frequencies can be influenced by the type of framework the molecular copper species are being hosted in⁴¹³. Based on this, it may be reasonable to consider that the band at 830 cm^{-1} could be associated with species featuring an O-O bond and that the band at 630 cm^{-1} could be linked to a Cu-O structure. Future computational studies could be used to clarify the nature of these Raman vibrations.

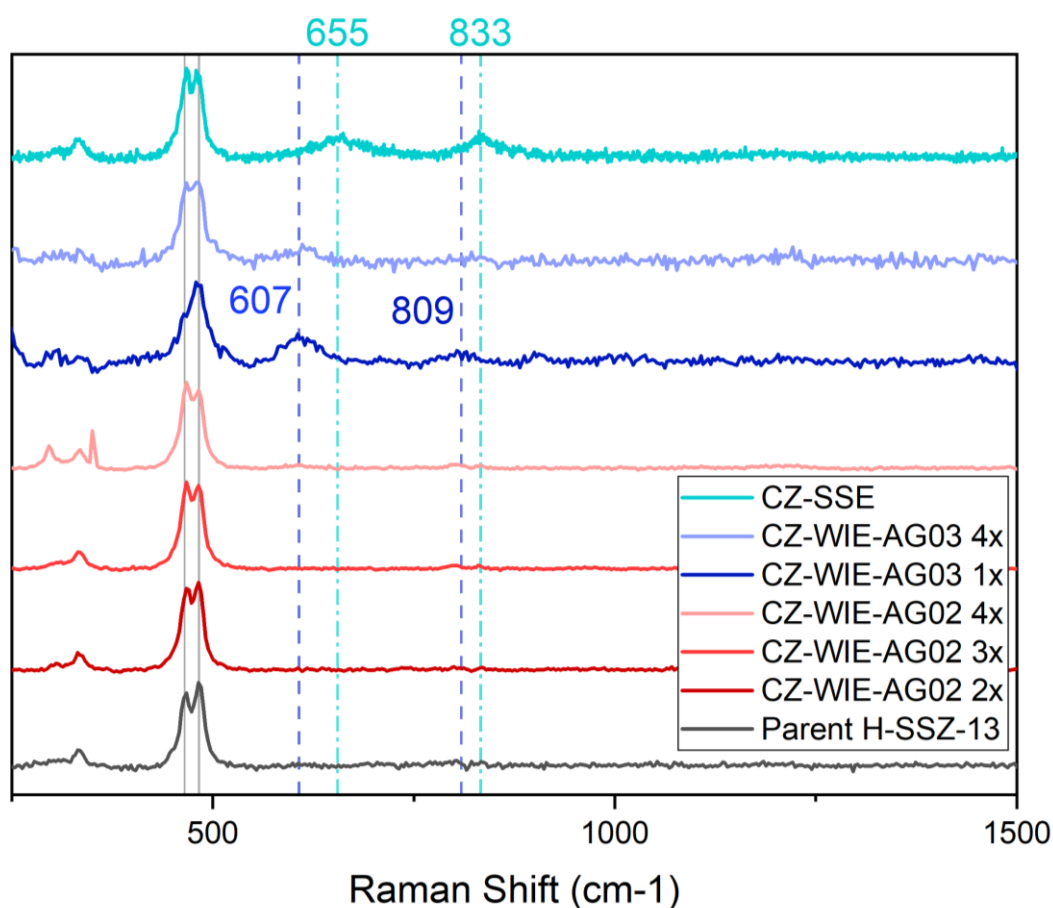


Figure 92 **Averaged Raman spectra of CZ-WIE and CZ-SSE acquired at 830 nm** including the parent H-SSZ-13 batch (dark grey), the solid-state exchanged Cu-SSZ-13 (aqua), and two batches of wet ion exchanged samples denoted AG02 (red) and AG03 (blue).

3.1.3 XRD

Figure 93 shows XRD patterns for both Cu-zeolite samples. Each sample shows agreement with the expected peaks for a CHA zeolite^{8,414}. The signal-to-noise of these unsmoothed spectra shows a high level of crystallinity, with neither sample appearing to have diminished crystallinity as a result of the ion-exchange preparation. Diffraction peaks from alternative copper phases (e.g. CuO at 35.6° & 38.8°⁴¹⁵; CuAl₂O₄ at 36.8°⁴¹⁶; CuAlO₂ at 36.6° & 37.8°⁴¹⁶) were not visible in the XRD patterns, which may relate to either no such phase being present, too low in concentration for the sensitivity of the system, or a distribution of small non-periodic particles.

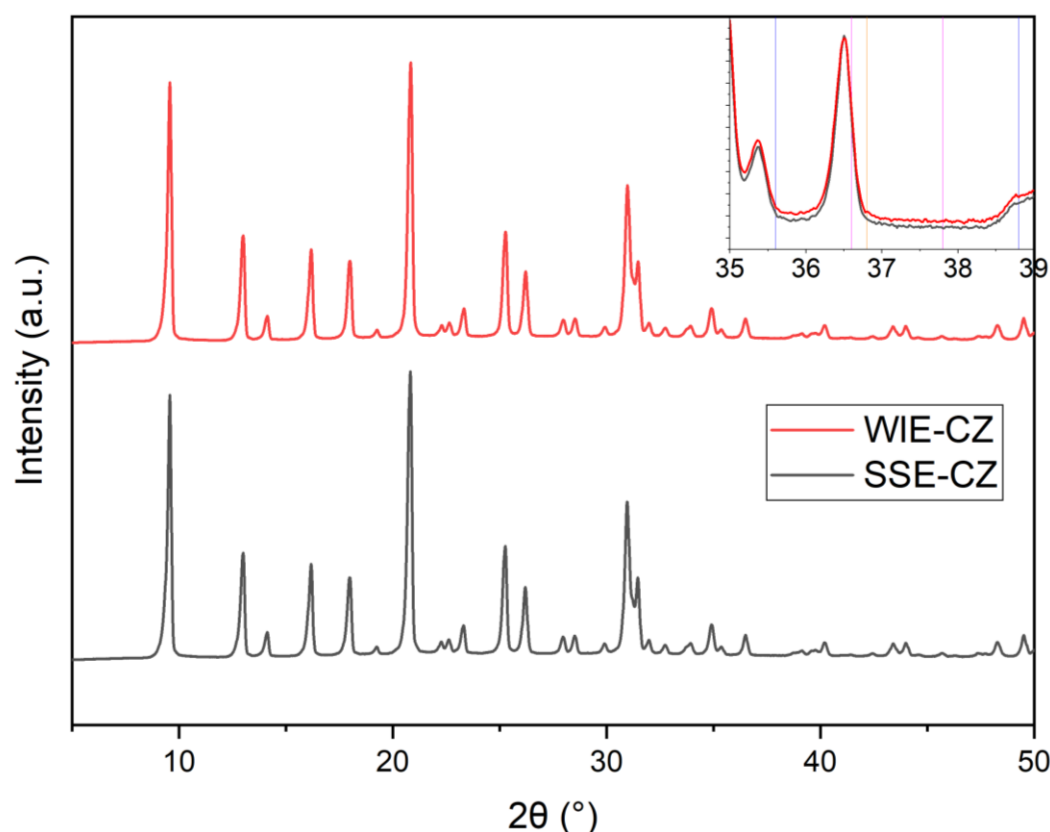


Figure 93 XRD of Cu-SSZ-13 including WIE-CZ (red) and SSE-CZ (black)

3.2 Advanced Characterisation

3.2.1 XRF & XANES

Nano-XRF and -XANES analysis was conducted to establish the nature and distribution of copper species across each SCR catalyst. In particular, XANES is used to establish the presence of an aluminate phase in the CZ-SSE preparation.

Overlaid XRF elemental maps of silicon (red), aluminium (green), and copper (blue) acquired with 100 nm resolution are shown in Figure 94. The crystals in Figure 94A show the CZ-WIE samples are larger than the CZ-SSE sample in Figure 94B with an average crystal size of 60 μm compared to 15 μm . In both cases, a regular cubic structure can be seen.

CZ-WIE shows a relatively uniform distribution of copper across the sample and thin regions of copper depletion on the crystal edges where the silicon map appears more pronounced. Copper distribution is expected to be even across the sample considering the wet-ion exchange preparation method, which sees copper starting in solution as a Cu^{2+} hexaaqua ions and being drawn in a sponge-like fashion into the porous structure when water ligands are dropped during dehydration. Conversely, in the CZ-SSE sample the copper appears to be zoning around the edge of the crystal, with a region of copper depletion instead being present in the centre of the crystal.

This can be attributed to the synthesis method of mechanical incorporation, which forces ion-exchange to occur in the solid-state almost exclusively via surface diffusion.

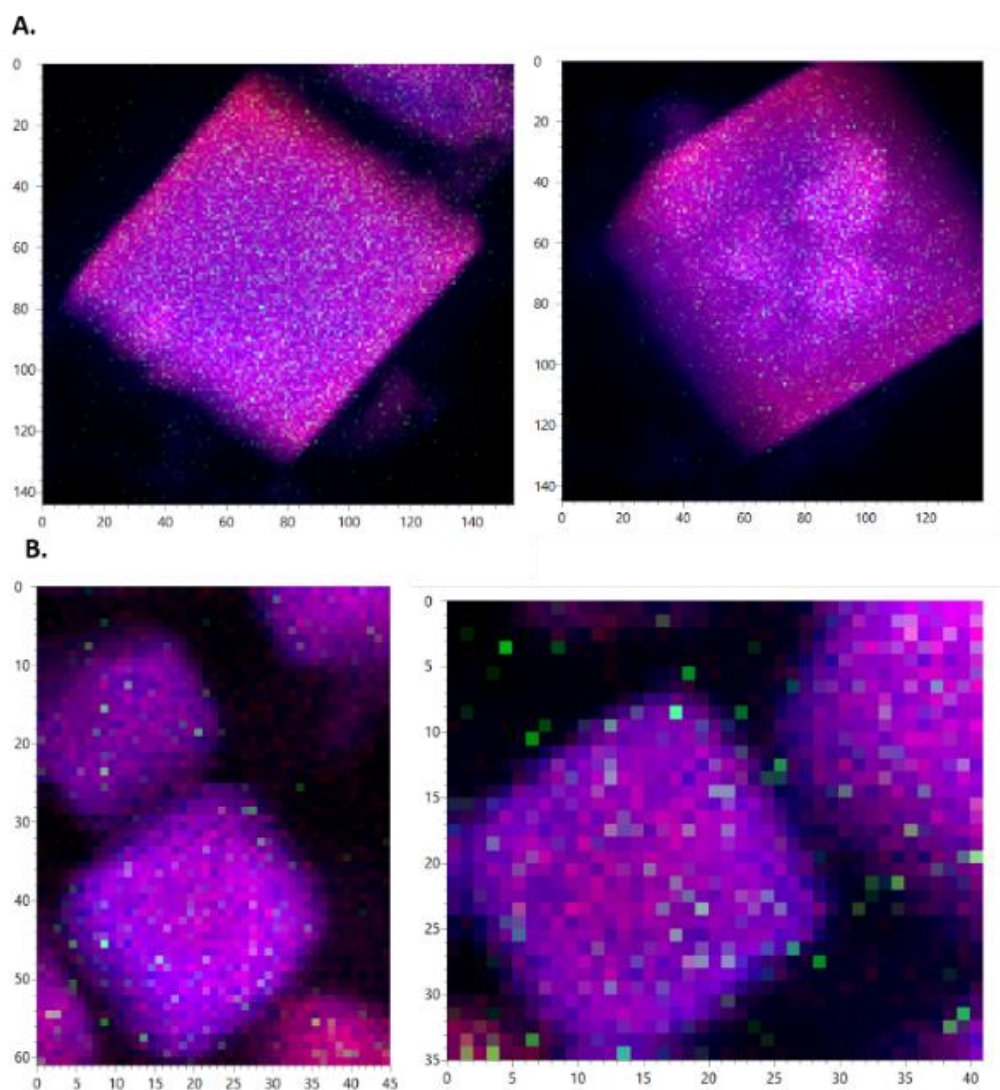


Figure 94 **Nano-XRF images of copper SSZ-13 catalysts prepared by two different ion-exchange methods.** A) nano-XRF (step size = 100 nm, detector 0.05) elemental map of CZ-WIE showing silicon (red) and copper (blue) b) nano-XRF (step size = 100 nm, detector 0.05) elemental map of CZ-SSE showing silicon (red) and copper (blue). Scale bars on the axes are shown in microns.

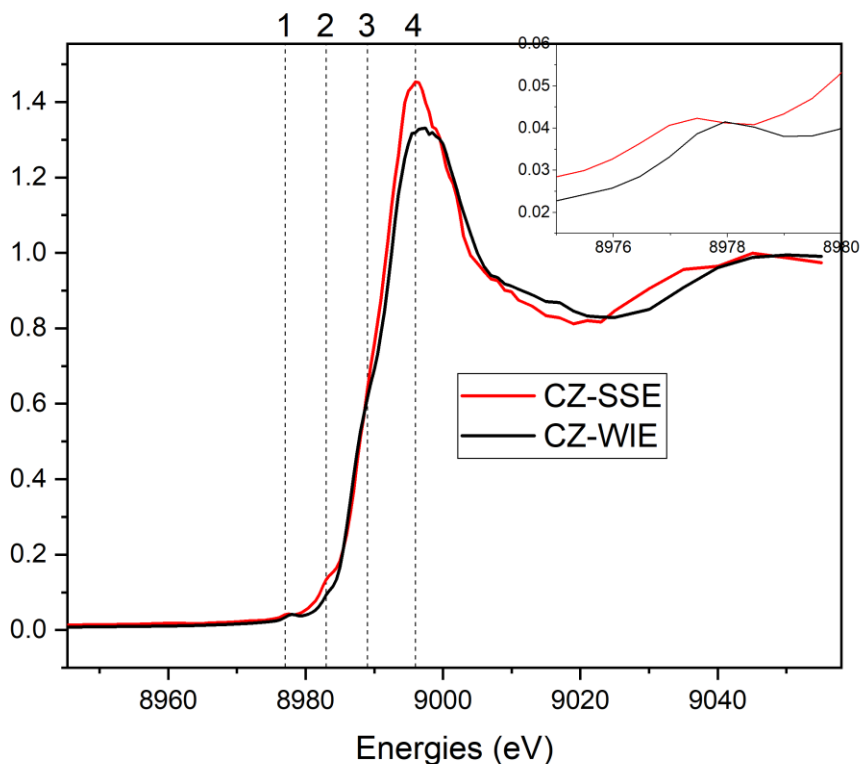


Figure 95 **Normalised XANES spectra of CZ-WIE and CZ-SSE.** Feature 1 at 8975-8980 eV; feature 2 at 8982 eV; feature 3 at 8986 eV; feature 4 at 8995 eV.

Figure 95 shows normalised XANES spectra of CZ-WIE and CZ-SSE. In total, four features of interest have been identified, all of which have been previously assigned by Deka et al.³⁹⁸. Feature 1, expanded for clarity between 8975 and 8980 eV, is assigned to dipole forbidden $1s \rightarrow 3d$ transition in Cu^{2+} . The feature is present in both samples but shifted from 8977 in the CZ-SSE sample to 8978 in CZ-WIE sample. Feature 2 at 8982 eV is associated with $1s$ orbital to double degenerate $3p_{xy}$ transitions in linear Cu^+ systems like CuAlO_2 . Although present in both samples, the feature is much more prominent in the Cu-SSE sample indicating a higher concentration of Cu(I) species. Feature 3 at 8986 eV is only seen in CZ-WIE and is associated with a $\text{Cu}^{2+} 1s \rightarrow 4p_z$ ligand Cu^{2+} charge transfer. Feature 4 at 8995 eV is seen in both samples. In contrast to the XANES presented by Deka et al. the peak height ratio appears different, with the CZ-SSE sample being higher than the CZ-WIE sample. Difference can also be seen in the tail of the spectra. CZ-SSE appears to be experiencing a frequency shift relative to the CZ-WIE sample that is consistent with the longer bond length associated with Cu^+ systems.

Overall, XANES indicates that both samples are exhibiting multiple copper environments. However, a side-by-side comparison of the two catalysts show considerable differences in the intensity ratios of all the edge-features discussed. In particular, the prominence of feature 2 indicate that there is more Cu^+ in the CZ-SSE sample than the CZ-WIE sample. Additionally, the CZ-SSE sample is in good agreement with a Cu-SSZ-13 zeolite previously shown to have an aluminate phase present. It is worth

noting that although Deka et al. use a vapour deposition method to create an aluminate rich catalyst, solid-state exchange is generally a more systematic preparation method as vapour deposition is known to have problems with gradients of copper impregnation across the zeolite bed³⁹⁸.

3.2.2 *In situ* IR Spectroscopy

In situ synchrotron IR micro-spectroscopy was used to understand the role of key surface species in NH_3 -SCR reaction and to find their correlation with Cu speciation. Figure 96 shows *in situ* IR spectra for CZ-WIE and CZ-SSE exposed to $\text{NO} + \text{O}_2$ and $\text{NO} + \text{O}_2 + \text{NH}_3$ respectively at 180 °C. Figure 97 shows the concentration of N_2O recorded from the mass spectrometer in the $\text{NO} + \text{O}_2 + \text{NH}_3$ experiment, confirming that N_2O production is higher in the CZ-SSE sample.

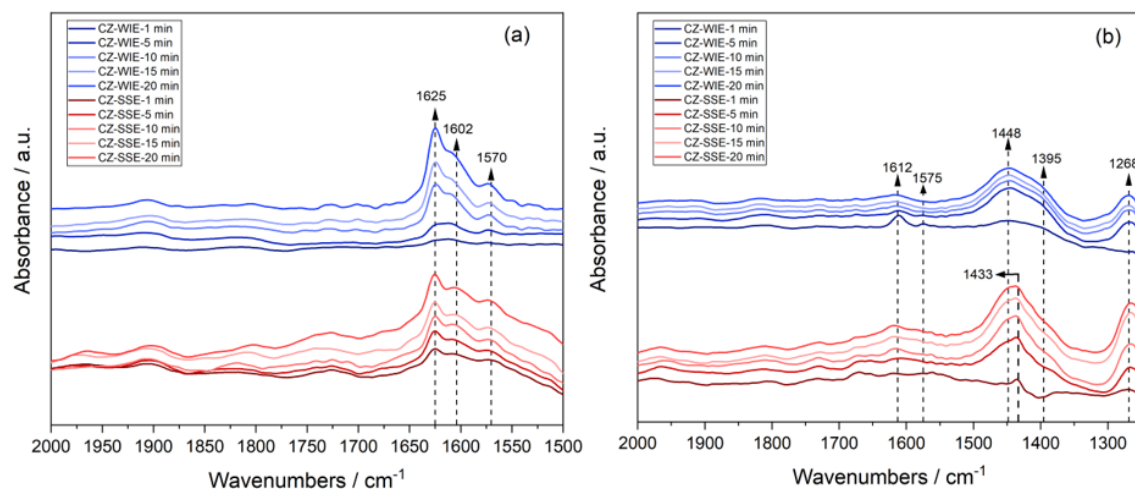


Figure 96 *In situ* FTIR spectra of CZ-WIE and CZ-SSE exposed to (a) $\text{NO} + \text{O}_2$ and (b) $\text{NO} + \text{O}_2 + \text{NH}_3$ at 180 °C

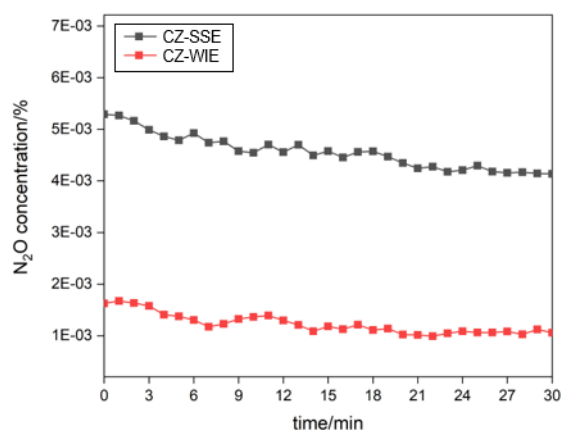


Figure 97 Mass spectroscopy data for N_2O concentration in CZ-WIE and CZ-SSE upon exposure to $\text{NO} + \text{O}_2 + \text{NH}_3$ at 180 °C.

The region between 1200–2000 cm^{-1} was selected to focus on viewing nitrogen-associated bands. In the $\text{NO} + \text{O}_2$ experiment, over the course of 20 minutes bands at 1625, 1602, and 1570 cm^{-1} appeared in both samples. Bands in the region 1500–1650 cm^{-1} are usually attributed to surface nitrate groups with different co-ordinations. The band at 1570 cm^{-1} has previously been assigned

to monodentate nitrate on Cu sites, whereas the band at 1602 cm^{-1} has been linked to monodentate nitrate on Al sites. Bridging nitrates on Al sites have been observed as a band at 1625 cm^{-1} . Initially, it would appear that bridging nitrates on surface Al sites formed in the first 5 minutes of gas exposure. The CZ-WIE sample appears to show greater evolution in the peak ratio of 1625 cm^{-1} over the 20 minute period, compared to the CZ-SSE sample, which exhibits less evolution after the first 5 minutes.

With the introduction of NH_3 , the IR spectra appear markedly different. The trio of bands at 1625 , 1602 , and 1570 cm^{-1} are no longer immediately visible. The absence of bands between 1500 – 1650 cm^{-1} can be explained by nitrate species being rapidly consumed by gaseous NH_3 . In the first minute of exposure, the CZ-WIE sample has two bands at 1612 and 1575 cm^{-1} , which rapidly deplete by 5 minutes under gas flow. Emergent from this time point onwards are two main bands at 1448 and 1268 cm^{-1} as well as a shoulder feature at 1395 cm^{-1} . The CZ-SSE sample also appears to show these three bands at 1448 , 1395 , and 1268 cm^{-1} with the addition of a band at 1433 cm^{-1} . Four of these bands (i.e. 1612 , 1448 , 1395 , 1268 cm^{-1}) might be ascribed in the following manner. Exposure to NH_3 is expected to generate bands associated with at least three types of adsorbed NH_3 species in Cu-SSZ-13⁴¹⁷. These include ammonium ions formed on Brønsted acid sites as a result of incomplete ion exchange ($\delta(\text{NH}_4^+)_{\text{as}}$ at 1448 and $\delta(\text{NH}_4^+)_{\text{s}}$ at 1395 cm^{-1}), $[\text{Cu}(\text{NH}_3)_4]^{2+}$ complexes arising from NH_3 coordination with Cu^{2+} Lewis sites ($\delta(\text{NH}_3)_{\text{as}}$ at 1612 cm^{-1} , and NH_3 wagging in $[\text{Cu}(\text{NH}_3)_4]^{2+}$ at 1268 cm^{-1} ^{417–421}. Given that the band at 1448 cm^{-1} appears stronger than at 1612 cm^{-1} , it could be speculated that the absorption of NH_4^+ ions is stronger on Brønsted acid sites rather than Lewis acid sites. This has previously been explored by Lezcano-Gonzalez *et al.* who found that NH_4^+ ions formed on Brønsted acid sites react very slowly and usually behave as NH_3 storage sites⁴¹⁷.

Less readily assigned is the intermediate band at 1433 cm^{-1} , which is present in the CZ-SSE sample from as early as 1 minute of exposure to gases but not in the CZ-WIE sample. This unique band accompanies both unique bands observed in the Raman characterisation and edge features in the XANES spectra, implying that there is reasonable cause to consider an association between the intermediate 1433 cm^{-1} band and the copper environment of the CZ-SSE preparation. It is speculated based on preliminary analysis that this band is related to the linear Cu species observed in the XANES data and may also be associated with the higher N_2O concentration observed in Figure 97. For example, a species like CuAlO_2 may have more coordinated NH_3 ligands or more Cu^{2+} ions accessible to NH_3 . More confident assignments can be made with further simulation work, which is currently underway. Understanding what is co-ordinating the copper will likely have the greatest bearing on future interpretation. Some features that could be investigated include aluminates, mixed valence structures, O-O stretches, and copper-oxo complexes. Simulating the likelihood of different structures forming as a function of copper loading might also be useful if

it is thought that localised copper concentration may be occurring based on some of the zoning features seen in XRF imaging.

3.3 Conclusion

In this chapter, a multimodal study of two types of Cu-SSZ-13 preparations was presented. One type, prepared by a solid-exchange method, was shown to exhibit features in XANES spectra that could be attributed to a linear copper species. In *in situ* IR spectroscopy experiments, the traditionally prepared wet-ion exchanged sample and the CZ-SSE sample were shown to have similar responses when exposed to a combination of NO + O₂ gases, but markedly different responses when exposed to NO + O₂ + NH₃. Bands in NO + O₂ exposed samples were assigned to surface nitrate groups linked to either Cu or Al sites. Bands in NO + O₂ + NH₃ exposed samples were generally assigned to ammonium ions on Brønsted acid sites and copper complexes.

The data presented indicates that the different preparation methods have yielded Cu-SSZ-13 samples with subtle yet visible differences in their characterisation and behaviour. While the XANES indicates the presence of a linear copper species like Cu₂O or CuAlO₂, the data generated is not able to comment on what this species might ‘look’ like or how it might be distributed. Given that both samples have been subjected to standard high temperature activations and gas experiments, it is expected that the Cu(I) species must be stable, making a compound such as an aluminate phase one such possibility. Based on the higher production rate of N₂O, this would also indicate that the species should be readily accessible. By exclusion, a crystalline phase might not constitute a large enough surface area to be considered ‘readily accessible’, meaning it may instead be a disperse species occurrent throughout the sample.

These results are part of an ongoing body of research and represent the first stages of characterisation. So far, the data imply that catalyst performance in a reaction might be affected by the synthesis process, highlighting the importance of utilising advanced characterisation techniques (like XRF, XANES, or optical methods) early on in the zeolite preparation process to gain a thorough understanding of how the native material originally presents and how it might evolve in the course of a reaction. In the context of this particular system, the observations documented here would undoubtedly be enhanced by computational interventions like DFT, which are currently underway. In a more generic vein, further comparative studies on zeolites prepared in different manners when applied as catalysts might provide further useful insight into the mechanism of SCR.

Chapter IX

Summary & Conclusion

1 Summary of Chapters

This thesis has explored the different ways in which light can interact with a zeolite. To achieve this, a range of characterisation techniques were utilised featuring excitation sources spanning different regions of the electromagnetic spectrum, as summarised in Figure 98.

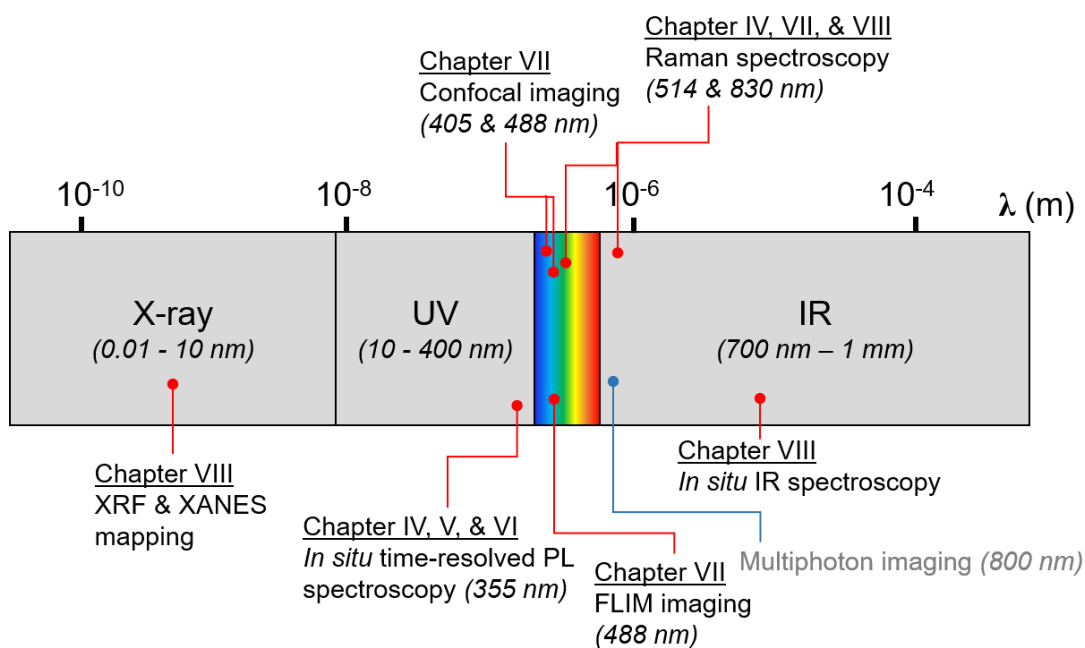


Figure 98 Placing the experiments of the thesis into context against the broader electromagnetic spectrum

In Chapter IV, time-resolved photoluminescence spectroscopy was used to analyse a set of SSZ-13 samples that were representative of different stages of the detemplation process. An as-synthesised zeolite, partially detemplated zeolite, and fully detemplated zeolite were characterised with CW spectra, gated spectra, and lifetime measurements. The results of this chapter

demonstrated that by considering temporal evolution, characteristic emission spectra with unique features could be obtained for each sample. The three principle observations were:

- 1) That a characteristic emission spectrum for the OSDA was established with a red-shift occurring upon confinement;
- 2) That phosphorescence signal can be used to signature the presence of occluded organic material; and,
- 3) That an intrinsic zeolite emission related to framework defects was recorded in the calcined sample.

In Chapter V, a power study was conducted to determine the stability of calcined and uncalcined SSZ-13 samples at high and low temperature under a range of different laser powers. The samples were found to be broadly stable between 0.9-900 μW of 355 nm irradiation. Some spectral variation was seen in the uncalcined sample however this was attributed to the tendency for organic materials to bleach. One particular observation of interest was the tendency for all samples to exhibit high levels of broadband emission at elevated temperatures. Where PL emission is assigned to organic molecules, this behaviour is unexpected. This phenomenon was explored in further *in situ* studies in the following chapter.

Chapter VI focused on a series of *in situ* studies of zeolite samples with different temperature protocols. The primary aim of these studies was to determine how reproducible responses to temperature were, whether they were reversible, and whether they happened in all samples or only selected types. In the first part of this chapter, an *in situ* detemplation was performed, followed by a temperature cycling experiment, and then a heating experiment on silicon-rich SSZ-13. It was found that at room temperature, the emission spectra acted as a more simple reflection of the type of guest molecules present in the framework. However, at higher temperature, an abrupt change in emission intensity meant that the emission spectrum no longer appeared to reflect speciation in such a simple manner. Additionally, the point at which emission intensity appeared to increase seemed to occur consistently between 360-400 $^{\circ}\text{C}$. It was instead speculated that an alternative emission mechanism in the form of structural point defects was the reason for this behaviour. Further to this, the silicon-rich sample did not experience an increase in emission intensity, supporting the theory that the leap in intensity could be associated with oxygen vacancies surrounding aluminium sites.

In the second part of this chapter, an *in situ* MTO reaction was performed. Unlike the *in situ* detemplation studies, the system did not experience a broadband increase in emission intensity, instead showing a distinct evolution in the peaks present. This was attributed to the addition of a constant source of reactant, which promoted continuous catalytic activity throughout the duration of the experiments. Rather than begin to form significant amounts of structural defects, the abundance of newly forming organic products on the internal surfaces of the framework meant

that the emission signal at high temperature continued to be broadly representative of the chemical species present in the system.

Chapter VII took the same type of samples analysed in Chapter IV tracking the detemplation process and placed them under a microscope. The samples were imaged in confocal modality at 405 nm and in FLIM modality at 488 nm. Where the UV irradiation in Chapter IV meant that it was possible to comment on the presence or absence of OSDA, the visible wavelength excitation meant that a different category of species was being studied. In this case, distributions of organic products of the combustion process and hydrocarbon pool chemistry were being mapped. Based on a comparative study that used imaging, lifetime information, fluorescence emission spectra information and Raman data, it was found that there were at least four types of emissive behaviours present in the samples. They are summarised as follows:

1. An emissive species (type 1) distributed fairly evenly throughout the zeolite matrix with a shorter lifetime, primarily seen in the partially detemplated sample and possibly associated with smaller molecules directly resulting from the template decomposition process;
2. An agglomerated emissive species (type 2) with a highly characteristic morphology and medium duration lifetime, appearing to originate from the centre of the crystal in the partially detemplated sample, and emanating towards the surface of the crystal in the twice calcined sample, possibly comprised of late hydrocarbon pool products like substituted PAHs;
3. An emissive species localised both subsurface and close to the surface, with an emission centred more towards the red but with a shorter lifetime, seen in both calcined materials (type 3/5), which is tentatively assigned to carbon nanostructures; and
4. An emissive species spanning across larger subsurface regions with a significantly longer lifetimes (type 4), and seen in both calcined materials, possibly associated with late products of hydrocarbon pool chemistry and also potentially influenced by both the local microstructural changes that promote their production and the confinement effects of the framework.

In Chapter VIII, two types of Cu-exchanged SSZ-13 samples, prepared via different methods, used in the SCR reaction were analysed in an extended multimodal Diamond synchrotron study using XRF and XANES mapping to image the crystals and IR spectroscopy to probe chemical species forming on the zeolite during an *in situ* reaction. In this study, XRF mapping showed that copper distributions across the crystals were not uniform with preparation, with solid-state exchanged samples having slightly higher concentrations around the outer perimeters of the crystals. IR spectroscopy showed the evolution of nitrate species, showing differences depending on the sample preparation method.

2 Considerations for the Presented Work

As experimental subjects, zeolites are decidedly demanding in the face of laser excitation, requiring not only exceedingly stable environmental controls for temperature and humidity, but large wavelength windows to accommodate their broadband signal and gentle irradiation sources. Far from needing an amenably cushioned environment to coax out some statistically improbable event, as might be the case in, say, a neutrino observatory, zeolites seem to produce instrumental responses somewhat frustratingly readily. Especially at elevated temperatures or in the presence of reactants, the absence of rigorous control over the experimental setup can see zeolites expressing themselves in a histrionic and cacophonous manner across the dynamic range of a spectrometer. A multitude of rapidly changing signals arising from sample burning, unwanted chemical interactions, and environmental heating can serve to confound the ‘real’ signal arising from the actual catalytic reaction. Consequently, although this writeup has focused on the results that constitute a relative success, the undocumented portion of the work in this project was largely concerned with establishing the best operational parameters under which the data should be acquired. Indeed, an underlying theme of the results is that despite being broadly reproducible, which is certainly relevant for the bulk scale upon which industrial catalysis generally operates, there is repeated evidence to suggest that on a nanoscale, zeolites exhibit a considerable degree of variability. Some examples to be considered include the results of Chapter VIII, which focused on the performance of two Cu-zeolites prepared *via* different routes and implied that despite appearing similar in bulk characterisation methods, changes in the synthesis process appeared to visibly affect certain recorded elements of catalytic behaviours. A more visually compelling example are the micrographs in Chapter VII, which showed, especially in widefield views, that distributions of emissive deposits were variable from crystal to crystal. *In situ* spectroscopic studies also showed that although trends in peak position, height, and spectral profile were broadly reproducible in experimental repeats, they did not exhibit exact agreement. Additionally, the postulate that high temperature emission profile changes were evidence of oxygen deficiencies further implies that under more extreme environmental conditions, the frameworks in fact become more labile and capable of reassembling themselves on a local level with an as yet undetermined amount of variation. Advanced interrogation of these samples, therefore, necessitates thoughtful accommodation of the idiosyncrasies of each zeolite sample, which are themselves uniquely dependent on a vast number of factors such as the framework, dopant composition, et cetera.

The changing energy and characteristics of each wavelength range brings with it a different set of challenges for characterisation. Firstly, changing the irradiation wavelength probes different aspects of the sample. For example, deeper UV excitation can stimulate a response from the framework or the organic templating agent, as demonstrated in Chapter IV. Due to their decreasing energy, visible range wavelengths will not be capable of probing the aluminosilicate

framework but rather certain classes of fluorescent molecules like polycyclic aromatic hydrocarbons. UV and visible excitation will generally excite some form of luminescence, which can be problematic if using techniques like Raman spectroscopy, so wavelength selection becomes important in the experimental design. Secondly, changing the irradiation wavelength changes the way in which the samples become damaged. Higher energy UV sources have a higher tendency to photobleach organic products, but NIR sources at high power can globally damage the sample by heating the framework and causing the entire sample to either physically move across the field of view or sustain visible thermal damage. Finally, UV irradiation can be challenging to manipulate in imaging mode given that the beam is not visible to the naked eye and that standard microscope optics can't handle the higher energy associated with it. One way around this could be multiphoton excitation.

3 Future Work

The work in this thesis is differentiated from contemporary work by its focus on label-free emission signal. This positions the spectroscopic signatures and images uniquely within the field as they provide insight into the characteristics and distribution of 'real' emissive products that can be interpreted with respect to the chemistry of the catalytic systems they represent. Future work in this area will likely be earmarked by further studies that push the boundaries of label-free experimentation.

To this end, these experiments will undoubtedly be improved with the advent of more sensitive detectors with improved signal-to-noise ratios and expanded dynamic ranges. As discussed in the conclusion for Chapter IV, customised spectroscopic setups and microscopes using minimal optical components that are trained with a geometrically offset excitation and detection pathway are recommended for future studies.

On the *in situ* and *operando* front, the commercial market for reaction cells, dominated by Linkam and Harrick, is surprisingly small with available options having a number of design features that make them functionally incompatible with more complex experimental setups. Some issues include large dead volumes, unreliable connections, and limited configuration options for experiments performed in transmission mode in inverted microscopes. The size and orientation of the reaction chamber eventually becomes a limiting factor when being integrated into optical pathways, so customising their construction will ultimately be an important step in creating *in situ* and *operando* experiments with optimised experimental parameters.

The simplest and most immediate extension to this current work would be to simply repeat the room temperature imaging and spectroscopic studies of early stage zeolite synthesis samples using different frameworks templated in different ways, of which such permutations there would

be many. At certain wavelengths, these types of studies would give a clearer idea of which framework groups exhibit greater amounts of intrinsic fluorescence and indeed whether some families have a greater potential to retain organic material even after post-synthesis heat treatments.

A more involved but higher impact extrapolation of the work would be to utilise correlative techniques that allow the same crystal or sample area to be characterised across different imaging modalities. This could be readily performed on commercial options like the Zeiss ZEN Shuttle & Find exist, which enable samples to be moved between Zeiss optical microscopes and Zeiss electron microscopes, although it is more likely that this will be achieved using the more traditional method of fiducial markers. For example, it could be possible to correlate XRF and XANES mapping, electron microscopy, and optical microscopy if the samples were loaded onto metallic TEM grids.

Although advanced optical microscopy techniques like super-resolution or lightsheet may be more widely practiced in the future, it is unlikely that these will be realised without the use of targeted dyes. This is due to the generally low-level, broadband nature of zeolite autofluorescence, which does not lend itself to stimulated emission depletion or structured illumination. Certainly, the ability to resolve finer structures will provide greater scope to see product distribution on a length scale that tends closer to the dimensions of the framework channels.

In a bid to correlate UV spectroscopy studies with imaging, multiphoton excitation could also be attempted. Multiphoton FLIM using 600-900 nm excitation from a Ti:Sapphire laser was in fact attempted during the early stages of this project, although the, at the time, insurmountable challenge of heating from the NIR wavelengths caused the samples to behave in a non-representative manner and burn. Using a pulsed laser with a lower repetition rate may be one way to overcome this problem

References

1. Grandjean, F. Optical study of the absorption of the heavy vapors by certain zeolites. *C. R. Acad. Sci* **149**, 866–868 (1910).
2. Weigel, O. & Steinhoff, E. Adsorption of organic liquid vapors by chabazite. *Z. Krist.* **61**, 125–154 (1925).
3. Milligan, W. O. & Weiser, H. B. The Mechanism of the Dehydration of Zeolites. *J. Phys. Chem.* **41**, 1029–1040 (1937).
4. Dana, E. *System of Mineralogy*. (John Wiley and Sons, 1942).
5. Pauling, L. The Structure of Sodalite and Helvite. *Zeitschrift fur Krist.* **74**, 213–225 (1930).
6. Pauling, L. The Structure of the Chlorites. *Proc. Natl. Acad. Sci. U. S. A.* **16**, 578–582 (1930).
7. Reed, T. B. & Breck, D. W. Crystalline Zeolites. II. Crystal Structure of Synthetic Zeolite, Type A. *J. Am. Chem. Soc.* **78**, 5972–5977 (1956).
8. Baerlocher, C. & McCusker, L. Database of Zeolite Structures. Available at: <http://www.iza-structure.org/databases/>.
9. Breck, D. W. *Molecular Sieve Zeolites*. (American Chemical Society, 1968).
10. Fischer, K. & Meier, W. Kristallchemie der zeolithe. *Fortschr.* **42**, 50–86 (1965).
11. Smith, J. V. Special Paper 1. *Miner. Soc. Am.* (1963).
12. Smith, J. V. Definition of a zeolite. *Zeolites* **4**, 309–310 (1984).
13. Liebau, F. Zeolites and clathrasils—Two distinct classes of framework silicates. *Zeolites* **3**, 191–193 (1983).
14. Lok, B. M. *et al.* Silicoaluminophosphate molecular sieves: another new class of microporous crystalline inorganic solids. *J. Am. Chem. Soc.* **106**, 6092–6093 (1984).
15. Fletcher, R. E., Ling, S. & Slater, B. Violations of Löwenstein's rule in zeolites. *Chem. Sci.* **8**, 7483–7491 (2017).
16. Csicsery, S. M. Shape-selective catalysis in zeolites. *Zeolites* **4**, 116–126 (1984).
17. Paul, G. *et al.* Combined solid-state NMR, FT-IR and computational studies on layered and porous materials. *Chem. Soc. Rev.* **47**, 5684–5739 (2018).
18. Jiang, Y., Huang, J., Dai, W. & Hunger, M. Solid-state nuclear magnetic resonance investigations of the nature, property, and activity of acid sites on solid catalysts. *Solid State Nucl. Magn. Reson.* **39**, 116–141 (2011).
19. Yi, F. *et al.* Origin of weak Lewis acids on silanol nests in dealuminated zeolite Beta. *J. Catal.* **380**, 204–214 (2019).
20. Huang, M., Kaliaguine, S. & Auroux, A. Lewis basic and Lewis acidic sites in zeolites. in *Zeolites: A Refined Tool for Designing Catalytic Sites* (eds. Bonneviot, L. & Kaliaguine, S. B. T.-S. in S. S. and C.) **97**, 311–318 (Elsevier, 1995).
21. Mazur, M., Prech, J. & Cejka, J. Zeolites and Other Micro-Mesoporous Molecular Sieves. *Kirk-Othmer Encyclopedia of Chemical Technology* 880 (2019). doi:10.1002/0471238961.zeolcejka01.pub2
22. Satterfield, C. *Heterogenous Catalysis in Practice*. (McGraw-Hill, 1980).
23. Bish, D. Thermal Behavior of Natural Zeolites. *Proc. Zeolite '93 Conf.* (1993).

24. Alberti, A. & G, V. Topological changes in dehydrated zeolites: breaking of T-O-T bridges. *Proc 6th Int Conf Zeolite* 834–841 (1984).
25. Zhi, Y. *et al.* Dehydration Pathways of 1-Propanol on HZSM-5 in the Presence and Absence of Water. *J. Am. Chem. Soc.* **137**, 15781–15794 (2015).
26. Pugh, S. M., Wright, P. A., Law, D. J., Thompson, N. & Ashbrook, S. E. Facile, Room-Temperature ¹⁷O Enrichment of Zeolite Frameworks Revealed by Solid-State NMR Spectroscopy. *J. Am. Chem. Soc.* **142**, 900–906 (2020).
27. Heard, C. J. *et al.* Fast room temperature lability of aluminosilicate zeolites. *Nat. Commun.* **10**, (2019).
28. Van Speybroeck, V. *et al.* Advances in theory and their application within the field of zeolite chemistry. *Chem. Soc. Rev.* **44**, 7044–7111 (2015).
29. Berzelius, J. Årsberättelsen om framsteg i fysik och kemi. *R. Swedish Acad. Sci.* (1835).
30. Dumesic, J. A., Huber, G. W. & Boudart, M. Principles of Heterogeneous Catalysis. *Handbook of Heterogeneous Catalysis* (2008). doi:doi:10.1002/9783527610044.hetcat0001
31. Matsukura, M. & Kurosaki, F. Development of Zeolite-based Adsorbents for Highly Contaminated Water in Fukushima. *J. Ion Exch.* **28**, 51–57 (2017).
32. Lauriente D, I. Y. *The SRI Consulting Chemical Economics Handbook.* (2005). doi:599.1000 F
33. Yilmaz, B. & Muller, U. Catalytic Applications of Zeolites in Chemical Industry. *Top. Catal.* **52**, 888–895 (2009).
34. Shelef, M. Selective Catalytic Reduction of NO_x with N-Free Reductants. *Chem. Rev.* **95**, 209–225 (1995).
35. Inomata, Y. *et al.* Bulk Vanadium Oxide versus Conventional V₂O₅/TiO₂: NH₃–SCR Catalysts Working at a Low Temperature Below 150 °C. *ACS Catal.* **9**, 9327–9331 (2019).
36. Beale, A. M., Gao, F., Lezcano-Gonzalez, I., Peden, C. H. F. & Szanyi, J. Recent advances in automotive catalysis for NO_x emission control by small-pore microporous materials. *Chem. Soc. Rev.* **44**, 7371–7405 (2015).
37. Tian, P., Wei, Y., Ye, M. & Liu, Z. Methanol to Olefins (MTO): From Fundamentals to Commercialization. *ACS Catal.* **5**, 1902–1938 (2015).
38. Honeywell's UOP Helping Meet Petrochemicals Demand in China with Breakthrough Coal-to-Plastics Technology. 1 Available at: https://www.uop.com/?press_release=honeywells-uop-helping-meet-petrochemicals-demand-in-china-with-breakthrough-coal-to-plastics-technology. (Accessed: 14th May 2019)
39. Vogt, E. T. C. & Weckhuysen, B. M. Fluid catalytic cracking: recent developments on the grand old lady of zeolite catalysis. *Chem. Soc. Rev.* **44**, 7342–7370 (2015).
40. Vermeiren, W. & Gilson, J. P. Impact of zeolites on the petroleum and petrochemical industry. *Top. Catal.* **52**, 1131–1161 (2009).
41. Finocchio, E., Cort, M., Busca, G., Larrubia, M. A. & Alemany, L. J. Microporous and Mesoporous Materials A study of Cu-SAPO-34 catalysts for SCR of NO_x by ammonia. **241**, 258–265 (2017).
42. Yarulina, I. *et al.* Methanol-to-olefins process over zeolite catalysts with DDR topology: Effect of composition and structural defects on catalytic performance. *Catal. Sci. Technol.* **6**, 2663–2678 (2016).
43. Kianfar, E., Hajimirzaee, S., mousavian, S. & Mehr, A. S. Zeolite-based catalysts for methanol to gasoline process: A review. *Microchem. J.* **156**, 104822 (2020).
44. Derouane, E. G. Conversion of Methanol to Gasoline over Zeolite Catalysts I. Reaction

Mechanisms BT - Zeolites: Science and Technology. in (eds. Ribeiro, F. R., Rodrigues, A. E., Rollmann, L. D. & Naccache, C.) 515–528 (Springer Netherlands, 1984).
doi:10.1007/978-94-009-6128-9_18

45. Kulkarni, A. R., Zhao, Z.-J., Siahrostami, S., Nørskov, J. K. & Studt, F. Monocopper Active Site for Partial Methane Oxidation in Cu-Exchanged 8MR Zeolites. *ACS Catal.* **6**, 6531–6536 (2016).
46. Hammond, C. *et al.* Aqueous-Phase Methane Oxidation over Fe-MFI Zeolites; Promotion through Isomorphous Framework Substitution. *ACS Catal.* **3**, 1835–1844 (2013).
47. *Handbook of Natural Zeolites*. (Bentham Science Publishers, 2012).
doi:10.2174/97816080526151120101
48. Eroglu, N., Emekci, M. & Athanassiou, C. G. Applications of natural zeolites on agriculture and food production. *J. Sci. Food Agric.* **97**, 3487–3499 (2017).
49. Shurson, G. C., Ku, P. K., Miller, E. R. & Yokoyama, M. T. Effects of Zeolite a or Clinoptilolite in Diets of Growing Swine. *J. Anim. Sci.* **59**, 1536–1545 (1984).
50. Ghiasi, F. & Jasour, M. S. Effects of Natural Zeolite (Clinoptilolite) on Water Quality , Growth Performance and Nutritional Parameters of fresh water aquarium fish , Angel. (2012).
51. Khodanazary, A., Boldaji, F., Tatar, A. & Dastar, B. Effects of Dietary Zeolite and Perlite Supplementations on Growth and Nutrient Utilization Performance , and Some Serum Variables in Common Carp , (*Cyprinus carpio*). **501**, 495–501 (2013).
52. Paritova, A. *et al.* The Influence of Chankanay Zeolites as Feed Additives on the Chemical, Biochemical and Histological Profile of the Rainbow Trout (*Oncorhynchus mykiss*). *J. Aquac. Res. Dev.* **5**, 1–8 (2013).
53. Danabas, D. Fatty Acids Profiles of Rainbow Trout (*Oncorhynchus Mykiss* Walbaum , 1792) Fed with Zeolite (Clinoptilolite). *J. Anim. Plant Sci.* **21**, 561–565 (2014).
54. Sekhon, B. S. & Sangha, M. K. Detergents — Zeolites and enzymes excel cleaning power. *Resonance* **9**, 35–45 (2004).
55. Cinar, S. & Beler-Baykal, B. Ion exchange with natural zeolites: An alternative for water softening? *Water Sci. Technol.* **51**, 71–77 (2005).
56. Jubin, R. Organic Iodine Removal From Simulated Dissolver Off-Gas Systems Utilising Silver-Exchanged Mordenite. in *7th Annual AIChE Meeting* 28 (1981).
57. Izumi, J. Waste Gas Treatment Using Zeolites in Nuclear-Related Industries. in *Handbook of Zeolite Science and Technology* (eds. Auerbach, S., Carrado, K. & Dutta, P.) 928 (Taylor & Francis Inc, 2003).
58. Rimoli, M. G. *et al.* Synthetic zeolites as a new tool for drug delivery. *J. Biomed. Mater. Res. Part A* **87A**, 156–164 (2008).
59. Khodaverdi, E., Soleimani, H. A., Mohammadpour, F. & Hadizadeh, F. Synthetic Zeolites as Controlled-Release Delivery Systems for Anti-Inflammatory Drugs. *Chem. Biol. Drug Des.* **87**, 849–857 (2016).
60. Alarcos, N., Cohen, B., Ziólek, M. & Douhal, A. Photochemistry and Photophysics in Silica-Based Materials: Ultrafast and Single Molecule Spectroscopy Observation. *Chem. Rev.* **117**, 13639–13720 (2017).
61. Carro-Temboury, M. R., Arppe, R., Vosch, T. & Sørensen, T. J. An optical authentication system based on imaging of excitation-selected lanthanide luminescence. *Sci. Adv.* **4**, 1–8 (2018).
62. Calzaferri, G. *et al.* Light-harvesting host-guest antenna materials for photonic devices. *Org. Optoelectron. Photonics II* **6192**, 619216 (2006).
63. Li, J., Corma, A. & Yu, J. Synthesis of new zeolite structures. *Chem. Soc. Rev.* **44**, 7112–7127 (2015).

64. Cundy, C. S. & Cox, P. A. The hydrothermal synthesis of zeolites: History and development from the earliest days to the present time. *Chem. Rev.* **103**, 663–701 (2003).
65. Cundy, C. S. & Cox, P. A. The hydrothermal synthesis of zeolites: Precursors, intermediates and reaction mechanism. *Microporous Mesoporous Mater.* **82**, 1–78 (2005).
66. Coronas, J. Present and future synthesis challenges for zeolites. *Chem. Eng. J.* **156**, 236–242 (2010).
67. Wang, W. *et al.* Mild-acid-assisted thermal or hydrothermal dealumination of zeolite beta, its regulation to Al distribution and catalytic cracking performance to hydrocarbons. *J. Catal.* **362**, 94–105 (2018).
68. Beyer, H. K. Dealumination Techniques for Zeolites BT - Post-Synthesis Modification I. in 203–255 (Springer Berlin Heidelberg, 2002). doi:10.1007/3-540-69750-0_3
69. Melián-Cabrera, I., Kapteijn, F. & Moulijn, J. A. Room temperature detemplation of zeolites through H₂O₂-mediated oxidation. *Chem. Commun.* **1**, 2744–2746 (2005).
70. Soulard, M., Bilger, S., Kessler, H. & Guth, J. L. Thermoanalytical characterization of MFI-type zeolites prepared either in the presence of OH⁻ or of F⁻ ions. *Zeolites* **7**, 463–470 (1987).
71. Ferone, C., Esposito, S. & Pansini, M. Thermally induced structural and microstructural evolution of barium exchanged zeolite A to celsian. in *Oxide Based Materials* (eds. Gamba, A., Colella, C. & Coluccia, S. B. T.-S. in S. S. and C.) **155**, 249–260 (Elsevier, 2005).
72. Lang, L., Zhao, S., Jiang, J., Yang, W. & Yin, X. Importance of hydrogen for low-temperature detemplation of high-silica MFI zeolite crystals. *Microporous Mesoporous Mater.* **235**, 143–150 (2016).
73. Zhao, S. H., Lang, L., Yin, X. L., Yang, W. S. & Wu, C. Z. TPAOH template removal from high-silica ZSM-5 by low-temperature hydrocracking. *Wuli Huaxue Xuebao/ Acta Phys. - Chim. Sin.* **31**, 793–799 (2015).
74. Dong, J., Lin, Y. S., Hu, M. Z. C., Peascoe, R. A. & Payzant, E. A. Template-removal-associated microstructural development of porous-ceramic-supported MFI zeolite membranes. *Microporous Mesoporous Mater.* **34**, 241–253 (2000).
75. Mateo, E., Paniagua, A., Güell, C., Coronas, J. & Santamaría, J. Study on template removal from silicalite-1 giant crystals. *Mater. Res. Bull.* **44**, 1280–1287 (2009).
76. Choi, J. *et al.* Grain Boundary Defect Elimination in a Zeolite Membrane by Rapid Thermal Processing. *Science* (80-.). **325**, 590–593 (2009).
77. Rudham, R. & Winstanley, A. W. Effects of dry-air calcination on the physico-chemical and catalytic properties of HZSM-5 zeolite. *J. Chem. Soc. Faraday Trans.* **90**, 3191–3199 (1994).
78. Parker, L. M., Bibby, D. M. & Patterson, J. E. Thermal decomposition of ZSM-5 and silicalite precursors. *Zeolites* **4**, 168–174 (1984).
79. Jirka, I., Sazama, P., Zikánová, A., Hrabánek, P. & Kocirik, M. Low-temperature thermal removal of template from high silica ZSM-5. Catalytic effect of zeolitic framework. *Microporous Mesoporous Mater.* **137**, 8–17 (2011).
80. Qian, Q., Mores, D., Kornatowski, J. & Weckhuysen, B. M. Template removal processes within individual micron-sized SAPO-34 crystals: Effect of gas atmosphere and crystal size. *Microporous Mesoporous Mater.* **146**, 28–35 (2011).
81. He, J., Yang, X., Evans, D. G. & Duan, X. New methods to remove organic templates from porous materials. *Mater. Chem. Phys.* **77**, 270–275 (2003).
82. Kuhn, J., Gascon, J., Gross, J. & Kapteijn, F. Detemplation of DDR type zeolites by ozonation. *Microporous Mesoporous Mater.* **120**, 12–18 (2009).

-
83. Heng, S., Lau, P. P. S., Yeung, K. L., Djafer, M. & Schrotter, J. C. Low-temperature ozone treatment for organic template removal from zeolite membrane. *J. Memb. Sci.* **243**, 69–78 (2004).
84. Kuhn, J., Motegh, M., Gross, J. & Kapteijn, F. Detemplation of [B]MFI zeolite crystals by ozonation. *Microporous Mesoporous Mater.* **120**, 35–38 (2009).
85. Bilger, S., Soulard, M., Kessler, H. & Guth, J. L. Identification of the volatile products resulting from the thermal decomposition of tetra-, tri-, di-, and mono-n-propylammonium cations occluded in MFI-type zeolites. *Zeolites* **11**, 784–791 (1991).
86. Bourgeat-Lami, E., Di Renzo, F., Fajula, F., Mutin, P. H. & Des Courieres, T. Mechanism of the thermal decomposition of tetraethylammonium in zeolite β . *J. Phys. Chem.* **96**, 3807–3811 (1992).
87. Valange, S., Garrone, E., Geobaldo, F., Onida, B. & Gabelica, Z. 04-O-01-Direct synthesis of Cu(I)-MFI zeolite in the presence of Cu(II) methylamino complexes as mineralizing and reducing agents. *Stud. Surf. Sci. Catal.* **135**, 175 (2001).
88. Ren, L. *et al.* Designed copper-amine complex as an efficient template for one-pot synthesis of Cu-SSZ-13 zeolite with excellent activity for selective catalytic reduction of NO_x by NH₃. *Chem. Commun.* **47**, 9789–9791 (2011).
89. Muller, J. C. M., Hakvoort, G. & C, J. J. DSC and TG study of water adsorption and desorption on zeolite NaA. *J. Therm. Anal.* **53**, 449–466 (1998).
90. Chakrabarti, A. *et al.* A decade+ of operando spectroscopy studies. *Catal. Today* **283**, 27–53 (2017).
91. Qi, L. *et al.* Operando Solid-State NMR Observation of Solvent-Mediated Adsorption-Reaction of Carbohydrates in Zeolites. *ACS Catal.* **7**, 3489–3500 (2017).
92. Kadam, S. A. & Shamzhy, M. V. IR Operando study of ethanol dehydration over MFI zeolite. *Catal. Today* **304**, 51–57 (2018).
93. Lezcano-González, I. *et al.* Molybdenum Speciation and its Impact on Catalytic Activity during Methane Dehydroaromatization in Zeolite ZSM-5 as Revealed by Operando X-Ray Methods. *Angew. Chemie - Int. Ed.* **55**, 5215–5219 (2016).
94. Lakowicz, J. *Principles of Fluorescence Spectroscopy*. (Springer US, 2006). doi:10.1007/978-0-387-46312-4
95. Sauer, M., Hofkens, J. & Enderlein, J. *Handbook of Fluorescence Spectroscopy and Imaging*. (Wiley-VCH Verlag GmbH & Co, 2011).
96. Toffolo, M. B., Ricci, G., Caneve, L. & Kaplan-Ashiri, I. Luminescence reveals variations in local structural order of calcium carbonate polymorphs formed by different mechanisms. *Sci. Rep.* **9**, 1–15 (2019).
97. Gaft, M. L., Bershov, L. V., Krasnaya, A. R. & Yaskolko, V. Y. Luminescence centers in anhydrite, barite, celestite and their synthesized analogs. *Phys. Chem. Miner.* **11**, 255–260 (1985).
98. Calderon, T., Khanlary, M.-R., Rendell, H. M. & Townsend, P. D. Luminescence from natural fluorite crystals. *Int. J. Radiat. Appl. Instrumentation. Part D. Nucl. Tracks Radiat. Meas.* **20**, 475–485 (1992).
99. Takigami, M. & Ishikawa, H. Studies on Halogen Quenching Through the Stern-Volmer Plot. *Radioisotopes* **27**, 74–79 (1978).
100. Van, S.-P. & Hammond, G. S. Amine quenching of aromatic fluorescence and fluorescent exciplexes. *J. Am. Chem. Soc.* **100**, 3895–3902 (1978).
101. Lishan, D. G., Hammond, G. S. & Yee, W. A. Amine quenching of fluorescence of phenylated anthracenes. *J. Phys. Chem.* **85**, 3435–3440 (1981).
102. Patterson, L. K., Porter, G. & Topp, M. R. Oxygen quenching of singlet and triplet states. *Chem. Phys. Lett.* **7**, 612–614 (1970).

103. Gan, Z., Xu, H. & Fu, Y. Photon Reabsorption and Nonradiative Energy-Transfer-Induced Quenching of Blue Photoluminescence from Aggregated Graphene Quantum Dots. *J. Phys. Chem. C* **120**, 29432–29438 (2016).
104. Arnaut, L. Solar Energy Conversion. in *Applied Photochemistry* (eds. Evans, R., Douglas, P. & Burrow, H.) 598 (Springer Netherlands, 2013). doi:10.1007/978-90-481-3830-2
105. Edgar, A. Luminescent Materials. in *Springer Handbook of Electronic and Photonic Materials* (eds. Kasap, S. & Capper, P.) 1 (Springer International Publishing, 2017). doi:10.1007/978-3-319-48933-9_38
106. Demkov, A. A. & Sankey, O. F. Electronic Structure Theory for Zeolites. in (eds. Pinnavaia, T. J. & Thorpe, M. F.) 273–294 (Springer US, 2002). doi:10.1007/0-306-47066-7_18
107. Göttl, F. & Hafner, J. Structure and properties of metal-exchanged zeolites studied using gradient-corrected and hybrid functionals. III. Energetics and vibrational spectroscopy of adsorbates. *J. Chem. Phys.* **136**, 64501 (2012).
108. Becker, W. *et al.* Fluorescence Lifetime Imaging by Time-Correlated Single-Photon Counting. *Microsc. Res. Tech.* **63**, 58–66 (2004).
109. Betzig, E. & Trautman, J. K. Near-Field Optics: Microscopy, Spectroscopy, and Surface Modification Beyond the Diffraction Limit. *Science* (80-.). **257**, 189 LP – 195 (1992).
110. Rust, M. J., Bates, M. & Zhuang, X. Sub-diffraction-limit imaging by stochastic optical reconstruction microscopy (STORM). *Nat. Methods* **3**, 793–796 (2006).
111. Hell, S. W. Toward fluorescence nanoscopy. *Nat. Biotechnol.* **21**, 1347–1355 (2003).
112. Hell, S. W. & Wichmann, J. Breaking the diffraction resolution limit by stimulated emission: stimulated-emission-depletion fluorescence microscopy. *Opt. Lett.* **19**, 780–782 (1994).
113. Calzaferri, G. Nanochannels: Hosts for the supramolecular organization of molecules and complexes. *Langmuir* **28**, 6216–6231 (2012).
114. Roeffaers, M. B. J. *et al.* Fluorescence microscopy: Bridging the phase gap in catalysis. *Catal. Today* **126**, 44–53 (2007).
115. Janssen, K. P. F. *et al.* Single molecule methods for the study of catalysis: From enzymes to heterogeneous catalysts. *Chem. Soc. Rev.* **43**, 990–1006 (2014).
116. De Cremer, G., Sels, B. F., De Vos, D. E., Hofkens, J. & Roeffaers, M. B. J. Fluorescence micro(spectro)scopy as a tool to study catalytic materials in action. *Chem. Soc. Rev.* **39**, 4703–4717 (2010).
117. Hashimoto, S. Zeolite photochemistry: Impact of zeolites on photochemistry and feedback from photochemistry to zeolite science. *J. Photochem. Photobiol. C Photochem. Rev.* **4**, 19–49 (2003).
118. Calzaferri, G., Huber, S., Maas, H. & Minkowski, C. Host-guest antenna materials. *Angew. Chemie - Int. Ed.* **42**, 3732–3758 (2003).
119. Lin, H. & Fujii, M. Luminescent Zeolites. in 135–152 (IntechOpen, 2016). doi:http://dx.doi.org/10.5772/63805
120. Sola-Llano, R. *et al.* One-Directional Antenna Systems: Energy Transfer from Monomers to J-Aggregates within 1D Nanoporous Aluminophosphates. *ACS Photonics* **5**, 151–157 (2018).
121. Gartzia-Rivero, L., Bañuelos-Prieto, J., Martínez-Martínez, V. & Arbeloa, I. L. Versatile photoactive materials based on zeolite L doped with laser dyes. *Chempluschem* **77**, 61–70 (2012).
122. Chrétien, M. N., Shen, B., García, H., English, A. M. & Scaiano, J. C. Ship-in-a-Bottle Synthesis of Fluorescence-labeled Nanoparticles: Applications in Cellular Imaging¶.

123. Alvaro, M., Carbonell, E., Garcia, H., Lamaza, C. & Narayana Pillai, M. Ship-in-a-bottle synthesis of 2,4,6-triphenylthiapyrylium cations encapsulated in zeolites Y and beta: a novel robust photocatalyst. *Photochem. Photobiol. Sci.* **3**, 189–193 (2004).
124. Hashimoto, S., Moon, H. R. & Yoon, K. B. Optical microscopy study of zeolite-dye composite materials. *Microporous Mesoporous Mater.* **101**, 10–18 (2007).
125. Pfenniger, M. & Calzaferri, G. Intrazeolite Diffusion Kinetics of Dye Molecules in the Nanochannels of Zeolite L, Monitored by Energy Transfer. *ChemPhysChem* **1**, 211–217 (2000).
126. Seebacher, C. *et al.* Visualization of Mesostructures and Organic Guest Inclusion in Molecular Sieves with Confocal Microscopy. 1374–1377 (2001).
127. Roeffaers, M. B. J. *et al.* Morphology of large ZSM-5 crystals unraveled by fluorescence microscopy. *J. Am. Chem. Soc.* **130**, 5763–5772 (2008).
128. Roeffaers, M. B. J. *et al.* Relating pore structure to activity at the subcrystal level for ZSM-5: An electron backscattering diffraction and fluorescence microscopy study. *J. Am. Chem. Soc.* **130**, 13516–13517 (2008).
129. Ameloot, R. *et al.* Three-dimensional visualization of defects formed during the synthesis of metal-organic frameworks: A fluorescence microscopy study. *Angew. Chemie - Int. Ed.* **52**, 401–405 (2013).
130. De Cremer, G., Sels, B., De Vos, D., Hofkens, J. & Roeffaers, M. NASCA Microscopy: Super-Resolution Mapping of Chemical Reaction Centers. in 245–261 (2011). doi:10.1007/4243_2011_33
131. Bates, M., Jones, S. A. & Zhuang, X. Stochastic optical reconstruction microscopy (STORM): A method for superresolution fluorescence imaging. *Cold Spring Harb. Protoc.* **8**, 498–520 (2013).
132. Ristanović, Z. *et al.* High-resolution single-molecule fluorescence imaging of zeolite aggregates within real-life fluid catalytic cracking particles. *Angew. Chemie - Int. Ed.* **54**, 1836–1840 (2015).
133. Demkov, A. A. & Sankey, O. F. Clusters stuffed inside frameworks: Electronic structure theory. *J. Comput. Mater. Des.* **3**, 128–138 (1996).
134. Grandjean, D. *et al.* Origin of the bright photoluminescence of few-atom silver clusters confined in LTA zeolites. *Science (80-.)*. **361**, 686–690 (2018).
135. Baekelant, W. *et al.* Confinement of Highly Luminescent Lead Clusters in Zeolite A. *J. Phys. Chem. C* **122**, 13953–13961 (2018).
136. Coutiño-Gonzalez, E. *et al.* Silver Clusters in Zeolites: From Self-Assembly to Ground-Breaking Luminescent Properties. *Acc. Chem. Res.* **50**, 2353–2361 (2017).
137. Göltl, F. & Hafner, J. Structure and properties of metal-exchanged zeolites studied using gradient-corrected and hybrid functionals. II. Electronic structure and photoluminescence spectra. *J. Chem. Phys.* **136**, 64501 (2012).
138. Chai, Y. *et al.* Noble Metal Particles Confined in Zeolites: Synthesis, Characterization, and Applications. *Adv. Sci.* **6**, 1900299 (2019).
139. Claffy, E. W. & Schulman, J. H. Preliminary observations on the luminescence activation of zeolite minerals by base exchange*. *Am. Mineral.* **36**, 272–281 (1951).
140. Joshi, M. S. & Bhoskar, B. T. Luminescence studies on zeolite crystals. *Cryst. Res. Technol.* **18**, 213–218 (1983).
141. Yeritsyan, H. *et al.* The effect of electron irradiation on the optical properties of the natural Armenian Zeolite-clinoptilolite. *Cent. Eur. J. Phys.* **3**, 623–635 (2005).
142. Kobayashi, S., Sidike, A. & Yamashita, N. Luminescence spectra of chabazite-Ca, a zeolite mineral. *Phys. Chem. Miner.* **39**, 465–470 (2012).

143. Karwacki, L., Stavitski, E., Kox, M. H. F., Kornatowski, J. & Weckhuysen, B. Intergrowth Structure of Zeolite Crystals as Determined by Optical and Fluorescence Microscopy of the Template-Removal Process. *Angew. Chemie - Int. Ed.* **46**, 7228–7231 (2007).
144. Mores, D. *et al.* Space- And time-resolved in-situ spectroscopy on the coke formation in molecular sieves: Methanol-to-olefin conversion over H-ZSM-5 and H-SAPO-34. *Chem. - A Eur. J.* **14**, 11320–11327 (2008).
145. Karwacki, L. & Weckhuysen, B. M. New insight in the template decomposition process of large zeolite ZSM-5 crystals: An in situ UV-Vis/fluorescence micro-spectroscopy study. *Phys. Chem. Chem. Phys.* **13**, 3681–3685 (2011).
146. Matousek, P. *et al.* Fluorescence suppression in resonance Raman spectroscopy using a high-performance picosecond Kerr gate. *J. Raman Spectrosc.* **32**, 983–988 (2001).
147. Velsko, S. P., Webb, M., Davis, L. & Huang, C. Phase-matched harmonic generation in lithium triborate (LBO). *IEEE J. Quantum Electron.* **27**, 2182–2192 (1991).
148. The Numerical Algorithms Group (NAG). The NAG Library.
149. Ranjit, S., Malacrida, L., Jameson, D. M. & Gratton, E. Fit-free analysis of fluorescence lifetime imaging data using the phasor approach. *Nat. Protoc.* **13**, 1979–2004 (2018).
150. Warren, S. C. *et al.* Rapid Global Fitting of Large Fluorescence Lifetime Imaging Microscopy Datasets. *PLoS One* **8**, (2013).
151. Laptенок, S. *et al.* Fluorescence Lifetime Imaging Microscopy (FLIM) data analysis with TIMP. *J. Stat. Softw.* **18**, 1–20 (2007).
152. Dent, L. & Smith, J. Crystal Structure of Chabazite, a Molecular Sieve. *Nature* **181**, 1794–1796 (1958).
153. Xu, R., Zhang, R., Liu, N., Chen, B. & Zhang Qiao, S. Template Design and Economical Strategy for the Synthesis of SSZ-13 (CHA-Type) Zeolite as an Excellent Catalyst for the Selective Catalytic Reduction of NO_x by Ammonia. *ChemCatChem* **7**, 3842–3847 (2015).
154. Bing, L. *et al.* Template-Free Synthesis of Hierarchical SSZ-13 Microspheres with High MTO Catalytic Activity. *Chem. – A Eur. J.* **24**, 7428–7433 (2018).
155. Muraoka, K., Chaikittisilp, W. & Okubo, T. Multi-objective de novo molecular design of organic structure-directing agents for zeolites using nature-inspired ant colony optimization. *Chem. Sci.* **11**, 8214–8223 (2020).
156. Lewis, D., Willock, D., Catlow, R., Thomas, J. & Hutchings, G. De novo design of structure-directing agents for the synthesis of microporous solids. *Nature* **382**, 604–606 (1996).
157. Muraoka, K., Chaikittisilp, W., Yanaba, Y., Yoshikawa, T. & Okubo, T. Directing Aluminum Atoms into Energetically Favorable Tetrahedral Sites in a Zeolite Framework by Using Organic Structure-Directing Agents. *Angew. Chemie - Int. Ed.* **57**, 3742–3746 (2018).
158. Wardani, M. K. *et al.* Highly crystalline mesoporous SSZ-13 zeolite obtained via controlled post-synthetic treatment. *RSC Adv.* **9**, 77–86 (2019).
159. Moliner, M., Franch, C., Palomares, E., Grill, M. & Corma, A. Cu-SSZ-39, an active and hydrothermally stable catalyst for the selective catalytic reduction of NO_x. *Chem. Commun.* **48**, 8264–8266 (2012).
160. Lezcano-Gonzalez, I. *et al.* Determining the storage, availability and reactivity of NH₃ within Cu-Chabazite-based Ammonia Selective Catalytic Reduction systems. *Phys. Chem. Chem. Phys.* (2014). doi:10.1039/c3cp54132k
161. Bordiga, S., Lamberti, C., Bonino, F., Travert, A. & Thibault-Starzyk, F. Probing zeolites by vibrational spectroscopies. *Chem. Soc. Rev.* **44**, 7262–7341 (2015).
162. Knops-Gerrits, P. P., De Vos, D. E., Feijen, E. J. P. & Jacobs, P. A. Raman

spectroscopy on zeolites. *Microporous Mater.* **8**, 3–17 (1997).

163. Liu, D. R. *et al.* Facile synthesis of large-pore zeolite ITQ-26 by using an easily-available imidazolium as structure-directing agent. *Microporous Mesoporous Mater.* **276**, 232–238 (2019).
164. Yamashita, H. *et al.* In-situ XAFS, photoluminescence, and IR investigations of copper ions included within various kinds of zeolites. Structure of Cu(I) ions and their interaction with CO molecules. *J. Phys. Chem.* **100**, 397–402 (1996).
165. Matsuoka, M. & Anpo, M. Photoluminescence properties and photocatalytic reactivities of Cu+/zeolite and Ag+/zeolite catalysts prepared by the ion-exchange method. *Curr. Opin. Solid State Mater. Sci.* **7**, 451–459 (2003).
166. Remillard, J. T., Poindexter, B. D. & Weber, W. H. Fluorescence characteristics of Cu-ZSM-5 zeolites in reactive gas mixtures: mechanisms for a fiber-optic-based gas sensor. *Appl. Opt.* **36**, 3699–3707 (1997).
167. Li, H. & Li, P. Luminescent materials of lanthanoid complexes hosted in zeolites. *Chem. Commun.* **54**, 13884–13893 (2018).
168. Lin, H. Y. *et al.* Crystalline inorganic frameworks with 56-ring, 64-ring, and 72-ring channels. *Science (80-.)*. **339**, 811–813 (2013).
169. Li, H., Ding, Y. & Wang, Y. Photoluminescence properties of Eu³⁺-exchanged zeolite L crystals annealed at 700 °C. *CrystEngComm* **14**, 4767–4771 (2012).
170. Ruivo, A. *et al.* Highly Photoluminescent Sulfide Clusters Confined in Zeolites. *J. Phys. Chem. C* **122**, 14761–14770 (2018).
171. Planells, A., You, J., Triplett, G. & Hunt, H. K. Investigation of the photoluminescence of microporous silicalite-1 (MFI) films. *Microporous Mesoporous Mater.* **220**, 73–80 (2016).
172. Wang, M., Gu, S., Jiang, W., Lin, H. & Fan, Y. Origin of ultraviolet photoluminescence in zeolite-derived glass. *J. Non. Cryst. Solids* **471**, 462–466 (2017).
173. Wang, L., Jiang, W., Chen, L. & Shen, Z. Formation of a unique glass by spark plasma sintering of a zeolite. *J. Mater. Res.* **24**, 3241–3245 (2009).
174. Dozzi, M. V., D'Andrea, C., Ohtani, B., Valentini, G. & Selli, E. Fluorine-Doped TiO₂ Materials: Photocatalytic Activity vs Time-Resolved Photoluminescence. *J. Phys. Chem. C* **117**, 25586–25595 (2013).
175. Warringham, R. *et al.* Insights into the mechanism of zeolite detemplation by positron annihilation lifetime spectroscopy. *J. Phys. Chem. C* **120**, 25451–25461 (2016).
176. Beale, A. M., Lezcano-Gonzalez, I., Slawinski, W. A. & Wragg, D. S. Correlation between Cu ion migration behaviour and deNO_x activity in Cu-SSZ-13 for the standard NH₃-SCR reaction. *Chem. Commun.* **52**, 6170–6173 (2016).
177. Greenaway, A. G. *et al.* Operando Spectroscopic Studies of Cu – SSZ-13 for - NH₃ – SCR deNO_x Investigates the Role of - NH₃ in Observed Cu (II) Reduction at High NO Conversions. *Top. Catal.* **61**, 175–182 (2018).
178. Systems, D. Biovia Materials Studio. (2017).
179. Sun, H. COMPASS: An ab Initio Force-Field Optimized for Condensed-Phase Applications Overview with Details on Alkane and Benzene Compounds. *J. Phys. Chem. B* **102**, 7338–7364 (1998).
180. Stevens, A. P., Gorman, A. M., Freeman, C. M. & Cox, P. A. Prediction of template location via a combined Monte Carlo–simulated annealing approach. *J. Chem. Soc. Faraday Trans.* **92**, 2065–2073 (1996).
181. Dozzi, M. V. *et al.* Effects of Photodeposited Gold vs Platinum Nanoparticles on N,F-Doped TiO₂ Photoactivity: A Time-Resolved Photoluminescence Investigation. *J. Phys. Chem. C* **122**, 14326–14335 (2018).
182. Ware, W. R. & Cunningham, P. T. Lifetime and quenching of anthracene fluorescence in

- the vapor phase. *J. Chem. Phys.* **43**, 3826–3831 (1965).
183. Hashimoto, S. & Yamaji, M. Observation of intramolecular singlet and triplet excimers of tethered naphthalene moieties under the geometric constraints imposed by the host framework of zeolites. *Phys. Chem. Chem. Phys.* **10**, 3124–3130 (2008).
 184. Hashimoto, S., Fukazawa, N., Fukumura, H. & Masuhara, H. Observation and characterization of excimer emission from anthracene included in NaX zeolite. *Chem. Phys. Lett.* **219**, 445–451 (1994).
 185. Jenkins, T. E. & Lewis, J. A Raman study of adamantane (C₁₀H₁₆), diamantane (C₁₄H₂₀) and triamantane (C₁₈H₂₄) between 10 K and room temperatures. *Spectrochim. Acta Part A Mol. Spectrosc.* **36**, 259–264 (1980).
 186. Krishnamurti, D. The raman spectrum of quartz and its interpretation. *Proc. Indian Acad. Sci. - Sect. A* **47**, 276–291 (1958).
 187. Krishnan, R. S. Raman Spectrum of Quartz. *Nature* **155**, 452 (1945).
 188. Xiao, C. *et al.* PdO x /Silicalite-1 Catalyst Prepared by Room Temperature Ozone Treatment: Preparation Chemistry and Catalytic Performance for Methane Combustion. *Catal. Letters* **147**, 1775–1782 (2017).
 189. Miecznikowski, A. & Hanuza, J. Infrared and Raman studies of ZSM-5 and silicalite-1 at room, liquid nitrogen and helium temperatures. *Zeolites* **7**, 249–254 (1987).
 190. Kalita, A., Deka, K. & Kalita, M. P. C. On the influence of Raman scattering of water in the photoluminescence measurement of water dispersed ZnO nanocrystals. *Methods Appl. Fluoresc.* **5**, (2017).
 191. Ramamurthy, V., Caspar, J. V., Eaton, D. F., Kuo, E. W. & Corbin, D. R. Heavy-atom-induced phosphorescence of aromatics and olefins included within zeolites. *J. Am. Chem. Soc.* **114**, 3882–3892 (1992).
 192. Ramamurthy, V. & Turro, N. J. Photochemistry of organic molecules within zeolites: Role of cations. *J. Incl. Phenom. Mol. Recognit. Chem.* **21**, 239–282 (1995).
 193. Casal, H. L. & Scaiano, J. C. Intrazeolite photochemistry. I. Phosphorescence enhancement of aromatic ketones included in silicalite. *Can. J. Chem.* **62**, 628–629 (1984).
 194. Glinka, Y. D., Lin, S.-H., Hwang, L.-P. & Chen, Y.-T. Photoluminescence Spectroscopy of Silica-Based Mesoporous Materials. *J. Phys. Chem. B* **104**, 8652–8663 (2002).
 195. Xu, G. Q., Zheng, Z. X., Tang, W. M. & Wu, Y. C. Multi-peak behavior of photoluminescence of silica particles heat-treated in hydrogen at elevated temperature. *J. Lumin.* **126**, 43–47 (2007).
 196. Lu, S. *et al.* Photoluminescence of pure silicon quantum dots embedded in an amorphous silica wire array. *J. Mater. Chem. C* **5**, 6713–6717 (2017).
 197. Hosono, H., Kawazoe, H. & Matsunami, N. Experimental Evidence for Frenkel Defect Formation in Amorphous SiO₂ by Electronic Excitation. *Phys. Rev. Lett.* **80**, 317–320 (1998).
 198. Itoh, C., Tanimura, K., Itoh, N. & Itoh, M. Threshold energy for photogeneration of self-trapped excitons in SiO₂. *Phys. Rev. B* **39**, 11183–11186 (1989).
 199. Skuja, L. & Güttler, B. Detection of Interstitial Oxygen Molecules in SiO₂ Glass by a Direct Photoexcitation of the Infrared Luminescence of Singlet O₂. *Phys. Rev. Lett.* **77**, 2093–2096 (1996).
 200. Pacchioni, G. & Ieraño, G. Ab initio theory of optical transitions of point defects in SiO₂. *Phys. Rev. B* **57**, 818–832 (1998).
 201. Griscom, D. L. & Mizuguchi, M. Determination of the visible range optical absorption spectrum of peroxy radicals in gamma-irradiated fused silica. *J. Non. Cryst. Solids* **239**, 66–77 (1998).

202. Guisnet, M. & Magnoux, P. Fundamental description of deactivation and regeneration of acid zeolites. *Stud. Surf. Sci. Catal.* **88**, 53–68 (1994).
203. Goetze, J. *et al.* Insights into the Activity and Deactivation of the Methanol-to-Olefins Process over Different Small-Pore Zeolites As Studied with Operando UV-vis Spectroscopy. *ACS Catal.* **7**, 4033–4046 (2017).
204. Qi, G. *et al.* Behaviors of coke deposition on SAPO-34 catalyst during methanol conversion to light olefins. *Fuel Process. Technol.* **88**, 437–441 (2007).
205. Roefsaers, M. B. J. *et al.* Spatially resolved observation of crystal-face-dependent catalysis by single turnover counting. *Nature* **439**, 572–575 (2006).
206. Chung, Y. M., Mores, D. & Weckhuysen, B. M. Spatial and temporal mapping of coke formation during paraffin and olefin aromatization in individual H-ZSM-5 crystals. *Appl. Catal. A Gen.* **404**, 12–20 (2011).
207. Kiefer, W. & Bernstein, H. J. Rotating Raman Sample Technique for Colored Crystal Powders; Resonance Raman Effect in Solid KMnO₄. *Appl. Spectrosc.* **25**, 609–613 (1971).
208. Müller, A. & Weber, T. In situ raman investigation of hydrodesulphurization catalysts. *Appl. Catal.* **77**, 243–250 (1991).
209. Beato, P., Schachtl, E., Barbera, K., Bonino, F. & Bordiga, S. Operando Raman spectroscopy applying novel fluidized bed micro-reactor technology. *Catal. Today* **205**, 128–133 (2013).
210. Chua, Y. T. & Stair, P. C. A Novel Fluidized Bed Technique for Measuring UV Raman Spectra of Catalysts and Adsorbates. *J. Catal.* **196**, 66–72 (2000).
211. Zecchina, A., Rivallan, M., Berlier, G., Lamberti, C. & Ricchiardi, G. Structure and nuclearity of active sites in Fe-zeolites: comparison with iron sites in enzymes and homogeneous catalysts. *Phys. Chem. Chem. Phys.* **9**, 3483–3499 (2007).
212. Fan, F., Feng, Z. & Li, C. UV Raman spectroscopic study on the synthesis mechanism and assembly of molecular sieves. *Chem. Soc. Rev.* **39**, 4794–4801 (2010).
213. Fan, F., Feng, Z. & Li, C. UV Raman Spectroscopic Studies on Active Sites and Synthesis Mechanisms of Transition Metal-Containing Microporous and Mesoporous Materials. *Acc. Chem. Res.* **43**, 378–387 (2010).
214. Zhao, Z. *et al.* Mapping Al Distributions in SSZ-13 Zeolites from ²³Na Solid-State NMR Spectroscopy and DFT Calculations. *J. Phys. Chem. C* **122**, 9973–9979 (2018).
215. Bordiga, S. *et al.* Assessing the acidity of high silica chabazite H-SSZ-13 by FTIR using CO as molecular probe: Comparison with H-SAPO-34. *J. Phys. Chem. B* **109**, 2779–2784 (2005).
216. Leroux, M. *et al.* Temperature quenching of photoluminescence intensities in undoped and doped GaN. *J. Appl. Phys.* **86**, 3721–3728 (1999).
217. Zhao, Y. *et al.* High-temperature luminescence quenching of colloidal quantum dots. *ACS Nano* **6**, 9058–9067 (2012).
218. Hanagodimath, S. M., Siddlingeshwar, B., Thipperudrappa, J. & Hadimani, S. K. B. Fluorescence-quenching studies and temperature dependence of fluorescence quantum yield, decay time and intersystem crossing activation energy of TPB. *J. Lumin.* **129**, 335–339 (2009).
219. Jullien, M., Garel, J.-R., Merola, F. & Brochon, J.-C. Quenching by acrylamide and temperature of a fluorescent probe attached to the active site of Ribonuclease. *Eur. Biophys. J.* **13**, 131–137 (1986).
220. Acree, W. E. Comments Concerning “The Effect of Temperature on the Fluorescence Quenching of Perylene by Tetrachloromethane in Mixtures with Cyclohexane and Benzene”. *Zeitschrift fur Naturforsch. - Sect. A J. Phys. Sci.* **48**, 1265–1266 (1993).

221. Bai, Z., Fujii, M., Imakita, K. & Hayashi, S. Strong white photoluminescence from annealed zeolites. *J. Lumin.* **145**, 288–291 (2014).
222. Mech, A. *et al.* White light excitation of the near infrared Er³⁺ emission in exchanged zeolite sensitised by oxygen vacancies. *Phys. Chem. Chem. Phys.* **13**, 5605–5609 (2011).
223. Chen, Y., Dong, X., Zhang, Z. & Feng, L. Multicolor photoluminescence in ITQ-16 zeolite film. *Chem. Res. Chinese Univ.* **32**, 713–718 (2016).
224. Brown, S. L. *et al.* Enhancing Silicon Nanocrystal Photoluminescence through Temperature and Microstructure. *J. Phys. Chem. C* **120**, 18909–18916 (2016).
225. Aspetti, C. O., Cho, C. H., Agarwal, R. & Agarwal, R. Studies of hot photoluminescence in plasmonically coupled silicon via variable energy excitation and temperature-dependent spectroscopy. *Nano Lett.* **14**, 5413–5422 (2014).
226. Boscaino, R., Cannas, M., Gelardi, F. M. & Leone, M. Photoluminescence band at 4.4 eV in oxygen-deficient silica: Temperature effects. *J. Phys. Condens. Matter* **8**, 6–11 (1996).
227. Nakamura, T., Ogawa, T., Hosoya, N. & Adachi, S. Effects of thermal oxidation on the photoluminescence properties of porous silicon. *J. Lumin.* **130**, 682–687 (2010).
228. Li, K. H., Tsai, C., Campbell, J. C., Hance, B. K. & White, J. M. Investigation of rapid-thermal-oxidized porous silicon. *Appl. Phys. Lett.* **62**, 3501–3503 (1993).
229. Cullis, A. G., Canham, L. T., Williams, G. M., Smith, P. W. & Dosser, O. D. Correlation of the structural and optical properties of luminescent, highly oxidized porous silicon. *J. Appl. Phys.* **75**, 493–501 (1994).
230. Cullis, A. G. & Canham, L. T. Visible Light Emission Due to Quantum Size Effects in Porous Silicon. *Nature* **353**, 335 (1991).
231. Tanaka, K., Komatsu, Y. & Choo, C. K. Time-resolved photoluminescence spectra of Si species encapsulated in zeolite supercages. *J. Phys. Chem. B* **109**, 736–742 (2005).
232. Skuja, L. OPTICAL PROPERTIES OF DEFECTS IN SILICA BT - Defects in SiO₂ and Related Dielectrics: Science and Technology. in (eds. Pacchioni, G., Skuja, L. & Griscom, D. L.) 73–116 (Springer Netherlands, 2000). doi:10.1007/978-94-010-0944-7_3
233. Salh, R. Defect Related Luminescence in Silicon Dioxide Network: A Review. in *Crystalline Silicon - Properties and Uses* (ed. Sukumar, B.) 41 (IntechOpen, 2016). doi:http://dx.doi.org/10.5772/57353
234. Griscom, D. L. Optical properties and structure of defects in silica glass. *Nippon Seramikkusu Kyokai Gakujutsu Ronbunshi/Journal Ceram. Soc. Japan* **99**, 923–942 (1991).
235. Pacchioni, G., Ieranò, G. & Márquez, A. M. Optical Absorption and Nonradiative Decay Mechanism of E' Center in Silica. *Phys. Rev. Lett.* **81**, 377–380 (1998).
236. Stapelbroek, M., Griscom, D. L., Friebele, E. J. & Sigel, G. H. Oxygen-associated trapped-hole centers in high-purity fused silicas. *J. Non. Cryst. Solids* **32**, 313–326 (1979).
237. *Defects in SiO₂ and Related Dielectrics: Science and Technology.* (Springer Netherlands, 2000).
238. Munekuni, S. *et al.* Various types of nonbridging oxygen hole center in high-purity silica glass. *J. Appl. Phys.* **68**, 1212–1217 (1990).
239. Hosono, H., Abe, Y., Imagawa, H., Imai, H. & Arai, K. Experimental evidence for the Si-Si bond model of the 7.6-eV band in SiO_2 glass. *Phys. Rev. B* **44**, 12043–12045 (1991).
240. Imai, H., Arai, K., Imagawa, H., Hosono, H. & Abe, Y. Two types of oxygen-deficient centers in synthetic silica glass. *Phys. Rev. B* **38**, 12772–12775 (1988).

241. Skuja, L. Section 1. Defect studies in vitreous silica and related materials: Optically active oxygen-deficiency-related centers in amorphous silicon dioxide. *J. Non. Cryst. Solids* **239**, 16–48 (1998).
242. Nishikawa, H., Watanabe, E., Ito, D. & Ohki, Y. Decay kinetics of the 4.4-eV photoluminescence associated with the two states of oxygen-deficient-type defect in amorphous SiO_2 . *Phys. Rev. Lett.* **72**, 2101–2104 (1994).
243. Kajihara, K., Skuja, L., Hirano, M. & Hosono, H. Role of Mobile Interstitial Oxygen Atoms in Defect Processes in Oxides: Interconversion between Oxygen-Associated Defects in $\text{Si}\text{--}\text{O}$ Glasses. *Phys. Rev. Lett.* **92**, 15504 (2004).
244. Skuja, L., Suzuki, T. & Tanimura, K. Site-selective laser-spectroscopy studies of the intrinsic 1.9-eV luminescence center in glassy SiO_2 . *Phys. Rev. B* **52**, 15208–15216 (1995).
245. Skuja, L. The origin of the intrinsic 1.9 eV luminescence band in glassy SiO_2 . *J. Non. Cryst. Solids* **179**, 51–69 (1994).
246. Catlow, C. R. A., Sinclair, P. E. & Sokol, A. A. Model for the formation of point defects in zeolites. *Radiat. Eff. Defects Solids* **151**, 235–241 (1999).
247. Hoff, T. C., Thilakaratne, R., Gardner, D. W., Brown, R. C. & Tessonnier, J. P. Thermal Stability of Aluminum-Rich ZSM-5 Zeolites and Consequences on Aromatization Reactions. *J. Phys. Chem. C* **120**, 20103–20113 (2016).
248. Maher, P. K., Hunter, F. D. & Scherzer, J. Crystal Structures of Ultrastable Faujasites. in *Molecular Sieve Zeolites-I* **101**, 21–266 (AMERICAN CHEMICAL SOCIETY, 1974).
249. Van Bokhoven, J. A., Van der Eerden, A. M. J. & Koningsberger, D. C. Three-coordinate aluminum in zeolites observed with in situ x-ray absorption near-edge spectroscopy at the Al K-edge: Flexibility of aluminum coordinations in zeolites. *J. Am. Chem. Soc.* **125**, 7435–7442 (2003).
250. Bugaev, L. A., Van Bokhoven, J. A., Sokolenko, A. P., Latokha, Y. V. & Avakyan, L. A. Local structure of aluminum in zeolite mordenite as affected by temperature. *J. Phys. Chem. B* **109**, 10771–10778 (2005).
251. Al-majnouni, K. A., Yun, J. H. & Lobo, R. F. High-Temperature Produced Catalytic Sites Selective for n-Alkane Dehydrogenation in Acid Zeolites: The Case of HZSM-5. *ChemCatChem* **3**, 1333–1341 (2011).
252. Yun, J. H. & Lobo, R. F. Effects of temperature pretreatment on propane cracking over H-SSZ-13 zeolites. *Catal. Sci. Technol.* **5**, 264–273 (2015).
253. Nash, M. J., Shough, A. M., Fickel, D. W., Doren, D. J. & Lobo, R. F. High-temperature dehydrogenation of Brønsted acid sites in zeolites. *J. Am. Chem. Soc.* **130**, 2460–2462 (2008).
254. Balint, I., Springuel-Huet, M. A., Aika, K. I. & Fraissard, J. Evidence for oxygen vacancy formation in HZSM-5 at high temperature. *Phys. Chem. Chem. Phys.* **1**, 3845–3851 (1999).
255. Warren, K. J. & Scheffe, J. R. Role of Surface Oxygen Vacancy Concentration on the Dissociation of Methane over Nonstoichiometric Ceria. *J. Phys. Chem. C* **123**, 13208–13218 (2019).
256. Datka, J. Dehydroxylation of NaHY zeolites studied by infrared spectroscopy. *J. Chem. Soc. Faraday Trans. 1 Phys. Chem. Condens. Phases* **77**, 2877–2881 (1981).
257. Sushko, P. V., Mukhopadhyay, S., Stoneham, A. M. & Shluger, A. L. Oxygen vacancies in amorphous silica: Structure and distribution of properties. *Microelectron. Eng.* **80**, 292–295 (2005).
258. Cuko, A., Bromley, S. T. & Calatayud, M. Oxygen Vacancies in Oxide Nanoclusters: When Silica Is More Reducible Than Titania. *Frontiers in Chemistry* **7**, 37 (2019).
259. Dobretsov, G. E., Syrejschikova, T. I. & Smolina, N. V. On mechanisms of fluorescence

- quenching by water. *Biofizika* **59**, 231–237 (2014).
260. William De, W. H. & Sudnick, D. R. Lanthanide Ion Probes of Structure in Biology. Laser-Induced Luminescence Decay Constants Provide a Direct Measure of the Number of Metal-Coordinated Water Molecules. *J. Am. Chem. Soc.* **101**, 334–340 (1979).
 261. Prestopino, G. *et al.* Emerging switchable ultraviolet photoluminescence in dehydrated Zn/Al layered double hydroxide nanoplatelets. *Sci. Rep.* **9**, 1–12 (2019).
 262. Tiseanu, C., Geßner, A. & Kumke, M. U. Dehydration and rehydration effects on the photoluminescence properties of terbium-exchanged MFI-type materials. *J. Non. Cryst. Solids* **354**, 1969–1975 (2008).
 263. Coutino-Gonzalez, E. *et al.* Thermally activated LTA(Li)-Ag zeolites with water-responsive photoluminescence properties. *J. Mater. Chem. C* **3**, 11857–11867 (2015).
 264. Lin, H., Imakita, K. & Fujii, M. Reversible emission evolution from Ag activated zeolite Na-A upon dehydration/hydration. *Appl. Phys. Lett.* **105**, 5–9 (2014).
 265. Tian, P., Wei, Y., Ye, M. & Liu, Z. Methanol to olefins (MTO): From fundamentals to commercialization. *ACS Catal.* **5**, 1922–1938 (2015).
 266. Estruch-Samper, D., Vanstone, L., Hillier, R. & Ganapathisubramani, B. Toluene-based planar laser-induced fluorescence imaging of temperature in hypersonic flows. *Exp. Fluids* **56**, 1–13 (2015).
 267. Koban, W., Koch, J. D., Hanson, R. K. & Schulz, C. Absorption and fluorescence of toluene vapor at elevated temperatures. *Phys. Chem. Chem. Phys.* **6**, 2940–2945 (2004).
 268. Dow, W.-P. & Huang, T.-J. Yttria-Stabilized Zirconia Supported Copper Oxide Catalyst. *J. Catal.* **160**, 171–182 (1996).
 269. Lu, G., Linsebigler, A. & Yates, J. T. Ti³⁺ defect sites on TiO₂(110): Production and chemical detection of active sites. *J. Phys. Chem.* **98**, 11733–11738 (1994).
 270. Ito, T., Wang, J. X., Lin, C. H. & Lunsford, J. H. Oxidative Dimerization of Methane over a Lithium-Promoted Magnesium Oxide Catalyst. *J. Am. Chem. Soc.* **107**, 5062–5068 (1985).
 271. Tian, D. *et al.* DFT insights into oxygen vacancy formation and CH₄ activation over CeO₂ surfaces modified by transition metals (Fe, Co and Ni). *Phys. Chem. Chem. Phys.* **20**, 11912–11929 (2018).
 272. Liang, T. *et al.* Conversion of Methanol to Olefins over H-ZSM-5 Zeolite: Reaction Pathway Is Related to the Framework Aluminum Siting. *ACS Catal.* **6**, 7311–7325 (2016).
 273. Lee, K. & Hong, S. B. Hydrocarbon Pool Mechanism of the Zeolite-Catalyzed Conversion of Ethene to Propene. *ACS Catal.* **9**, 10640–10648 (2019).
 274. Schmidt, J. E. *et al.* Probing the Location and Speciation of Elements in Zeolites with Correlated Atom Probe Tomography and Scanning Transmission X-Ray Microscopy. *ChemCatChem* **11**, 488–494 (2019).
 275. Pernicone, N. Scale-up of catalyst production. *Catal. Today* **34**, 535–547 (1997).
 276. Wang, A. *et al.* Unraveling the mysterious failure of Cu/SAPO-34 selective catalytic reduction catalysts. *Nat. Commun.* **10**, 1–10 (2019).
 277. Ye, M., Li, H., Zhao, Y., Zhang, T. & Liu, Z. MTO Processes Development: The Key of Mesoscale Studies. *Adv. Chem. Eng.* **47**, 279–335 (2015).
 278. Wan, W., Su, J., Zou, X. D. & Willhammar, T. Transmission electron microscopy as an important tool for characterization of zeolite structures. *Inorg. Chem. Front.* **5**, 2836–2855 (2018).
 279. Devaraj, A. *et al.* Discerning the Location and Nature of Coke Deposition from Surface to Bulk of Spent Zeolite Catalysts. *Sci. Rep.* **6**, 1–11 (2016).

-
280. Schmidt, J. E., Peng, L., Poplawsky, J. D. & Weckhuysen, B. M. Nanoscale Chemical Imaging of Zeolites Using Atom Probe Tomography. *Angew. Chemie - Int. Ed.* **57**, 10422–10435 (2018).
281. Bonilla, G., Tsapatsis, M., Vlachos, D. G. & Xomeritakis, G. Fluorescence confocal optical microscopy imaging of the grain boundary structure of zeolite MFI membranes made by secondary (seeded) growth. *J. Memb. Sci.* **182**, 103–109 (2001).
282. Buurmans, I. L. C. *et al.* Catalytic activity in individual cracking catalyst particles imaged throughout different life stages by selective staining. *Nat. Chem.* **3**, 862–867 (2011).
283. Whiting, G. T. *et al.* Selective staining of Brønsted acidity in zeolite ZSM-5-based catalyst extrudates using thiophene as a probe. *Phys. Chem. Chem. Phys.* **16**, 21531–21542 (2014).
284. Ristanović, Z. *et al.* Quantitative 3D Fluorescence Imaging of Single Catalytic Turnovers Reveals Spatiotemporal Gradients in Reactivity of Zeolite H-ZSM-5 Crystals upon Steaming. *J. Am. Chem. Soc.* **137**, 6559–6568 (2015).
285. Heilemann, M. *et al.* Subdiffraction-resolution fluorescence imaging with conventional fluorescent probes. *Angew. Chemie - Int. Ed.* **47**, 6172–6176 (2008).
286. Busby, M. *et al.* Time, space, and spectrally resolved studies on J-aggregate interactions in zeolite L nanochannels. *J. Am. Chem. Soc.* **130**, 10970–10976 (2008).
287. Yatskou, M. M., Meyer, M., Huber, S., Pfenniger, M. & Calzaferri, G. Electronic excitation energy migration in a photonic dye-zeolite antenna. *ChemPhysChem* **4**, 567–587 (2003).
288. Schrimpf, W. *et al.* Chemical diversity in a metal-organic framework revealed by fluorescence lifetime imaging. *Nat. Commun.* **9**, (2018).
289. Omori, N. *et al.* Understanding the Dynamics of Fluorescence Emission during Zeolite Detemplation Using Time Resolved Photoluminescence Spectroscopy. *J. Phys. Chem. C* (2019). doi:10.1021/acs.jpcc.9b09050
290. Lezcano-Gonzalez, I. *et al.* Chemical deactivation of Cu-SSZ-13 ammonia selective catalytic reduction (NH₃-SCR) systems. *Appl. Catal. B Environ.* **154–155**, 339–349 (2014).
291. Gregor, I. *et al.* Fast algorithms for the analysis of spectral FLIM data. in *Proc.SPIE* **7903**, (2011).
292. PicoQuant. *Lifetime Fitting Using the TCPSC Fitting Script Step-by-Step Tutorial*. (2013).
293. Ofner, J. *et al.* Chemometric Analysis of Multisensor Hyperspectral Images of Precipitated Atmospheric Particulate Matter. *Anal. Chem.* 9413 (2015).
294. Mosca, S. *et al.* Raman mapping and time-resolved photoluminescence imaging for the analysis of a cross-section from a modern gypsum sculpture. *Microchem. J.* **139**, 500–505 (2018).
295. Lohninger, H. & Ofner, J. Multisensor hyperspectral imaging as a versatile tool for image-based chemical structure determination. *Spectrosc. Eur.* **26**, 6–10 (2014).
296. Yu, Y., Xiong, G., Li, C. & Xiao, F. S. Characterization of aluminosilicate zeolites by UV Raman spectroscopy. *Microporous Mesoporous Mater.* **46**, 23–34 (2001).
297. Pappas, D. K. *et al.* Methane to Methanol: Structure-Activity Relationships for Cu-CHA. *J. Am. Chem. Soc.* **139**, 14961–14975 (2017).
298. Ipek, B. *et al.* Formation of [Cu₂O₂]²⁺ and [Cu₂O]²⁺ toward C-H Bond Activation in Cu-SSZ-13 and Cu-SSZ-39. *ACS Catal.* **7**, 4291–4303 (2017).
299. Attila, Ö., King, H. E., Meirer, F. & Weckhuysen, B. M. 3D Raman Spectroscopy of Large Zeolite ZSM-5 Crystals. *Chem. - A Eur. J.* **25**, 7158–7167 (2019).
300. Dutta, P. K., Shieh, D. C. & Puri, M. Raman spectroscopic study of the synthesis of zeolite Y. *J. Phys. Chem.* **91**, 2332–2336 (1987).

301. Wheatley, A. D. & Sadhra, S. Use of fluorescence emission spectra for the routine identification of polycyclic aromatic hydrocarbons in liquid chromatography. *J. Liq. Chromatogr. Relat. Technol.* **21**, 2509–2521 (1998).
302. Boens, N. *et al.* Fluorescence lifetime standards for time and frequency domain fluorescence spectroscopy. *Anal. Chem.* **79**, 2137–2149 (2007).
303. Rivera-Figueroa, A. M., Ramazan, K. A. & Finlayson-Pitts, B. J. Fluorescence, Absorption, and Excitation Spectra of Polycyclic Aromatic Hydrocarbons as a Tool for Quantitative Analysis. *J. Chem. Educ.* **81**, 242–245 (2004).
304. Selli, E., Zaccaria, C., Sena, F., Tomasi, G. & Bidoglio, G. Application of multi-way models to the time-resolved fluorescence of polycyclic aromatic hydrocarbons mixtures in water. *Water Res.* **38**, 2269–2276 (2004).
305. Thomas Brownrigg, J. & Kenny, J. E. Fluorescence intensities and lifetimes of aromatic hydrocarbons in cyclohexane solution: Evidence of contact charge-transfer interactions with oxygen. *J. Phys. Chem. A* **113**, 1049–1059 (2009).
306. Peter, L., Engel, W. & Vaubel, G. Delayed Fluorescence and Triplet Lifetime of Crystalline Chrysene. *Mol. Cryst. Liq. Cryst.* **19**, 207–215 (1973).
307. Chen, S., Inskeep, W. P., Williams, S. A. & Callis, P. R. Fluorescence Lifetime Measurements of Fluoranthene, 1-Naphthol, and Napropamide in the Presence of Dissolved Humic Acid. *Environ. Sci. Technol.* **28**, 1582–1588 (1994).
308. Rasouli, M., Tavassoli, S. H., Mousavi, S. J. & Darbani, S. M. R. Measuring of naphthalene fluorescence emission in the water with nanosecond time delay laser induced fluorescence spectroscopy method. *Optik (Stuttg.)* **127**, 6218–6223 (2016).
309. Meidinger, R., St Germain, R., Dohotariu, V. & Gillispie, G. *Fluorescence of Aromatic Hydrocarbons in Aqueous Solution*. (1993). doi:10.1090/dimacs/029/20
310. Mu, Y. *et al.* Carbogenic nanodots derived from organo-Templated zeolites with modulated full-color luminescence. *Chem. Sci.* **7**, 3564–3568 (2016).
311. Movia, D., Del Canto, E. & Giordani, S. Purified and oxidized single-walled carbon nanotubes as robust near-IR fluorescent probes for molecular imaging. *J. Phys. Chem. C* **114**, 18407–18413 (2010).
312. Guldi, D. M., Holzinger, M., Hirsch, A., Georgakilas, V. & Prato, M. First comparative emission assay of single-wall carbon nanotubes—solutions and dispersions. *Chem. Commun.* **3**, 1130–1131 (2003).
313. Zhou, J. *et al.* Highly efficient fluorescent multi-walled carbon nanotubes functionalized with diamines and amides. *J. Mater. Chem.* **22**, 11912–11914 (2012).
314. Miyauchi, Y., Matsuda, K., Yamamoto, Y., Nakashima, N. & Kanemitsu, Y. Length-dependent photoluminescence lifetimes in single-walled carbon nanotubes. *J. Phys. Chem. C* **114**, 12905–12908 (2010).
315. Shang, J. *et al.* The origin of fluorescence from graphene oxide. *Sci. Rep.* **2**, 1–8 (2012).
316. Shinohara, H., Yamakita, Y. & Ohno, K. Raman spectra of polycyclic aromatic hydrocarbons. Comparison of calculated raman intensity distributions with observed spectra for naphthalene, anthracene, pyrene, and perylene. *J. Mol. Struct.* **442**, 221–234 (1998).
317. Cloutis, E., Szymanski, P., Applin, D. & Goltz, D. Identification and discrimination of polycyclic aromatic hydrocarbons using Raman spectroscopy. *Icarus* **274**, 211–230 (2016).
318. Williams, R. T. & Bridges, J. W. Fluorescence of Solutions: a Review. *J. Clin. Pathol.* **17**, 371–394 (1964).
319. Najbar, J. & Mac, M. Mechanisms of fluorescence quenching of aromatic molecules by potassium iodide and potassium bromide in methanol–ethanol solutions. *J. Chem. Soc. Faraday Trans.* **87**, 1523–1529 (1991).

-
320. Russo, C., Apicella, B. & Ciajolo, A. Blue and green luminescent carbon nanodots from controllable fuel-rich flame reactors. *Sci. Rep.* **9**, 1–8 (2019).
321. Wu, J. *et al.* Reduction of PAH and soot in premixed ethylene-air flames by addition of dimethyl ether. *Combust. Sci. Technol.* **178**, 837–863 (2006).
322. Irimiea, C. *et al.* A comprehensive protocol for chemical analysis of flame combustion emissions by secondary ion mass spectrometry. *Rapid Commun. Mass Spectrom.* **32**, 1015–1025 (2018).
323. Mercier, X., Carrivain, O., Irimiea, C., Faccineto, A. & Therssen, E. Dimers of polycyclic aromatic hydrocarbons: The missing pieces in the soot formation process. *Phys. Chem. Chem. Phys.* **21**, 8285–8294 (2019).
324. Azumi, T. & McGlynn, S. P. Energy of excimer luminescence. I. A reconsideration of excimer processes. *J. Chem. Phys.* **41**, 3131–3138 (1964).
325. Birks, J. B. & Christophorou, L. G. Excimer Fluorescence of Aromatic Hydrocarbons in Solution. *Nature* **194**, 442–444 (1962).
326. Benten, H. *et al.* Intramolecular Singlet and Triplet Excimers of Triply Bridged [3.3.n](3,6,9)Carbazolophanes. *J. Phys. Chem. B* **111**, 10905–10914 (2007).
327. Tani, K. *et al.* Synthesis and photophysical properties of [3.3](3,9)carbazolophanes. *Chem. Commun.* 1914–1915 (2001). doi:10.1039/B104101K
328. Miletic, T. *et al.* Leveraging Fluorescent Emission to Unitary Yield: Dimerization of Polycyclic Aromatic Hydrocarbons. *Helv. Chim. Acta* **102**, e1900004 (2019).
329. Sweat, M. L. Sulfuric Acid-Induced Fluorescence of Corticosteroids. *Anal. Chem.* **26**, 773–776 (1954).
330. Widhalm, G. *et al.* 5-Aminolevulinic Acid Induced Fluorescence Is a Powerful Intraoperative Marker for Precise Histopathological Grading of Gliomas with Non-Significant Contrast-Enhancement. *PLoS One* **8**, (2013).
331. Signorile, M., Bonino, F., Damin, A. & Bordiga, S. In situ resonant UV-Raman spectroscopy of polycyclic aromatic hydrocarbons. *J. Phys. Chem. C* **119**, 11694–11698 (2015).
332. Geus, E. R., Jansen, J. C. & van Bekkum, H. Calcination of large MFI-type single crystals: Part 1. Evidence for the occurrence of consecutive growth forms and possible diffusion barriers arising thereof. *Zeolites* **14**, 82–88 (1994).
333. Belén-Cordero, D. S., Méndez-González, S. & Hernández-Maldonado, A. J. SBE type cobalt aluminophosphate nanoporous materials: Degradation of the structure-directing agent. *Microporous Mesoporous Mater.* **109**, 287–297 (2008).
334. Schnabel, K. H. *et al.* Decomposition of template in SAPO-5 and AlPO₄-5 molecular sieves studied by IR and Raman spectroscopy. *Microporous Mater.* **11**, 293–302 (1997).
335. Briend, M., Lamy, A., Peltre, M. J., Man, P. P. & Barthomeuf, D. Thermal stability of tetrapropylammonium (TPA) and tetra methylammonium (TMA) cations occluded in SAPO-37 molecular sieves. *Zeolites* **13**, 201–211 (1993).
336. Erley, W., Xu, R. & Hemminger, J. C. Thermal decomposition of trimethylamine on Pt (111): Spectroscopic identification of surface intermediates. *Surf. Sci.* **389**, 272–286 (1997).
337. Xiao, D., Han, X., Bao, X., Hou, G. & Blanc, F. Identification of different carbenium ion intermediates in zeolites with identical chabazite topology: Via ¹³C-¹³C through-bond NMR correlations. *RSC Adv.* **9**, 12415–12418 (2019).
338. Chua, Y. T. & Stair, P. C. An ultraviolet Raman spectroscopic study of coke formation in methanol to hydrocarbons conversion over zeolite H-MFI. *J. Catal.* **213**, 39–46 (2003).
339. Kasry, A. *et al.* Highly efficient fluorescence quenching with graphene. *J. Phys. Chem. C* **116**, 2858–2862 (2012).

340. Dong, H., Gao, W., Yan, F., Ji, H. & Ju, H. Fluorescence Resonance Energy Transfer between Quantum Dots and Graphene Oxide for Sensing Biomolecules. *Anal. Chem.* **82**, 5511–5517 (2010).
341. Wang, Y., Li, Z., Wang, J., Li, J. & Lin, Y. Graphene and graphene oxide: Biofunctionalization and applications in biotechnology. *Trends Biotechnol.* **29**, 205–212 (2011).
342. Zhang, H. *et al.* Fluorescent biosensors enabled by graphene and graphene oxide. *Biosens. Bioelectron.* **89**, 96–106 (2017).
343. Arthi G, P. B. & BD, L. A Simple Approach to Stepwise Synthesis of Graphene Oxide Nanomaterial. *J. Nanomed. Nanotechnol.* **06**, 1–4 (2015).
344. Lu, J. *et al.* One-pot synthesis of fluorescent carbon nanoribbons, nanoparticles, and graphene by the exfoliation of graphite in ionic liquids. *ACS Nano* **3**, 2367–2375 (2009).
345. Ray, S. C., Saha, A., Jana, N. R. & Sarkar, R. Fluorescent carbon nanoparticles: Synthesis, characterization, and bioimaging application. *J. Phys. Chem. C* **113**, 18546–18551 (2009).
346. Wang, X. *et al.* Fluorescence decoration of defects in carbon nanotubes. *J. Phys. Chem. C* **114**, 20941–20946 (2010).
347. Zhao, W., Basnet, B. & Kim, I. J. Carbon nanotube formation using zeolite template and applications. *J. Adv. Ceram.* **1**, 179–193 (2012).
348. Souza, N. *et al.* Upcycling spent petroleum cracking catalyst: Pulsed laser deposition of single-wall carbon nanotubes and silica nanowires. *RSC Adv.* **6**, 72596–72606 (2016).
349. Xiu, Y., Gao, Q., Li, G. D., Wang, K. X. & Chen, J. S. Preparation and tunable photoluminescence of carbogenic nanoparticles confined in a microporous magnesium-aluminophosphate. *Inorg. Chem.* **49**, 5859–5867 (2010).
350. Wang, Y. *et al.* Luminescent carbon dots in a new magnesium aluminophosphate zeolite. *Chem. Commun.* **49**, 9006–9008 (2013).
351. Baldovi, H. G., Valencia, S., Alvaro, M., Asiri, A. M. & Garcia, H. Highly fluorescent C-dots obtained by pyrolysis of quaternary ammonium ions trapped in all-silica ITQ-29 zeolite. *Nanoscale* **7**, 1744–1752 (2015).
352. Ortega-Liebana, M. C. *et al.* Uniform luminescent carbon nanodots prepared by rapid pyrolysis of organic precursors confined within nanoporous templating structures. *Carbon N. Y.* **117**, 437–446 (2017).
353. Okamura, T., Obi, K. & Tanaka, I. The fluorescence lifetimes of the methyl-substituted benzyl, triphenylmethyl and diphenylmethyl radicals. *Chem. Phys. Lett.* **20**, 90–91 (1973).
354. Nijegorodov, N., Vasilenko, V., Monowe, P. & Masale, M. Systematic investigation of the influence of methyl groups upon fluorescence parameters and the intersystem crossing rate constant of aromatic molecules. *Spectrochim. Acta - Part A Mol. Biomol. Spectrosc.* **74**, 188–194 (2009).
355. Ossler, F., Metz, T. & Aldén, M. Picosecond laser-induced fluorescence from gas-phase polycyclic aromatic hydrocarbons at elevated temperatures. I. Cell measurements. *Appl. Phys. B Lasers Opt.* **72**, 465–478 (2001).
356. Kristoffersen, A. S., Erga, S. R., Hamre, B. & Frette, Ø. Testing fluorescence lifetime standards using two-photon excitation and time-domain instrumentation: Rhodamine B, coumarin 6 and lucifer yellow. *J. Fluoresc.* **24**, 1015–1024 (2014).
357. Johnson, G. E. Effect of Concentration on the Fluorescence Spectra and Lifetimes of Pyrene in Polystyrene Films. *Macromolecules* **13**, 839–844 (1980).
358. Gannot, I., Ron, I., Hekmat, F., Chernomordik, V. & Gandjbakhche, A. Functional optical detection based on pH dependent fluorescence lifetime. *Lasers Surg. Med.* **35**, 342–348 (2004).

-
359. Tang, R., Lee, H. & Achilefu, S. Induction of pH sensitivity on the fluorescence lifetime of quantum dots by NIR fluorescent dyes. *J. Am. Chem. Soc.* **134**, 4545–4548 (2012).
360. Burdikova, Z. *et al.* Measurement of pH micro-heterogeneity in natural cheese matrices by fluorescence lifetime imaging. *Front. Microbiol.* **6**, 1–10 (2015).
361. Bai, X. *et al.* Three-dimensional imaging and analysis of the internal structure of SAPO-34 zeolite crystals. *RSC Adv.* **8**, 33631–33636 (2018).
362. García-Martínez, J. & Li, K. Mesoporous zeolites: Preparation, characterization and applications. *Mesoporous Zeolites Prep. Charact. Appl.* 1–575 (2015). doi:10.1002/9783527673957
363. Sastre, G. Confinement effects in methanol to olefins catalysed by zeolites: A computational review. *Front. Chem. Sci. Eng.* **10**, 76–89 (2016).
364. Wahono, S. K. *et al.* Transformation of Mordenite-Clinoptilolite Natural Zeolite at Different Calcination Temperatures. *IOP Conf. Ser. Earth Environ. Sci.* **251**, (2019).
365. Li, G. & Pidko, E. A. The Nature and Catalytic Function of Cation Sites in Zeolites: a Computational Perspective. *ChemCatChem* **11**, 134–156 (2019).
366. Mauzerall, D. L., Sultan, B., Kim, N. & Bradford, D. F. NO_x emissions from large point sources: Variability in ozone production, resulting health damages and economic costs. *Atmos. Environ.* **39**, 2851–2866 (2005).
367. European Environment Agency. *European Union emission inventory report 1990-2011 under the UNECE Convention on Long-range Transboundary Air Pollution (LRTAP)*. (2013). doi:10.2800/44480
368. Deka, U. *et al.* Confirmation of isolated Cu 2+ ions in SSZ-13 zeolite as active sites in NH₃-selective catalytic reduction. *J. Phys. Chem. C* **116**, 4809–4818 (2012).
369. Ma, L. *et al.* Characterization of commercial Cu-SSZ-13 and Cu-SAPO-34 catalysts with hydrothermal treatment for NH₃-SCR of NO_x in diesel exhaust. *Chem. Eng. J.* **225**, 323–330 (2013).
370. Fu, M. *et al.* A review on selective catalytic reduction of NO_x by supported catalysts at 100–300 °C—catalysts, mechanism, kinetics. *Catal. Sci. Technol.* **4**, 14–25 (2014).
371. Yadav, D. & Prasad, R. Low Temperature de-NO_x Technology-a Challenge for Vehicular Exhaust and its Remedation: An Overview. *Procedia Technol.* **24**, 639–644 (2016).
372. Shan, Y., Shi, X., Du, J., Yu, Y. & He, H. Cu-exchanged RTH-type zeolites for NH₃-selective catalytic reduction of NO_x: Cu distribution and hydrothermal stability. *Catal. Sci. Technol.* **9**, 106–115 (2019).
373. Chen, H. Cu/Zeolite SCR Catalysts for Automotive Diesel NO_x Emission Control. in *Urea-SCR Technology for deNO_x After Treatment of Diesel Exhausts* (eds. Nova, I. & Troconi, E.) (Springer New York, 2014).
374. Zhang, D. & Yang, R. T. N₂O Formation Pathways over Zeolite-Supported Cu and Fe Catalysts in NH₃-SCR. *Energy and Fuels* **32**, 2170–2182 (2018).
375. Yang, S. *et al.* Mechanism of N₂O Formation during the Low-Temperature Selective Catalytic Reduction of NO with NH₃ over Mn–Fe Spinel. *Environ. Sci. Technol.* **48**, 10354–10362 (2014).
376. Yagiela, J. A. Health Hazards and Nitrous Oxide: A Time for Reappraisal. *Anaesth Prog* **38**, 1–11 (1991).
377. Forster, P. *et al.* Changes in Atmospheric Constituents and in Radiative Forcing. in *Climate Change 2007: The Physical Science Basis. Contribution of Working Group I to the Fourth Assessment Report of the Intergovernmental Panel on Climate Change* (Cambridge University Press, 2007).
378. Lee, S. G. *et al.* Suppressed N₂O formation during NH₃ selective catalytic reduction using vanadium on zeolitic microporous TiO₂. *Sci. Rep.* **5**, 1–7 (2015).

379. Wang, X. *et al.* New insights into the N₂O formation mechanism during selective catalytic reduction of NO_x with NH₃ over V-based catalyst. *Catal. Today* 0–1 (2019). doi:10.1016/j.cattod.2019.06.052
380. Kwak, J. H. *et al.* Effects of hydrothermal aging on NH₃-SCR reaction over Cu/zeolites. *J. Catal.* **287**, 203–209 (2012).
381. Ozkan, U. S., Kumthekar, M. W. & Cai, Y. P. Selective Catalytic Reduction of Nitric Oxide over Vanadia/Titania Catalysts: Temperature-Programmed Desorption and Isotopically Labeled Oxygen-Exchange Studies. *Ind. Eng. Chem. Res.* **33**, 2924–2929 (1994).
382. Ozkan, U. S., Cai, Y. & Kumthekar, M. W. Mechanistic studies of selective catalytic reduction of nitric oxide with ammonia over V₂O₅/TiO₂ (anatase) catalysts through transient isotopic labeling at steady state. *J. Phys. Chem.* **99**, 2363–2371 (1995).
383. Qi, G., Yang, R. T. & Chang, R. MnO_x-CeO₂ mixed oxides prepared by co-precipitation for selective catalytic reduction of NO with NH₃ at low temperatures. *Appl. Catal. B Environ.* **51**, 93–106 (2004).
384. Liu, Z. *et al.* Selective catalytic reduction of NO_x with NH₃ over Mn-Ce mixed oxide catalyst at low temperatures. *Catal. Today* **216**, 76–81 (2013).
385. Janssens, T. V. W. *et al.* A consistent reaction scheme for the selective catalytic reduction of nitrogen oxides with ammonia. *ACS Catal.* **5**, 2832–2845 (2015).
386. Tang, X., Li, J., Sun, L. & Hao, J. Origination of N₂O from NO reduction by NH₃ over β-MnO₂ and α-Mn₂O₃. *Appl. Catal. B Environ.* **99**, 156–162 (2010).
387. Suárez, S., Martín, J. A., Yates, M., Avila, P. & Blanco, J. N₂O formation in the selective catalytic reduction of NO_x with NH₃ at low temperature on CuO-supported monolithic catalysts. *J. Catal.* **229**, 227–236 (2005).
388. Tronconi, E., Nova, I., Ciardelli, C., Chatterjee, D. & Weibel, M. Redox features in the catalytic mechanism of the ‘standard’ and ‘fast’ NH₃-SCR of NO_x over a V-based catalyst investigated by dynamic methods. *J. Catal.* **245**, 1–10 (2007).
389. Ciardelli, C., Nova, I., Tronconi, E., Chatterjee, D. & Bandl-Konrad, B. A “Nitrate Route” for the low temperature “Fast SCR” reaction over a V₂O₅-WO₃/TiO₂ commercial catalyst. *Chem. Commun.* 2718–2719 (2004). doi:10.1039/B411613E
390. Kwak, J. H., Tran, D., Szanyi, J., Peden, C. H. F. & Lee, J. H. The effect of copper loading on the selective catalytic reduction of nitric oxide by ammonia over Cu-SSZ-13. *Catal. Letters* **142**, 295–301 (2012).
391. Centi, G., Perathoner, S., Biglino, D. & Giamello, E. Adsorption and reactivity of NO on copper-on-alumina catalysts: I. Formation of nitrate species and their influence on reactivity in NO and NH₃ Conversion. *Journal of Catalysis* **152**, 75–92 (1995).
392. Gao, F., Kwak, J. H., Szanyi, J. & Peden, C. H. F. Current understanding of Cu-exchanged chabazite molecular sieves for use as commercial diesel engine DeNO_x catalysts. *Top. Catal.* **56**, 1441–1459 (2013).
393. Leistner, K. *et al.* Impact of copper loading on nh₃-selective catalytic reduction, oxidation reactions and N₂O formation over Cu/SAPO-34. *Energies* **10**, (2017).
394. Brandenberger, S., Kröcher, O., Tissler, A. & Althoff, R. *The state of the art in selective catalytic reduction of NO_x by ammonia using metal-exchanged zeolite catalysts. Catalysis Reviews - Science and Engineering* **50**, (2008).
395. Shin, Y. *et al.* NO_x abatement and N₂O formation over urea-SCR systems with zeolite supported Fe and Cu catalysts in a nonroad diesel engine. *Chem. Eng. J.* **381**, 122751 (2020).
396. Zhu, M., Lai, J. K. & Wachs, I. E. Formation of N₂O greenhouse gas during SCR of NO with NH₃ by supported vanadium oxide catalysts. *Appl. Catal. B Environ.* **224**, 836–840 (2018).

-
397. Lee, J. H. *et al.* Synthesis of zeolite UZM-35 and catalytic properties of copper-exchanged UZM-35 for ammonia selective catalytic reduction. *Appl. Catal. B Environ.* **200**, 428–438 (2017).
398. Deka, U. *et al.* Changing active sites in Cu-CHA catalysts: DeNO_x selectivity as a function of the preparation method. *Microporous Mesoporous Mater.* **166**, 144–152 (2013).
399. Durá, O. J. *et al.* Transport, electronic, and structural properties of nanocrystalline CuAlO₂ delafossites. *Phys. Rev. B* **83**, 45202 (2011).
400. Deka, U., Lezcano-Gonzalez, I., Weckhuysen, B. M. & Beale, A. M. Local environment and nature of Cu active sites in zeolite-based catalysts for the selective catalytic reduction of NO_x. *ACS Catal.* **3**, 413–427 (2013).
401. Schmidt, J. E., Oord, R., Guo, W., Poplawsky, J. D. & Weckhuysen, B. M. Nanoscale tomography reveals the deactivation of automotive copper-exchanged zeolite catalysts. *Nat. Commun.* **8**, 1–8 (2017).
402. Greenaway, A. G. *et al.* Operando Spectroscopic Studies of Cu–SSZ-13 for NH₃–SCR deNO_x Investigates the Role of NH₃ in Observed Cu(II) Reduction at High NO Conversions. *Top. Catal.* **61**, 175–182 (2018).
403. Francisco de la Peña, Vidar Tonaas Fauske, Pierre Burdet, Eric Prestat, Petras Jokubauskas, Magnus Nord, ... Alexander Skorikov. hyperspy. (2018). doi:<http://doi.org/10.5281/zenodo.1469364>
404. Clemens, A. K. S. *et al.* Reaction-driven Ion Exchange of Copper into Zeolite SSZ-13. *ACS Catal.* **5**, 6209–6218 (2015).
405. Leistner, K., Xie, K., Kumar, A., Kamasamudram, K. & Olsson, L. Ammonia Desorption Peaks Can Be Assigned to Different Copper Sites in Cu/SSZ-13. *Catal. Letters* **147**, 1882–1890 (2017).
406. Bates, S. A. *et al.* Identification of the active Cu site in standard selective catalytic reduction with ammonia on Cu-SSZ-13. *J. Catal.* **312**, 87–97 (2014).
407. Dědeček, J. & Wichterlová, B. Role of Hydrated Cu Ion Complexes and Aluminum Distribution in the Framework on the Cu Ion Siting in ZSM-5. *J. Phys. Chem. B* **101**, 10233–10240 (1997).
408. Wilken, N. *et al.* Investigation of the effect of accelerated hydrothermal aging on the Cu sites in a Cu-BEA catalyst for NH₃-SCR applications. *Top. Catal.* **56**, 317–322 (2013).
409. Giordanino, F. *et al.* Characterization of Cu-exchanged SSZ-13: A comparative FTIR, UV-Vis, and EPR study with Cu-ZSM-5 and Cu-β with similar Si/Al and Cu/Al ratios. *Dalt. Trans.* **42**, 12741–12761 (2013).
410. Akyildiz, H. Synthesis of CuAlO₂ from chemically precipitated nano-sized precursors. *Ceram. Int.* **41**, 14108–14115 (2015).
411. Henson, M. J., Mukherjee, P., Root, D. E., Stack, T. D. P. & Solomon, E. I. Spectroscopic and Electronic Structural Studies of the Cu(III)₂ Bis-μ-oxo Core and Its Relation to the Side-On Peroxo-Bridged Dimer. *J. Am. Chem. Soc.* **121**, 10332–10345 (1999).
412. Woertink, J. S. *et al.* A [Cu₂O]₂²⁺ core in Cu-ZSM-5, the active site in the oxidation of methane to methanol. *Proc. Natl. Acad. Sci. U. S. A.* **106**, 18908–18913 (2009).
413. Vanelderen, P. *et al.* Spectroscopic definition of the copper active sites in mordenite: Selective methane oxidation. *J. Am. Chem. Soc.* **137**, 6383–6392 (2015).
414. Akporiaye, D. E., Dahl, I. M., Mostad, H. B. & Wendelbo, R. Aluminum distribution in chabazite: An experimental and computational study. *J. Phys. Chem.* **100**, 4148–4153 (1996).
415. Zhang, T., Qiu, F., Chang, H., Li, X. & Li, J. Identification of active sites and reaction mechanism on low-temperature SCR activity over Cu-SSZ-13 catalysts prepared by

- different methods. *Catal. Sci. Technol.* **6**, 6294–6304 (2016).
416. Hu, C. Y., Shih, K. & Leckie, J. O. Formation of copper aluminate spinel and cuprous aluminate delafossite to thermally stabilize simulated copper-laden sludge. *J. Hazard. Mater.* **181**, 399–404 (2010).
417. Lezcano-Gonzalez, I. *et al.* Determining the storage, availability and reactivity of NH₃ within Cu-Chabazite-based Ammonia Selective Catalytic Reduction systems. *Phys. Chem. Chem. Phys.* **16**, 1639–1650 (2014).
418. Suzuki, K., Sastre, G., Katada, N. & Niwa, M. Ammonia IRMS-TPD measurements and DFT calculation on acidic hydroxyl groups in CHA-type zeolites. *Phys. Chem. Chem. Phys.* **9**, 5980–5987 (2007).
419. Elzey, S., Mubayi, A., Larsen, S. C. & Grassian, V. H. FTIR study of the selective catalytic reduction of NO₂ with ammonia on nanocrystalline NaY and CuY. *J. Mol. Catal. A Chem.* **285**, 48–57 (2008).
420. Jentys, A., Warecka, G. & Lercher, J. A. Surface chemistry of H-ZSM5 studied by time-resolved IR spectroscopy. *J. Mol. Catal.* **51**, 309–327 (1989).
421. Howard, J., Ts, C. & Nicolt, J. M. Fourier-Transform Infrared Studies of Copper-containing. **85**, 1233–1244 (1989).
422. Colella, C. & Gualtieri, A. F. Cronstedt's zeolite. *Microporous Mesoporous Mater.* **105**, 213–221 (2007).